Università degli Studi di Genova

Doctorate Course in Sciences and Technologies of Chemistry and Materials

Curriculum: Material Sciences and Technologies

XXXIII Cycle

Electrospun Nanofibers as a Green Approach for the Development of Advanced Biomedical, Pharmaceutical, and Filter Materials

Candidate

ANDREA DODERO

Supervisor

Prof. Maila Castellano

Abstract

The present Thesis focuses on the fabrication of polysaccharide – based nanofibrous mats via electrospinning technique primarily for, but not limited to, the development of wound healing patches with enhanced tissue regeneration capabilities. Specifically, this project arose to overcome the lack of methodologies concerning the proficient electrospinning of polysaccharides due to their poor processability, the requirement of hazardous and/or toxic solvents, and nanofiber inadequate stability in aqueous environments. To tackle this task, this Thesis proposes the use of poly(ethylene oxide), a biocompatible and water – soluble synthetic polymer able to increase the polysaccharide – based formulation spinnability, along with a simple washing – physical crosslinking treatment to fabricate pure polysaccharide nanofibers with boosted water resistance and marked biocompatibility.

In the first Chapters, after a general discussion concerning the technological relevance and versatility of electrospinning technique together with its main applications, this Thesis concentrates on briefly presenting the properties of polysaccharide materials and their advantages with respect to synthetic polymers, as well as the experimental methodologies and characterization approaches used to achieve the investigated purpose. Then, either alginate or chitosan polysaccharides are employed for the fabrication of nanofibrous mats, whose physical – chemical properties, drug delivery capabilities, and biological responses are fully characterized. As a matter of fact, the developed systems effectively display a significant capacity to promote cell adhesion and proliferation along with proper mechanical, water – related, and drug release features, hence representing promising materials to be used in several biomedical and pharmaceutical products. Finally, the preparation of a multilayer nanofibrous patch comprised of an external hydrophobic stratum and an internal bioactive one is explored and discussed. To this end, combining a polyurethane nanofibrous layer with an alginate nanofibrous layer enriched with ZnO nanoparticles allows the fabrication of potential wound healing patches endowed with superior support and protective performances.

These results are an important first step in making straightforward the electrospinning of polysaccharide materials granting the possibility to easily prepare nanofibrous meshes with potential uses in various application fields, with particular relevance in the biomedical and pharmaceutical industries where the bioactivity of these materials with respect to synthetic polymers plays a topical role.

Acknowledgments

I want to express my deepest and sincere gratitude to my supervisor, Prof. Maila Castellano, for providing me invaluable guidance throughout this PhD work. Her dynamism, vision, sincerity, and motivation have deeply inspired me. It was a great privilege and honour to work and study under her direction and I am extremely grateful for what she has offered me.

I would also like to acknowledge the several collaborators I had during these years:

- Prof. Silvia Vicini and Prof. Marina Alloisio of the Department of Chemistry and Industrial Chemistry of the University of Genova for the precious assistance provided during the whole Thesis project.
- Prof. Sonia Scarfì and Prof. Marina Pozzolini of the Department of Earth, Environment and Life Sciences of the University of Genova for the help with experimental biological procedures related to this Thesis project.
- Prof. Guy Schlatter and Prof. Anne Hébraud of the Institute of Chemistry and Processes for Energy, Environment and Health of the University of Strasbourg for having granted me the possibility to work under their supervision for a few months.
- Prof. Davide Comoretto and Prof. Paola Lova of the Department of Chemistry and Industrial Chemistry of the University of Genova for the help with experimental procedures related to this Thesis project.
- Prof. Ivan Donati of the Department of Life Sciences of the University of Trieste for providing some of the alginate polysaccharides employed in this Thesis project.
- Prof. Alina Sionkowska of the Department of Chemistry of Biomaterials and Cosmetics of Nicolaus Copernicus University in Toruń for providing the chitosan polysaccharide employed in this Thesis project.

Completing this work would not have been possible if not for the support of several colleagues and students: Giulia Gaggero, Stefano Alberti, Elisabetta Brunengo, Stefania Boi, Lara Pianella, Silvia Vita, Nicolas Resio, and Francesco Mancioppi.

Last but not least, I am extremely grateful to my mom and my entire family for their love, caring, and sacrifices for educating and preparing me for my future, and especially to all my closest friends who have given me their support, put up with my odd hours, and provided me with lifts and help.

List of Abbreviations

η	Apparent viscosity
γ	Deformation amplitude
ν	Frequency
σ	Mechanical stress
λ	Relaxation time
τ	Shear stress
η_∞	Infinite – shear viscosity
η_0	Zero – shear viscosity
ε_b	Elongation at break
σ_b	Tensile strength
η_{inh}	Inherent viscosity
η_r	Relative viscosity
η_{red}	Reduced viscosity
η_s	Solvent viscosity
η_{sp}	Specific viscosity
τ_y	Yield stress
$\bar{M}_{lim}$	Limiting molecular weight
$\bar{M}_v$	Viscosity average molecular weight
$\bar{M}$	Average molecular weight
$\dot{\gamma}$	Shear rate
$[\eta]$	Intrinsic viscosity
1D	One – dimensional
2D	Two – dimensional
3D	Three – dimensional
A.nod	Ascophyllum nodosum
Ac	Acetone
AFM	Atomic force microscopy
AS	Amplitude sweep test

c*	Overlap concentration
c**	Concentrated regime concentration
c[η]	Coil overlap parameter
CC	Concentric cylinder geometry
c_e	Entanglement concentration
C_e	Equilibrium concentration
c_{max}	Fedors maximum concentration
CP	Cone – plate geometry
CR	Congo red
CWA	Chemical warfare agent
DD	Degree of deacetylation
DDS	Drug delivery systems
DG	Double – gap geometry
DLS	Dynamic light scattering
DMA	Dynamic – mechanical analysis
DMTA	Dynamic – mechanical – thermal analysis
DSC	Differential scanning calorimetry
DTG	Derivative thermogravimetry
E.coli	Escherichia Coli
E’	Extensional storage modulus
E”	Extensional loss modulus
E_a	Flow activation energy
ECM	Extracellular matrix
EDX	Energy dispersive X – ray
EGDE	Ethylene glycol diglycidyl ether
ES	Electrospinning
FBS	Fetal bovine serum
FESEM	Field – emission scanning electron microscopy
FET	Field – effect transistor
FS	Frequency sweep test
FTIR	Fourier – transform infrared spectroscopy
G’	Shear storage modulus
G”	Shear loss modulus

GAA	Glacial acetic acid
HaCaT	Human keratinocyte cell line
HEPA	High – efficiency particulate air
HS	Human serum
L.hyp	Laminaria hyperborea
L929	Murine fibroblast cell line
LED	Light – emitting diode
LVER	Linear viscoelastic region
M.pyr	Macrocystis pyrifera
MALDI	Matrix – assisted laser desorption/ionization
MB	Methylene blue
MC	Moisture content
Mg – 63	Human osteoblast cell line
MO	Methyl orange
NPs	Nanoparticles
PBS	Phosphate buffer solution
PCL	Poly(caprolactone)
PEO	Poly(ethylene oxide)
PM	Particulate matter
PP	Plate – plate geometry
PU	Polyurethane
PVA	Poly(vinyl alcohol)
PVK	Poly(N-vinylcarbazole)
PVP	Poly(vinyl pyrrolidone)
q_e	Equilibrium adsorption capacity
QF	Quality factor
q_t	Time adsorption capacity
R%	Cumulative release percentage
R^2	Coefficient of determination
RSM	Root mean squared roughness
SA LV	Sodium alginate low viscosity
SA MV	Sodium alginate medium viscosity
SA	Sodium alginate
SAc	Salicylic acid

Saos – 2	Human osteoblast cell line
SEC	Size – exclusion chromatography
SEM	Scanning electron microscopy
SERS	Surface – enhanced raman scattering
TEM	Transmission electron microscopy
T_g	Glass transition temperature
TGA	Thermogravimetric analysis
T_m	Melting temperature
TS	Temperature sweep test
T_{trans}	Shape – memory transition temperature
TTS	Time – temperature superposition principle
WBPU	Water – borne polyurethane
WCA	Water contact angle
WVP	Water vapour permeability
Y	Young modulus
ZnAc	Zinc acetate dihydrate
α	Scaling factor
ζ	Zeta potential

Table of Contents

Abstract **1**

Acknowledgments **3**

List of Abbreviations **5**

Summary **15**

Chapter 1. Electrospinning **23**

1.1 Introduction **25**

1.2 General Principles **28**

1.3 Methods of Electrospinning **32**

1.4 Materials for Electrospinning **36**

1.4.1 Polymers 36

1.4.1.1 Natural Polymers *39*

1.4.2 Small Molecules 40

1.4.3 Colloidal Particles 41

1.4.4 Composites 41

1.5 Applications of Electrospun Nanofibers **43**

1.5.1 Electrospun Nanofibers for Biomedical and Pharmaceutical Applications 43

1.5.1.1 Tissue Repair or Regeneration. *43*

Wound Healing 45

Musculoskeletal Tissue Regeneration 46

1.5.1.2 Drug Delivery *47*

Electrospun Nanofiber Implants for Local Therapy 47

Injectable Short Nanofibers for Local Therapy 48

1.5.1.3 Cancer Research *49*

1.5.1.4 Other Biomedical Applications *49*

1.5.2 Electrospun Nanofibers for Environment and Sustainability 49

1.5.2.1 Purification of Air *50*

1.5.2.2 Treatment of Water *51*

1.5.2.3 Degradation of Harmful Chemicals *52*
1.5.2.4 Recovery of Precious Metals *53*
1.5.3 Electrospun Nanofibers for Catalysis, Energy, Photonics, and Electronics 53
1.5.3.1 Catalysis *53*
1.5.3.2 Energy Harvesting, Conversion, and Storage *54*
1.5.3.3 Light – Emitting Devices *54*
1.5.3.4 Field – Effect Transistors *54*
1.5.4 Electrospun Nanofibers with "Smart" Properties 55
1.5.4.1 Stimuli – Responsive *55*
1.5.4.2 Shape – Memory *55*
1.5.4.3 Self – Cleaning *56*
1.5.4.4 Self – Healing *56*
1.5.4.5 "Living" *57*
1.5.4.6 Sensing *58*
1.5.5 Electrospun Nanofibers in Industrial Applications 58

Chapter 2. Polysaccharides 61

2.1 General Properties 63
2.1.1 Alginate 64
2.1.2 Chitosan 66

2.2 Biomedical and Pharmaceutical Applications of Polysaccharides 69
Tissue Engineering *69*
Wound Healing and Wound Dressing *69*
Drug Delivery and Controlled Release *70*

Chapter 3. Experimental Methodologies and Characterization Techniques 73

3.1 Electrospinning Methodology and Instrumentation 75

3.2 Rheological Investigation 75
Steady – State Viscosity Measurements 75
Amplitude Sweep Measurements 76
Frequency Sweep Measurements 77
Temperature Sweep Measurements 77

3.3 Thermal Investigation 78

3.4 Morphological Investigation 78

3.5 Mechanical and Dynamic – Mechanical Investigation 78

Amplitude Sweep Measurements 79

Frequency Sweep Measurements 79

Temperature Sweep Measurements 79

3.6 Spectroscopic Investigation 79

3.7 Uptake – Release Investigation 79

Kinetic Adsorption Experiments 80

Equilibrium Adsorption Experiments 81

Release Experiments 81

3.8 Water – Related Properties Investigation 82

3.9 Zeta – Potential Investigation 82

Chapter 4. Polysaccharide – Based Electrospun Mats as Wound Healing Patches 85

4.1 Alginate – Based Nanofibrous Mats 87

4.1.1 Optimization of Alginate Electrospinning Process 88

Conclusions 96

4.1.2 Alginate Electrospun Mats Embedding Zinc – Oxide Nanoparticles 98

Conclusions 120

4.1.3 Electrospun Mat Capability to Foster Cell Viability: Effect of Alginate Molecular Structure 121

Conclusions 128

4.1.4 Alginate – Poly(caprolactone) Multilayer Patches 129

Conclusions 141

4.1.5 Alginate – Polyurethane Multilayer Mats 142

Conclusions 157

4.2 Chitosan – Based Electrospun Mats 159

4.2.1 Optimization of Chitosan Electrospinning 160

Conclusions 169

4.2.2 Biological, Physical – Chemical, and Uptake - Release Properties of Chitosan Mats 171

Conclusions 179

4.3 Outcomes 181

Chapter 5. Rheological Characterization of Sodium Alginate – Based Solutions 183

5.1 Introduction 185

5.2 Alginate Molecular Weight and Polyelectrolyte Effect Evaluation 187

Huggins – Kraemer Method 189

Wolf Method 190

Fedors Method 191

Conclusions 197

5.3 Alginate Depolymerization Via Ultrasonic Treatment 198

Conclusions 208

5.4 Outcomes 209

Chapter 6. Other Projects 211

6.1 Polysaccharide – Based Hydrogels 213

6.1.1 Alginate Hydrogels 213

6.1.1.1 Alginate – Based Hydrogels Prepared via an Ionic Gelation Methodology: An Experimental Design Study to Predict the Crosslinking Degree 213

6.1.1.2 Sodium Alginate Cross – Linkable Planar 1D Photonic Crystals as a Promising Tool for Pb^{2+} Detection in Water 214

6.1.2 Agar – Based Hydrogels 214

6.2 Synthetic Polymer – based Electrospun Mats 216

6.2.1 Investigation of the Mechanical and Dynamic-Mechanical Properties of Electrospun Polyvinylpyrrolidone Mats: A Design of Experiment Approach 216

6.2.2 Water – Borne Polyurethane Electrospun Mats Embedding TiO_2 Nanoparticles for Photocatalytic Applications 216

6.2.3 Composite Poly(vinyl alcohol) – Based Nanofibers Containing Gold Nanoparticles as SERS Amplifiers for Wastewater Monitoring 217

List of Figures and Tables 219

List of Figures 219

List of Tables 229

Appendix A: List of Publications 231

Appendix B: Conference Contributions 235

Oral communications 235

Poster Communications 236

References 237

Summary

The present PhD thesis primarily deals with the exploitation of electrospinning technique as a green approach for the fabrication of nanofibrous mats with potential uses as wound dressing patches with superior tissue regeneration capabilities. A wound is a type of injury that can be classified into two distinct categories, namely acute wounds and chronic wounds. Chronic wounds show a prolonged and abnormal inflammation process, with frequent superinfections, the presence of drug – resistant microbial biofilms, and dermal and epidermal cells unresponsive to reparative stimuli. In contrast, acute wounds follow a predictable, well – organized reparative process involving platelets, fibroblasts, keratinocytes, and immune cells. To this end, dressing materials play a crucial role in providing surface protection and drug delivery, regulating bacteriostatic activities, as well as accelerating cell and tissue regeneration. As broadly discussed in Chapter 1, electrospinning is a fabrication approach widely employed to produce two and three – dimensional scaffolds that can be made of different nanofibers with random orientations and in various shapes. In the past decade, these non – woven scaffolds have been widely utilized in regenerative tissue engineering and are efficient for drug delivery in wound treatments. As a matter of fact, previous studies showed that the great porosity and the large surface area make nanofibers efficient to facilitate wound healing through enabling fluid absorption, drug delivery, cell respiration, and gas permeation, at the same time preventing the infiltration of microbial particles and inducing tissue ingrowth. Nevertheless, to date, the exploitation of electrospinning at an industrial level for the large – scale production of nanofibrous products still represents an unsolved challenge with the hit of several practical issues in terms of productivity rate, environmental impact, and product quality. Specifically, it is noteworthy that electrospun nanofibrous wound dressings can be obtained from natural polymers, synthetic polymers, and mixed polymers. Natural polymers offer a wide range of advantages with respect to synthetic ones, including biocompatibility, non – toxicity, solubility in benign solvents, biodegradability, antibacterial features, and favourable mechanical structure, which make them extremely suitable for biomedical applications. In this sense, the use of polysaccharide materials, considered as long carbohydrates composed of monosaccharide units bound together by glycosidic linkages, as main constituents to prepare electrospun meshes represents both an ambitious and intricate research topic, which is currently assuming an increasing deal of interest from the worldwide academic and industrial

community. Owing to their unique features, polysaccharide – based electrospun yarns are of high technological importance in the development of biomedical and/or pharmaceutical products, as well as for a broad range of other applications. However, despite the above – mentioned advantages, the proficient electrospinning of polysaccharides, even at a laboratory scale, is not yet completely understood and it usually implies the use of synthetic co – spinning agents that can affect the overall response of the obtained nanofibers. Additionally, because of their high solubility in aqueous environments, polysaccharide – based products might often be subjected to a crosslinking reaction, which is a critical aspect in ensuring their long – term stability in physiological – like conditions but may also result in the raising of significant toxicity issues. Due to these reasons, sodium alginate (i.e., an anionic copolymer usually extracted from brown algae and comprised of (1 – 4) – linked β-D-mannuronate and α-L-guluronate residues) and chitosan (i.e., a cationic polymer obtained from the partial deacetylation of chitin and comprised of (1 – 4) linked 2-amino-2-deoxy-β-D-glucopyranose) have been selected within this Thesis project to fabricate effective electrospun wound healing patches owing to their unique characteristics, including not only their bioactivity but also the low cost, the abundance in nature, the minimal environmental impact, and the gelling capabilities.

With these premises, the first target of the present Thesis work was to optimize the electrospinning process of polysaccharide – based formulations aiming to establish a simple protocol to fabricate nanofibrous mats with a proper morphology, manageability, and stability in physiological – like environments. As such, as discussed in Section 4.1.1, various alginate raw materials were employed for the purpose with rheology being exploited as a fundamental tool to understand the main parameters affecting the electrospinning phenomenon and the related nanofiber morphology. In detail, the use of poly(ethylene oxide), a biocompatible and water – soluble synthetic polymer, as co – spinning agent was proved to be of topical importance in ensuring a proper electrospinnability of the prepared alginate – based mixtures. Noticeably, once prepared, the obtained nanofibers were subjected to a simple crosslinking treatment consisting of the use of bivalent ions as physical crosslinkers. This process allowed the stabilization of alginate, consequently endowing the nanofibers with the capability to maintain their structure in aqueous environments without the potential risk of incurring in toxicity issues. In addition, despite not being the main goal of this preliminary investigation, the co – spinning agent was proved to be to some extent removable from the prepared nanofibers via a humble washing treatment in water. Thereby, providing useful insights

concerning the electrospinning process of alginate – based mixtures, this initial work allowed us to establish the best working conditions (i.e., raw material type and processing parameters) to develop an electrospun mat with highly promising characteristics in terms of the planned purpose. Subsequently, to obtain a wound healing patch with antibacterial properties, ZnO nanoparticles have been employed as biocide materials due to their biocompatibility, low cost, and ease of fabrication. Specifically, as described in Section 4.1.2, the nanoparticles were synthesized ad – hoc via a green sol – gel approach by using alginate itself as stabilizing agent and directly mixed with the polysaccharide – based formulations prior to the electrospinning process, aiming to ensure their good and homogeneous distribution within the nanofibrous structure. In this case, beyond the physical crosslinking reaction previously optimized, a washing treatment was specially developed and applied to the prepared composite mats to completely remove the co – spinning agent (i.e., poly(ethylene oxide)) without affecting the nanofiber morphology. Successively, the most promising of the so obtained alginate – ZnO electrospun mat was fully characterized to evaluate its effective applicability as a wound healing patch. As such, a complete physical – chemical characterization was first carried out with both the mechanical (i.e., uniaxial tensile test and dynamic – mechanical analysis) and water – related (i.e., water contact angle, water vapour permeability, and moisture content) results indicating the appropriateness of the investigated product for being used as a wound dressing material. Additionally, since the controlled release of drugs and/or other bioactive substances is of topical importance in wound healing processes, the capability of the mat to act as a drug delivery system with tuneable administration kinetics was assessed through uptake – release studies. Noticeably, the results suggested the effective possibility to upload a considerable quantity of drugs within the composite mat by a straightforward impregnation method meanwhile modulating their release by simply changing their chemical structure and loading concentration. Despite the above – mentioned outcomes provided important information concerning the applicability of the explored composite mat as a wound healing patch, much more critical conclusions were then raised from the evaluation of its biological response. In this sense, cell adhesion and proliferation, protein adsorption, as well as antibacterial properties, were evaluated by using a collagen commercial mat as a control sample. Interestingly, despite being collagen a biological material within the human body, both cell adhesion and proliferation results were almost completely comparable, but the presence of ZnO nanoparticles conferred to the alginate – based mat considerably stronger antibacterial capabilities. Based on these preliminary yet promising results, a similar approach was then followed for the development of a wound healing patch comprised of chitosan – based

nanofibers, as described in Section 4.2.1 and in Section 4.2.2. To this end, after an initial optimization of the electrospinning process by means of rheological and morphological investigation, being the stabilization of chitosan nanofibers somehow more difficult with respect to alginate, various coagulation and crosslinking approaches were explored to compare a commonly employed chemical reticulation with a safer and more eco – friendly physical method. Specifically, the use of phosphate ions as physical crosslinkers led to outstanding well – defined nanofibers with a much more homogeneous and defect – free structure compared to the covalently crosslinked ones, at the same time allowing the complete elimination of the used co – spinning agent. Consequently, the achieved physically crosslinked chitosan – based nanofibrous patch was deeply characterized in terms of mechanical and water – related features, as well as for its drug delivery capabilities, showing promising properties in terms of tissue regeneration applications, similarly to what observed for alginate – based nanofibers. In addition, the evaluation of cell adhesion and cell proliferation indicated the explored mat as capable of especially foster osteoblast cell viability, hence being to some extent even more suitable to promote bone healing and repair.

The results summarized so far undoubtedly indicated the prepared polysaccharide – electrospun mats as extremely promising to be used as wound healing patches. However, beyond the fact that the microstructure, the physical – chemical, and the biological features of such products are critical aspects in conditioning their capability to promote tissue regeneration, wound dressing materials should also be able to act as both mechanical supports and protective systems with respect to the wound site and toward the external environment. However, due to their great hydrophilicity and tendency to absorb a high amount of water, alginate and chitosan – based nanofibers do not fully satisfy the described requirements. Consequently, the second target of this Thesis work consisted in the development and optimization of an advanced multilayer system comprised of an internal/inferior alginate electrospun layer enriched with ZnO nanoparticles, which was supposed to act as the bioactive stratum for tissue reparation, and an external/superior electrospun layer with marked hydrophobicity and mechanical resistance, which was supposed to act as the protective stratum. As such, poly(caprolactone), a broadly employed polymer in the biomedical industry, was first selected owing to its biocompatibility, biodegradability, and ease of processability via electrospinning. As examined in Section 4.1.4, after a brief optimization of the fabrication procedure of poly(caprolactone) – based nanofibers, alginate – ZnO nanofibers were directly electrospun on such a layer hence obtaining a multilayer structure that was subjected to a washing – crosslinking treatment based on the previous results. Despite the water – related

properties (especially the marked hydrophobicity of the external layer) and the drug delivery capabilities indicated such a system as promising to be employed for tissue reparation purposes, the poor mechanical performances displayed by the multilayer structure considerably reduced its effective applicability. Therefore, hoping to solve this unexpected limitation, polyurethanes were finally investigated for the fabrication of the external stratum of the multilayer electrospun scaffolds. In this regard, aiming to keep the overall biocompatibility as high as possible and to reduce the environmental impact of the entire preparation procedure, water – borne polyurethanes (i.e., polyurethane nanoparticles dispersed in water) were especially employed to avoid the use of hazardous organic solvents. Thereby, as presented in Section 4.1.5, the electrospinning of the mat external layer was optimized by using poly(ethylene oxide) as carrier polymer and investigating the effect of the component ratio on the resultant mat properties. Specifically, beyond the fact that pure polyurethane nanofibers could be obtained by a simple post – processing washing treatment, increasing the percentage of polyurethanes in the starting formulations led to better defined nanofibers with enhanced mechanical and water – repellent performances. Remarkably, the combination of such an external polyurethane electrospun layer with that comprised of alginate nanofibers embedding ZnO nanoparticles allowed the fabrication of a multilayer wound healing patch endowing both marked protective capabilities and noticeable tissue regeneration features, as well as tuneable drug delivery properties.

This Thesis work demonstrated a simple and novel methodology for the development of stable multilayer nanofibrous mats comprised of a bioactive polysaccharide – based stratum capable of effectively promoting tissue regeneration and an inert polyurethane – based stratum able to confer both mechanical stability and protective capabilities. However, the preparation of such a product on a large – scale requires to be optimized along with its extensive testing. As such, the likewise future path of the present Thesis project aims to develop commercial systems through the following steps:

i) Optimization of high production rate electrospinning procedures. To ensure the large – scale applicability of the proposed wound healing patches, the development of a high throughput electrospinning setup requires to be optimized aiming to completely fulfil the market requirements.

ii) Use of various drugs and evaluation of polysaccharide degradation kinetic. Despite the drug delivery capabilities of the proposed wound healing patches were vastly assessed in this Thesis work, the use of various drugs and the evaluation of their release kinetics is of fundamental importance in developing safe and efficient drug delivery systems. In addition, the degradation

kinetics of the polysaccharide – based nanofibers in physiological – like conditions need to be investigated to ensure compatibility with the tissue regeneration time.

iii) In vitro experimentation. Even if various biological tests, such as cell adhesion, cell proliferation, protein adsorption, and antibacterial properties, were performed during this Thesis work on the proposed wound healing patches providing outstanding promising results, these still represent a preliminary investigation. As such, a deeper characterization of the mat biological response must be assessed *in vitro*.

iv) Development of an actual prototype and in vivo experimentation. Finally, an actual prototype should be developed and used to perform *in vivo* testing.

Fundamentals

Chapter 1. Electrospinning

This Chapter aims to provide a comprehensive description of both electrospinning technology and applications of electrospun nanofibers. After a brief introduction concerning the history of electrospinning, the attention is then focused on the general physical principles regulating such a process. Subsequently, the main materials employed to prepare nanofibers are deeply discussed along with several possible methods of electrospinning. Finally, a summary of the applications of electrospun nanofibers is reported with a great emphasis on the development of biomedical and pharmaceutical products

1.1 Introduction

Fibers, both as continuous filaments and elongated objects, are ubiquitous in nature. For instance, cellulosic fiber – like structures are easily found in almost any plants,[1] whereas spiders commonly rely on webs of silk fibers to capture their preys.[2] These and many other natural systems have served as an important source of inspiration for the development of man – made fibers. Indeed, fibers have been a fundamental part of human life since the dawn of civilization with the possibility to trace the history of mankind fiber production back to prehistoric times. However, it is only since the spindle invention around 1300 that fibers from wool and cotton started to be fabricated for the production of fabrics and clothes. Then, this practice slowly evolved into the textile industry in the 1880s with rayon, which is made of cotton or wood cellulose fibers and was first reported in 1891 but commercialized only in 1911, hence representing the first man – made fabric.[3] About 50 years later, synthetic fibers started to be produced along with the development of chemistry and polymer science. For instance, in 1938, nylon was presented by DuPont as the first commercially available synthetic fiber and immediately caught the public attention,[4,5] with many other types of polyesters and synthetic polymers shortly after employed for the manufacturing of synthetic fibers.[6]

Many methods have been developed for producing fibers from both natural and synthetic polymers, and the most notable are those based on wet, dry, melt, and gel spinning.[7] Wet spinning involves a spinneret submerged in a coagulation bath. When a polymer solution is extruded from the spinneret into the bath, the polymer is precipitated due to dilution effects with the subsequent generation of fibers via solidification.[8] For dry spinning, a polymer solution is extruded into the air through a spinneret and fibers are obtained as result of solvent evaporation from the jets aided by a stream of hot air.[9] During melt spinning, a polymer melt is extruded from a spinneret to generate fibers upon cooling.[10] Gel spinning is instead used to produce fibers with high mechanical strength or other special properties by spinning a polymer in the "gel" state, followed by drying in the air and then cooling in a liquid bath.[11] In all these spinning processes, jets are mainly formed under external shearing forces and/or mechanical drawing when passing through spinnerets, and fibers are formed upon solidification of the jets as a result of precipitation or drying. Thus, jets are only stretched to a limited extent, corresponding to the formation of fibers with diameters typically in the range of 10 – 100 μm.[12] Even applying further mechanical stress during the solidification process or after complete cooling of the jets, the resultant fibers can hardly reach the sub – micrometer scale.

In 1887, Charles V. Boys reported that fibers could be drawn from a viscoelastic liquid in the presence of an external electric field by using an insulated dish connected to an electrical supply.[13] Today largely known as electrospinning (ES), such technique opened the door to the production of polymer fibers with diameters ranging from tens of nanometers to several micrometers,[14] even if ultrathin electrospun fibers with diameters down to 1 nm have also been reported.[15] Actually, the history of electrospinning starts in the 17th century and continues till today.[16] In 1600, William Gilbert is the first who observed the formation of a cone – shaped water droplet in the presence of an electric field. About 100 years later, Stephen Gray observed the electrohydrodynamic atomization of a water droplet from which a very fine stream was generated. Then, in 1747 Abbé Nollet carried out the first known electrospraying experiment, proving that water could be sprayed as an aerosol when passing through an electrostatically charged vessel placed next to the ground. However, only in 1882 the behaviour of charged droplets was systematically investigated by Lord Rayleigh, who theoretically estimated the maximum quantity of charges that a liquid droplet could carry before liquid jets would be ejected from the surface, thereby introducing electrospinning as a simple variant of electrospraying. The major differences between the two phenomena consist in the viscosity and viscoelasticity of the involved liquids, with electrospinning allowing to maintain a continuous polymer jet to produce fibers instead of breaking into droplets as with electrospraying. With these premises, in the early 20th century, two patents describing a prototype setup for electrospinning were filed by John Cooley and William Morton, respectively. Subsequently, two other patents were recorded in 1934 and 1944 by Anton Formhals moving towards the commercialization of electrospinning for the fabrication of textile yarns. Nanofibers prepared via electrospinning were also implemented in the Soviet Union in 1938 for the development of air filters for capturing aerosol particles, which led to the establishment of a factory for the manufacturing of smoke filters with nanofiber – based mats as gas masks. Simultaneously, a mechanistic deep understanding of electrospinning was slowly developed. Geoffrey Taylor published several pioneering papers between 1964 and 1969, showing how to mathematically describe and model the spherical to conical shape change of a polymer solution or melt droplet under the influence of a strong electric field, which is now commonly referred to as Taylor cone. Despite a broad number of applications and related patents were proposed in the following years for electrospun mats, the development of electrospinning technique experienced two decades of stagnancy and it did not gain a lot of attention from academia or industry. It was only in the early 1990s that several research groups began to intensively explore electrospinning again. In particular, Darrell Reneker and Gregory

Rutledge demonstrated that many different polymers could be electrospun into nanofibers, thus bringing new life to this technique that subsequently became the method of choice for producing long and continuous fibers with diameters down to the nanometer scale. At the beginning of the current century, when its capability was further expanded by switching to new materials and formulations for the fabrication of composite and ceramic nanofibers, electrospinning started to acquire an even greater interest.[17,18] As such, owing to the possibility to obtain completely novel materials, a broad number of innovative applications such as catalysis and energy harvesting, which were traditionally dominated by inorganic nanoparticles, quickly started to emerge for nanofibers prepared via electrospinning technique. At the same time, various strategies were developed to control the structure and alignment of electrospun nanofibers[19], to prepare continuous yarns[20], and to obtain core – shell and hollow nanostructures via coaxial electrospinning.[21] These outstanding achievements make electrospinning a versatile and viable technology for the production of nanofiber – based materials to target a broad range of applications. Indeed, to date industrial production lines have been designed and implemented by several companies to manufacture electrospun nanofibers in large volumes, enabling downstream commercial products. For instance, electrospun nanofibers are nowadays widely used for water and air filtration, ranging from industrial products to civilian goods, with more and more biomedical products based on electrospun nanofibers being approved for clinical uses. A schematic summary of the major milestones for the development of electrospinning is shown in Figure 1.[22]

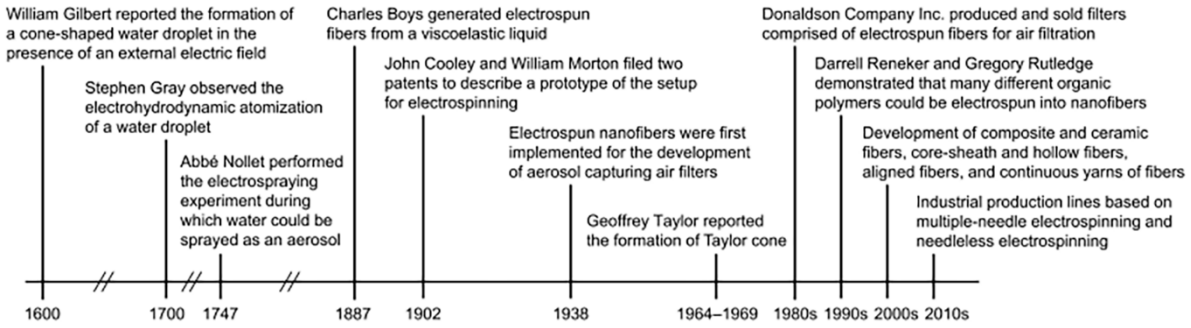

Figure 1. Summary of the development history of electrospinning. Reproduced with permission from Ref. [22].

1.2 General Principles

Electrospinning mainly consists of an electrohydrodynamic process during which a liquid droplet is electrified to generate a jet, followed by stretching and elongation phenomena to generate fibers. The basic setup for electrospinning is rather simple and involves a high voltage supply, a syringe pump, a spinneret (i.e., usually a flat – tip needle), and a conductive collector as shown in Figure 2-a.[22,23] During the process, the liquid is extruded from the spinneret to obtain a stable pendant droplet as a consequence of the surface tension. Upon the application of a strong electric field, the electrostatic repulsions among the surface charges deform the droplet into the Taylor cone, from which a charged polymer jet is then ejected. The jet first extends in a straight line and subsequently undergoes a strong whipping motion due to bending instabilities. As the jet is forced into thinner diameters, it quickly solidifies leading to the formation of solid fibers that are deposited on the grounded collector.[24]

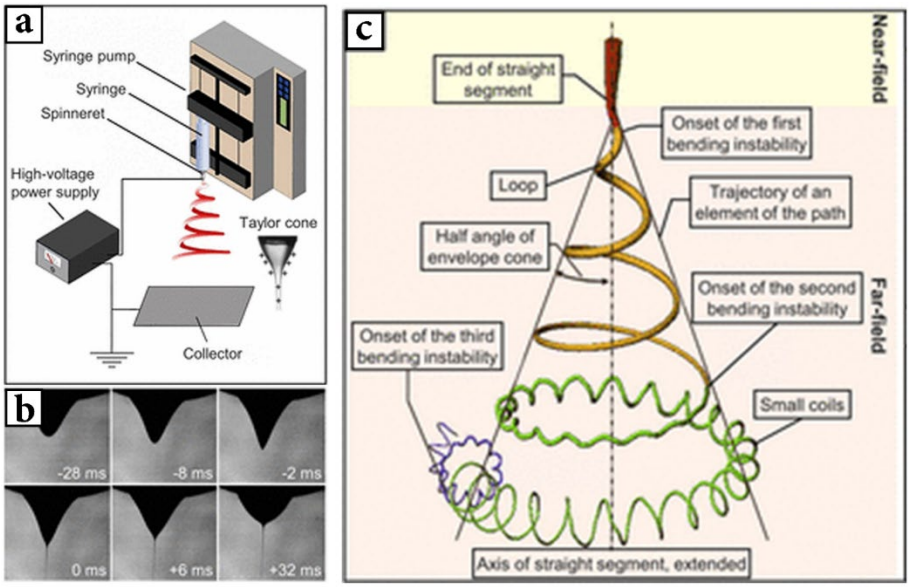

Figure 2. (a) Basic setup for electrospinning. (b) Photographs showing the evolution of a pendant drop of poly(ethylene oxide) in water from a spherical to a conical shape, followed by the ejection of a jet. (c) Diagram showing the path of an electrospun jet. Reproduced with permission from Ref. [22].

The electrospinning process can be divided into four consecutive steps:

i) Formation of Taylor cone upon charging a liquid droplet. During electrospinning, the liquid is commonly fed through the spinneret at a constant and tuneable rate using a syringe pump. When a potential difference between the spinneret and the collector is applied, positive and negative charges undergo separation within the liquid and the ones with the same sign as the spinneret polarity migrate toward the surface of the droplet, hence producing a charge excess.

While the surface tension effect is to favour a spherical shape to minimize the total surface free energy, electrostatic repulsion tends to deform the droplet shape to increase its surface area and minimize the repulsion. As such, the droplet is assumed to take a shape that minimizes the sum of the electrostatic energy and the surface free energy.[25] When the electric field reaches an adequate strength at a critical voltage, which is dependent on the properties of the liquid, the electrostatic repulsion becomes strong enough to overcome the droplet surface tension. Consequently, the droplet is deformed into a conical shape (i.e., Taylor cone).[26] Pictures in Figure 2-b represent the gradual deformation of a pendant drop of poly(ethylene oxide) in water into a conical shape before a polymer jet is ejected.[27]

ii) Stretching of the charged jet. From the apex of the Taylor cone, an electrically charged jet is ejected, accelerated, and extended in the direction of the electric field while moving towards the collector.[28] In the past years, based on both experimental observations and electrohydrodynamic theories, several models have been developed and proposed to describe the behaviour of the charged jet allowing to achieve a deep understanding of the electrospinning mechanism,[29–31] at the same time greatly assisting in the design of new setups and in the control of the processing parameters to obtain nanofibers with desirable diameters and structures. As reported in Figure 2-c,[25] the jet initially follows a straight line for a certain length, which is known as the near – field region, from the tip of the spinneret with the viscoelastic properties of the fluid suppressing the so – called Rayleigh instability and avoiding the breakage of the jet into droplets.[32]

iii) Thinning of the jet. During the acceleration of the jet as a straight line, both the surface tension and viscoelastic forces tend to prevent it from moving forward, which results in a gradual attenuation of its acceleration.[27] Meanwhile, the jet diameter in the straight segment decreases with distance away from the tip due to the stretching phenomenon. Once the acceleration is almost completely annulled, even the smallest perturbation can destroy the straight movement. As such, instabilities can easily arise due to the electrostatic repulsions among the surface charges residing on the jet leading to the far – field regime.[33] Three different types of instabilities may occur within this region, as illustrated in Figure 2-c. The first one is axisymmetric and known as Rayleigh instability, which may lead to the jet breakup with the formation of droplets being dominated by the surface tension. The second one is also axisymmetric and occurs at a higher electric field with respect to the first type. The third instability, which is known as whipping or bending instability, is non – axisymmetric and describes long wave perturbations to the jet caused by the electrostatic repulsion among surface charges in a strong electric field.[22] All these instabilities grow at different rates and are

dependent on both the physical – chemical properties of the liquid and the electrospinning working parameters, with the rapid growth of whipping instability being critical to achieving thin nanofibers. As a matter of fact, the bending perturbation creates a lateral force perpendicular to the jet axis, which in turn generates a radial component for the velocity forcing the jet to quickly bends by an angle of about 90°. Hence, the jet trajectory evolves into a series of loops leading to a coil with many turns around the original direction and consisting of one continuous, looping, spiralling, and gradually thinning jet that whips at a very high frequency assuming a conical shape known as "envelope cone". During the whipping process, the length of the jet can be elongated by up to 10000 times within a very short time period and with an extremely high elongation rate, resulting in the reduction of the fiber diameter by several orders of magnitude prior to deposition on collector.[34] In addition to bending phenomena, other typical instabilities such as branching and capillary instability have also been observed.[35]

iv) Solidification of the jet and deposition of fibers. As the elongation process occurs, the jet solidifies to form fibers because of the solvent evaporation or the cooling of the melt. The slower the solidification phenomenon, the longer is the elongation process of the charged jet with the consequent formation of fibers with a thinner diameter. Even if the charges can still be trapped on the surface of the dried fibers, all the instabilities cease after the solidification of the jet occurred.[36] The final step of the electrospinning process consists of the deposition of fibers on a grounded collector, with their morphology being mainly determined by the stage of bending instability in which the fibers are deposited. Commonly, the fibers are collected in the loop region of the first bending instability as a nonwoven mat on a stationary or moving collector. However, the fibers collected within the second and third whipping instability regions may take complex patterns. In any case, most of the charges on the fibers are quickly dissipated through the grounded collector besides a measurable amount of residual charges still remain on their surface due to the low conductivity of most polymer materials.[37] These residual charges tend to repel the similarly charged jet causing a pendulum – like motion of the electrified jet, which in turn reduces the thickness of nonwoven electrospun mats to an upper limit of about 0.5 – 1 mm.[38]

The fiber formation during electrospinning and the control of their diameter are strongly determined by the processing parameters, among which the applied voltage, the flow rate of the liquid, and the distance between the spinneret and the collector play the most important role. The applied voltage directly influences the charge carried by the jet and the intensity of the repulsions between the charges, along with the magnitude of the interactions occurring

between the jet and the external electric field. In general, a higher voltage promotes the formation of thinner fibers, despite it could also favour the ejection of more fluid with the consequent raising of fibers with thicker diameters.[39,40] Concerning the flow rate of the liquid, any increase typically leads to enlarged fibers due to the higher amount of materials ejected from the spinneret. For what concerns the distance between the tip of the spinneret and the collector, it influences the stage of instability at which the jet is deposited. A long enough distance is required to achieve the full extension and solidification of the jet, with thinner fibers usually obtained as the distance is increased. However, beyond a certain distance range, due to the complete solidification of the jet during the electrospinning, the fibers do not show any diameter decrease. In general, it is the intricate interplay of all the described processing parameters involved in the process that controls the morphology and dimension of the fibers.

1.3 Methods of Electrospinning

Electrospinning is commonly carried out in the far – field mode by using a hollow needle as spinneret and a metal substrate (e.g., aluminium foil) as collector. This simple setup is mainly exploited to produce small nanofiber volumes in a laboratory setting, for evaluating the electrospinnability of novel materials, or for optimizing the parameters of electrospinning before starting a large – scale production. Based on this general and simple setup, various modifications (Figure 3) have been developed to further increase the capability and versatility of electrospinning:

i) Far – field versus near – field. During electrospinning, the working distance between the spinneret and the collector influences the stage at which the fibers are deposited on the collector. Conventional electrospinning is conducted in the far – field mode leading to nonwoven mats because of the difficulty in controlling the deposition of the formed fibers. If the distance is reduced, near – field electrospinning can be instead obtained with the jet impacting onto the collector within the straight segment.[41] In this case, since the electric field is strongly concentrated between the spinneret and the collector, the applied voltage can be lowered to several hundred volts (typically 0.6 – 3 kV). Additionally, the flow rate of the liquid must be reduced to 0.01 – 1 mL/h to support a stable jet.[42] Due to the lack of bending instability, near – field electrospinning allows for the deposition of fibers with a high spatial definition despite they commonly take a large diameter on the scale of several micrometers.[43]

ii) Single needle versus multiple needles. The typical setup for electrospinning consists in a single needle, with a consequent low throughput usually corresponding to 1 – 5 mL/h by flow rate or 0.1 – 1 g/h by fiber mass. Multiple – needle electrospinning offers a straightforward route to enhance productivity by means of an array of hollow needles, as shown in Figure 3-a, from which several jets can be simultaneously ejected. Besides the already above – discussed classic parameters, the spacing between the needles, their number, and the layout of the array are fundamental features to be considered and optimized to enable multiple – needle electrospinning.[44]

iii) Hollow spinneret versus solid spinneret. Both hollow and solid spinneret can be employed in combination with electrospinning as long as the external electric field can initiate the ejection of a jet. Hollow spinnerets are associated with an enclosure through which the liquid is extruded, whereas solid spinnerets allow multiple jets to emanate simultaneously from a surface for electrospinning. Typical hollow spinnerets are represented by hypodermic needles with an inner diameter in the range of 0.3 – 1 mm or by tubes containing multiple holes on

their wall.[45] Examples of solid spinnerets consist of solid pins,[46] flat plates,[47] jagged metallic plates (Figure 3-b),[48] and stepped pyramids (Figure 3-c).[49]

iv) Simple spinneret versus coaxial spinneret. Typically, a simple hollow needle is used for electrospinning. However, a coaxial needle consisting of two concentric hollow needles can also be employed to generate a coaxial electrified jet, as shown in Figure 3-d.[50]

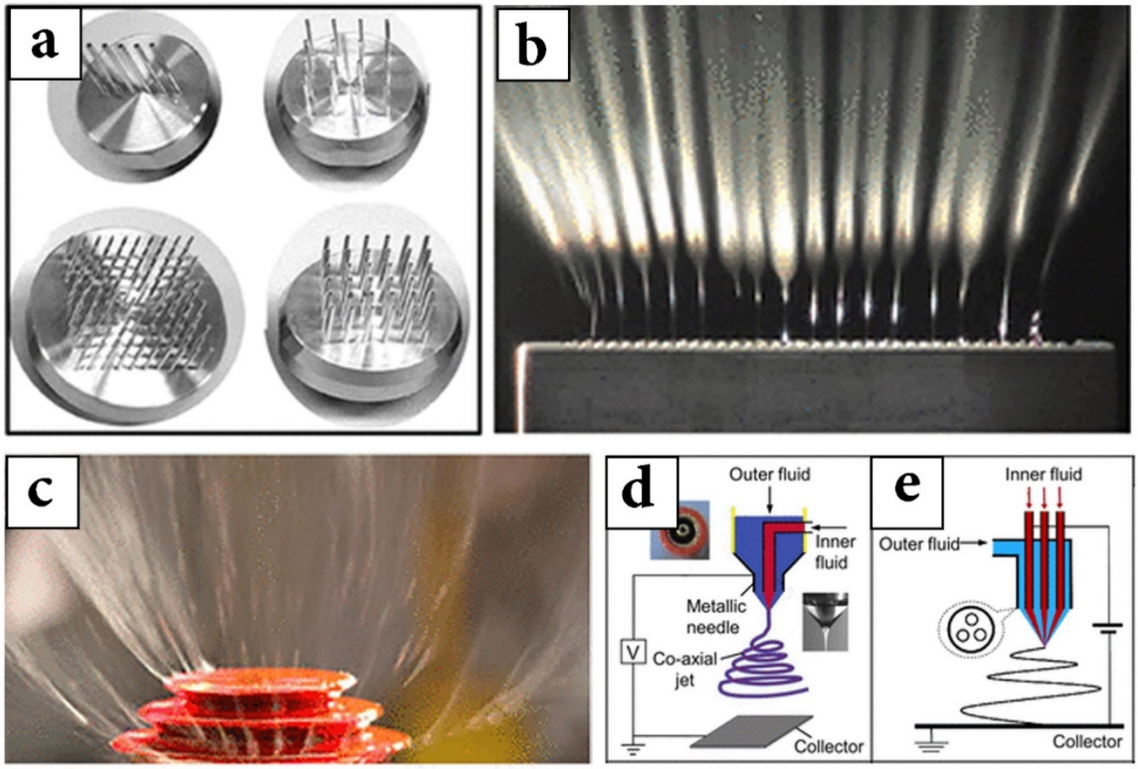

Figure 3. (a) Examples of needle arrangement for multiple – needle electrospinning. Reproduced with permission from Ref. [51]. (b) Photograph of an electrospinning process that uses a jagged metallic plate as solid spinneret. Reproduced with permission from Ref. [48]. (c) Photograph of an electrospinning process that uses a stepped pyramid as solid spinneret. Reproduced with permission from Ref. [52]. (d) Schematic illustration of a coaxial electrospinning setup. Reproduced with permission from Ref. [50]. (e) Schematic illustration of an electrospinning setup using a spinneret comprised of three metallic needles inserted in an outer needle in the pattern of an equilateral triangle. Reproduced with permission from Ref. [53].

When the core and shell fluids get in contact at the exit end of the needle, the shell fluid wraps around the core one to create a compound Taylor cone in the presence of an external electric field, with the subsequent ejection of a coaxial jet that in turn allows obtaining core – sheath nanofibers. The key factor in coaxial electrospinning is to ensure that the inner and outer fluids form a compound jet and stay concentrically together,[54] with both the properties of the fluids and the processing parameters playing an instrumental role in the process. Specifically, the two fluids must have sufficient viscosities to keep the jet continuous and be immiscible to allow their simultaneous stretching avoiding mixing and/or inversion phenomena. If the core and

shell fluids are partially miscible with each other, a blend of the two materials can be formed at the interface of the core – sheath nanofibers. Additionally, the two fluids should possess similar dielectric properties, whereas the flow rates need to be adjusted to ensure the wrapping of the inner fluid by the external one.[55] Different types of materials, such as polymers, oligomers, metal salts, proteins, oils, liquid crystals, and even cells, bacteria, and viruses can be incorporated into the inner layer of core – sheath nanofibers. Coaxial electrospinning also makes it possible to fabricate hollow nanofibers by selectively removing the core from the as – spun nanofibers[56] and multiple core – sheath nanofibers (Figure 3-e).[53]

v) Conductive solid collector versus liquid bath collector. Typically, electrospun nanofibers are collected on a grounded collector such as an aluminium foil, but to better control the deposition procedure various types of conductive solid collectors, as well as liquid bath collectors, have been developed. Some examples are reported in Figure 4. Conductive solid collectors can be employed either in a stationary or movable configuration. Stationary collectors can modulate the distribution of the electric field and guide the collection of the nanofibers in two ways: patterning the surface of a conductive substrate with specific structures[57,58] or combining substrates with different conductivities to form a pattern.[59,60] As such, nanofibers can be collected in well – controlled designs such as parallel lines, woven lines, regular hexagons, and circular holes. Other types of much more sophisticated homemade static collectors have also been designed to further extend the capability of electrospinning.[61–63] Beyond static configurations, solid collectors can also be programmed to move along various directions or be designed as rotating objects (e.g., mandrel, wire, disc, drum, wheel, conveyor, cone, etc.) to offer a straightforward method to produce aligned nanofibers.[64,65] Other unique collectors, such as rotary funnel and rotary rings, have been developed to obtain nanofibers with specific structures. Alternatively, an insulating liquid placed in a container below the spinneret can also be employed as collector. The liquid can act as coagulation bath in order to enhance the solidification of the jet[66] or enable the generation of fibers with unique features.[67] On pair with insulating liquids, conductive liquids (e.g., electrolyte solutions) can also be employed as collectors generating an electric field distribution similar to the case of the metallic ones, therefore promoting the selective deposition of the fibers towards their surface.[68,69]

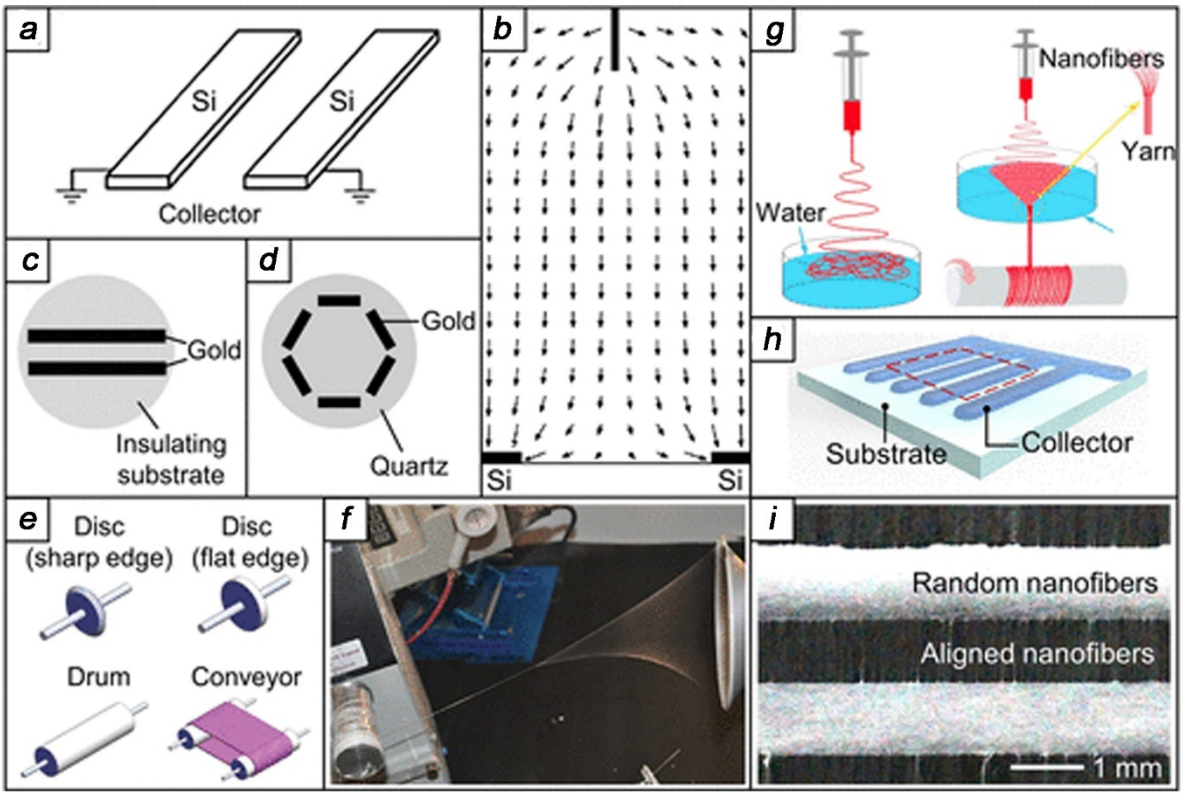

Figure 4. (a) Schematic illustration of a collector comprising two conductive substrates and (b) calculated electric field vectors. Reproduced with permission from Ref. [60]. (c) and (d) Schematic illustrations of patterned collectors consisting in gold electrodes deposited on an insulating substrate. Reproduced with permission from Ref. [59]. (e) Schematic illustration of rotatory solid collectors. Reproduced with permission from Ref. [64]. (f) Formation of a nanofibrous yarn using a rotatory metal funnel as collector. Reproduced with permission from Ref. [70]. (g) Schematic illustration of a liquid bath collector setup. Reproduced with permission from Ref. [67]. (h) Schematic illustration showing the use of a conductive liquid as collector and (i) SEM micrograph of a patterned mat. Reproduced with permission from Ref. [69].

1.4 Materials for Electrospinning

Electrospinning has been employed in the past decade to prepare nanofibers from various types of materials, with the most common ones consisting of organic polymers in the form of solutions or melts. However, even small molecules can be electrospun into nanofibers if they self – assemble and generate enough chain entanglements. Additionally, by exploiting sol – gel chemistry, a broad variety of composite materials have also been prepared in the form of nanofibers via electrospinning.[71] A brief account of all these materials in the context of electrospinning is given in the following Sections.

1.4.1 Polymers

Most of the organic polymers can be directly electrospun as long as they dissolve in appropriate solvents to obtain solutions (i.e., solution electrospinning) or melts without showing degradation (i.e., melt electrospinning). In solution electrospinning, the jet of a polymer solution is stretched, elongated, and thinned by whipping instability while the solvent is quickly evaporated leading to the solidification of the jet and the deposition of solid nanofibers on the collector.[72] Figure 5-a shows a scanning electron microscopy micrograph of a typical electrospun sample, indicating that the nanofibers are deposited in the form of a nonwoven mat. More than 100 different organic polymers, including both synthetic and natural ones, have been successfully employed in solution electrospinning to prepare nanofibers. For instance, synthetic polymers such as polystyrene and poly(vinyl chloride) have been electrospun into nanofibers for applications related to environmental protection. Several biocompatible and biodegradable polyesters, such as poly(caprolactone), poly(lactic acid), and poly(lactic – co – glycolic acid) have been exploited to prepare nanofibrous scaffolds for biomedical and pharmaceutical applications. Natural biopolymers (i.e., proteins and polysaccharides) have also been electrospun from their solutions for various purposes. Additionally, conductive polymers, such as polyaniline and polypyrrole, and several functional polymers, such as poly(vinylidene fluoride), have been used to prepare nanofibers with electromechanical, piezoelectric, and pyroelectric features. Solution electrospinning and the morphology of the related nanofibers are dependent on a set of parameters related to the used polymer, solvent, polymer solution, processing parameters, and ambient conditions.[23,73] For instance, the molecular weight of the polymer has a great influence on the rheological behaviour and electrical properties of the solution. Usually, lowering the molecular weight promotes the formation of beads rather than

fibers due to the limited entanglements between the chains.[74] Yet, solvents with a high solubility parameter do not necessarily produce suitable solutions for electrospinning. For highly volatile solvents the jet may solidify immediately after its ejection from the spinneret, whereas for poorly volatile solvents the fibers could be still too wet during the deposition step. Additionally, solvents with a greater dielectric constant require a higher applied voltage to achieve a stable jet due to the attenuation of the electrostatic repulsion among the surface charges residing on the jet.[75] Other important features influencing a polymer solution spinnability are represented by its concentration and electrical conductivity. A minimum concentration is indeed required to ensure the chain entanglement critical to the transition between electrospraying and electrospinning.[76] Below this concentration, the polymer chain interactions are too weak to overcome the Rayleigh instability and the jet tends to break into droplets leading to the collection of fine polymer beads rather than continuous nanofibers. As the concentration increases, the shape of the beads changes from spherical to spindle – like until uniform fibers are obtained due to the increase of chain entanglements and viscosity. However, if the concentration is too high, the viscoelastic forces may be extremely difficult to overcome and no jet is formed. In general, within a certain range, reducing the concentration allows obtaining thinner nanofibers with the related decrease of solution viscosity and surface tension further promoting the phenomenon. Still, the same effect can also be obtained by using surfactants rather than reducing the polymer concentration.[39,77] For the electrical conductivity, poorly conductive solutions can be hardly electrospun due to the difficulty to conduct charges from the interior of the solution to its surface. Conversely, it is challenging to generate the Taylor cone or initiate bending instability for highly conductive solutions since the charges cannot be accumulated on the surface of a conductive droplet or jet.[78,79] The processing parameters (e.g., applied voltage, flow rate of the polymer solution, and spinneret – collector working distance between, etc.) affect the morphology and size of the fibers as already discussed in Section 1.2. The environmental conditions, such as temperature and relative humidity, also play an important role in conditioning solution electrospinning. The relative humidity influences the solvent evaporation rate. Too low values may indeed hinder the proper extension of the jet, whereas too high values can induce the water vapour permeation within the fibers with consequent changes in their morphology.[80] Concerning the temperature, higher values lead to a decrease of solution viscosity and surface tension favouring the formation of thinner fibers despite the increase of solvent evaporation rate may reduce the jet extension.[81]

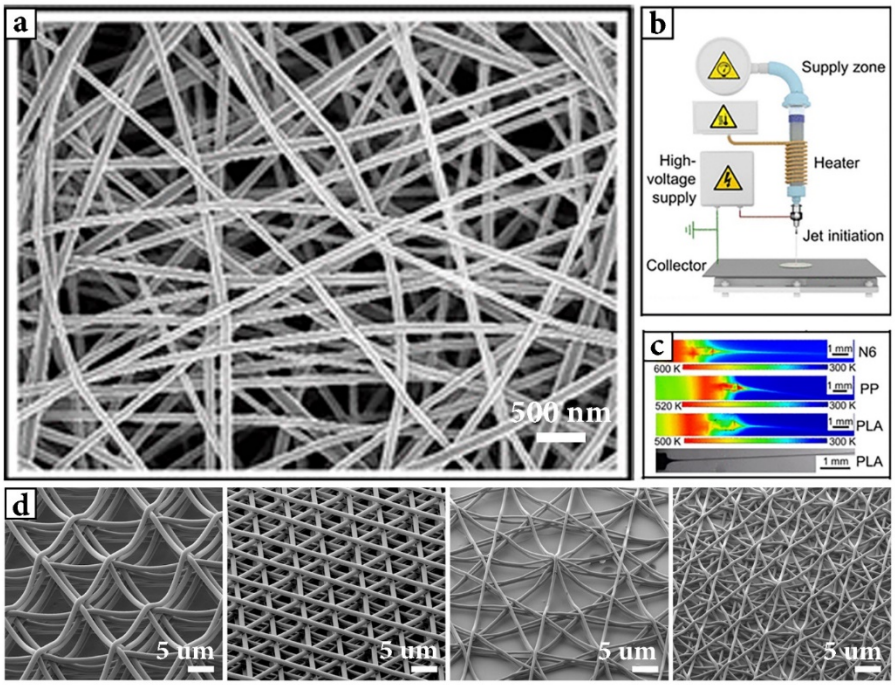

Figure 5. (a) SEM micrograph of a typical example of electrospun nanofibers. (b) Schematic illustration of a setup for melt electrospinning onto a static collector. Reproduced with permission from Ref. [82]. (c) Temperature profiles showing the rapid cooling of electrospun nylon-6, poly(propylene), and poly(lactic acid) molten jets. Reproduced with permission from Ref. [83]. (d) Electrospun structures obtained via melt electrospinning. Reproduced with permission from Ref. [84].

In melt electrospinning, polymers are directly electrospun from their high temperature melts by using a suitable heating device to maintain the molten state in the spinneret (e.g., electrical heating tape, circulating fluid, lased, etc.),[85] with the typical setup illustrated in Figure 5-b. After the ejection from the spinneret, the molten jet cools and solidifies to generate fibers with the presence of the electric field strongly enhancing the heat transfer (up to 1 order of magnitude) due to the electrodynamic effects.[86] Figure 5-c reports the images captured using an infrared camera revealing the temperature profiles of the molten jets of nylon – 6, poly(propylene), and poly(lactic acid), respectively.[83] The electrodynamic quenching leads to the fast cooling and solidification of the jet, hence strongly reducing the degree of stretching of the jet. Additionally, since in melt electrospinning the whipping instability is largely suppressed compared to solution electrospinning due to the lower electrical conductivity and higher viscosity, the jet usually travels in a simple straight line and much thicker fibers (i.e., micrometer scale) are achieved.[87] To date, only a small number of commercially available polymers have been successfully employed for melt electrospinning due to the fact that they must possess a glass transition and melt at a temperature not involving degradation. Therefore, it does not work for thermosets, proteins, and thermally unstable polymers. The electrospinnability of a polymer melt critically relies on its viscosity and electrical

conductivity, but also the processing parameters have impacts on the process. For example, the flow rate is typically low (i.e., < 0.1 mL/h) to obtain thin fibers. The temperature of the melt in the spinneret, the applied voltage, and the working distance are other important factors to be considered.[88] In addition, the lateral movement of the spinneret and/or of the collector strongly affects the shape of the jet with consequent marked changes in the fiber morphology. The temperature of the surrounding air is another critical parameter to be considered. Specifically, if the air is heated, the jet cooling rate is slower so helping the formation of thinner nanofibers.[87] Generally speaking, owing to the absence of solvents, melt electrospinning represents a much "greener", safe, and highly productive alternative with respect to solution electrospinning. Additionally, melt electrospinning allows to precisely control the deposition of the fibers during electrospinning opening the way to the possibility of obtaining complex three – dimensional (3D) structures, as reported in Figure 5-d. Nevertheless, the reduced variety of available polymers, the degradation issues, and the difficulties in obtaining submicrometer fibers are to date strong limitations in melt electrospinning exploitation.

1.4.1.1 Natural Polymers

During the past decades, either synthetic and naturally derived polymers have been successfully electrospun with each category presenting both significant advantages and disadvantages. Synthetic polymers are usually easier to electrospun and allow a good reproducibility of the process, consequently leading to more homogenous and uniform nanofibers. Moreover, by using hydrophobic materials, water resistant mats able to maintain their peculiar structure in contact with aqueous media can be easily obtained without the need for a post – production treatment. However, besides they also show enhanced mechanical and thermal performances, such polymers generally require the use of organic hazardous solvents to be efficiently electrospun, thus representing a substantial environmental and human health threat. In contrast, the electrospinning of naturally occurring polymers, such as polysaccharides and proteins (Figure 6), is starting to be widely investigated on behalf of a greener and less impacting alternative. As a matter of fact, apart from the possibility to use eco – friendly and non – toxic solvents such as water, these materials can be often extracted from food and agricultural industrial wastes and/or as by – products hence representing a chance to develop green circular economy manufactures.[89–93] Significant examples are chitosan, a polysaccharide that can be easily obtained from the shellfish exoskeleton,[94,95] and gelatin, a protein abundantly found in farm animal carcasses and fishes.[96] Moreover, naturally occurring materials are

usually biocompatible, weakly immunogenic, biodegradable, digestible, and possess a wide variety of other peculiar properties that make them extremely suitable for the development of biomedical and pharmaceutical products, as well as for food packaging and biosensor applications.[97] Nevertheless, natural polymers are characterized by drawbacks such as intrinsic poor reproducibility, reduced mechanical properties and thermal resistance, and usually require an additional crosslinking reaction to exhibit appropriate stability and performances. Furthermore, the electrospinning of such materials is considerably harder compared to synthetic polymers due to their tendency to form highly viscous solutions likewise to the presence of weak but multiple electrostatic intermolecular interactions.[98,99] Because of such drawbacks, so far good results in terms of natural polymer spinnability have been mainly obtained by processing them in combination with a synthetic polymer in a different ratio.[100]

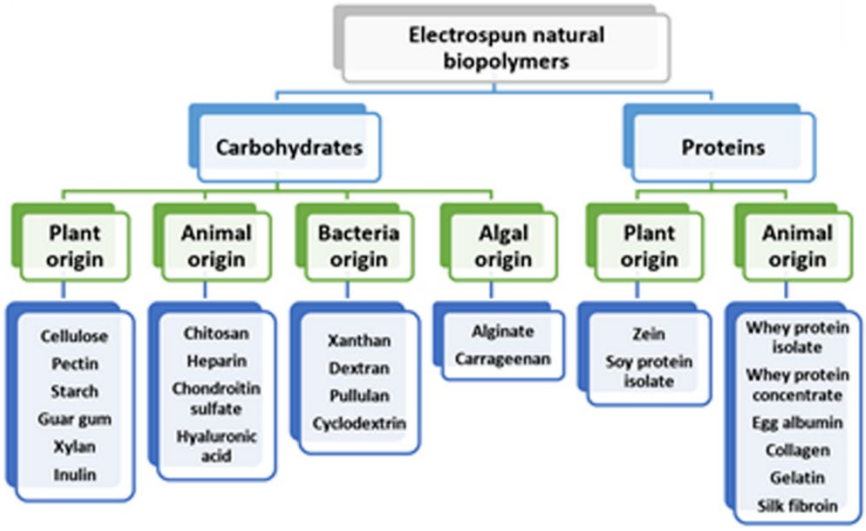

Figure 6. Summary of the most commonly electrospun natural derived polymers.

1.4.2 Small Molecules

The electrospinning of small molecules is possible when the intermolecular interactions are large enough to form self – assembled structures (both in their highly concentrated solutions or pure melts) able to stabilize the electrified jet and suppress the Rayleigh instability. As such, the solution – phase electrospinnability of small molecules is mainly determined by their structures and concentration together with the solvent type, with the current reports mostly including amphiphiles and cyclodextrin derivates.[101,102] Some small molecules can also form entanglements in their melts, thus allowing to obtain fibers via melt electrospinning.

1.4.3 Colloidal Particles

A colloid consists of a dispersed phase (i.e., the suspended particles) and a continuous phase (i.e., the medium of suspension) and can be adapted for electrospinning if enough entanglements are formed between the particles to keep the jet as a continuous structure. In particular, the colloidal particles must possess both a certain size and crosslinking among them to maintain the jet stable, with the viscosity playing a topical role in determining the morphology of the fibers. However, it is noteworthy that the ability to control the size and the homogeneity of the fibers is usually quite low due to the difficulties in precisely regulating the rheological properties of colloidal systems.[103]

1.4.4 Composites

Composites, which are typically prepared via the addition of sol – gel precursors or nanoscale components into polymer solutions, have been broadly investigated for solution electrospinning. In the case of sol – gel precursors, the sol – gel reaction (e.g., hydrolysis, condensation, gelation, etc.) must be avoided in the stock solution but should be instead initiated in the jet when in contact with the surrounding air.[104,105] As such, a continuous network of the inorganic phase is formed within the polymer matrix with the formation of composite nanofibers. The electrospinning of these systems is mostly governed by the sol – gel precursor, the nature of the carrier polymer, the viscosity, and the electrical conductivity of the solution. The sol – gel precursor type affects the sol – gel reaction rate in the jet, with rapid hydrolysis often causing the blockage of the spinneret and fast gelation resulting in thicker nanofibers.[104] The carrier polymer must be spinnable, with either a high molecular weight or a great chain entanglement. Poly(vinyl pyrrolidone) is so far one of the most popular carrier polymers due to its high solubility in water and ethanol, together with its good compatibility with a vast number of sol – gel precursors. The viscosity of the solution plays a fundamental part in stretching the jet and it can be controlled by varying the concentration of both precursor and carrier polymer. The electrical conductivity can instead be increased by adding a salt (e.g., NaCl) to promote the formation of thinner fibers. Additionally, an atmosphere with low relative humidity and/or saturated with the solvent vapours may significantly reduce the rate of hydrolysis and gelation, thus giving rise to continuous electrospinning.[103] Composite nanofibers have also been prepared by directly adding nanoscale structures within a polymer solution. Commonly used nanostructures consist of nanoparticles made of Ag, Au, TiO_2, and

ZnO, one – dimensional (1D) nanostructures such as Au nanorods, Au or Ag nanowires, and carbon nanotubes, together with two – dimensional (2D) nanostructures such as clay tablets and graphene nanosheets.[106] The electrospinnability of these formulations critically relies on the type, size, and concentration of the added nanostructures. A stable dispersion of the nanoscale components is instrumental to the production of homogenous nanofibers, also considering the difficulties in obtaining a continuous jet if the nanostructures are prone to aggregate. In this sense, the nanoscale structures must often be modified with a functional group to achieve high enough stability over time.[107] Examples of composite nanofibers prepared via the electrospinning of polymer solutions containing nanostructures are reported in Figure 7.

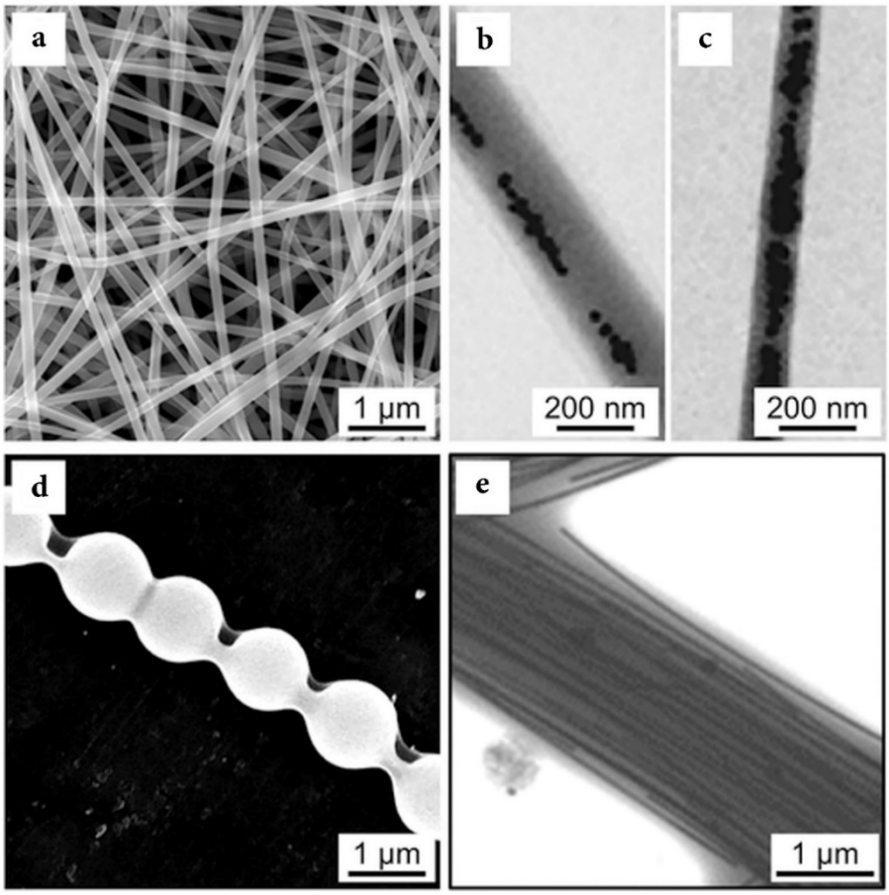

Figure 7. (a) SEM micrograph of composite poly(vinyl pyrrolidone) – TiO_2 electrospun nanofibers. Reproduced with permission from Ref. [104]. (b) and (c) TEM micrographics of nanofibers containing a different amount of Ag nanoparticles. Reproduced with permission from Ref. [108]. (d) SEM micrograph reporting the necklace – like structure of a composite poly(vinyl alcohol) – SiO_2 nanofiber. Reproduced with permission from Ref. [109]. (e) TEM micrograph of a composite poly(vinyl pyrrolidone) – based fibers containing aligned Ag nanowires. Reproduced with permission from Ref. [110].

1.5 Applications of Electrospun Nanofibers

1.5.1 Electrospun Nanofibers for Biomedical and Pharmaceutical Applications

Over the past two decades, electrospun nanofibers have found widespread use in a variety of distinctive biomedical and pharmaceutical applications. By engineering their structure and properties, including diameter, porosity, alignment, stacking, patterning, surface functional groups, mechanical properties, and biodegradability, nanofibrous meshes have been employed in tissue regeneration, drug delivery, cancer research, implant coatings, and barrier membranes, as well as for the improvement or development of biomedical devices. In the following Sections, a summary of the main applications in the biomedical and pharmaceutical fields is reported and discussed.

1.5.1.1 Tissue Repair or Regeneration.

Tissue repair or regeneration involves the integration of scaffolding materials, cells, and/or biological factors to promote tissue growth by providing an appropriate combination of mechanical support, topographic guidance, and biochemical instruction to the cells. Above all, in developing the scaffolds, it is of fundamental importance to mimic the extracellular matrix (ECM) as close as possible in terms of composition, architecture, and other physical – chemical properties. The composition of ECM varies across tissues, but it commonly contains three major classes of macromolecules: structural proteins (e.g., collagen and elastin), complexes of proteins and polysaccharides (e.g., proteoglycans), and adhesive glycoproteins (e.g., fibronectin and laminin).[111] In addition, the ECM contains intrinsic biochemical cues including growth factors and other soluble biomolecules that play a vital role in regulating the phenotype and function of cells.[112] In terms of architecture, native ECM can be considered as a 3D network assembled from fibrous structures, with collagen representing the most abundant structural protein existing in the form of nanofibers with diameters in the range 50 – 500 nm.[113] To efficiently mimic the function of ECM, electrospun nanofibers have been widely investigated as scaffolding materials owing to their unique ability to well reproduce the composition, length scale, and architecture of native extracellular matrix.[114] Due to the topic of the present Thesis, the focus is here pointed on the use of electrospun patches for wound healing and musculoskeletal tissue regeneration, with some examples shown in Figure 8.

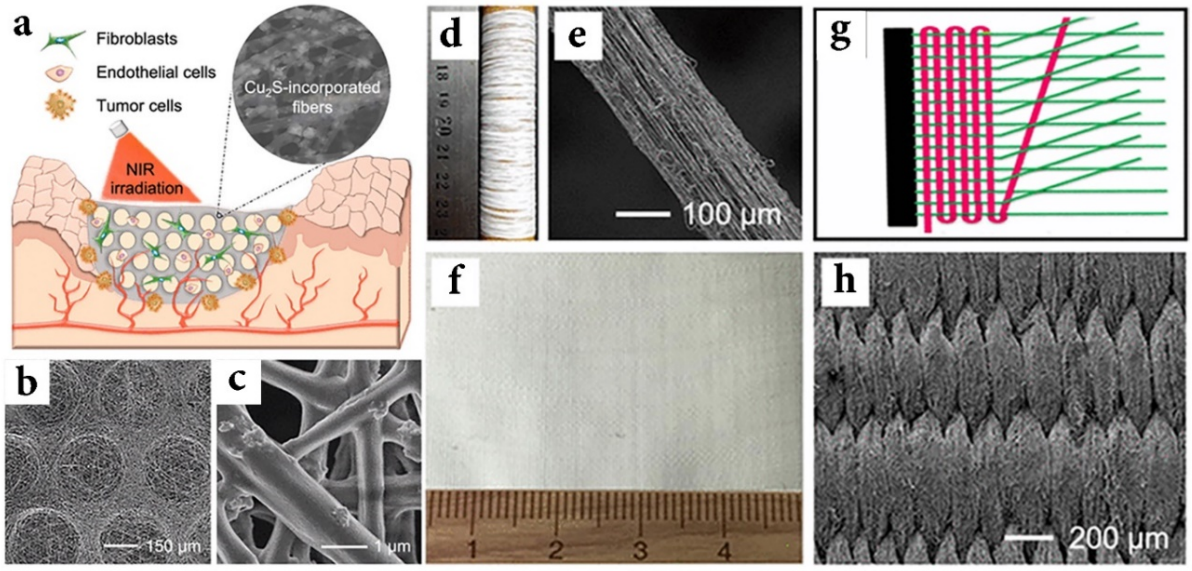

Figure 8. (a) Schematic showing the localized treatment of skin tumour and wound healing with the use of a micropatterned nanofibrous scaffolds. (b) SEM micrograph showing the morphology of the micropatterned scaffold. (c) SEM micrograph showing the nanofiber morphology. Reprinted with permission from Ref. [115]. (d) Photograph and (e) SEM micrograph of a nanofiber yarn. (g) Schematic of the textile – weaving process. (f) Photograph and (h) SEM micrograph of a plain – weaving fabric made of PCL nanofiber yarns and multiple PLA filaments. Reproduced with permission from Ref. [116].

From the viewpoint of composition, a broad number of synthetic and natural polymers can be directly electrospun into nanofibers, and nanoparticles can also be readily integrated with the nanofibers.[117] In particular, collagen, elastin, and some other proteoglycans present in human ECM can be either used separately or blended together, as well as mixed with synthetic polymers to produce ECM substitutes with the desirable mechanical strength and biodegradability.[118,119] Furthermore, the adhesive glycoproteins found in native ECM can be simply coated onto the surface of the as – spun nanofibers, whereas growth factors and other soluble biomolecules can be incorporated within the fibers to accelerate the establishment of a microenvironment that replicates the natural tissues.[120] In general, at the microscopic level it is straightforward to engineer the surface topography of a scaffold to manipulate the behaviour and fate of cells, meanwhile at the macroscopic level it is possible to control the bulk structure of a scaffold to match the shape and/or morphology of the target tissue. In addition to replicating the composition and architecture of native ECM, other requirements must be met to fully recover the function of the target tissue. For example, during tissue regeneration, the scaffold should serve only as temporary support to promote the recruitment and proliferation of cells that are supposed for the construction of a permanent ECM. Therefore, the scaffold is expected to degrade and eventually disappear during tissue neogenesis and it is of critical importance for the inward growth of cells to exactly fill the space left behind by the degradation

of the scaffold. By combining structural guidance with cellular components and/or bioactive molecules, electrospun nanofibers can improve the repair or regeneration of various types of tissues, including the repair of nerve injury, healing of wound, patching of myocardium defect, bridging of vascular rupture, remodelling of musculoskeletal tissue, and construction of interfaces between different tissues.

Wound Healing

Wounds refer to injuries to living tissues. As a matter of fact, owing to its unique location, the skin is highly susceptible to injuries. As a multi – layered structure, mammalian skin is mainly comprised of epidermis and dermis, which encompass keratinocytes and fibroblasts, respectively, and are located above the subcutaneous tissue.[121] Skin wounds are typically trauma – induced defects that involve a number of cellular reactions from different types of cells, and their healing normally experiences four consecutive phases: haemostasis, inflammation, migration/proliferation, and maturation/remolding.[122,123]

Minor wounds can heal through the body intrinsic repair process, whereas healing of large – scale or full – thickness wounds usually requires the assistance of scaffolding materials. In this regard, electrospun nanofibers have been actively explored as a dressing material for wound healing. Indeed, by engineering the nanofibers to provide topographical and biological cues, the migration and infiltration of repairable cells can be significantly enhanced. For instance, crossed nanofibers inspired by the basketweave – like pattern of collagen fibrils in the native skin have been recently fabricated,[124] as well as a sandwich – type scaffold,[125] and other systems containing a variety of bioactive agents.[126] Additionally, in order to prevent the insurgence of infection and abnormal inflammation, the development of wound dressings coupled with localized drug delivery for anti – infection and anti – inflammation represents an avenue for healing large wounds and promoting effective repair,[127] along with the use of embedded metal nanoparticles. Electrospun meshes have also been to some extent successfully employed in the inhibition of scar formation[128] and to promote wound healing in diabetic patients.[129,130] As a new trend, bifunctional scaffolds with capabilities for localized skin tumour therapy and skin tissue regeneration showed great promise to avoid tumour recurrence meanwhile healing the tumour – induced wounds.[115]

Musculoskeletal Tissue Regeneration

The musculoskeletal system is comprised of the skeleton, muscles, cartilages, tendons, ligaments, joints, and connective tissues. The primary functions of the human musculoskeletal system are to provide support, stability, protection, and movement to the body.[131] A musculoskeletal injury refers to damage to the muscular or skeletal tissue caused by trauma, a congenital defect, or tumour ablation.[132] Generally, nonwoven mats of nanofibers are used to induce the specific differentiation of stem cells into osteogenic, chondrogenic, or tenogenic tissues, but 3D scaffolds have also been developed from nanofibers to provide space for tissue remodelling.

As a hard tissue, bone is mainly composed of type I collagen fibrils and hydroxyapatite nanoparticles. Together with their critical role in protecting and supporting various organs of the body, bones also represent a major storage system of calcium, phosphorus, and other important components of the hematopoietic system. Owing to the strong mechanical strength and high mineral content, scaffolds employed for bone regeneration are often designed by reinforcing biodegradable polymers with biocompatible inorganic phase, such as hydroxyapatite, bioactive glass, silica, and ZnO nanoparticles.[133–137]

Cartilage is a resilient and smooth elastic tissue that covers and protects the ends of long bones at the joints.[138] For the repair of cartilage defects, electrospun nanofibers have shown promise as a basis for chondrogenesis or chondrogenic differentiation. However, it is an ongoing challenge to achieve completely cellular infiltration throughout the full thickness of the defect side when 2D mats are used.[139] In this sense, a 3D nanofiber – based scaffold with a hierarchical structure, interconnected pores, capable of promoting chondrogenesis, and possessing compressive strength is desirable for the regeneration of thick cartilage tissue.[140]

Tendon is a dense and fibrous connective tissue that attaches a muscle to a bone and is capable of withstanding great tensions.[141] Similarly, the ligament is the fibrous connective tissue that connects bone to another bone. Histologically, both tendon and ligament comprise parallel arrays of dense regular connective tissue bundles encased in sheaths made of dense irregular connective tissues. Various 2D mats composed of uniaxially aligned nanofibers have been employed in tendon and ligament tissue engineering as they can mimic the alignment of native tissue. However, since healthy tendon/ligament tissues are normally in bulk volume, biomimetic 3D scaffolds are required to provide structural, physical, and biochemical features to simulate native tissues.[142] In addition, nanofibrous yarns and the braided, wove, or knitted yarn networks are attractive for tendon and ligament tissue regeneration due to their high mechanical strength, anisotropic architecture, and enlarged porosity for cell infiltration.

Skeletal muscles, consisting of bundles of highly oriented, densely packed myofibers derived from the multinucleated muscle cells, are connected to bone through tendons.[143] Without proper alignment of myofibers it is impossible to impose effective force transmission and contractility in the regeneration of functional muscle fibers.[144] Hence, scaffolds capable of guiding muscle cell alignment and allowing the formation of myotubes via topographical, chemical, and/or biological cues are critical in myogenesis. As such, 3D porous scaffolds with uniaxial fibers alignment are advantageous in prealigning muscle cells, thereby facilitating the early stage myogenic differentiation and the formation of long, thick myotubes.[144]

1.5.1.2 Drug Delivery

Beyond their large surface area – to – volume ratio, porosity, uniformity in fiber size, and flexibility in assembled structures, electrospun mats can be easily functionalized with various bioactive molecules. As such, drug delivery systems based on nanofibers prepared via electrospinning have been lately the new horizon in drug delivery.[145,146] To date, a number of therapeutic agents including antibiotics, proteins, DNA, RNA, growth factors, and living cells have been incorporated within electrospun nanofibers via either encapsulation during electrospinning or surface modification post – electrospinning. Nanofiber – based scaffolds are suitable for topical, transdermal, and oral drug delivery, but the local injection to diseased sites has also been reported.[147–149] In addition, electrospun nanofibers offer significant advantages in controlling drug release rates by varying the composition, microstructure, and macrostructure. Recently, stimuli – responsive nanofibers have been as well developed to provide a completely new strategy of controlled drug delivery and release temporally and spatially.[150]

Electrospun Nanofiber Implants for Local Therapy

Various electrospun drug delivery systems have been prepared for the local administration of therapeutic agents owing to the great variability in material choice, ease of drug encapsulation, and high versatility in drug formulations. Figure 9-a summarizes some of the possible drug release kinetics that can be obtained with nanofiber – based drug delivery systems.

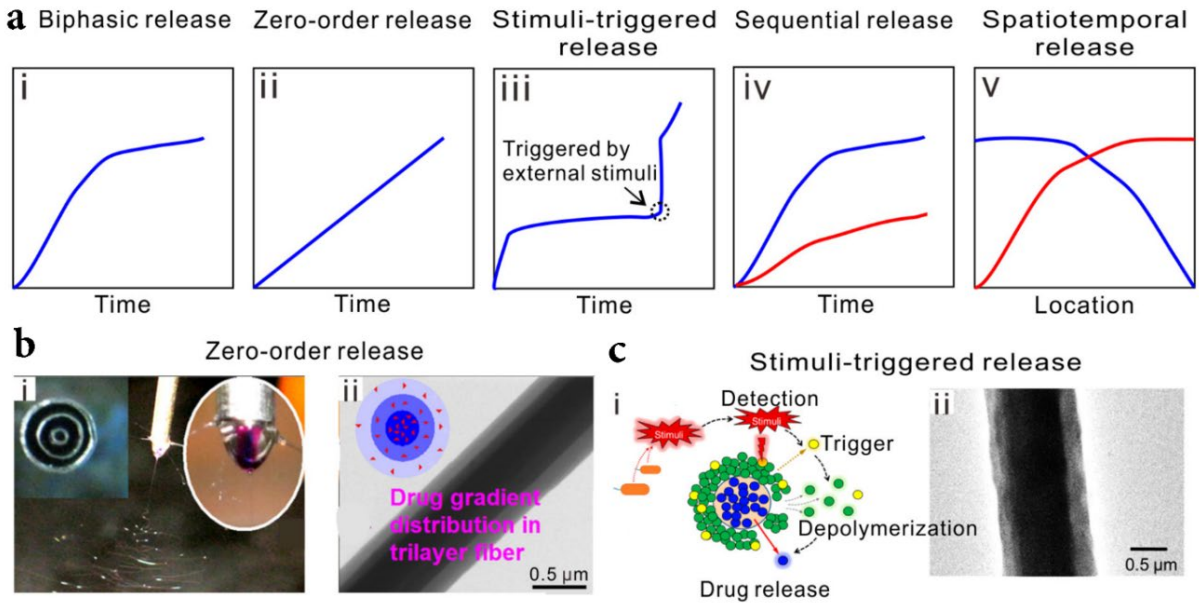

Figure 9. (a) Representative release curves, including (i) biphasic release, (ii) zero – order release, (iii) stimuli – triggered release, (iv) sequential release and (v) spatiotemporal release. Reprinted with permission from Ref. [145]. (b) Zero – order release from three – layered nanofibers fabricated using triaxial electrospinning. Reprinted with permission from Ref. [151]. (c) Stimuli – triggered release from nanofibers fabricated by coaxial electrospinning of stimuli-responsive polymers. Reprinted with permission from Ref. [150].

Usually, a biphasic release behaviour consisting of an initial burst release followed by a prolonged release is achieved for electrospun nanofiber formulations due to both drug diffusion and polymer degradation phenomena.[152] An optimized biphasic drug delivery system can lead to enhanced local treatment efficacy owing to the availability of a high drug content at the lesion site within a short period, followed by the maintenance of a high drug concentration for a long duration. If the initial burst release is undesired, the development of core – sheath structures is of great significance to mitigate or even eliminate such phenomenon, as illustrated in Figure 9-b.[151] Additionally, electrospun nanofibers comprised of stimuli – responsive polymers could topically deliver drugs in an on – demand way (Figure 9-c),[153] hence being extremely promising in cancer therapy.[154,155] Specifically, such systems provide a way to tune drug release in the right place and time, resulting in the augmented therapeutic efficacy and minimization of side effects.

Injectable Short Nanofibers for Local Therapy

Normally, drug – loaded nanofibrous mats or scaffolds are directly implanted to the lesion site, despite the surgical implantation is often invasive. In this regard, the development of injectable formulations containing short or fragmented nanofibers represents a minimally invasive approach for drug local administration.[149]

1.5.1.3 Cancer Research

With respect to a solid substrate, a mat of electrospun nanofibers offers a much higher surface area – to – volume ratio thereby providing a much larger contact area with analytes and cancer cells. Moreover, electrospun meshes can be readily loaded with drugs for their controlled and localized release to achieve a much more effective chemotherapy effect. Thus, both organic, inorganic, and composite electrospun nanofibers have been vastly employed in cancer research in the context of diagnosis, construction of 3D tumour models, and treatments.[156]

1.5.1.4 Other Biomedical Applications

As functional materials, nanofibers prepared via electrospinning can be deposited on an implant acting as coatings to improve its biocompatibility and provide additional topographic features and/or biological cues.[157] Similarly, nonwoven mats based on electrospun nanofibers can successfully serve as barrier membranes to prevent post – surgery adhesion, enhance osteogenesis, and fight against bacteria. Finally, electrospun meshes are well – developed as filter materials for biomedical purposes, such as the separation of bacteria and white blood cells.

1.5.2 Electrospun Nanofibers for Environment and Sustainability

Upon deposition on a proper collector, electrospun nanofibers usually form nonwoven mats with a high surface area – to – volume ratio and porosity, which make them useful as filter materials for various applications. Specifically, since the highly porous structure greatly facilitates the mass transport of both gaseous and liquid phases, a gas stream or a solution can flow through an electrospun nonwoven mat in high flux without experiencing much resistance. Hence, nanofiber – based mats have been actively developed as advanced filters for removing pollutants such as particulate matters (PMs), toxic ions, and organic molecules from both air and wastewater, as well as to decompose harmful chemicals and recover precious metals. As a matter of fact, the available reports suggest that electrospun nanofibers are superior in rapidly and effectively removing pollutants and recovering precious metals with high selectivity, good recyclability, and noticeable stability with respect to polymer bulk matrices. In the following Sections, the most important environmental and sustainable applications of nanofibrous mats are briefly described.

1.5.2.1 Purification of Air

To date, air pollution has long – lasting impacts on the atmospheric environment and public health, with the major concerns including PMs in a liquid or solid form, CO_x, NO_x, SO_2, and ozone.[158] Specifically, $PM_{2.5}$ and PM_{10} (i.e., particles with aerodynamic equivalent diameters less than 2.5 and 10 μm, respectively) can easily infiltrate the human body, causing several mortal diseases.[159] Conventional air filter materials are plagued by three key issues: low filtration efficiency, large air pressure drop across the filter, and safety hazards such as dust explosion and fire.[160] To this end, the high porosity, good interconnectivity, micrometer – sized interstitial space, and large surface area – to – volume ratio make electrospun nanofibers outstanding materials for the purification of air. An ideal filter should possess a high filtration efficiency and a low – pressure drop to maximize the quality factor (QF), which depends mainly on the filter overall porosity, average pore size, and specific surface area.[161] The higher the QF value, the greater is the filtration performance. Depending on the size of the particles in the air that are supposed to be filtered out, the size of void spaces in the mat and the pores in individual nanofibers can be tuned to attain notable filtration efficiency, which can also be enhanced by reducing the nanofiber diameter hence increasing the specific surface area of the mat.[162] In recent years, nanofiber – based nonwoven mats made of polymers, composites, and ceramics have all been explored as advanced high – efficiency particulate air (HEPA) filters:
i) Polymer – based electrospun nanofibers. Polymer – based electrospun nanofibers are particularly suitable for use as facial masks owing to the lightweight and breathable features while maintaining good mechanical robustness.[163] In general, the filtration efficiency is significantly enhanced when the polarity of the polymer is increased since the dipole – dipole or dipole – induced dipole forces can strongly promote the binding of PMs to the surface of nanofibers.[164] Additionally, the filtration efficiency can be also improved by increasing the electrostatic charges on the surface of the nanofibers for capturing targeted pollutants through long – range electrostatic interactions.[165] Permanent surface charges can be generated either by the co – electrospinning of polymers with different triboelectric properties or by incorporating an electret into the nanofibers. Remarkably, the high filtration efficiency of electrospun nonwoven mats allows for the reduction of packing density and number or layer in a filtration device to provide promising features such as optical transparency.[164] In addition to the purification of polluted air, nanofibrous mats can also be employed to remove pollutants from an exhaust line before they are discharged into the environment.[166] Regarding safety issues, electrospun nanofibers with extraordinary flame retardation are highly desirable, especially for

industrial purposes. Electrospun nonwoven mats often possess a long service lifetime, up to several hundred hours, and can be eventually reused after removing the captured particles with mechanical shaking or air back – blowing.[163]

ii) Composite – based electrospun nanofibers. Composite – based electrospun nanofibers have been broadly investigated for the fabrication of filter materials with high filtration efficiency by introducing new functionalities via the synergistic effects between the components. For instance, antibacterial activity, healthcare, and self – cleaning features can be readily achieved by incorporating active components (e.g., metal, oxide, or organic molecules) into the nanofibers.[162,166,167] It is worth pointing out that the capture efficiency toward pollutants is very sensitive to the surface of the nanofibers. As such, introducing new components into the nonwoven mats may cause changes to the surface properties and the binding affinity between pollutants and nanofibers. Therefore, multifunctional filters must be carefully optimized considering each component without affecting the PM filtration efficiency.

iii) Ceramic – based electrospun nanofibers. Ceramic – based electrospun nanofibers, if endowed with good mechanical strength, can serve as efficient filter materials for air purification with excellent thermal and chemical stability. Specifically, even without any chemical modification, ceramic nanofibers represent a promising class of filters for harsh environments such as extremely humid weather and high – temperature pollutant source. Despite QF values are usually not as high as those of polymer or composite – based nonwoven mats, ceramic nanofibers often offer greater performances with respect to the current commercial products.[168] Additionally, by taking advantage of the photocatalytic activity of many ceramic materials, the meshes can be potentially utilized to degrade or decompose the organic species in PMs, particularly with the aid of light irradiation. To date, the primary shortcoming of mats based on ceramic nanofibers as air filters is the need for heat treatment at high temperatures during their fabrication, together with their intrinsic rigidity, fragility, and poor mechanical performances.

1.5.2.2 Treatment of Water

Electrospun nonwoven mats have been extensively investigated as filters for the treatment of water due to their capability to simultaneously separate and degrade the pollutants in wastewater. Filter materials based on electrospun nanofibers can easily remove particles of 3 – 10 μm in size from water without any significant drop in flow flux,[169] proving also a simple approach to the removal of toxic ions and organic pollutants via physisorption, chemisorption,

electrostatic attraction, or a combination of these phenomena. The large specific surface area of nanofiber – based filter directly offers a great number of adsorption sites and high adsorption capacity,[170] and such filter materials can be readily recycled in a short period of time avoiding secondary pollution effects towards the environment. Additionally, the mats comprised of materials with intrinsic high chemical stability, such as those made of ceramics, may be employed under harsh conditions in the presence of acids, bases, and/or salts. Superior purification capacity can be obtained for electrospun nanofibers by the combination with active adsorbents. Upon their immobilization within the nanofibers, the adsorbents are hence endowed with enhanced adsorption capacity, stability, and recyclability.[171] Moreover, the selective removal of a targeted pollutant from water can be easily achieved by immobilizing a specific capturing agent on the nanofiber surface or by tailoring their surface wettability. For example, a nanofibrous mat with a low surface free energy and rough surface structure can selectively remove oil from polluted water thereby serving as an efficient method for oil – water separation.[172] Noticeably, when made of semiconductor oxides, electrospun nanofibers can use sunlight to degrade organic molecules to nontoxic molecules (e.g., CO_2 and H_2O) or photocatalytically reduce toxic heavy metal ions to nontoxic products.[173] Moreover, controlling the intrafiber porosity may enable the selective degradation of targeted pollutants along with water filtration.[174] Photocatalytic nanofiber – based mats can also be integrated with microfluidic devices for water purification in microreactors, by taking advantage of fine control over reaction pathways and short diffusion distance.[175,176]

1.5.2.3 Degradation of Harmful Chemicals

Owing to their high adsorption capacity, electrospun nanofibers have gained a great deal of interest in the decontamination of harmful chemicals.[177] Specifically, while serving the decontamination role, nanofibrous mats may also improve the durability and strength of the protected textile. The decontamination capability can be greatly enhanced by incorporating active materials into the nanofibers through chemical modification.[178] Filters with self – detoxification capability against lethal chemical warfare agents (CWAs) are highly desirable for the protection of human beings and the environment, with the use of metal nanoparticles (e.g., Ag, Ni, and Ti) encapsulated within the electrospun nanofibers showing promising results to further enhance their performances.[169]

1.5.2.4 Recovery of Precious Metals

The leaching of precious metals from the catalyst during a catalytic process is a critical issue in both industrial catalysis and environmental remediation. Specifically, there is a strong need to maintain the leached metal ions at a level below 1 ppm in the final products, as well as to recover the scarce and expensive metals for reuse. Thereby, nanofibers with suitable surface functional groups can scavenge previous metal ions from the solution phase with high efficiency, specifically due to the strong binding between the functional groups and the metal ions and the high surface area – to – volume ratio.[179]

1.5.3 Electrospun Nanofibers for Catalysis, Energy, Photonics, and Electronics

Nanofibers prepared via electrospinning technique have been broadly explored for purposes related to catalysis, energy, photonics, and electronics. Due to their great porosity, high specific surface area, and good stability, electrospun nanofibers comprised of polymers, ceramics, and carbon are naturally efficient supports for various catalytic systems. Additionally, if fabricated with the right composition, nanofibers may favour rapid conduction of electrons and/or intercalation of ions, hence opening the door to applications in energy harvesting, conversion, and storage fields. On the other hand, the possibility to tune the composition, structure, morphology, and alignment of nanofibers has enabled their use in the fabrication of photonic and electronic devices, exemplified by both light – emitting diodes (LEDs) and field – effect transistors (FETs). In the following Sections, the promise of electrospun nanofibers in all these application fields are briefly showcased.

1.5.3.1 Catalysis

Depending on the catalyst and reactants involved, a catalytic process can be classified into three categories: heterogeneous, homogeneous, and enzymatic catalysis.[180] Nonwoven electrospun mats are especially attractive for heterogeneous catalysis, which is usually based on nanoparticles immobilized on a solid support to enhance the ratio of surface area – to – volume. Hence, nanofibers are interesting to be used as supports due to their large specific surface area, high porosity with fully accessible pores, ability to protect the catalytic nanoparticles, easy separation or recovery from the reaction medium, and simple incorporation into a continuous – flow system.[181] To this end, several strategies involving nanofibers – based

mats have been developed including immobilization of enzymes, immobilization of catalytic nanoparticles, and sinter – resistant heterogeneous catalysts.

1.5.3.2 Energy Harvesting, Conversion, and Storage

To date, the effective harvesting, converting, and storage of energy represent one of the persistent issues faced by our society. A wide variety of devices, which are commonly comprised of two electrodes and an electrolyte, have been fabricated to address these issues, such as solar cells, rechargeable batteries, supercapacitors, and fuel cells. Nanostructured electrodes are excellent candidates for these applications due to their high surface area – to – volume ratio, large specific area, and short diffusion distance.[182] With these premises, electrospun nanofibers have been extensively investigated to be used as electrode materials, especially those made of metal oxides and/or carbon. A nanofiber – based electrode offers indeed a vast number of desirable advantages, such as a large electrode/electrolyte contact area, rapid transfer of electrons and ions, versatility for functionalization to improve electroactivity, lightweight, and good flexibility.[183]

1.5.3.3 Light – Emitting Devices

Light – emitting devices can produce light in a variety of colours on the basis of electroluminescence or photoluminescence.[184] A LED is commonly constructed by sandwiching p – type and n – type semiconductor layers comprised of inorganic or organic materials placed between an anode and a cathode. Upon the application of a suitable voltage between the two electrodes, the electrons recombine with holes at the p – n junction, releasing the energy in the form of photons.[185] Till now, how to further enhance the efficiency of LEDs remains a major challenge. In this sense, the intrinsic features of nanofibers, including ultrafast charge carrier transfer and good molecular alignment along the fiber axis, make them appealing in exploiting new LEDs with high efficiency, good stability, and flexibility.[186]

1.5.3.4 Field – Effect Transistors

FETs utilize an external dielectric field to control the charge transport behaviours of a target device. A typical device includes three main components: three terminal electrodes (namely source, drain, and gate), an active channel, and a dielectric separating the gate electrode from the channel.[187] Hence, when charge carriers flow from the source to the drain through the

channel, a drain – source current is generated. If a nanofiber – based mat is employed as the channel, the charge carriers move through it at a rate several order of magnitude higher than that through a thin film.[188,189] The coverage density of the nanofibers on the substrate of a FET represents a critical parameter affecting the charge carrier mobility in the channel, thus strongly influencing the device performances. In general, a low fiber density can cause an inadequate number of pathways for electrons, whereas excessive fiber density can weaken the ability for current modulation due to the uneven morphology and overlapping among the nanofibers.[190]

1.5.4 Electrospun Nanofibers with "Smart" Properties

Beyond traditional applications, over the last decade, electrospun nanofibers have been enriched with "smart" properties to enable a variety of new and advanced manufacturers. Among others, stimuli – responsive nanofibers can undergo volume and/or wettability changes upon external stimulation, shape – memory nanofibers are able to assume different shapes, and self – healing nanofibers can be used as vehicles to deliver healing agents. In the following, a summary of "smart" electrospun nanofibers with various potential applications is presented.

1.5.4.1 Stimuli – Responsive

Stimuli – responsive polymers undergo conformational and/or chemical modifications upon being triggered by an external stimulus with a response time inversely proportional to the rate at which the stimulus is able to reach the polymer chains, with this process being dominated by diffusion.[191,192] When stimuli – responsive polymers are manufactured in the form of nanofibers, the stimulus propagation is greatly accelerated owing to the highly porous structure, large surface area – to – volume ratio, and small diameter of the fibers, which in turn lead to a swifter response. Various types of stimuli – responsive nanofibers have been reported for applications such as cell – sheet harvest and controlled drug delivery systems. To this end, the external stimulus can be applied as a change in temperature or pH, as well as light and electric or magnetic field.[193]

1.5.4.2 Shape – Memory

Shape – memory nanofibers are able to transform from a deformed state, which is the temporary one, to the original state, which is the permanent one, upon the application of external stimulation.[194,195] Temperature is one of the most commonly used stimuli to induce

shape transitions, with shape – memory nanofibers often being fabricated with polymers that can take two or multiple conformations at different temperatures.[196] Commonly, the employed polymers are comprised of two components, namely soft segments that provide a low T_g or T_m and hard segments that ensure the formation of a stable network structure.[197] The simplest demonstration involves a one – way mode where the nanofiber – based meshes can exhibit two different shapes as illustrated in Figure 10-a and Figure 10-b. At room temperature, the mat typically assumes its permanent shape. Upon heating to a temperature above its shape – memory transition temperature (T_{trans}, usually the glass transition of melting temperature of the polymer), the mat becomes a soft elastomer due to the increased mobility of the polymer chains, hence being susceptible to deformation upon the application of an external force. If the temperature drops below T_{trans}, the deformation is permanently retained due to the freezing of the polymer chains with the entropic energy being stored within the mat. When heated again above T_{trans}, the entropic energy is finally released forcing the mat to take on again its permanent shape. Owing to the high porosity, nanofibrous mats offer a much quicker and sharper shape recovery with respect to bulk films,[198] with the shape – memory effect and the transition temperature being mainly determined by the structure of the used polymer, as well as by the diameter and the morphology of the nanofibers.[199]

1.5.4.3 Self – Cleaning

Self – cleaning coatings have been developed and commercialized for various applications.[172,200] Among these materials, nonwoven mats comprised of electrospun nanofibers are advantageous for their breathable, flexible, and self – supporting properties. Specifically, by simply controlling the nanofiber surface structure and chemical composition the wettability of the mats can be tuned to obtain self – cleaning abilities.[201] For examples, such products can be applied to prevent contamination in medical devices or to produce protective clothes.[202] Nowadays, two different routes have been reported to the purpose, comprising the formation of a “film flow” on a super hydrophilic surface similar to the behaviour of water on the fish scales in the air (Figure 10-c)[203] or a “droplet flow” on a superhydrophobic surface similar to the behaviour of water on the plant leaf (Figure 10-d).[204]

1.5.4.4 Self – Healing

Engineering materials are often susceptible to damage in the form of cracks, which are almost impossible to be repaired due to the difficulty in detecting their precise position in a bulk

material. Hence, self – healing materials, which are capable of self – repair damages and recover their pristine features, are highly desirable. Self – healing is a key feature of the biological system that prolongs the lifespan of living organism.[205] By simply mimicking this natural phenomenon, self – healing composites have been prepared by using electrospun nanofibers with an interconnected network – like structure.[206] Specifically, electrospun nanofibers are advantageous in introducing self – healing properties since, instead of using microcapsules as a vehicle for the delivery of the healing agents, they allow their rapid diffusion along the boundary of the damaged cracks hence shortening the healing time.[207] For example, self – healing composites containing electrospun nanofibers have been investigated as the " barrier" coatings of steel to prevent corrosion, as schematically illustrated in Figure 10-e.

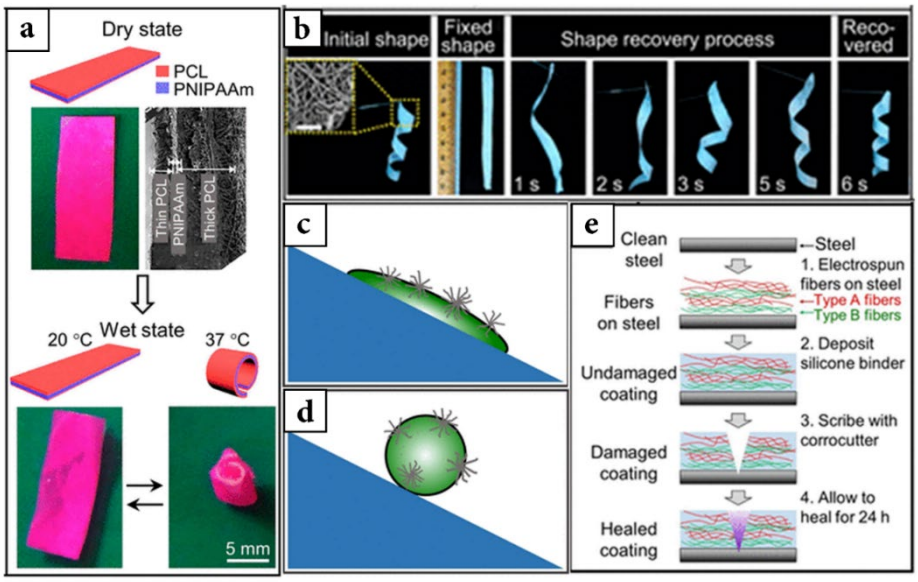

Figure 10. (a) Thermoresponsive properties of a three – layer mat for actuating. Reproduced with permission from Ref. [208]. (b) Series of photographs showing the shape – memory recovery process of composite electrospun nanofibers. Reproduced with permission from Ref. [209]. (c) Super hydrophilic and (d) super hydrophobic surfaces to form a film flow or a drop flow, respectively. Reproduced with permission from Ref. [22]. (e) Schematic of a self – healing composite containing nanofibers to be utilized as protective coating to avoid steel corrosion. Reproduced with permission from Ref. [210].

1.5.4.5 "Living"

Live microorganisms, such as microbes and cells, may also be incorporated during electrospinning to produce "living" nanofibers, which are highly useful in a broad variety of biotechnological products.[211] From a formulation prepared by dispersing the microorganisms in a polymer solution, a jet containing the organism is projected. Typically, the encapsulated microorganisms are not electrically affected since the excess of charges is mainly distributed

on the jet surface. Nevertheless, several mechanical drawbacks require to be considered. Indeed, viscous forces acting on the microorganisms must be controlled to avoid their destruction, drastic changes in the osmotic environment of the microorganisms are expected because of the rapid solvent evaporation, and toxicity issues need to be taken into account aiming to minimize the microorganism exposure to organic solvents.[212]

1.5.4.6 Sensing

Owing to the highly porous structure and large surface area – to – volume ratio, nanofibers prepared via electrospinning have been widely explored in the area of sensing with high sensitivity and rapid response rate. For instance, electrospun nanofibers can be employed to sense the changes in concentration for chemical species, biomolecules, and even gas species.[213] Sensitive detection of physiologically important molecules, such as glucose and proteins, has also drawn much attention.[214,215] In addition, nanofiber – based mats can also act as highly sensitive optical sensors.[216]

1.5.5 Electrospun Nanofibers in Industrial Applications

According to the data released by "Research and Markets", the global market for nanofibers may reach 1 billion U.S. dollars by the end of 2021.[217] However, to meet the market huge demand, there is an impellent need to scale – up the production of electrospun nanofibers by developing and/or implementing new technologies. In this sense, the main issues in transferring electrospinning technology from laboratory scale to industrial production include large – volume production, precision in controlling the products, an increase of the diversity and functionality of nanofibers, and environmental concerns.[51,64] To achieve large – volume production, both high throughput and large areas are required for the produced mats. Hence, multiple – needle and needleless electrospinning hold great promise in increasing the volume of production. The reproducible manufacturing of high – quality products critically depends on both the accuracy and duplicability of a production process.[64] An integration of theoretical modelling and real – time manipulation of the parameters for electrospinning plays an important role in improving reproducibility. A climate – controlled electrospinning system is also beneficial in terms of keeping the temperature and relative humidity within suitable ranges to maintain reproducibility. In addition, another key aspect in the scale – up production of nanofibers is to ensure the generation and/or retention of functions because nanofibers with

unconventional structures or assembled into ordered arrays may be of greater value with respect to conventional nonwoven mats of nanofibers. The last but not least, environmental issues, such as pollution and safety concerns, must be fully considered when scaling up a spinning technique. During solution electrospinning, solvent typically represents 70 – 90 wt% of the solution, with its evaporation into the environment resulting in an environmental burden, safety issues, and waste of chemicals. Hence, when operated on a large scale, a solvent recovery system must be developed for collecting and recycling the evaporated solvent. Alternatively, green techniques such as melt electrospinning should be considered to avoid solvent employment.

To date, although a high number of issues still requires to be addressed, a broad variety of industrial – scale electrospinning instrumentations with different types of spinning/collecting devices and accessories are already available (Figure 11) and some entrepreneurs have indeed translated electrospun nanofibers from academic research to commercial applications. There are at least twenty companies in the world that manufacture a bunch of upstream nanofibers for over fifty different types of downstream products. These are predominantly employed for gas and liquid filtration, including the removal of dust, diesel particulate, smoke, and aerosol particles from an air intake system, as well as the separation of oil from wastewater. However, emerging products include reverse osmosis membranes for water purification, mats for fuel cells, separators for batteries, smart coatings, and biomedical scaffolds. In the near future, commercial products ready to debut are likewise those related to energy storage (e.g., separators for batteries) and smart coatings. For biomedical applications, new products keep entering clinical trials in recent years, despite most of the companies in the biomedical field are academic spinoffs or pharmaceutical companies that only develop proprietary products.

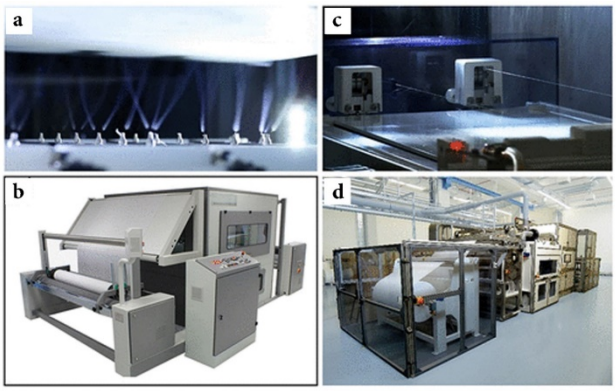

Figure 11. (a) Multiple – needle electrospinning developed by Inovenso Inc., which involves 110 needles and (b) a photograph of the industrial machine. Reproduced with permission from Ref. [218]. (c) Needleless electrospinning with the Nanospider Production Line developed by Elmarco Inc., and (d) a photograph of the Nanospider NS 8S1600U industrial machine. Reproduced with permission from Ref. [219].

Chapter 2. Polysaccharides

This Chapter briefly introduces and discusses the main properties of polysaccharides, which represent nowadays some of the most promising naturally occurring materials in various application fields in the viewpoint of greater sustainability. In particular, due to the topic of the present Thesis work, a complete description of alginate and chitosan is reported along with their main biomedical and pharmaceutical applications

.

2.1 General Properties

Polysaccharides represent, along with oligosaccharides, the most abundant group of naturally occurring biopolymers and have been found to play a topical role in many biological processes, such as cell – cell communication, embryonic development, infection of bacteria and/or viruses, and humoral and cellular immunity.[220–223] Specifically, together with polynucleotides, proteins, and lipids, polysaccharides constitute the four most important biomacromolecules in life science. Among them, bioactive polysaccharides usually refer both to those polysaccharides that show biological effects on organisms and those polysaccharides that can be produced by living organisms or functionalized from sugar – based materials.[224] In general, the biological activities of polysaccharides are strongly affected by their chemical structure and chain conformations. In this sense, the macromolecular structure of plant cell wall polysaccharides is extremely complex due to the presence of different monosaccharides as building blocks, which are usually isobaric stereoisomers, variations in sequence, linkage, branching, and distribution of side chains.[225,226] In addition, polysaccharides in microorganism (i.e., fungi, yeasts, and bacteria), algae, plants, and animals are always physically and/or chemically tangled with other biomolecules and some inorganic mineral substances.[227] In this sense, polysaccharides can be classified in many possible ways. Regarding the chemical composition, polysaccharides are classified into two groups, homopolysaccharides, which are made up of a single type of monosaccharides (e.g., cellulose), and heteropolysaccharides, which comprise more than one type of monosaccharides (e.g., heparin). Alternatively, polysaccharides can be classified according to the glycoside type as proteoglycans, glycoproteins, glycolipids, and glycoconjugates.[228] Additionally, based on the origins, bioactive polysaccharides can be categorized in plant, algae and lichen, microorganism, and animal – derived.

Polysaccharides are usually present together with various other components, including proteins, polynucleotides, lipids, extractives, lignin, and even some inorganic mineral substances. As such, the desired biological activities of polysaccharides are often undermined by these compounds, which may even cause antagonist effects or undesirable toxicity. Hence, pure bioactive polysaccharides are required to enable the safe, reproducible, and accurate dosage for experimental and therapeutic applications, as well as to enable the investigation of structure – properties relationship and facilitate the development of new compounds.[229] Specifically, since the bioactivity of polysaccharides is greatly dependent on their structural

information (e.g., molecular weight, presence of side chains and/or functional groups, etc.), how to properly isolate polysaccharides from complex matrix networks represents one of the most important tasks to deal with. As a consequence, in recent years novel extraction methods including supercritical fluid extraction, microwave – assisted extraction, and hot – water extraction have gained an increasing interest owing to their environmentally friendly process, higher extraction efficiency, cost effectiveness, and structure – preservation ability.[230–232] However, further purification of bioactive polysaccharides from crude extracts is of high importance ensuring the understanding of the relationship between structures and the safety of biomedical, pharmaceutical, and food products.[233]

2.1.1 Alginate

Alginate is a naturally occurring anionic polysaccharide broadly explored for many applications due to its biocompatibility, low toxicity, reduced cost, and mild gelation properties in presence of divalent ions. Alginate is known as a whole family of linear copolymers containing blocks of (1 – 4) – linked β-D-mannuronate (M unit) and α-L-guluronate (G unit) residues. The blocks may be composed of consecutive G residues (GG), consecutive M residues (MM), and alternating G and M residues (GM), as shown in Figure 12-a.[234,235] Commercially available alginate is usually extracted from brown algae, including *Laminaria hyperborea*, *Laminaria digitata*, *Laminaria japonica*, *Ascophyllum nodosum*, and *Macrocystis pyrifera*.[236] Hence, since polymers derived from different sources differ in composition (i.e., M/G ratio), sequence, block length, and molecular weight, all these parameters are critical factors affecting the physical – chemical properties of alginate and its resultant hydrogels.[237]

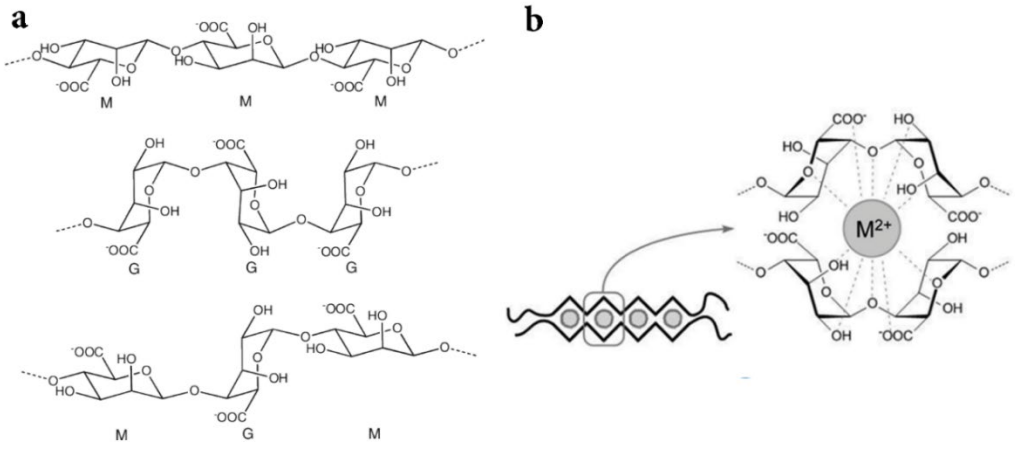

Figure 12. (a) Alginate chemical structure and chain structure depending on M/G ratio. (b) Schematic of alginate "egg - box" crosslinking model upon contact with bivalent ions.

The molecular weight of commercially available alginates usually ranges between 32 and 500 kg/mol, and the viscosity of alginate solutions increases as pH decreases reaching a maximum around pH = 3 – 3.5 as the carboxylates groups in the alginate backbone become protonated and vastly form hydrogen bonds. Despite increasing the molecular weight of alginate may improve some of its physical properties, alginate solutions obtained from high molecular weight polymers are greatly viscous, which is often undesirable for processing.[238] Although the biocompatibility of alginate has been extensively evaluated *in vitro* as well *in vivo*, there is still debate regarding the impact of alginate composition. However, much of this confusion is most likely related to varying levels of purity in the alginate studied in different reports. Generally speaking, as a matter of fact, alginate purified by a multi – step extraction procedure to a very high purity does not induce any significant foreign body reaction.[239,240]

Alginate is typically employed in the form of hydrogels, which consist of three – dimensional crosslinked networks comprised of hydrophilic polymers with a high – water content. Hydrogels are often biocompatible and can be delivered into the body via minimally invasive administration.[241] Chemical and/or physical crosslinking of hydrophilic polymers are typical approached to form hydrogels, whose physical – chemical properties are highly dependent on the crosslinking type and crosslinking density, in addition to the molecular weight and chemical composition of the employed polymers.[242,243] The most common method to prepare hydrogels from an aqueous alginate solution is to combine the solution with ionic crosslinking agents, such as divalent cations, which are believed to bind solely to guluronate blocks of alginate chains as their structure allows a high degree of coordination. The guluronate blocks of one polymer then form junctions with the guluronate blocks of the adjacent polymer chains in what is termed “egg – box” model of crosslinking, resulting in a gel structure (Figure 12-b).[244] The gelation rate is a topical factor in controlling gel uniformity and strength when using divalent cations, and slower gelation produces more uniform structures and greater mechanical integrity.[245] The gelation temperature also influences the gelation rate and the resultant mechanical properties of gels. Indeed, at lower temperatures, the reactivity of ionic crosslinkers is reduced and crosslinking becomes slower. As such, the resulting crosslinked network structures have greater order, leading to enhanced mechanical properties.[246] Additionally, the mechanical properties of ionically crosslinked alginate gels can vary significantly depending on the chemical structure of alginate. For instance, gels prepared from alginates with a high content of G residues exhibit higher stiffness than those with a high amount of M residues.[247] One critical drawback of ionically crosslinked alginate gels is the limited long – term stability in physiological – like conditions because these gels can be dissolved due to the exchange of

divalent ions into the surrounding media as a consequence of occurring exchange reactions with monovalent cations.

The conventional role of alginate in pharmaceutics includes serving as a thickening, gel forming, and stabilizing agent, as it plays a significant role in controlled – release drug products. Oral dosage forms currently represent the most frequent uses of alginate in pharmaceutical applications, but the development of alginate hydrogels as depots for tissue localized drug delivery is continuously growing. In addition, considering that the treatment of acute and chronic wounds is a pressing need in many facets of medicine, alginate – based wound dressings offer many advantageous features. Yet, alginate gels are increasingly being utilized as a model system for mammalian cell culture in biomedical studies. These gels can indeed be readily adapted as either 2D or more physiologically relevant 3D culture systems. Finally, alginate gels have been broadly explored over the past decades as a vehicle to deliver proteins or cell populations that can direct the regeneration or engineering of various tissues and organs in the body.[248–250]

2.1.2 Chitosan

Chitosan, consisting of β-(1 – 4) linked 2-amino-2-deoxy-β-D-glucopyranose, is an N – deacetylated derivative of chitin obtained by transforming the acetamide groups into primary amino groups,[251] as illustrated in Figure 13. Chitin is a naturally abundant mucopolysaccharide primarily obtained as a by – product of the fishery industry, hence representing a regenerating raw material only second to cellulose in terms of abundance.

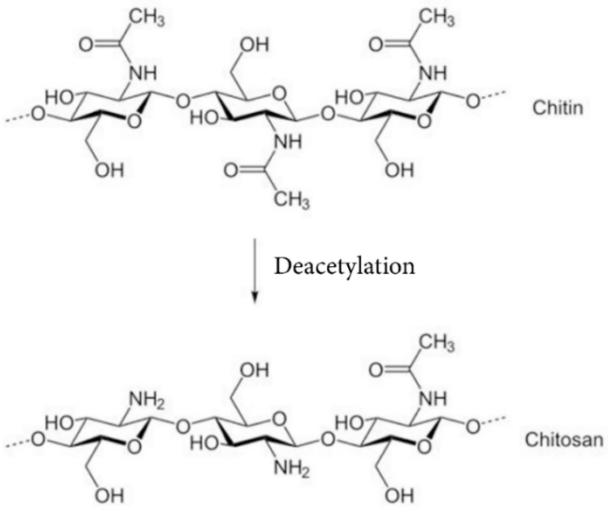

Figure 13. Chitin and chitosan chemical structure.

Chitin is the main component of the shells in crustaceous such as shrimps, crabs, and lobsters, but is also found in the exoskeleton of molluscs and insects, as well as in the cell walls of some fungi.[252,253] Deacetylation of chitin is almost never complete and commercially available chitosan usually still contains acetamide groups to some extent. However, chitosan is chemically much more reactive than chitin due to the presence of both primary and secondary hydroxyl groups on each repeating unit and amine groups on each deacetylated unit. The existence of amine groups in chitosan represents a great advantage since they enable distinctive biological functionalities, as well as the simple applicability of modification reactions.[254] The excellent properties of chitosan in terms of biocompatibility, biodegradability, bioactivity, non – toxicity, and good adsorption properties make this polysaccharide an extremely suitable and essential biomaterial drawing a great deal of industrial attention as a future probable alternative to synthetic polymers.[255,256] Crab and shrimp shell wastes are currently utilized as the major industrial sources of biomass for the large – scale production of chitosan. Processing biowastes from marine food factories help to recycle the wastes and make the derivatives or by – products useful in other fields. The crustaceous shell wastes are comprised of protein, inorganic salts, chitin, and lipids as main structural components. Hence, the extraction of chitin and chitosan is usually carried out by stepwise chemical methods.[257] Specifically, the deacetylation process involves the treatment of chitin with sodium hydroxide solutions at high temperatures for 1 – 3 hours in absence of oxygen followed by purification procedures to form chitosan with a cationic nature.[258] The deacetylation process results in the removal of acetyl group from chitin molecules and it determines the content of free amine groups ($-NH_2$) in the resultant chitosan. Depending on the production method and source, the degree of deacetylation (DD) is proportional to the degree of transformation of the chitosan from chitin, which depends on NaOH concentration, reaction time, and reaction temperature.[259] In general, DD ranges from 55 to 99%, but at least 85% deacetylation is required for a good solubility of chitosan.[260]

Chitosan has some special properties that make him suitable for versatile applications. Specifically, its use in the medical and pharmaceutical sector has grown rapidly currently receiving great interest from researchers throughout the globe due to its unique features including antibacterial effect, biocompatibility, biodegradability, non – toxicity, and high humidity absorption. The majority of chitosan biological properties are directly related to its physical – chemical properties, such as molecular weight, degree of deacetylation, and amount of moisture content.[251] For instance, chitosan – mediated inhibition of bacterial and fungi growth primarily relies on the molecular weight and functional groups of the polymer. Comparing to high molecular weight chitosan, small oligomeric chitosan can easily penetrate

the cell membrane of a microorganism and thereby prevents the growth of the cell by inhibiting RNA transcription.[261] The length of the polymer chain and the distribution of acetyl groups also affect the biodegradation kinetics of chitosan.[262,263] Additionally, the biological properties and antimicrobial activity of chitosan are persuaded by its cationic behaviour, which allows chitosan to predominantly interact with anionic components resulting in changes in permeability that lead to the death of the cell by inducing leakage of intracellular components.[264]

2.2 Biomedical and Pharmaceutical Applications of Polysaccharides

Polysaccharides and their derivatives hold several advantages over synthetic polymers because they are non – toxic, biodegradable, biocompatible, and less expensive compared to their synthetic counterparts. All these features endow polysaccharides with a broad spectrum of possible purposes in different areas, such as biomedical or pharmaceutical, food, textile, and cosmetic applications. To date, polysaccharides predominantly play an instrumental role in traditional disease control and health care, meanwhile many new application areas are explored such as tissue engineering, drug delivery, wound treatment, cancer prevention, diagnosis, and therapy, and handling bacterial and viral diseases. The main biomedical and pharmaceutical applications of polysaccharides are briefly summarized in the following Sections.

Tissue Engineering

The exploitation of polysaccharides and their derivatives for tissue engineering applications, such as biological signalling, cell adhesion, cell proliferation, cell differentiation, cell responsive degradation, and re – modelling, is attracting a great deal of interest in medical research for guiding and promoting new tissue regeneration or to define the shape and structure of cell growth.[265] A variety of polysaccharides, such as alginate, chitosan, hyaluronic acid, cellulose, starch, as well as their derivates, have been successfully developed as biomaterials for tissue engineering applications.[266] The use of polysaccharides as scaffolds in tissue engineering needs to fulfil the requirements like biocompatibility and non – toxicity, biodegradability with controllable degradation rate, appropriate porosity, and structural integrity.[265]

Wound Healing and Wound Dressing

Polysaccharides have been broadly explored to prepare wound healing materials because of their physical – chemical properties and specific interactions with cells and native extracellular matrix. It is generally accepted that bioactive polysaccharides play multifaceted roles in the mediation of the tissue repair processes and are involved in all the stages of wound healing, i.e., inflammation, granulation tissue formation, reepithelialisation, and re – modelling. Noticeably, wound healing – promoting activity of polysaccharides is also important in the designing of materials for tissue engineering.

Drug Delivery and Controlled Release

Polysaccharides hold promising potential in drug delivery and controlled release applications. As a matter of fact, numerous polysaccharide – based drug delivery systems have been developed for specific targeting delivery or controlled release, for protection of drugs from premature degradation, for improving intracellular penetration and transportation, for enhancing stability and bioavailability of drugs, or for the delivery of biomolecules such as genes, antigens, and small interfering RNA. These delivery systems are generally prepared in the form of 3D crosslinked networks, polyelectrolyte, or self – assembled structures, and polysaccharides – drug conjugates. The release of entrapped drugs or certain molecules can be triggered by the change of pH, ions, electrical or magnetic field, light, temperature, and redox potential.

Experimental

Chapter 3. Experimental Methodologies and Characterization Techniques

This Chapter aims to shortly present and summarize the main experimental methodologies, characterization techniques, and instrumentations employed in the present Thesis work to simplify the reader understanding of the following discussions.

3.1 Electrospinning Methodology and Instrumentation

In the present Thesis work, electrospinning was carried out either using a home – made setup comprised of an electrical power supply, a volumetric pump, and a proper collector (i.e., a flat aluminium foil in the case of a dry collection configuration or a coagulation bath in the case of a wet collection configuration) or an Electrospinning Professional Machine provided by Doxa Microfluidics and equipped with a flat or a rotating drum collector.

3.2 Rheological Investigation

Rheological measurements have been carried out on the polymer – based solutions explored in this Thesis work by means of a rotational rheometer MCR 301 (Anton Paar, Austria GmbH) equipped with a Peltier heating system and a solvent trap kit. Plate – plate (PP), cone – plate (CP), double – gap (DG), and concentric cylinders (CC) geometries were employed depending on the viscoelastic response of the sample of interest.

Steady – State Viscosity Measurements

Typically, steady – state viscosity measurements were conducted by applying an increasing shear – rate ($\dot{\gamma}$) at a fixed temperature to evaluate the sample flow behaviour. The most common performances that were observed for the tested samples are reported in Figure 14 and summarized in the followings:

i) Newtonian fluids. These fluids are described by Stoke law (Equation 1) and are characterized by a constant viscosity value independently on the applied shear stress:

Equation 1

$$\eta = \frac{\tau}{\dot{\gamma}}$$

where η is the apparent viscosity and τ is the shear stress.

ii) Shear – thinning fluids. These fluids present a viscosity value that depends on the applied shear stress. Most polymer – based formulations involve a constant viscosity region at low shear rate values (i.e., Newtonian plateau) followed by a gradual decrement of the viscosity as the shear rate increases. Such an outcome is mainly related to the polymer chain entanglement. Specifically, at very low shear stress, the macromolecules form a dense and continuous

polymer network creating topological constraints with each other (i.e., physical entanglements). As the applied stress is increased, entanglements are progressively disrupted and the polymer chains tend to assume an oriented configuration, which in turn leads to a decrease of the solution viscosity. In the present Thesis work, shear – thinning fluids have been described with the Carreau – Yasuda model:[267]

Equation 2

$$\eta = \frac{\eta_0 - \eta_\infty}{[1 + (\lambda\dot{\gamma})^a]^{\frac{1-n}{a}}}$$

where η_0 is the zero – shear viscosity (i.e., fluid viscosity at rest), η_∞ is the infinite – shear viscosity (i.e., fluid viscosity once all the polymer chains are aligned), λ is the fluid relaxation time, a is a fluid constitutive parameter, and n is the flow index.

iii) Bingham fluids. These materials behave as elastic solids at low shear stress and as viscous fluids at high shear stress. Specifically, these systems require a minimum stress (i.e., yield stress τ_y) to flow due to the existence of interactions between the components that form a weak solid structure preventing the movement of the fluid.

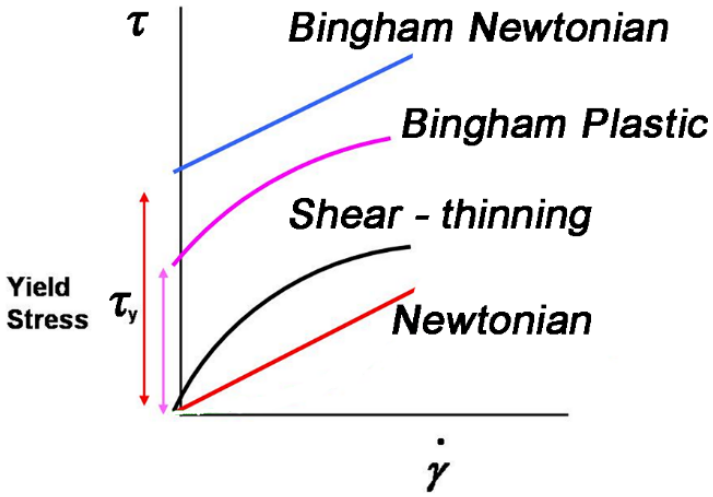

Figure 14. Commonly observed fluid flow behaviours.

Amplitude Sweep Measurements

Typically, amplitude sweep tests (AS) were performed at a fixed frequency ν (i.e., 1 Hz) and temperature varying the applied deformation amplitude γ to define the sample linear

viscoelastic region (LVER), in which the material is subjected to a stress insufficient to cause its structural breakdown (i.e., yielding) leading to the proper evaluation of its microstructural properties. If the applied stress overcomes a certain limit, non – linearities appear in the sample response, which therefore can no longer be easily correlated with the material microstructure.

Frequency Sweep Measurements

Typically, frequency sweep tests (FS) were carried out at a fixed amplitude within the LVER and temperature varying the applied deformation frequency. As such, the sample time dependence response was measured with low frequencies corresponding to long time scales and high frequencies corresponding to short time scales. Polymer – based solutions usually present a predominance of the viscous response (i.e., loss modulus G" > storage modulus G') at low frequencies, whereas an elastic response is observed (i.e., G' > G") at high frequencies. The crossover between the viscoelastic moduli corresponds to $1/\lambda$, with λ being the fluid relaxation time.

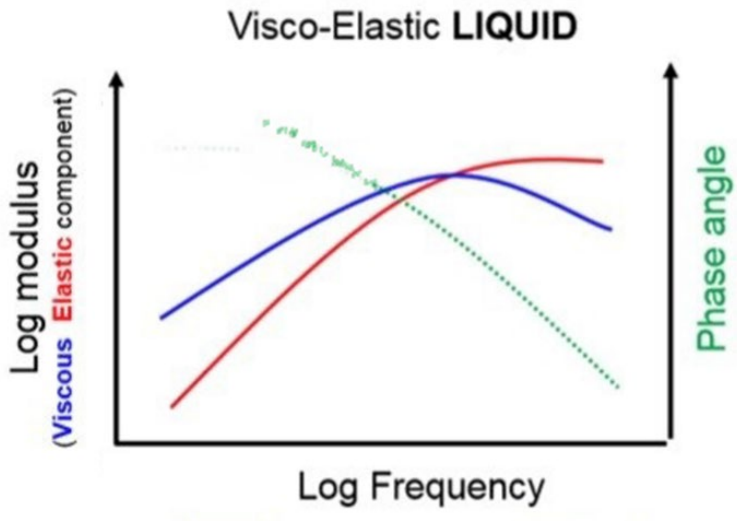

Figure 15. Typical frequency response of a viscoelastic liquid.

Temperature Sweep Measurements

Typically, temperature sweep tests (TS) were conducted at a fixed deformation amplitude within the LVER and frequency (i.e., 1 Hz) varying the temperature with a heating rate of 2 °C/min, unless otherwise indicated.

3.3 Thermal Investigation

Thermogravimetric analysis (TGA) has been carried out on the samples of interest by using a Mettler-Toledo TGA/DSC1 STARe instrument employed in dynamic mode from 30 °C up to 700 °C with a heating rate of 10 °C/min under a continuous nitrogen flow of 80 mL/min, unless otherwise indicated.
Differential scanning calorimetry (DSC) has been performed on electrospun mats by means of a Mettler DSC1 STARe instrument. Measurements were carried out under nitrogen atmosphere (10 mL/min) with a heating rate of 20 °C/min, unless otherwise indicated.

3.4 Morphological Investigation

Scanning electron microscopy (SEM) has been performed on electrospun meshes either using a Hitachi TM3000 benchtop microscope or a Tescan Vega 3 instrument. Good conductivity of the samples was achieved with a thin layer of silver or gold sputter – coated. Field – emission scanning electron microscopy (FESEM) has been carried out on electrospun mats by means of a ZEISS SUPRA 40 VP operating in direct or back scattering configuration. Good conductivity of the samples was achieved with a thin layer of carbon sputter – coated. In any case, the obtained micrographs have been analysed with the open – source software ImageJ.
Atomic force microscopy (AFM) has been executed on electrospun mats via a CoreAFM Nanosurf instrument operating in tapping mode with a sampling rate of 1024 points/line. Obtained micrographs have been analysed with the open – source software Gwyddion.

3.5 Mechanical and Dynamic – Mechanical Investigation

Mechanical investigation was performed on electrospun mats via uniaxial tensile test by using a displacement – controlled dynamometer Instron 5565. Sample testing has been performed on rectangular specimens (40 mm × 10 mm) at room temperature with an elongation rate of 25 mm/min. A preload of 0.1 MPa was always applied to ensure the correct sample loading. Young modulus (Y), tensile strength (σ_b), and elongation at break (ε_b) were derived from the obtain stress – deformation curves.
Dynamic – mechanical analysis (DMA) and dynamic – mechanical – thermal analysis (DMTA) have been carried out on electrospun meshes by means of a rotational rheometer MCR 301 (Anton Paar, Austria GmbH) either in torsional or extensional configuration. In the first case,

a SRF – 12 geometry and a CDT – 450 chamber were used. In the second one, a UXF geometry and a CTD – 450 chamber were used. A normal force equal to 0.25 N and constant stress of 2 MPa were always applied in the torsional and extensional configuration, respectively, to ensure the correct sample loading. As such, the storage modulus (i.e., G' or E') and the loss modulus (i.e., G" or E") were obtained for the investigated samples.

Amplitude Sweep Measurements

Typically, amplitude sweep tests were performed at a fixed frequency (i.e., 1 Hz) and temperature varying the applied deformation/stress amplitude to define the linear viscoelastic region.

Frequency Sweep Measurements

Typically, frequency sweep tests were carried out at a fixed amplitude within the LVER and temperature varying the applied deformation/stress frequency.

Temperature Sweep Measurements

Typically, temperature sweep tests were conducted at a fixed deformation/stress amplitude within the LVER and frequency (i.e., 1 Hz) varying the temperature with a heating rate of 2 °C/min, unless otherwise indicated.

3.6 Spectroscopic Investigation

Fourier – transform infrared spectroscopy (FTIR) has been conducted on electrospun mats by means of a Bruker Vertex 70 instrument, operating in ATR mode, in the 400 – 4000 cm^{-1} wavenumber length with a resolution of 4 cm^{-1}.

3.7 Uptake – Release Investigation

Electronic absorption spectra of dye aqueous solutions have been acquired by means of a UV-1800 spectrophotometer (Shimadzu, Japan) at room temperature in the 200 – 1000 nm wavelength range with fused silica cuvettes 1 cm pathlengths.

The dye absorption capacity at a given time t (q_t) and equilibrium (q_e) were determined by the following equations:

Equation 3

$$q_t = \frac{(C_i - C_t)V}{M}$$

Equation 4

$$q_e = \frac{(C_i - C_e)V}{M}$$

where C_i, C_t, and C_e are the dye concentration at the initial time, at a given time t, and at equilibrium, respectively, V is the solution volume, and M is the mass of the mat.

Kinetic Adsorption Experiments

In a typical kinetic adsorption experiment, around 5 mg of electrospun meshes were placed at the bottom of a cuvette and soaked with 3.5 mL of a dye aqueous solution at a given concentration (i.e., 5 – 500 mg/L). The system was gently shaken by means of a tilting agitator at room temperature and the concentration of the supernatant was periodically monitored through UV – vis spectroscopy.

Experimental adsorption data were fitted according to a pseudo – first – order kinetic model (Equation 5), to a pseudo – second – order kinetic model (Equation 6), and to an intra – particle diffusion model (Equation 7) according to the following equations:[266,268]

Equation 5

$$q_t = q_e(1 - \exp(-k_1 t))$$

Equation 6

$$q_t = \frac{k_2 q_e^2 t}{1 + k_2 q_e t}$$

Equation 7

$$q_t = k_t t^{1/2} + C$$

where k_1 is the pseudo – first – order rate constant, k_2 is the pseudo – second – order rate constant, k_t is a rate constant at a certain time t, and C is a constant related to the boundary thickness.

Equilibrium Adsorption Experiments

In a typical equilibrium adsorption experiment, around 50 mg of electrospun mats were soaked in 50 mL of dye solutions with increasing concentration (i.e., 5 – 500 mg/L) and left to equilibrate under gentle shaking for a week at room temperature. At the end of the sorption process, the supernatant fraction was analysed by UV – vis spectroscopy. Experimental adsorption data were fitted according to Langmuir model (Equation 8) and to Freundlich model (Equation 9), whose linear forms are expressed as:[269,270]

Equation 8

$$\frac{C_e}{q_e} = \frac{C_e}{q_{max}} + \frac{1}{q_{max}K_L}$$

Equation 9

$$\ln q_e = \ln K_F + \frac{1}{n}\ln C_e$$

where q_{max} is the maximum adsorption capacity, K_L is the affinity parameter, K_F is the Freundlich constant, and 1/n is the heterogeneity factor.

Release Experiments

In a typical desorption experiment, loaded electrospun nanofibers were removed from the loading medium, rapidly washed with EtOH, and placed in a cuvette with 3.5 mL of a phosphate buffer solution (PBS), composed of NaH_2PO_4 (10 mmol/L), Na_2HPO_4 (10 mmol/L) and NaCl (0.15 mol/L) at pH = 7.4 to simulate physiological conditions. Thereafter, the system was gently shaken by means of a tilting agitator, while maintained at a constant temperature of 37 °C, and the concentration of the supernatant was periodically monitored through UV – vis spectroscopy.

The cumulative release percentage (R%) was calculated according to:

Equation 10

$$R\% = \frac{m_r}{m_i} \cdot 100$$

where m_i is the dye loaded in the mat at time t and m_r is the dye amount released at time t.

3.8 Water – Related Properties Investigation

The water contact angle (WCA) of electrospun mats was measured by the deposition of a small drop of water on the sample surfaces using an Attention Theta Lite optical tensiometer.
The moisture content (MC) of electrospun meshes was assessed after thermal treatment at T = 110 °C under vacuum for 24 h according to:

Equation 11

$$MC\ (\%) = \frac{M_i - M_f}{M_i} \cdot 100$$

where M_i and M_f are the initial and the final weights of the sample, respectively.
The water vapour permeability (WVP) of electrospun meshes was evaluated at T = 37 °C and RH% = 50 following the ASTM E96-95 standard test method[271] according to:

Equation 12

$$WVP = \frac{WVTR \cdot d}{A \cdot \Delta p}$$

where WVPR is the water vapour transmission rate, d is the sample thickness, A is the area of the sample able to permit the vapour diffusion, and Δp is the partial vapour pressure difference between the two sides of the sample.

3.9 Zeta – Potential Investigation

Zeta potential (ζ) measurements have been carried out via Dynamic Light Scattering (DLS) analysis by using a Zetasizer Nano ZS90 (Malvern Instruments, Malvern, UK). All

measurements were performed at T = 25 °C by means of a Peltier thermostatic system and using 30 seconds as equilibration time prior to each analysis.

Chapter 4. Polysaccharide – Based Electrospun Mats as Wound Healing Patches

In the previous Chapters, the significance of electrospinning technique to prepare nanofibrous mats with potential applicability in various fields, with particular emphasis to biomedical and pharmaceutical industries, was presented and discussed together with the outstanding properties of polysaccharide materials that make them extremely suitable for such applications. These motivations drove us to develop novel polysaccharide – based meshes as simple, cost – effective, and highly promising wound healing patches with enhanced tissue regeneration capabilities. As such, in the present Chapter, we deeply describe the fabrication of alginate and chitosan – based nanofibrous mats and their full characterization as wound dressing materials.

4.1 Alginate – Based Nanofibrous Mats

Alginate scaffolds are a category of biomaterials that can be employed for the preparation of a wide range of biomedical and pharmaceutical products owing to their outstanding features, such as biocompatibility, biodegradability, ease of fabrication, and water – retention properties. One of the main advantages of alginate is its unique capability to bind bivalent ions, hence allowing the simply obtaining of physically crosslinked hydrogels without occurring in potential toxicity issues. However, these scaffolds have been rarely prepared in the form of nanofibrous mats since the mass production of alginate nanofibers is associated with several challenges. As a matter of fact, despite the importance and the various possible applications of alginate nanofibers, to date efforts have not been completely successful for the electrospinning of highly pure alginate nanofibers. In this sense, it is particularly difficult to obtain continuous and uniform nanofibrous structures from pure alginate solutions via electrospinning both in aqueous and other organic solvents. Hence, to fabricate alginate nanofibers, researchers have been using synthetic polymers such as poly(vinyl alcohol) or poly(ethylene oxide) as co – spinning agents, along with the implementation with surfactants or chemical modification. Nevertheless, the challenges of low content of alginate and the existence of impurities in resulting electrospun mats are still not completely solved. Beyond these drawbacks, alginate – based nanofibers represent a promising class of materials for the development of advanced wound dressing systems providing the ideal environment to promote tissue regeneration being able to foster cell viability, to allow gas exchange and exudate removal, and to offer mechanical support, as well as to deliver bioactive compounds.

4.1.1 Optimization of Alginate Electrospinning Process

This Section is substantially published at:

- *Dodero, A.; Vicini, S.; Alloisio, M.; Castellano, M. Sodium Alginate Solutions: Correlation between Rheological Properties and Spinnability. J. Mater. Sci. 2019, 54 (10), 8034–8046*

In this Section, aiming to understand both in which way the molecular structure of sodium alginate (SA) (i.e., molecular weight and M/G ratio) influences its processing via electrospinning technique, as well as how to optimize the nanofiber fabrication process, three different raw polysaccharides were explored by correlating their rheological properties in aqueous solutions with the capability to form electrospun nanofibers. Specifically, alginate – based formulations containing a proper amount of poly(ethylene oxide) (PEO) as co – spinning agent ($\bar{M}_v$ = 900 kg/mol) and of surfactant (i.e., Triton^{TM} X-100) were rheologically characterized and electrospun using either a dry – collector and a wet – collector electrospinning setup. The resultant alginate – based nanofibers were then crosslinked via calcium ions, leading to the formation of more or less morphologically adequate mats. The chemical structure of PEO and Triton^{TM} X-100 are reported in Figure 16.

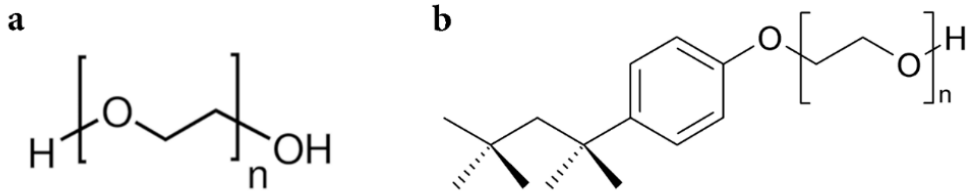

Figure 16. Chemical structure of (a) PEO and (b) Triton X-100.

Alginate samples employed in this preliminary work were sodium alginate low viscosity (SA LV) with $\bar{M}_v$ ~ 130 kg/mol and M/G ~ 1.5, sodium alginate medium viscosity (SA MV_M) with $\bar{M}_v$ ~ 415 kg/mol and M/G ~ 1.5, and sodium alginate medium viscosity (SA MV_G) with $\bar{M}_v$ ~ 300 kg/mol and M/G ~ 0.7. To be noted that a complete characterization of these materials, in terms of molecular weight and polyelectrolyte nature, is reported in Chapter 5.

As deeply discussed in Chapter 1, the solution viscosity and viscoelastic properties play a topical role in influencing the electrospinnability of polymer solutions likewise being directly related to chain entanglement. Hence, aiming to better understand how these properties are involved in the electrospinning of alginate, a detailed rheological characterization was carried

out either on pure alginate solutions or on alginate – PEO blends. In any case, the polymer concentration and the alginate – PEO ratio were fixed at 4 wt% and at 70 – 30, respectively, whereas Triton was added in a constant concentration of 1 wt%.

Steady – state viscosity measurements were employed to evaluate the flow behaviour of the prepared formulations at T = 20 °C, with the results reported in Figure 17. Zero – shear viscosity values of each tested sample were calculated with the Carreau – Yasuda model,[267] as described in Section 3.2, and are summarized in Table 1.

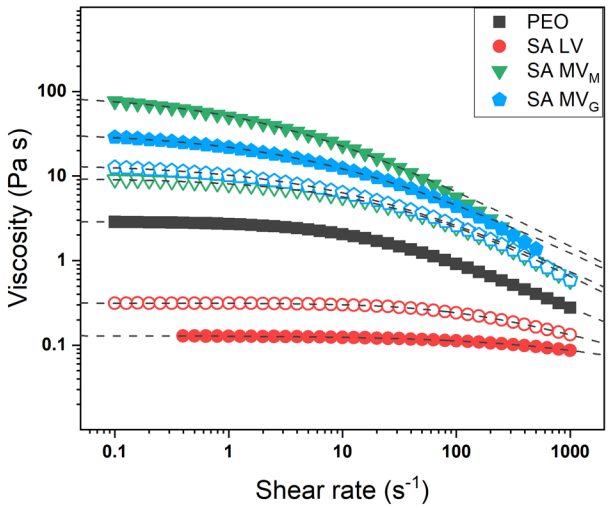

Figure 17. Flow curves of alginate – based formulations at T = 20 °C. Filled symbols represent pure component solutions, empty symbols represent blend solutions, and dashed lines represent the fitting of the experimental data with the Carreau – Yasuda model.

All samples clearly display a shear – thinning behaviour, involving a constant viscosity region at low shear rate values (i.e., Newtonian plateau) followed by a gradual decrement of the viscosity as the shear rate increases, which is related to the polymer chain disentanglement phenomenon.[272] Remarkably, the shear – thinning degree seems to be highly dependent on the polymer molecular properties. As a matter of fact, short and highly flexible chains require much higher shear stress before starting to align, whereas long chains start to disentangle as soon as the system is subjected to a shear solicitation. Hence, the results observed for the three different alginate – based formulations provide interesting insights into the macromolecule structure. SA LV solution presents a limited shear – thinning degree due to the shortness of the polymer chains thereby indicating a limited capability to form chain entanglements, despite the addition of PEO enhances to some extent the formation of a thicker polymer network. Conversely, SA MV_M and SA MV_G – based formulations present a marked viscosity decrement even at very low shear rate values, thus confirming the existence of a great number of entanglements, independently on the presence of PEO, because of their high molecular weight. However, SA

MV_G solution is characterized by a slightly smaller shear – thinning degree with respect to SA MV_M solution, which can be ascribable either to the shorter chains or to their greater rigidity. Indeed, as shown in Figure 12-a, the majority of G residues in the polymer backbone forces alginate chains to assume a "zig – zag" structure where a higher charge density is established, then increasing the repulsive forces among the backbone negative charges.[273] As such, these chains spontaneously exist in a partially aligned organization in solution, which in turn reduces the shear – thinning effect. The different viscosity drops after the addition of PEO and Triton for SA MV_M and SA MV_G – based formulations are a further proof of what reported. Specifically, the long and highly flexible PEO chains are effectively able to infiltrate between SA MV_M chain network leading to a considerable decrement of the zero – shear viscosity (i.e., ~ 90%). On the contrary, a much more contained effect is observed for SA MV_G sample (i.e., ~ 60%), in which the intrinsic rigidity of the chains reduces the effect of PEO.

Table 1. Calculated zero - shear viscosity values for alginate – based formulations.

Sample	η_0 (Pa·s)
PEO	2.89
SA LV	0.13
SA LV – PEO – Triton	0.32
SA MV_M	93.05
SA MV_M – PEO – Triton	9.46
SA MV_G	32.97
SA MV_G – PEO – Triton	13.86

Such an outcome was additionally studied by exploring the thixotropic behaviour of the prepared formulations via hysteresis loop tests at T = 20 °C. The higher the hysteresis area, the greater are the thixotropic properties of the tested fluid thereby indicating the need for a longer time for the polymer chains to disentangle and entangle.[274] SA MV_M and SA MV_G solutions are characterized by nearly the same hysteresis loop area, which however strongly decreases upon the addition of PEO and Triton likewise due to their help in increasing the macromolecule flexibility. Remarkably, as observed for the viscosity curves, SA MV_G – based formulation presents a less marked decrement of the thixotropic properties with respect to SA MV_M – based formulation, hence further suggesting the semi – rigid nature of its polymer chains. Concerning SA LV, the thixotropic behaviour is negligible since the very short chains can rapidly recreate the polymer network destroyed by the applied stress.

Other important information on the rheological properties of the prepared alginate – based mixtures was achieved via frequency sweep tests by using the time – temperature superposition principle (TTS) to calculate a master curve at T = 20 °C.[275] The viscoelastic spectrum of each tested sample is shown in Figure 18.

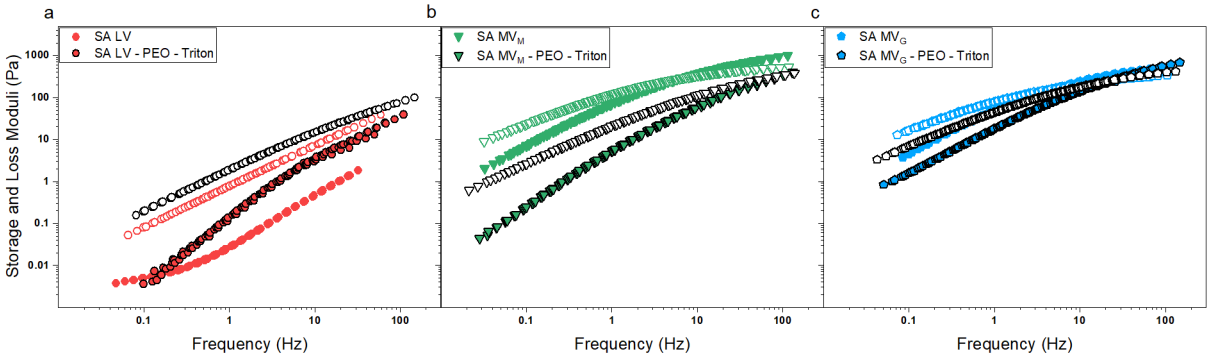

Figure 18. Viscoelastic spectrum of (a) SA LV, (b) SA MV_M, and (c) SA MV_G – based mixtures at T = 20 °C. Full and empty symbols represent the storage modulus G' and the loss modulus G", respectively.

The typical behaviour of polymer solutions is once again observed, with the predominance of the loss modulus at low frequencies, indicating a liquid – like performance, and the dominance of the storage modulus at high frequency, designating a transition from a liquid – like to a solid – like behaviour.[276] However, such a shift is not observed for SA LV – based formulation (Figure 18-a) because of the shortness of the polymer chains. It is worth to note that the crossover between G' and G", which corresponds to the relaxation time (λ) according to the reptation model, occurs at higher frequencies for SA MV_G solution (Figure 18-c) with respect to SA MV_M solution (Figure 18-b), and such finding can be ascribable to the greater stiffness of SA MV_G chains. In addition, comparably to what was observed for the other rheological measurements, the supplement of PEO and Triton decreases the viscoelastic response of SA MV_M (especially) and SA MV_G – based mixtures, whereas it increases G' and G" values for SA LV – based system.

Finally, the thermal stability of the prepared formulations was explored through rheological swing test,[277] in which the viscoelastic moduli were continuously measured while the temperature was cyclically varied between 0 °C and 40 °C. As a way of example, the data obtained for SA MV_G solution are reported in Figure 19. No differences are observed at all in the viscoelastic moduli of all the investigated formulations even after three and half cycles, indicating that no morphological transitions, phase separations, or degradation phenomena occur over consecutive thermal treatments, thereby confirming the stability of the prepared samples.

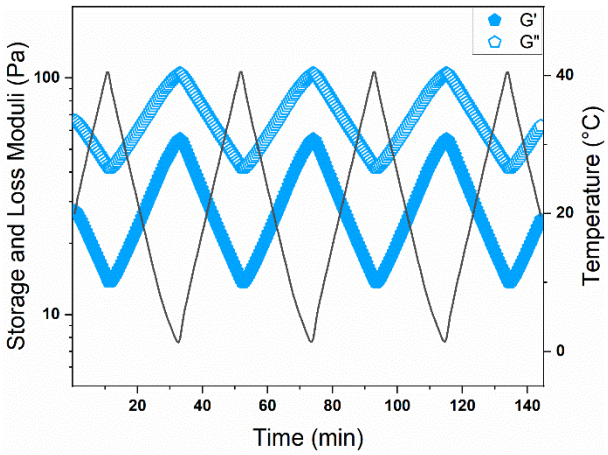

Figure 19. Variation of the viscoelastic moduli for SA MV_G solution upon several thermal stress cycles.

For what concerns the electrospinning process, based on what was reported in the literature, the rheological properties of pure alginate solutions should not allow such formulations to be successfully electrospun. As a matter of fact, SA MV_M and SA MV_G are characterized by way too high viscosity values at the selected concentration (i.e., 4 wt%), whereas SA LV presents the opposite issue due to the lack of enough chain entanglements. Despite changing the polymer concentration may somehow help to obtain proper viscosity values, the electrospinning of pure polysaccharide solutions could be hardly achieved.[278] Additionally, the aim of this preliminary study was primarily to understand the influence of the alginate molecular properties on the electrospinning process. To this end, the addition of PEO and Triton effectively allowed to obtain formulations with much more suitable rheological properties to be electrospun in the case of SA MV_M and SA MV_G, but SA LV – based system still displayed a way too low viscosity.[279,280] Therefore, only SA MV_M and SA MV_G – based formulation were electrospun at this stage.

It is extremely important to note that, due to the high water – solubility of alginate, a crosslinking treatment is of fundamental importance in enhancing the nanofiber stability in aqueous environments. To this end, as described in Chapter 2, divalent ions are the most employed approach to crosslinking alginate – based systems due to their biocompatibility, low toxicity, cost effectiveness, and reaction simplicity. Specifically, two different electrospinning setups and crosslinking procedures were explored to prepare alginate – based nanofibrous meshes:

i) Dry – Collector Setup. The selected alginate – based formulations were electrospun (5 mL) on an aluminium foil by using a flow rate of 0.5 mL/h, a spinneret – collector distance of 15 cm, a 22G flat – tip needle, and an applied voltage of 11 kV. The formed mats were then peeled

off from the collector, soaked for 30 min in an aqueous solution (EtOH – H_2O in a 60 – 40 ratio) containing 3 wt% of $CaCl_2$, and finally dried at T = 50 °C under vacuum.

ii) Wet – Collector Setup. The selected alginate – based formulations were electrospun (5 mL) directly on a liquid bath using a flow rate of 0.5 mL/h, a spinneret – collector distance of 15 cm, a 22G flat – tip needle, and an applied voltage of 11 kV. The liquid bath was comprised of an aqueous solution (EtOH – H_2O in a 60 – 40 ratio) containing 3 wt% of $CaCl_2$. After their preparation, the mats were dried at T = 50 °C under vacuum.

Both SA – based formulations could be electrospun independently on the used collector setup despite significant differences in the mat texture were obtained. Field – emission scanning electron microscopy (FESEM) was employed to investigate the morphology of the final samples (i.e., after the crosslinking treatment), with the related micrographs reported in Figure 20.

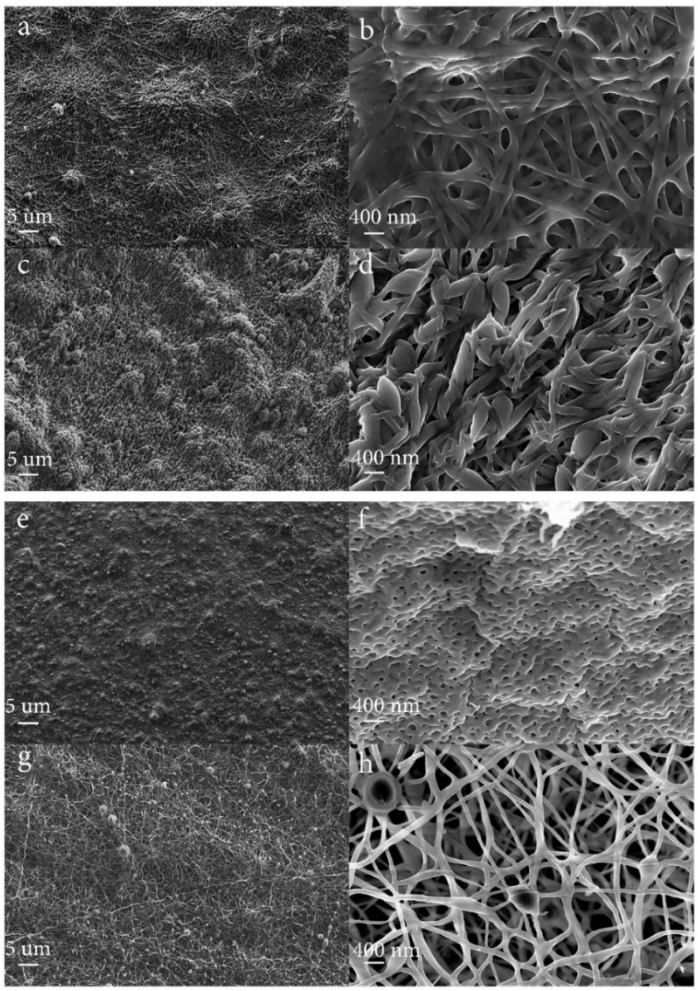

Figure 20. FESEM micrographs of (a – b) SA MV_M and (c – d) SA MV_G – based nanofibrous mats obtained by means of dry – collector setup. FESEM micrographs of (e – f) SA MV_M and (g – h) SA MV_G – based mats obtained by means of a wet – collector setup.

For what concerns the use of the dry – collector setup, it can be observed that both alginate – based formulations lead to promising but not completely satisfactory results. In detail, SA MV_M mat (Figure 20-a,b) is characterized by quite thin and homogeneous nanofibers with an average diameter of 150 nm, which however show a certain degree of coalescence with each other hence reducing the overall sample porosity. Such a result may be attributed to the alginate sample low amount of G units, which considerably reduces the crosslinking efficiency and does not allow to obtain isolate and well – defined nanofibers. Conversely, SA MV_G sample (Figure 20-c,d) presents strongly inhomogeneous nanofibers, which significantly affect the mat global morphology. However, owing to the high G moieties content in the explored alginate sample, the unsatisfactory results are likewise sought in the formulation viscosity that is probably too high to allow the efficient formation of homogenous nanofibers during the electrospinning process. Regarding the electrospun mats obtained by means of the wet – collector setup, strongly dissimilar results were achieved for the two investigated formulations. SA MV_M mesh presents a nearly continuous structure, in which the nanofibrous morphology can be hardly recognized and the porosity is extremely low. As a matter of fact, owing to the nature of this collector setup, the amount of G residues in the alginate backbone plays an even more critical role in obtaining homogeneous crosslinked nanofibers. Hence, the poor efficiency of the crosslinking reaction for SA MV_M leads to the almost complete coalescence of alginate nanofibers (Figure 20-e,f). The high G unit content in SA MV_G allows instead to obtain thin and stable nanofibers (average size of 100 nm) that provide the resultant mat with a really high porous structure (Figure 20-g,h), despite several inhomogeneities due to the improper formulation viscosity can still be observed.

Owing to their somehow promising microstructure, SA MV_M – based mat obtained via dry – collector electrospinning setup and SA MV_G – based mat obtained via wet – collector electrospinning setup were both selected to be further characterized. In detail, thermogravimetric analysis was employed to explore the sample composition and evaluate the presence of residual co – spinning agent. TGA curves are reported in Figure 21 and in Figure 22 for SA MV_M and SA MV_G – based mats, respectively, along with those of the polymers in powder form.

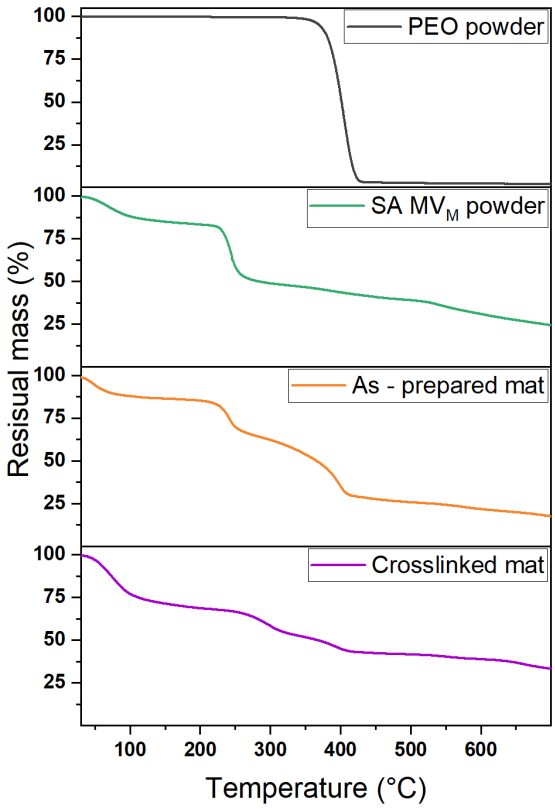

Figure 21. TGA profiles of PEO powder, SA MV$_M$ powder, as – prepared electrospun mat, and crosslinked electrospun mat in the case of a dry – collector electrospinning setup.

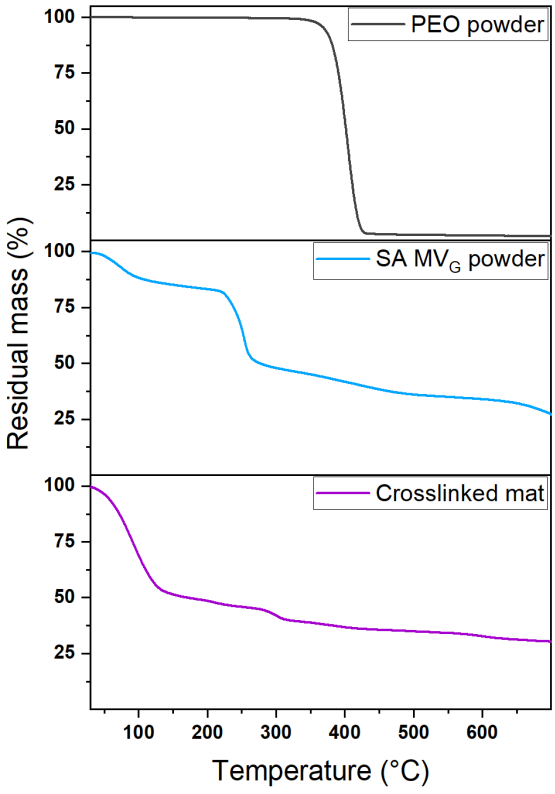

Figure 22. TGA profiles of PEO powder, SA MV$_G$ powder, and crosslinked electrospun mat in the case of a wet – collector electrospinning setup.

Both the investigated alginates (i.e., blue and green lines) present a multi – step degradation process where the most significant step occurs at T ~ 250 °C. PEO (i.e., grey line) is instead characterized by a single degradation step at T ~ 400 °C. Concerning the electrospun mats, all of them show an initial mass loss below 120 °C corresponding to the vaporization of residual humidity. The as – prepared SA MV_M – based mat (i.e., orange line) presents both the degradation signal of alginate and of PEO without significant temperature changes. Conversely, after the crosslinking treatment, alginate degradation occurs at T ~ 275 °C owing to the enhanced thermal stability induced by the crosslinking reaction, whereas the mass loss ascribable to PEO is significantly reduced suggesting the partial removal of the co – spinning agent. For what concerns the crosslinked SA MV_G – based mat, the degradation step related to alginate is depicted at T ~ 300 °C in agreement with its superior crosslinking capability and related improved thermal stability. Remarkably, PEO signal is not clearly detectable, which may suggest its complete elimination from the mat. As a matter of fact, being PEO highly soluble in water, it is most likely that it gets rapidly dissolved during the collection of the nanofibers within the liquid bath collector. In contrast, for the mat prepared with the dry – collector electrospinning setup, the 30 min of immersion within the crosslinking solution are apparently not sufficient to ensure the co – spinning agent complete removal.

Conclusions

The results presented in this Section, although being preliminary, provided important insights into the electrospinning of alginate – based formulations. First of all, a certain amount of synthetic co – spinning agent and surfactant are necessary to ensure a stable electrospinning process, as well as thin and homogeneous nanofibers. Moreover, the rheological properties of the mixtures play a critical role in conditioning the formation of the nanofibers and their resultant morphology. Significant viscoelastic properties and a zero – shear viscosity value around 10 Pa·s are found ideal to obtain homogeneous and well – defined alginate – based nanofibers, whereas lower and higher values do not lead to satisfactory results. In addition, the electrospinning setup, along with the way in which the crosslinking reaction is carried out and the alginate type, is found to strongly influence the resultant electrospun mat microstructure. The use of a wet – collector setup, despite it provides some advantages in terms of co – spinning agent removal and fiber morphology, requires the use of a G – rich alginate to ensure the rapid polymer crosslinking. Conversely, the more common dry – collector setup allows for greater versatility in the material selection but needs for better control of the mixture rheological

properties and does not allow for the easy washing of the co – spinning agent. Based on these results, the dry – collector setup was selected for the preparation of more advanced alginate – based electrospun mats.

4.1.2 Alginate Electrospun Mats Embedding Zinc – Oxide Nanoparticles

This Section is substantially published at:

- *Dodero, A.; Alloisio, M.; Vicini, S.; Castellano, M. Preparation of Composite Alginate-Based Electrospun Membranes Loaded with ZnO Nanoparticles. Carbohydr. Polym. 2020, 227, 115371*
- *Dodero, A.; Scarfi, S.; Pozzolini, M.; Vicini, S.; Alloisio, M.; Castellano, M. Alginate-Based Electrospun Membranes Containing ZnO Nanoparticles as Potential Wound Healing Patches: Biological, Mechanical, and Physicochemical Characterization. ACS Appl. Mater. Interfaces 2020, 12 (3), 3371–3381*
- *Dodero, A.; Vicini, S.; Lova, P.; Alloisio, M.; Castellano, M. Nanocomposite Alginate-Based Electrospun Membranes as Novel Adsorbent Systems. Int. J. Biol. Macromol. 2020, 165, 1939–1948*

The biological and antibacterial tests reported in this Section were carried out in collaboration with Prof. Sonia Scarfi and Prof. Marina Pozzolini of the Department of Earth, Environment and Life Sciences of the University of Genoa.

In this Section, alginate – based electrospun mats containing ad – hoc synthetized zinc – oxide nanoparticles (NPs) were prepared as potential wound – healing patches capable to promote cell adhesion and proliferation at the same time showing marked antibacterial properties. More in detail, after that the effect of the nanoparticles on the rheological properties of different alginate – based formulations (i.e., SA LV, SA MV_M, and SA MV_G) was investigated, a specific washing – crosslinking protocol was developed to endow the nanofibers with great stability in physiological – like conditions simultaneously removing the employed co – spinning agent. Subsequently, the most promising of the prepared mats was fully characterized to investigate its effectiveness in both promoting tissue regeneration and being exploited as a drug delivery system.

To date, bacterial infectious diseases are a serious health problem that has drawn the public attention worldwide as a human health threat, which is extended to economic and social complications. In this regard, antibacterial agents such as metal nanoparticles have started to gain an increasing deal of interest due to their capability to prevent bacterial contamination and proliferation. The properties of metal and ceramic NPs, such as Ag, ZnO, and TiO_2, are mainly determined by their size, composition, crystallinity, and morphology. Reducing the size to the nanoscale can indeed modify their chemical, mechanical, electrical, structural, morphological, and optical characteristics. Such features allow the nanoparticles to interact in a unique manner with cell biomolecules and thereby facilitate their physical transfer into the inner cellular structures.[281] Specifically, nano – sized ZnO structures exhibit significant antibacterial activity

over a wide spectrum of bacteria[282,283] owing to their capability to interact with the bacterial surface and/or with the bacterial core. These interactions are mostly toxic and have been broadly employed for antimicrobial applications in the biomedical, pharmaceutical, and food industries, despite the precise mechanisms are yet under debate.[284] Noticeably, ZnO – NPs are reported as non – toxic to human cells, which is a fundamental requirement to maintain good overall biocompatibility.[285,286] Owing to the aforementioned reasons, along with their easy, versatile, and cost – effective synthesis procedure, ZnO – NPs were selected as antimicrobial agents for the work carried out in the present Thesis project.

With these premises, zinc – oxide nanoparticles were first ad – hoc synthesized by following a green sol – gel procedure reported in the literature with some modifications.[287] One of the critical aspects concerning the preparation of bio – nanocomposites via electrospinning technique is represented by a good dispersion and stability of the nanoparticles within the starting polymer – based formulations. In addition, to exploit their full potentialities, the nanoparticles require to be homogeneously dispersed within the resultant nanofibers. Such features can be easily achieved without affecting the nanoparticle intrinsic biocompatibility by a simple surface functionalization with bio – based coatings. To this end, in a typical synthesis procedure, 1 mL of NaOH 1 M, 2 mL of zinc acetate dihydrate (ZnAc), and 5 mL of SA MV_M 1 wt% were vigorously mixed together and kept at T = 80 °C for 30 min. The obtained suspension was centrifugated at 4500 rpm for 30 min and the resultant white deposit was washed with deionized water three times to remove eventual unreacted chemicals. Finally, the nanoparticle powder was dried at T = 50 °C under vacuum and stored in desiccator.

FESEM micrographs, TGA degradation profile, and UV – vis spectrum of the so obtained ZnO – NPs are reported in Figure 23. Figure 23-a and Figure 23-b clearly indicate that the nanoparticles tend to aggregate in irregular star – like clusters with a dimension of several hundred nanometers, in which however single spherical – like nanoparticles with a diameter of 20 – 30 nm can still be recognized. In addition, the thermal degradation profile (Figure 23-c) of the synthesized ZnO – NPs presents a 20% weight loss in a temperature range between 30 and 400 °C ascribable to the vaporization of residual humidity (T < 100 °C) and physically bounded water (100 °C < T < 200 °C), as well as to the degradation of alginate chains (T > 250 °C) localized on the nanoparticle surface.[288] No additional degradation steps are observed at higher temperatures indicating the synthesized NPs to be highly stable. Figure 23-d reports the UV – vis absorption spectrum of ZnO – NPs dispersed in deionized water, in which two distinct absorption peaks can be clearly depicted.

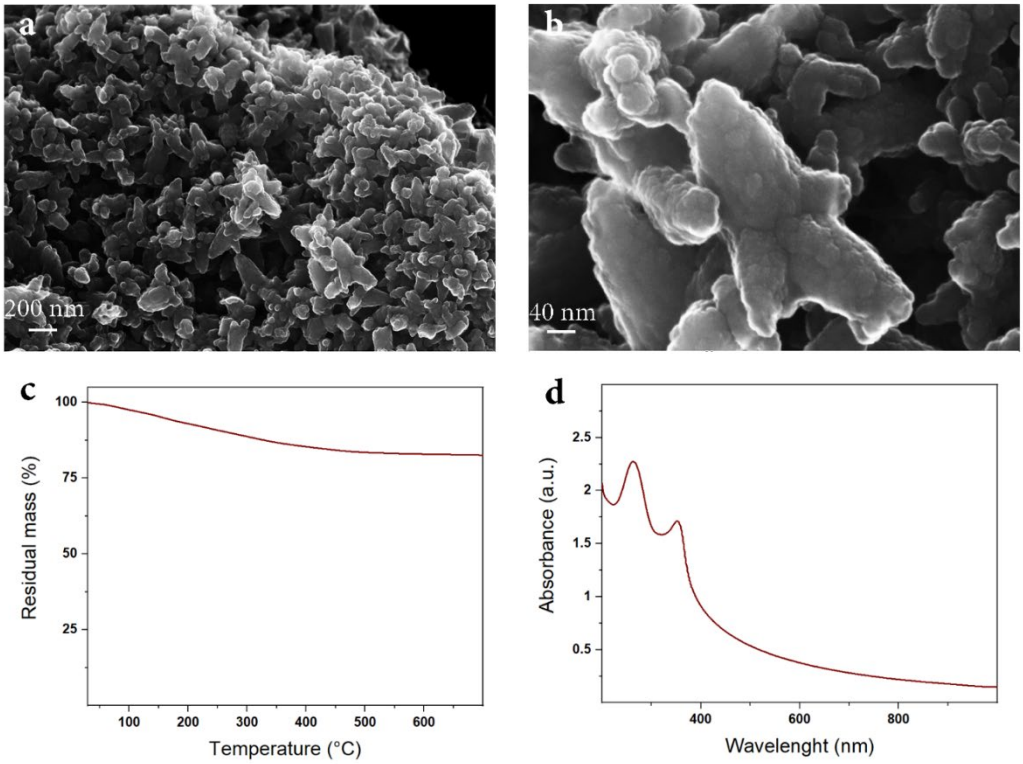

Figure 23. (a) and (b) FESEM micrographs of the synthetized ZnO nanoparticles at low and high magnification. (c) TGA profile of the synthetized ZnO nanoparticles. (d) UV – vis spectrum of a 0.025 wt% aqueous suspension of the synthetized ZnO nanoparticles.

The absorption at 352 nm is related to the nanoparticles, but it is blue – shifted with respect to the absorption of bulk ZnO (i.e., 380 nm) likewise due to both the presence of an alginate layer on the nanoparticle surface and to quantum confinement effects.[289,290] Remarkably, the sharp absorption profile of such band denotes the monodispersed nature of the nanoparticles, hence confirming the morphological investigation and demonstrating that, beyond their tendency to aggregate, the nanoparticles maintain their individuality and do not coalesce in a bulk structure.[291] The other absorption peak, which occurs at 263 nm, is instead directly ascribable to residual alginate chains.[292]

Considering the above – discussed results, it can be safely assumed that alginate can be effectively employed as stabilizing agent in the synthesis of ZnO - NPs via a simple sol – gel method creating a superficial coating layer able to protect the nanoparticles and prevent their aggregation. Hence, alginate – based formulations containing the synthesized nanoparticles were prepared and rheologically investigated before being electrospun. Firstly, ZnO – NPs were dispersed in deionized water and sonicated at 59 Hz for 3 hours. A proper amount of alginate powder was then added to the obtained suspensions, followed by the addition of PEO powder and Triton. Mixtures were kept under stirring for at least 48 hours to ensure

homogeneity. The total polymer concentration was varied between 3 and 4 wt% for SA MV_M and SA MV_G – based formulations and between 6 and 8 wt% for SA LV – based formulations. SA – PEO ratio, Triton concentration, and nanoparticle concentration were kept constant at 70 – 30, 1 wt%, and 0.25 wt%, respectively.

Steady – state viscosity measurements were first carried out on the prepared formulations at T = 20 °C, with the obtained flow curves shown in Figure 24.

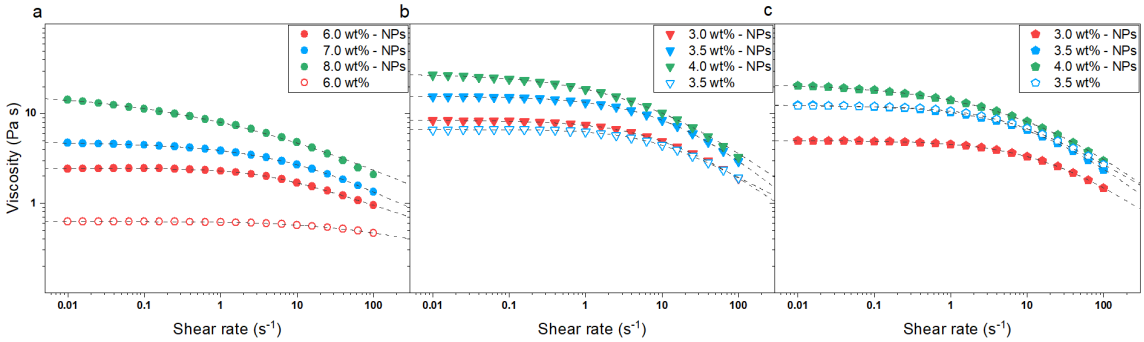

Figure 24. Flow curves of (a) SA LV, (b) SA MV_M, and (c) SA MV_G – based formulations containing ZnO - NPs. Dashed lines represent the fitting of the experimental data with the Carreau – Yasuda model. For comparison, flow curves of some alginate – based mixtures without nanoparticles are also reported with empty symbols.

All the tested mixtures display a shear – thinning behaviour with the zero – shear viscosity values raising with increasing the polymer concentration, as summarized in Table 2. Remarkably, the presence of an initial constant viscosity region (i.e., Newtonian plateau) along with the consistency of the experimental data with Carreau – Yasuda model indicate the good dispersion of ZnO – NPs within the alginate – based formulations.[293,294]

Table 2. Summary of the zero – shear viscosity for the tested alginate – based formulations containing ZnO nanoparticles calculated with the Carreau – Yasuda model. *Data reported in brackets represent the values calculated for the correspondent formulations without nanoparticles.

Sample	Polymer concentration (wt%)	η_0 (Pa·s)
SA LV - based	6.0	2.4 ± 0.1 *(0.6 ± 0.1)
	7.0	4.8 ± 0.1
	8.0	17.8 ± 2.7
SA MV_M – based	3.0	8.5 ± 0.1
	3.5	15.7 ± 0.1 *(6.7 ± 0.1)
	4.0	27.8 ± 0.3
SA MV_G – based	3.0	5.0 ± 0.1
	3.5	12.5 ± 0.1 *(12.2 ± 0.1)
	4.0	21.8 ± 0.2

By comparing the η_0 values of the formulations with and without ZnO – NPs, it can be observed that the nanoparticle presence induces a significant viscosity increment for SA LV and SA MV_M – based formulation but has an almost negligible effect on the SA MV_G – based one. This finding can be explained by considering the interactions occurring between ZnO – NPs with the polysaccharide chains. Specifically, the positively – charged nanoparticles are supposed to be predominantly linked by the negative charges present on the alginate backbone via electrostatic bonds. In addition, the contribution of the hydrogen bonding involving the hydroxyl groups of alginate and those of ZnO – NPs may also enhance such interactions.[295–297] Being M – rich alginates characterized by a "straight – line" chain structure (Figure 12-a), a great number of carboxyl and hydroxyl groups are exposed to promote the interactions with the nanoparticles, thus leading to a considerable increment of the formulation viscosity. In contrast, the majority of G units in the alginate backbone creates "cavities" in the "zig – zag" chain structure (Figure 12-a), thereby significantly reducing the capability of the aforementioned interactions to be established, which in turn prevents the raising of the sample viscosity.

Considering a reference zero – shear viscosity value around 10 Pa·s and keeping in mind the importance of chain entanglement to ensure the proper nanofiber formation during electrospinning, alginate – based formulations with a polymer concentration of 3.5 wt% were selected to be electrospun for SA MV_M and SA MV_G. Despite the low viscosity value, SA LV – based mixture with a polymer concentration of 6 wt% was instead chosen. Specifically, this choice was due to the fact that in such case a higher concentration did not allow to obtain a homogeneous solution owing to the difficulty to complete solubilize alginate polysaccharide. The electrospinning process was carried out for all the selected mixtures by using a spinneret – collector distance of 15 cm, a flow rate of 0.75 mL/h, a flat – tip 22G needle, and an applied voltage between 10 and 12.5 kV. Interestingly, SA MV_M – based formulation could not be electrospun at all likewise due to the establishment of very strong interaction between the polymer chains and the nanoparticles, as also evidenced by the rheological measurements, which somehow prevent the formation of a stable polymer jet with consequent difficulties in forming a nonwoven mat. Nevertheless, the same phenomenon is expected to play a critical role in the electrospinning of SA LV – based mixture with ZnO – NPs creating physical bridges between the very short polymer chains and acting as fictitious entanglements, thus enhancing the solution spinnability leading indeed to the formation of a consistent nonwoven mat. For

what concerns SA MV_G – based formulation, the absence of neat interactions between the polymer and the inorganic fillers does not significantly influence the electrospinning process allowing to prepare a nonwoven patch with really good manageability. Based on the results presented and discussed in the previous Section, a washing – crosslinking protocol was here developed to completely remove the co – spinning agent (i.e., PEO) at the same time stabilizing the nanofibers to make them water – insoluble. To this end, both SA LV and SA MV_G – mats were soaked in EtOH at T = 70 °C overnight (i.e., washing step) and subsequently in a 3 w/v% $SrCl_2$ medium for 30 s (i.e., crosslinking step). The mats were then washed several times with deionized water and finally dried at T = 50 °C under vacuum. It is noteworthy that strontium ions were selected as alginate crosslinkers due to their high affinity for the polysaccharide aiming to ensure complete stability to the nanofibers in aqueous environments.

FTIR and TGA were employed to evaluate the sample composition, as well as the effective crosslinking of alginate. As a way of example, Figure 25 shows FTIR spectra of SA MV_G powder, PEO powders, and crosslinked sample with similar results obtained for SA LV – based mat.

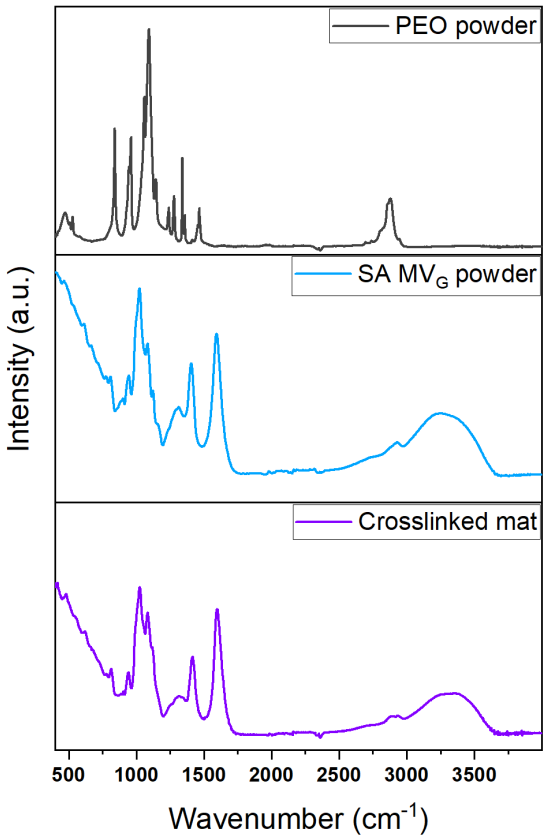

Figure 25. FTIR spectra collected in ATR mode for PEO powder (grey line), SA MV_G powder (blue line), and washed – crosslinked SA MV_G – based mat (violet line).

The spectral profile of the electrospun mat highly resembles that of alginate powder with slight differences due to both the presence of the nanoparticles and the occurred crosslinking reaction.[298–300] Specifically, the large unstructured band in the 3000 – 3600 cm^{-1} range, which corresponds to the stretching vibrations of hydroxyl groups, is broader and slightly shifted to lower wavenumbers suggesting the establishment of intermolecular H – bonds between alginate and ZnO – NPs. Regarding the bands at 1599 cm^{-1} and at 1417 cm^{-1}, they are assigned to the asymmetric and symmetric stretching vibrations of the carboxylic groups, respectively. Yet, in the fingerprint region, the signals at 1085 cm^{-1} and 1026 cm^{-1} correspond to C – O – C vibrations, whereas those falling at 940 cm^{-1} and 904 cm^{-1} are ascribable to C – O vibrations. Despite some of these bands may be related to both alginate and PEO polymers, the characteristic signal of the co – spinning agent are not detected in the electrospun mat spectrum, hence suggesting its complete removal. To this end, thermogravimetric analysis was employed to further verify the presence of residual co – spinning agent in the crosslinked mat. Figure 26 reports the TGA and DTG profiles for PEO powder, alginate powders, and crosslinked mats.

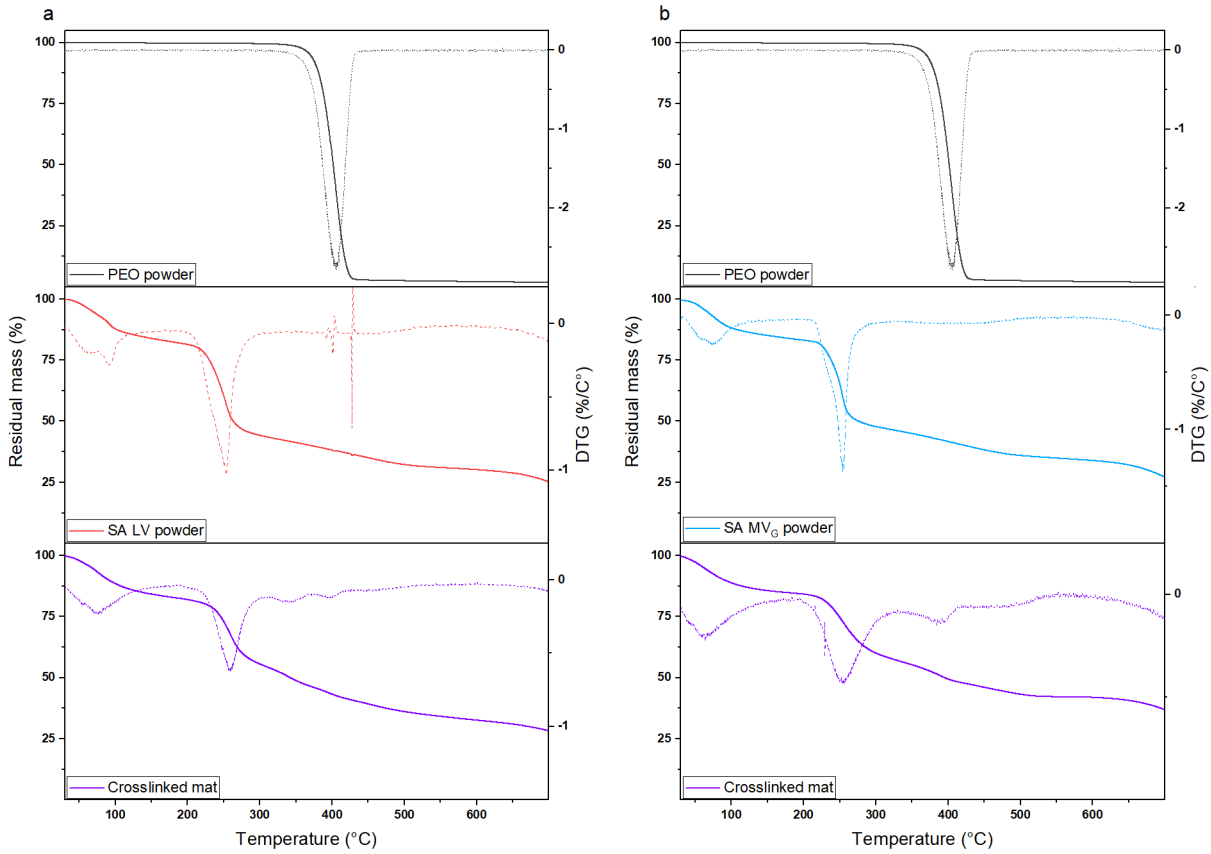

Figure 26. (a) TGA and DTG profiles for PEO powder (grey line), SA LV powder (red line), and washed – crosslinked SA LV – based mat (violet line). (b) TGA and DTG profiles for PEO powder (grey line), SA MV_G powder (blue line), and washed – crosslinked SA MV_G – based mat (violet line).

As previously described in Section 4.1.1, SA powders present different mass loss processes ascribable to the vaporization of residual humidity, the decomposition of the polymer backbone to form metal carbonates, and the final degradation step,[301] whereas a single and tight peak can be observed for PEO powder. For what concerns the crosslinked mats, the TGA profile mostly resembles that of alginate powders except for the presence of an additional decomposition step, which is however not attributable to the co – spinning agent. Specifically, this degradation step can be observed at T = 330 – 350 °C and at T = 360 – 380 °C for SA LV and SA MV_G – based mat, respectively, and is likewise related to the crosslinking reaction that is able to stabilize the polymer increasing its thermal stability. The observed difference in the degradation temperature can be easily explained by considering the fact that SA LV possesses a much smaller amount of G moieties in its backbone with respect to SA MV_G, as well as a considerably lower molecular weight, hence presenting a lower crosslinking degree and consequent thermal stability. By considering both FTIR and TGA results, it can be assumed that PEO component is mostly washed away from the final composite mats mainly due to the soaking process in hot ethanol. Indeed, while alginate is completely insoluble in alcohols, PEO becomes soluble in EtOH above its melting temperature (T_m ~ 60 °C),[302] which allows its removal meanwhile preserving the alginate nanofiber morphology.

Morphological investigation was then carried out on the obtained mats via scanning electron microscopy with the obtained micrographs reported in Figure 27.

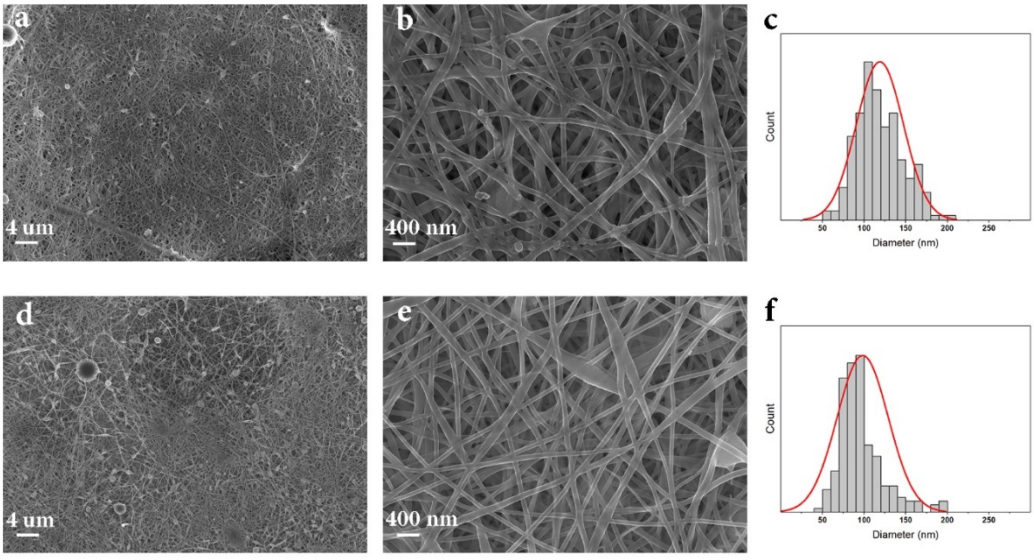

Figure 27. FESEM micrographs and fiber diameter distribution for (a – c) SA LV and (d – f) SA MV_G – based crosslinked mats containing ZnO nanoparticles.

Both mats are characterized by a uniform and highly porous microstructure consisting in well – formed nanofibers quite symmetrically distributed in a single population with only a few defects detectable. In particular, SA LV – based mat (Figure 27-a,b) presents fibers with an average diameter of 120 nm but a quite rough and wrinkled surface, as well as partially coalesced, which is most likely related to both the high M/G ratio and low molecular weight of the polymer. Indeed, as already mentioned above, the predominance of M units and the short polymer chains reduce the efficiency of the crosslinking treatment with bivalent ions thus leading to nanofibers with poor stability and shape defects. Conversely, owing to the low M/G ratio and the high molecular weight, SA MV_G – based mat (Figure 27-d,e) is characterized by well – separated and smooth nanofibers with an average diameter of 100 nm. Noticeably, in both cases, ZnO nanoparticles and their aggregates could not be clearly detected in FESEM micrographs, thus suggesting their complete and homogeneous incorporation within the nanofibers. To this end, EDX spectroscopy was carried out on the crosslinked samples to check for the effective presence and distribution of ZnO – NPs, as reported in Figure 28 for SA MV_G – based sample by a way of example.

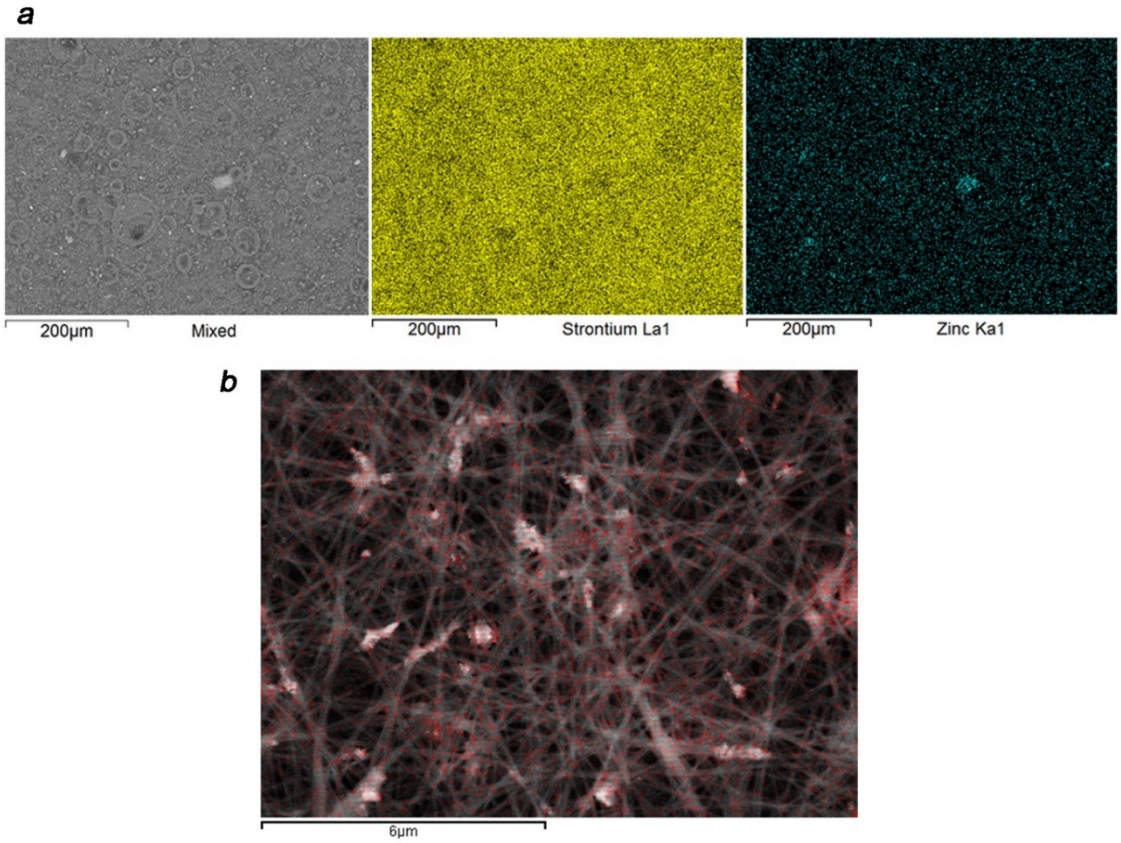

Figure 28. (a) EDX map of SA MV_G – based mat where strontium ions are represented in yellow and ZnO – NPs are represented in blue. (b) EDX mat of SA MV_G – based mat where ZnO – NPs distribution is indicated by red dots.

Remarkably, ZnO – NPs appear to be outstandingly well distributed within the mat in agreement with the FESEM micrographs. Additionally, the homogenous and dense strontium ion distribution clearly indicates the high crosslinking degree of alginate chains, further confirming the validation of the developed washing - crosslinking protocol to prepare stable alginate – based nanofibers.

By considering the discussed results, SA MV_G – based mat embedding ZnO nanoparticles was selected as the most promising among the prepared samples. Therefore, a complete characterization of its physical – chemical properties, biological response, and drug release capabilities will be examined in the following of the present Thesis aiming to use the mat as a proficient wound healing patch. For simplicity and to avoid misunderstandings, from now on till the end of the Section, such mat will be only labelled as alginate – based. At first, the mechanical performances and dynamic – mechanical behaviour of the mat were evaluated as described in Section 3.5 with the results shown in Figure 29. For better comparison, a control sample without nanoparticles, which has been prepared by following the same fabrication protocol, was evaluated as well.

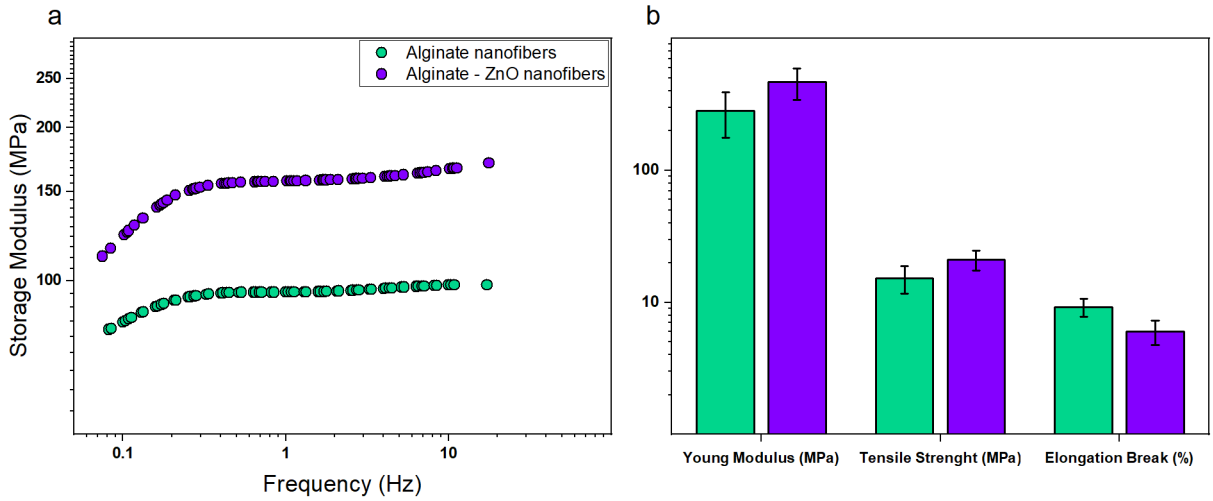

Figure 29. (a) DMA spectrum at T = 37 °C and (b) summary of the mechanical properties at room temperature of alginate – based mats with (violet) and without (green) nanoparticles. DMA analysis was carried out in torsional configuration with $\gamma = 0.002\%$.

Both the investigated mats are characterized by a similar dynamic – mechanical behaviour at T = 37 °C (Figure 29-a) showing an increase of G' at low frequencies (i.e., terminal region) followed, at intermediate frequencies, by a region in which G' shows an almost constant value (i.e., rubbery plateau) before starting to increase again at high frequencies (i.e., transition region).[303,304] However, a significant difference in the storage modulus values can be observed in the two samples, with the presence of the nanoparticles highly improving the stiffness of the

electrospun patch. Similar results were achieved by calculating the Young modulus, the tensile strength, and the elongation at break at room temperature via uniaxial tensile test (Figure 29-b). Specifically, the nanoparticles dispersed within the nanofiber structure provide a mechanical reinforcement, hence increasing the mechanical response of the tested material reducing at the same time its deformability.[305,306] In general, it can be observed that the prepared composite alginate – based mat presents a mechanical behaviour similar to that of human skin and soft tissue,[307,308] as such representing a promising product to be used for various biomedical and pharmaceutical purposes.

Beyond the mechanical behaviour, water – related properties, such as water contact angle, water vapour permeability, and moisture content are other important features to be considered when developing wound healing patches. Specifically, hydrophilic materials are usually preferred to induce cell adhesion and proliferation, and they should at the same time allow sufficient gas – vapour exchange to provide the wound with the proper amount of oxygen and ensure the exudate removal. Additionally, to be safely stored for a certain amount of time, such products must display a low content of humidity, which may otherwise affect their long – term physical – chemical properties. A summary of the measured water – related properties of alginate – based mat with and without ZnO – NPs is reported in Table 3. See Section 3.8 for a detailed description of the used methodologies.

Table 3. Summary of the water – related properties of alginate – based mats with and without ZnO nanoparticles.

Sample	WCA (°)	WVP (g/m·Pa·s)	MC (%)
Alginate fibers	22 ± 7	$4.7 \cdot 10^{-12}$	11 ± 1
Alginate – ZnO fibers	30 ± 8	$3.8 \cdot 10^{-12}$	11 ± 1

Both samples show high hydrophilicity (i.e., WCA << 90°), which is indeed a fundamental characteristic to provide the ideal environment to foster cell viability by promoting adhesion and proliferation.[309] The slightly lower water affinity observed for the composite mat with respect to the pure alginate nanofibers is likewise ascribable to the high hydrophobicity of ZnO – NPs, whose presence however does not significantly modify the intrinsic hydrophilic nature of the electrospun mat. The presence of the nanofillers is found to play a role also in conditioning the water vapour permeability of the prepared mats. In particular, the composite mat presents a higher water vapour barrier capability (i.e., lower WVP value) with respect to the pure alginate mat owing to the completely impermeable and hydrophobic nature of the

nanoparticles. Remarkably, despite the water vapour permeability of the prepared mats is considerably smaller compared to that of similar polysaccharide – based films, which is most likely because of the intrinsic microstructure of electrospun meshes,[295] the WVP measured values are in good agreement with those reported in the literature for effective wound healing patches.[310–312] Additionally, the presence of the nanofillers seems to not affect at all the moisture content of the mats, which is in fact quite low (i.e., 11%) for both samples, thereby indicating the possibility to safely store the samples for a long time period without risking to affect their performances.

Owing to its promising physical – chemical properties, the developed alginate – based electrospun mat was then subjected to a detailed biological evaluation to test its effective capability to promote cell adhesion and to avoid bacteria contamination, as well as to assess possible cytotoxicity issues. In this regard, the effect of the nanoparticles was especially explored as well. Two distinct cell lines consisting of murine fibroblasts (L929) and human keratinocyte (HaCaT) were employed. Cell adhesion was first evaluated qualitatively by stereomicroscopic observation of MTT – stained cells after 16h of culture onto the pure and composite alginate – based mats. From the microscopic observation (Figure 30), cell shape and adhesion to the substrate are very similar among the two samples for both cell lines.

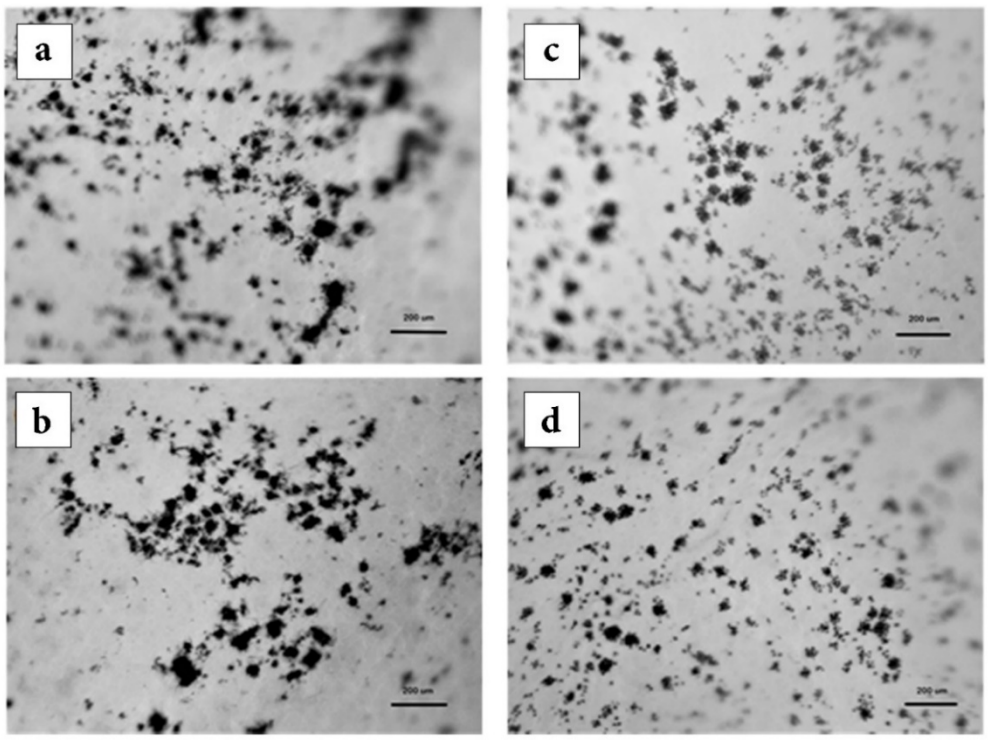

Figure 30. Microscopic observation of HaCaT cell adhesion after 16h on (a) alginate nanofibers and (b) alginate – ZnO nanofibers. Microscopic observation of L929 cell adhesion after 16h on (c) alginate nanofibers and (d) alginate – ZnO nanofibers.

Additionally, to assess the stability of the mats in physiological – like conditions, both samples were incubated in fetal bovine serum (FBS) at 37 °C for 10 days. Remarkably, no macroscopic modifications or deteriorations were depicted for both samples within the investigated time period, thus indicating a long – term stability of the materials maintained in conditions resembling those of physiological fluids.

Aiming to deeply explore the biocompatibility of the prepared mats, with particular attention paid to the presence of ZnO nanoparticles, the cytotoxicity of eventually released chemicals, the adhesion, and the cell growth of L929 and HaCaT cell lines were then evaluated within the present Thesis project. Firstly, the cytotoxicity of eventual substances released by the scaffolds after soaking them in complete culture medium for 6h was investigated by MTT test after 24h and 48h of incubation of the cells. As shown in Figure 31-a,b, no signs of cytotoxicity are ever observed for the two cell lines with respect to the untreated cells considered as the control (C). Such results clearly indicate that no significant release of toxic compounds from the mats occurs during the incubation with a complete cell medium and that no chemical residuals from the preparation of the samples are even present in the final products. Hence, it can be safely supposed that the proposed alginate – based nanofiber fabrication procedure is of no harm for animal use.

L929 fibroblasts and HaCaT keratinocytes were then evaluated for their adhesion capability, after 16h of incubation, and for their ability to grow, after 72h of incubation, on the alginate – based patches by means of MTT test. To this end, the results (Figure 31-c,d) were compared to a well – known commercial porcine collagen scaffold already used in bone and dental surgery (i.e., Bio – Gide scaffold). Compared to the control commercial collagen sample, L929 fibroblasts have a significantly lower capacity to adhere to the alginate – based mats as shown in Figure 31-c (grey bars), where the percentage of attached cells after 16h of incubation is below 50% independently on the nanoparticle presence. Conversely, when observing cell growth at a longer incubation time (i.e., 72h), no significant difference is detectable between fibroblast cell growth on pure alginate – based mat with respect to the collagen scaffold, whereas a marked cell reduction can be observed for the alginate – ZnO nanofibrous sample (i.e., $35.3 \pm 7.7\%$ cell growth compared to collagen mat, $p < 0.05$).

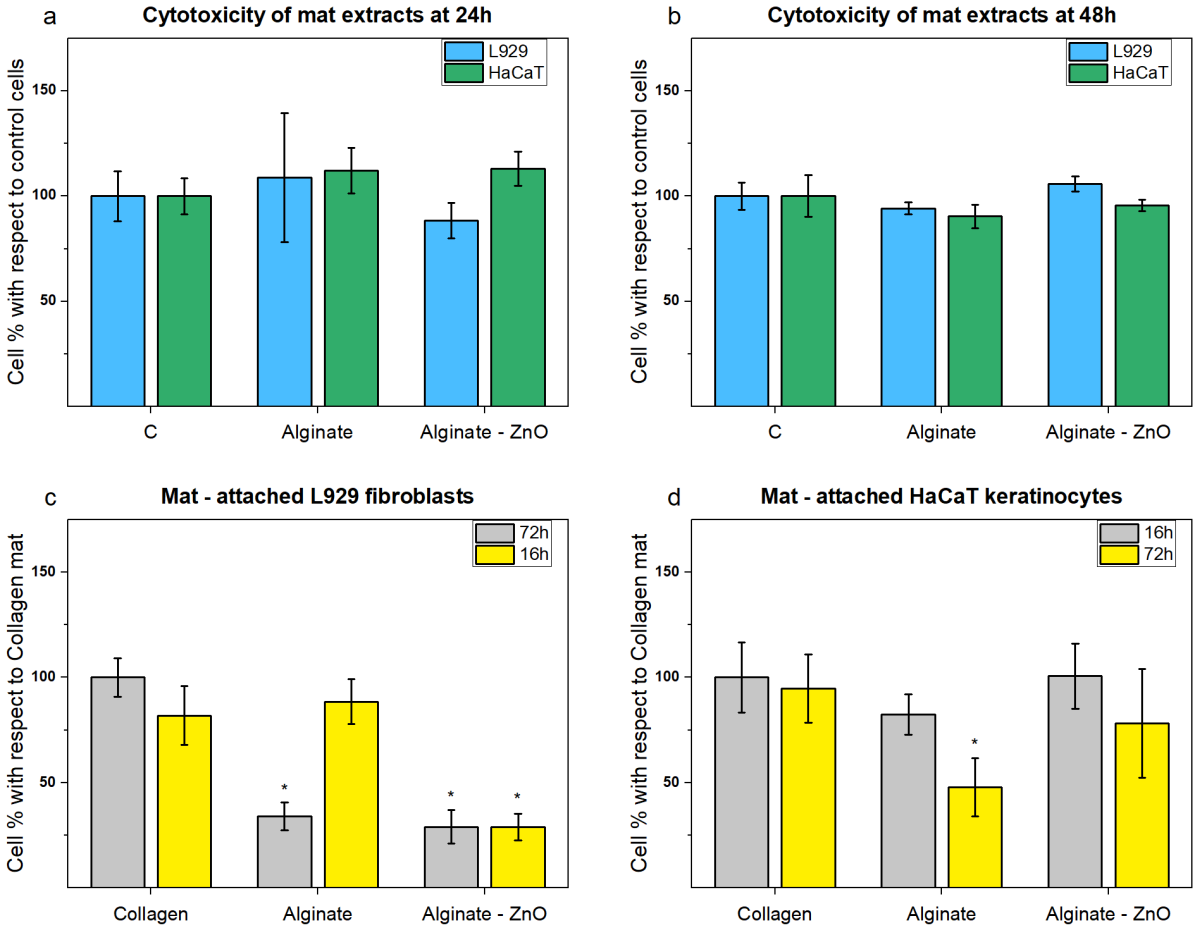

Figure 31. Cell cytotoxicity by the MTT test of mat extracts obtained by soaking them in complete medium for 6h and then adding to L929 fibroblasts (blue bars) or HaCaT keratinocytes (green bars) for (a) 24h and (b) 48h, respectively. Results are expressed as percentages with respect to control untreated cells (C). Cell adhesion and growth by the MTT test of (c) L929 fibroblasts and (d) HaCaT keratinocytes on the two different alginate patches and the collagen commercial scaffold after 16h (grey bars) and 72h (yellow bars) of incubation. Results are expressed as cell percentages with respect to the commercial collagen scaffold at the respective incubation time and are the mean ± S.D. of three experiments performed in quadruplicate. Asterisks indicate significance in Tukey's test ($p < 0.05$ vs the respective collagen).

For the fibroblasts the results indicate a preference for adherence to collagenous materials compared to the alginate ones although at longer incubation times the results are similar to the commercial control, but only if the ZnO nanoparticles are not embedded in the nanofibers. This is not completely surprising since the extremely good capacity of the Bio – Gide scaffold to sustain fibroblast adhesion and growth has already been reported,[313] also taking into account that skin fibroblasts are the main cell type producing the thick collagen matrix of the dermis in which cells are embedded. Nevertheless, at longer times of incubation, also the pure alginate mat seems to become appropriate to support fibroblast growth, whereas the presence of the nanoparticles does not appear to be beneficial negatively affecting the cell growth. Since it has been reported that ZnO – NPs can be cytotoxic for certain mammalian cells depending on the grade of the acidic environment of each cell type[314], which may induce the nanoparticle

dissolution and Zn^{2+} internalization and mitochondrial damage, this may be the case for explaining L929 fibroblast results. As a matter of fact, it is possible for these cells to have a lower extracellular pH with respect to keratinocytes, which are characterized by a lower cell division rate and metabolism, thereby explaining the different behaviour observed for the two cell lines. In this sense, the tested human keratinocytes present a higher adhesion capability on the alginate mats with respect to fibroblasts when compared to the commercial collagen scaffold (Figure 31-d). More in detail, cell adhesion at 16h on both alginate and alginate – ZnO nanofibers is comparable to the collagenous control, whereas a significant decrease is recorded for cell growth at longer incubation times only for alginate – based sample (i.e., 50.5 ± 14.5%). Therefore, for what concerns keratinocytes, the nanoparticle presence seems to partially enhance the cell growth most probably due to their reinforcement effect on the mat mechanical properties. Consequently, alginate – based patches containing ZnO – NPs can be considered as a suitable support for this cell type.

Another important characteristic of biocompatible patches and scaffolds is serum protein adsorption on their surface since this property is considered important in long – term performance of various types of implants.[315] More in detail, once proteins are adsorbed onto the material surface, cell adhesion and growth are often facilitated. This adsorbed protein layer can also mediate the type of cells that adhere to the surface, which ultimately can determine the type of tissues that are developed. However, it is worth noting that low protein retention may be beneficial and could be exploited in all those cases where adherence between tissues gives rise to pathological situations such as peritendinous adhesions and abdominal post – surgical fibrous adhesion.[316,317] As such, FBS (Figure 32-a) and human serum (HB) (Figure 32-d) protein adsorption rates onto alginate and alginate – ZnO mats were investigated and compared to the collagen scaffold in a time course experiment of 48h. Subsequently, HaCaT keratinocyte cell adhesion in the FBS (Figure 32-b) and HS (Figure 32-e) pre – incubates mats with respect to the untreated ones was explored as well.

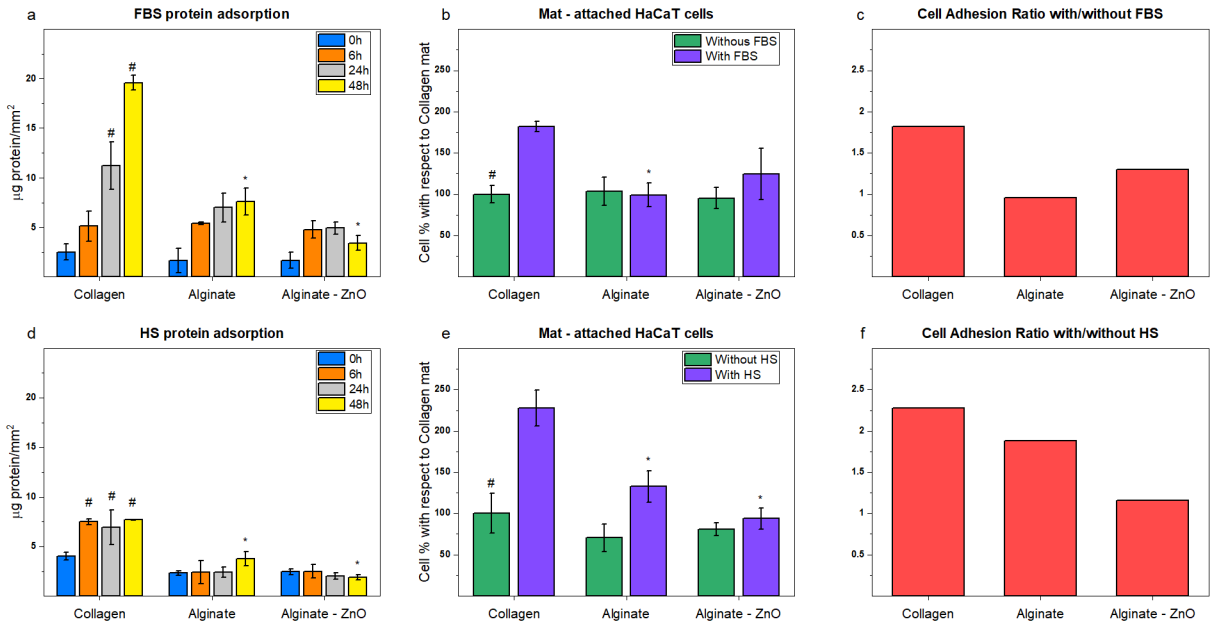

Figure 32. (a) and (d) Serum protein adsorption on the different alginate meshes and commercial collagen incubated for the indicated times in the presence of FBS or HS, respectively. The asterisks and the hashtag indicate significance in Tukey's test (# $p < 0.05$, 0h vs the various incubation times; * $p < 0.05$, the mats at 48h vs the collagen at 48h). (b) and (e) Cell adhesion (16h) by the MTT test of HaCaT keratinocytes on the different alginate patches and collagen commercial scaffold pre – incubated (green bars) or not (violet bars) for 48h in FBS or in HS, respectively. The asterisks and the hashtag indicate significance in Tukey's test (# $p < 0.05$, collagen without FBS vs collagen with FBS; * $p < 0.05$, compared to the respective collagen). (c) and (f) Ratio of the rate of cell adhesion between samples pre – incubated or not in FBS or HS, calculated using the data displayed in panels (b) and (e), respectively.

As displayed in Figure 32-a, in the Bio – Gide collagen scaffold the amount of fetal bovine serum – adsorbed proteins doubles after each time point, while in the same experimental conditions the amount of human serum – adsorbed proteins doubles at 6h with respect to t = 0 and does not further increase after (Figure 32-d). For what concerns the alginate – based mats, no significant increment of protein content is observed during the investigated time (i.e., from 6h up to 48h) both in FBS and HS – adsorbed proteins. In addition, comparing the amount of serum protein adsorbed on the electrospun meshes to that adsorbed onto collagen after 48h, the serum protein adsorbed onto collagen is significantly higher with respect to the amount coating the alginate mats in both FBS and HS – adsorbed proteins most likely due to the lack of protein binding sites in the alginate polymer. For what concerns keratinocyte cell adhesion (Figure 32-b), a marked increase of cell adhesion can be observed on the commercial collagen sample pre – incubates in FBS with respect to the same untreated sample, where an increase of 182.3 ± 6.4% of the cell number is measured. This response may be easily explained by the high amount of serum protein adsorbed after 48h in FBS in the Bio – Gide scaffold. On the contrary, no differences in keratinocytes adhesion rates are detected in the alginate – based mats pre – incubated or not in FBS. Compared to the collagen sample in the same condition, pre –

incubation in FBS shows a lower cell adhesion especially in alginate nanofibers (i.e., 54.4 ± 7.8% cell reduction with respect to collagen scaffold in FBS) but has a much less marked effect in the case of alginate – ZnO nanofibers where the cell adhesion difference is not statistically significant. The ratio of keratinocyte cell adhesion rate for the three tested samples pre – incubated or not with FBS is shown in Figure 32-c. The considerably high ratio (i.e., close to 2) between the rate of cell adhesion on FBS pre – incubated and not pre – incubated collagenous materials likewise indicates that keratinocyte cells prefer a protein – coated collagen as an adhesion substrate. On the contrary, no differences can be depicted in the case of alginate – based mats where the ratio between the rate of cell adhesion on FBS pre – incubated and not pre – incubated meshes is close to 1 or slightly higher, indicating that keratinocyte cell adhesion on alginate is not influenced by a serum protein coating. Such a finding may be due to the fact that protein adsorption on the alginate – based patches is significantly lower with respect to that observed on the Bio – Gide scaffold. Very similar results in keratinocytes adhesion rates and cell ratio after 16h between pre – incubated mats or not are obtained with the use of HS, as shown in Figure 32-e and Figure 32-f, thereby indicating that no differences can be observed in the cell adhesion rates between the bovine serum pre – coated and the human serum pre – coated explored samples.

Along with the above – discussed features, wound healing patches are supposed to possess strong antibacterial properties to avoid any microorganism contamination and/or proliferation. To this end, ZnO nanoparticles were specifically employed aiming to confer bacteriostatic and/or antibiotic properties to the alginate electrospun meshes. The extent of bacterial adhesion on the prepared mats, as well as on the collagen control, was evaluated by incubation of the sample for 5h in an *Escherichia Coli* (E.coli) as described in the literature.[318] The achieved results are summarized in Table 4.

Table 4. Evaluation of bacterial adhesion on different alginate electrospun mats and collagen scaffold.

Sample	Collagen	Alginate	Alginate - ZnO
E. coli cell number	1180.18 ± 159.56	77.53 ± 5.74	< 10

Remarkably, both alginate and alginate – ZnO nanofibers display a total number of bacterial cells adhered to their surface considerably lower with respect to the collagen control sample. In particular, the presence of the nanoparticles embedded within the nanofibrous structure completely inhibits bacterial colonization and proliferation, thus confirming the proficiency of the alginate – ZnO mat as an effective antibacterial material.

Owing to its unique and very promising mechanical, water – related, biological, and antibacterial properties, the possibility to enrich the prepared composite mat with drug delivery capabilities was as well explored within the present Thesis work. However, it is noteworthy that the uptake – release results presented in the following will be discussed considering the alginate – based mat both in terms of an advanced drug delivery system and an adsorbent material for wastewater treatments. In this sense, methylene blue (MB) and congo red (CR) were selected as model molecules due to their opposite surface charge, as shown in Figure 33.

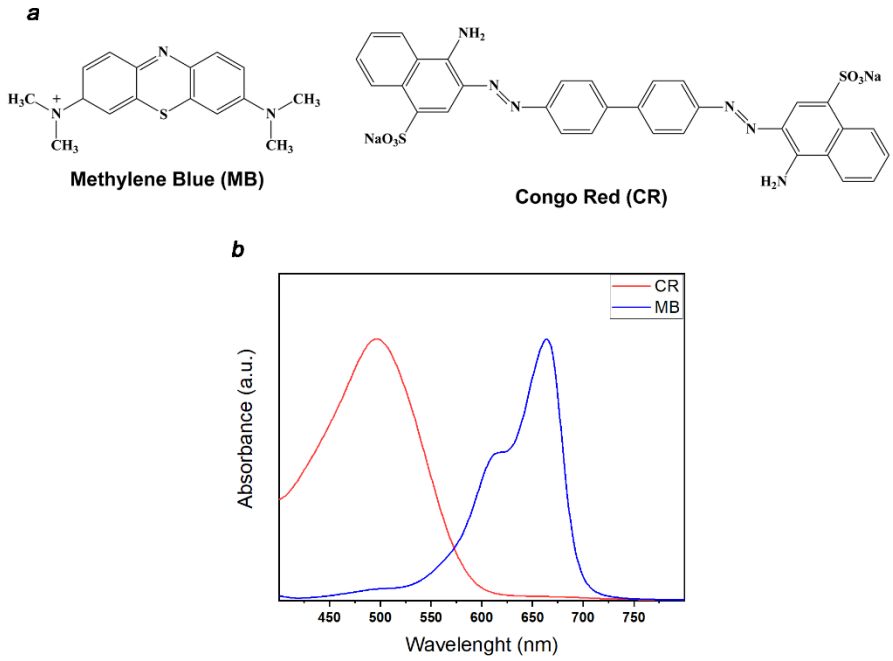

Figure 33. (a) Chemical structure and (b) normalized solution UV – vis spectra of methylene blue and congo red organic dyes.

Kinetic uptake studies were performed by soaking portions of the composite mat in dye solutions at different concentrations up to 48h, with the UV – vis spectra of the resulting mixtures being periodically evaluated as described in Section 3.7. The mat adsorption capacity (q_t) for methylene blue and congo red as a function of the initial dye concentration and contact time is shown in Figure 34-a and Figure 34-b, respectively. Independently on the explored colorant, the adsorption process on the composite mat appears to be a multi – step process. In detail, in the first phase, lasting about 3h, quite rapid uptake of the dyes is observed followed by a gradual slowing down of the adsorption rate until the equilibrium is finally achieved, approximately after 8h of immersion time. By comparing the results obtained for MB and CR, several important considerations on the process can be made. First of all, according to the coefficient of determination (R^2), methylene blue adsorption data are preferably fitted with a

pseudo – first – order kinetic model (Equation 5), whereas congo red adsorption data with a pseudo – second – order kinetic model (Equation 6). In addition, q_t values are found to increase with increasing the initial dye concentration for both dyes, hence suggesting that the uptake process becomes faster and more efficient at higher dosages. This is most likely due to the presence of vacant active binding sites still available for unabsorbed dye molecules. Yet, under the same experimental conditions, the adsorption of MB seems to be somehow preferred, both in terms of rate and adsorption capacity values, with respect to CR.

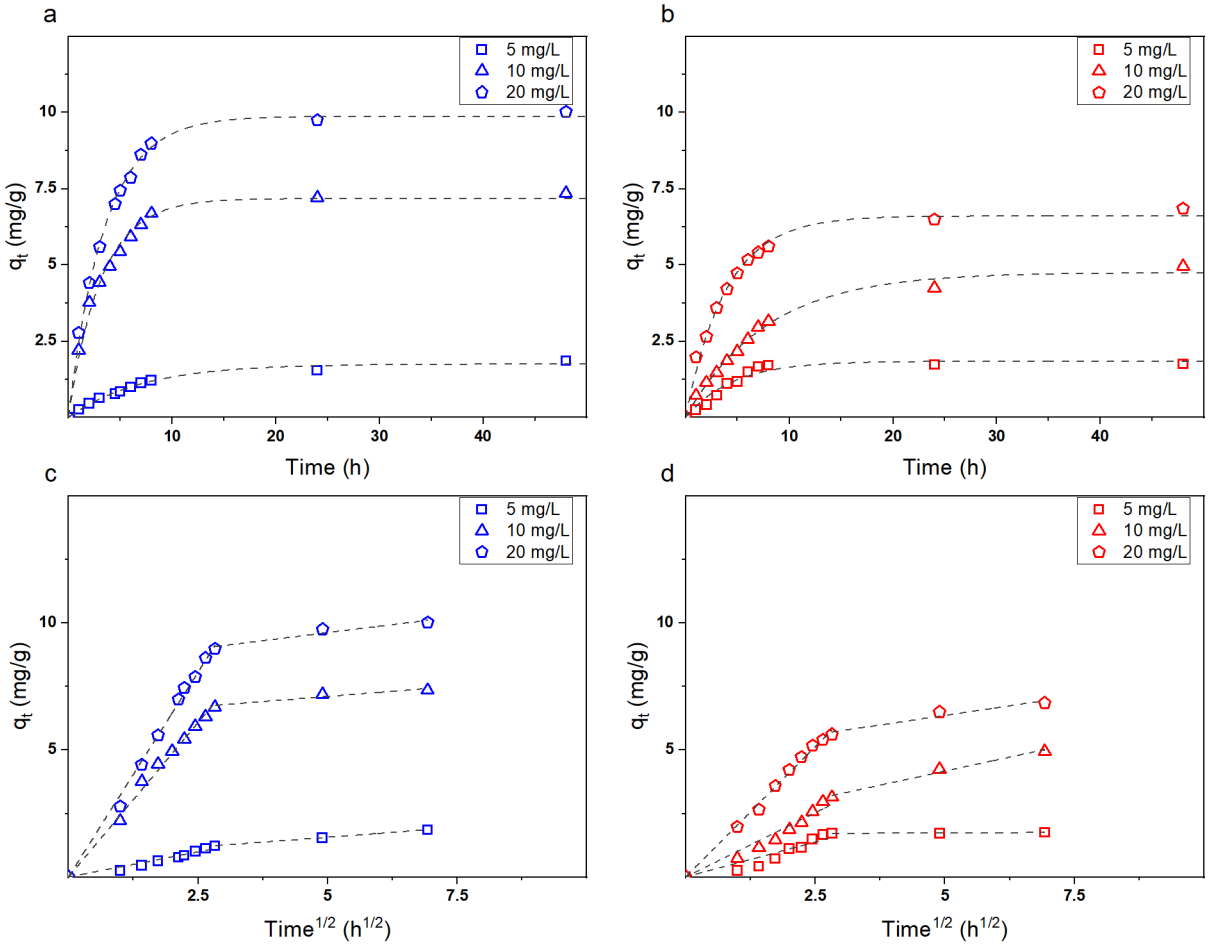

Figure 34. (a) and (b) Adsorption capacity of MB and CR on alginate – ZnO mesh. Experimental data were fitted for MB and CR with a pseudo – first – order and with a pseudo – second – order kinetic model (dashed lines), respectively. (c) and (d) Intra – particle diffusion plots of MB and CR adsorbed by the composite electrospun mat. Dashed segments interpolating the experimental points represent the two kinetic regimes of the adsorption process.

On the basis of these results, it can be assumed that the composite alginate – based mat presents the capacity to adsorb both dyes in spite of their different chemical structure to suggest that both MB and CR mostly interact with the same binding sites on the adsorbent platform, which are most likely represented by the hydroxyl substituents of the alginate chains.[319,320] However,

under the investigated experimental conditions, it should be considered also that MB molecules can establish electrostatic interactions with the carboxylate groups of the polymer backbone, thereby facilitating the surface adsorption at least in the early stage.

Further information of the uptake process is achieved by analysing the kinetic data according to the Weber – Morris intra – particle diffusion model (Equation 7), as represented in Figure 34-c and Figure 34-d. As clearly shown, the experimental data cannot be fitted by a single straight line suggesting that the adsorption process of the investigated dyes occurred through two distinct stages. Specifically, the initial step, which is characterized by a sharp increase of q_t for approximately 8h, is related to the fast mass transfer from the incubating solution to the mat surface (i.e., film or external diffusion). Remarkably, the linear fitting lines corresponding to step one pass through the origin to confirm that early adsorption stages are diffusion controlled. Step two is instead related to the dye diffusion within the mat fibers and is characterized by a much slower increase of q_t with time, whereas the corresponding linear plots have intercepts greater than zero to indicate that the dye diffusion within the internal pores is a process conditioned by boundary effects (i.e., intra – particle diffusion). Overall, the kinetic studies evidence that the uptake of the dyes on the composite mat is a complex process, the efficiency of which is only slightly conditioned by the chemical nature of the adsorbate, hence opening the way to the uploading of several different drug molecules by a simple impregnation method. Such finding can be explained by considering the mat texture, where the presence of interconnected, submicron – sized voids is supposed to facilitate internal diffusion even allowing the permeation of species having the same electrical charge of alginate chains because large enough to prevent electrostatic repulsions.

Together with the kinetic uptake studies, equilibrium adsorption isotherms of MB and CR were investigated as described in Section 3.7. In detail, the experimental data were analysed by the broadly exploited Langmuir (Equation 8) and Freundlich (Equation 9) models, as shown in Figure 35-a and in Figure 35-b, respectively. It is evident that, whereas Freundlich model fits well the experimental data of both MB and CR dyes, Langmuir model is not suitable to describe the uptake process. Such an outcome clearly points out that the binding sites are not homogeneously distributed on the composite alginate – based mat thereby preventing the formation of a uniform dye monolayer. Nevertheless, the limited yet existing capability of Langmuir model to fit the MB isotherm data may suggest that the deposition of the positively charged dye is somehow accomplished on the outmost surface of the mat, most likely via electrostatic bonds with the carboxylate substituents of alginate backbone. On the contrary, the

good linear fitting obtained with Freundlich model indicates that chemisorption events occur involving different binding sites and/or the formation of multilayers.

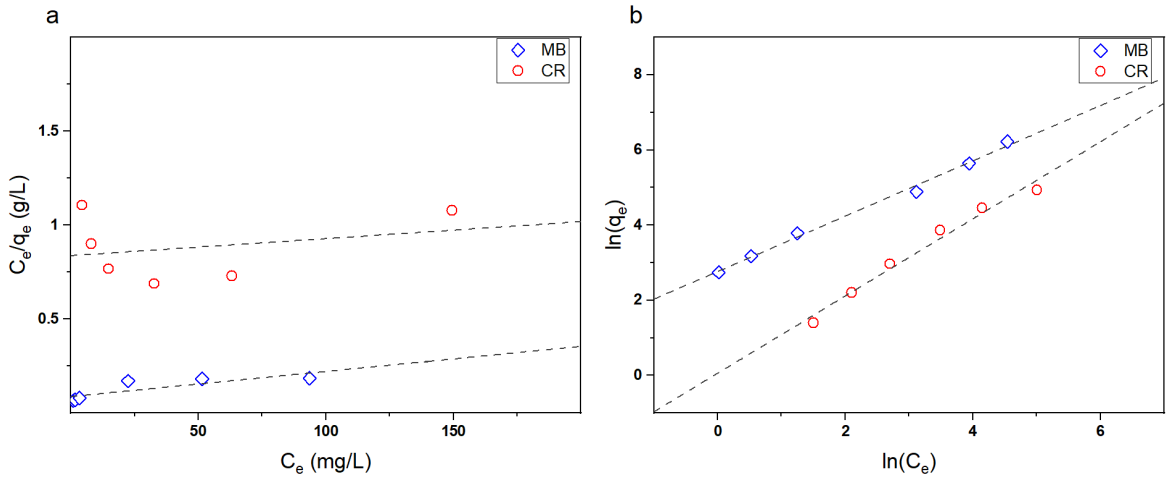

Figure 35. Equilibrium adsorption isotherms of MB (blue points) and CR (red points). The experimental data were fitted with (a) Langmuir and (b) Freundlich models.

The equilibrium studies confirm that the dye uptake on the composite mesh is a multi – step process that develops similarly for the two investigated dyes in agreement with the kinetic data. Specifically, in the first stages, adsorption occurs on outmost functional groups following mass transport of the dyes from the incubating solutions. Then, after diffusion of the molecules within the mat inner layers, also the internal active sites are occupied. Adsorbates and adsorbent platforms are supposed to be mainly linked by hydrogen bonds, although the establishment of electrostatic interactions could not be disregarded for the cationic MB dye.

Even if the uptake process provides important information regarding the possibility to easily upload a certain drug molecule within a candidate drug delivery system, release kinetic plays a much more critical role in determining its effective applicability in biomedical and pharmaceutical applications. To this end, release kinetic of MB and CR were explored in PBS (pH = 7.4) at T = 37 °C to simulate physiological conditions, as described in Section 3.7, for dye – loaded mats saturated at different dye concentrations. As a matter of fact, owing to their unique microstructure and high surface area, electrospun meshes represent an extremely promising class of drug delivery systems with enhanced and tuneable release capabilities. The achieved results are shown in Figure 36 in terms of cumulative release percentage (R%) versus contact time.

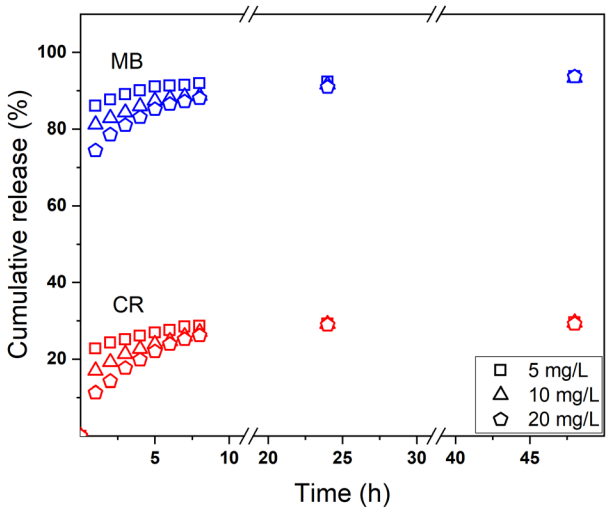

Figure 36. Cumulative release with time of MB and CR by dye – loaded patches at increasing dye concentration.

In any case, a strong burst release is observed in the first hour followed by a slower and more controlled release regime, which turned out to be completed after about 48h. The most interesting aspect arising from these data concerns the different desorption efficiency exhibited by the mat as a function of the dye nature. Interestingly, whereas MB molecules are almost completely delivered after 48h (i.e., final cumulative release around 95%), only a minority percentage of the adsorbed CR is freed in solution (i.e., final cumulative release around 35%). Such a result may be explained by considering the effects of the anionic and cationic counter ions present in the phosphate buffer solution on the adsorbate – adsorbent interactions. Indeed, Na^+ cations, which should be able to freely diffuse within the negatively charged alginate fibers, can effectively compete with MB molecules for the electrostatic and hydrogen bonding of the sample active sites even at the inner layers. Consequently, rapid and efficient desorption of the positively charged dye is observed in physiological – like conditions.[321] On the contrary, the counter ions – mediated desorption process is expected to be much less effective with loaded CR, in which HPO_4^{2-}, $H_2PO_4^-$, and Cl^- anions are supposed to hardly penetrate within the alginate mat because of electrostatic repulsions with carboxylate groups. As such, the internally linked CR molecules find themselves trapped within the polysaccharide matrix and cannot be easily diffuse outward. Consequently, a smaller fraction of the loaded dye is released in short times even in PBS. Although preliminary, these results attest that the desorption selectivity is significantly enhanced with respect to the uptake process and the release mechanism can be properly tuned according to the chemical properties of the loaded adsorbate and the experimental conditions adopted.

Conclusions

The results presented and discussed in this Section demonstrate the possibility to prepare promising nanofibrous wound healing alginate – based patches via electrospinning technique. More in detail, ZnO nanoparticles synthesized via a green sol – gel method are found to be easily and homogeneously embeddable within the nanofiber structure, whereas a simple, cheap, and potentially scalable washing – crosslinking protocol, consisting in the subsequent soaking of the mat in hot ethanol and in an aqueous medium containing strontium ions, allows to perfectly maintain the alginate nanofiber morphology meanwhile removing the employed co – spinning agent. To this end, selecting the appropriate alginate raw material plays a topical role in conditioning both the electrospinning process and the related nanofiber structure, where the predominance of G moieties and a high molecular weight seem to promote the nanofiber stability and homogeneity.

In general, the proposed composite nanofibrous patch presents mechanical and water – related features in the ideal range for the preparation of wound healing patches suitable to different human tissue types. Above all, the biological response indicates that alginate – based mat is biocompatible and its performances in terms of cell adhesion and growth are perfectly comparable to a well – known commercial collagen scaffolding material, but it additionally presents strong antibacterial properties due to the nanoparticle presence. Furthermore, adsorption – desorption studies demonstrate the possibility to easily upload within the composite mat, by means of a simple impregnation method, various molecules the release of which can be tailored according to their chemical nature and loading conditions. Thereby, this could lead to the development of safe and affordable surgical patches and scaffolds with drug delivery capabilities for wound dressing applications, with the advantage of using an economic biomaterial with a simpler production procedure with respect to the commercial animal collagen – derived materials. In this sense, it is noteworthy that collagen – derived scaffolds retain the risk of inflammation and allergic reactions and have elevated costs of production due to their derivation from porcine and bovine skin and bone waste, which must undergo a strict purification and safety validation procedure prior to commercialization.

4.1.3 Electrospun Mat Capability to Foster Cell Viability: Effect of Alginate Molecular Structure

This Section is substantially published at:

- *Dodero, A.; Donati, I.; Scarfì, S.; Mirata, S.; Alberti, S.; Lova, P.; Comoretto, D.; Alloisio, M.; Vicini, S.; Castellano, M. Effect of Sodium Alginate Molecular Structure on Electrospun Membrane Cell Adhesion. Mater. Sci. Eng. C 2021, 112067*

Some of the alginate samples employed in this Section were provided by Prof. Ivan Donati of the Department of Life Sciences of the University of Trieste.
The biological tests reported in this Section were carried out in collaboration with Prof. Sonia Scarfì of the Department of Earth, Environment and Life Sciences of the University of Genoa.

In the previous Sections, the electrospinning of various alginate – based mixtures has been broadly explored and discussed aiming to establish the ideal conditions to easily obtain electrospun mats with potential applicability in biomedical and pharmaceutical products. As a matter of fact, SA MV_G was selected as the most suitable alginate sample to prepare well – structured nanofibrous mats with highly promising mechanical, water – related, and drug – delivery capabilities, as well as marked biocompatibility. However, this choice was mainly made based on the electrospinning process itself and the morphological results, without considering the possible effects of alginate structure (i.e., molecular weight and M/G ratio) on the mat biological response. As such, in this Section, three alginates characterized by both a different molecular weight and composition are used to prepare nanofibrous mats by exploiting the previously optimized washing – crosslinking protocol and their capability to foster cell viability is deeply explored and discussed.

To this end, alginates extracted from *Macrocystis pyrifera* (M.pyr) (i.e., SA MV_M), from *Laminaria hyperborea* (L.hyp), and from *Ascophyllum nodosum* (A.nod), whose molecular properties are summarized in Table 5, were employed. To be noted that a complete characterization of these materials, in terms of molecular weight and polyelectrolyte nature, is reported in Chapter 5.

Table 5. Summary of alginate sample molecular weight and composition. F_M, F_G, and M/G ratio represent the fraction of mannuronic moieties, the fraction of guluronic moieties, and the ratio between them, respectively.[322] Zeta potential of alginate aqueous solutions at a concentration of 0.001 g/mL is also reported.

Sample	$\bar{M}_v$ (kg/mol)	F_M	F_G	M/G	ζ (mV)
M.pyr	500	0.62	0.39	1.56	-81.84 ± 3.59
L.hyp	150	0.35	0.65	0.53	-35.62 ± 3.55
A.nod	150	0.59	0.41	1.43	-71.52 ± 2.14

Generally speaking, as already reported in Section 4.1.1 and in Section 4.1.2, a predominance of G units in alginate macromolecules forces the chains to assume a "zig – zag" structure characterized by the presence of "cavities" along the polymer backbone, which in turn increase the chain charge density (Figure 12-a) but partially hinders the hydroxyl and carboxylate substituents of alginate. In contrast, a high amount of M units allows alginate chains to take on a "straight – line" structure hence exposing a greater number of functional groups, besides a decrease in the chain charge density is consequently observed. To evaluate such an effect on a macroscopic scale, zeta potential measurements were carried out as described in Section 3.9 on aqueous solutions of the three polymers at a concentration of 0.001 g/mL to ensure no topological interactions between the polymer chains (i.e., dilute concentration regime). Zeta potential is measured for the difference in potential expected between the alginate surface and the electrolyte medium for the uneven distribution of charges at their interface. This electrical potential can be directly related to the zeta potential by considering a simple model where a charged particle dispersed within an electrolyte is surrounded by an electrical double layer.[323] The first one, known as Stern Layer, involves steady electrolyte molecules that completely surround the charged particle. The second one, known as Diffuse Layer, is described as the point where the liquid begins to flow at small distances from the solid surface. Zeta potential is by definition the potential at the Diffuse Layer distance, and it is directly proportional to the surface charge that is developed on the surface of the particle but weakened by the oppositely charged layers. By evaluating ζ values reported in Table 5, important insights into how the molecular properties of alginate influence its surface charge can be deducted. Specifically, by comparing M.pyr and A.nod samples, which are characterized by a different molecular weight but a similar composition with the predominance of M units, it is possible to notice that longer chains present higher ζ values reflecting the greater number of chain negative charges. On the contrary, L.hyp and A.nod, which possess a similar molecular weight but a different composition, are characterized by a highly dissimilar zeta potential with L.hyp alginate

presenting a much lower value. As a matter of fact, as already discussed, the predominance of G units forces L.hyp to assume a "zig – zag" structure that somehow hinders the exposition of the carboxylate substituents, which in turn prevents the establishment of a strong surface charge. However, from a microscopic point of view, it can be supposed that since such a phenomenon considerably enhances the chain charge density, it may lead to the development of stronger repulsive interactions between the alginate monomers hence increasing the polyelectrolyte behaviour of the polymer chains.

Based on the previous results discussed in this Thesis work, alginate – based solutions containing PEO (i.e., alginate – PEO ratio of 70 – 30) were prepared with the suitable concentration aiming to obtain a zero – shear viscosity value in the range 5 – 10 Pa·s. In detail, M.pyr – based mixture was formulated with a polymer concentration of 3.5 wt%, whereas L.hyp and A.nod – based mixtures with a polymer concentration of 5.0 wt%. Triton was always added in 1 wt% concentration.

Steady – state viscosity curves of the prepared formulations at T = 20 °C were performed as described in Section 3.2 with the related flow curves reported in Figure 37.

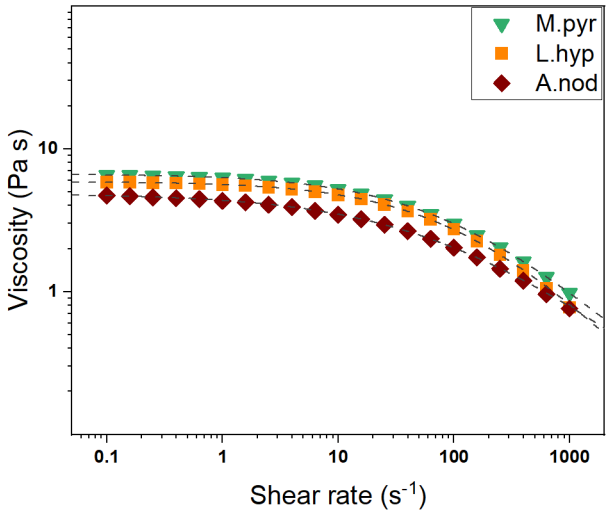

Figure 37. Flow curves of alginate – based solutions (SA – PEO weight ratio of 70 – 30) with a concentration of 3.5 wt% (M.pyr in green triangles) or 5.0 wt% (L.hyp in orange squares and A.nod in brown rhombus). Dashed lines represent the fitting of the experimental data with the Carreau – Yasuda model.

The investigated formulations show the typical behaviour of polymer solutions (i.e., shear – thinning) with a constant viscosity at low shear – rate values, corresponding to the Newtonian region, that decreases as the shear – rate increases.

In general, the tested mixtures present η_0 values in the ideal range to be successfully electrospun as deeply discussed in the previous Sections. As such, electrospinning has been

carried out by using a dry – collector setup with a flow rate of 0.75 mL/h, a spinneret – collector distance of 15 cm, a 22G flat – tip needle, and an applied voltage of 12.5 kV. Once prepared, the nanofibrous mats were subjected to the previously developed and optimized washing – crosslinking protocol, consisting of the immersion in EtOH at T = 70 °C overnight and in the subsequent soaking in a 3 w/v% $SrCl_2$ aqueous solution for 30 s. The morphology of the so obtained mats was evaluated via both FESEM and AFM, with the obtained micrographs reported in Figure 38.

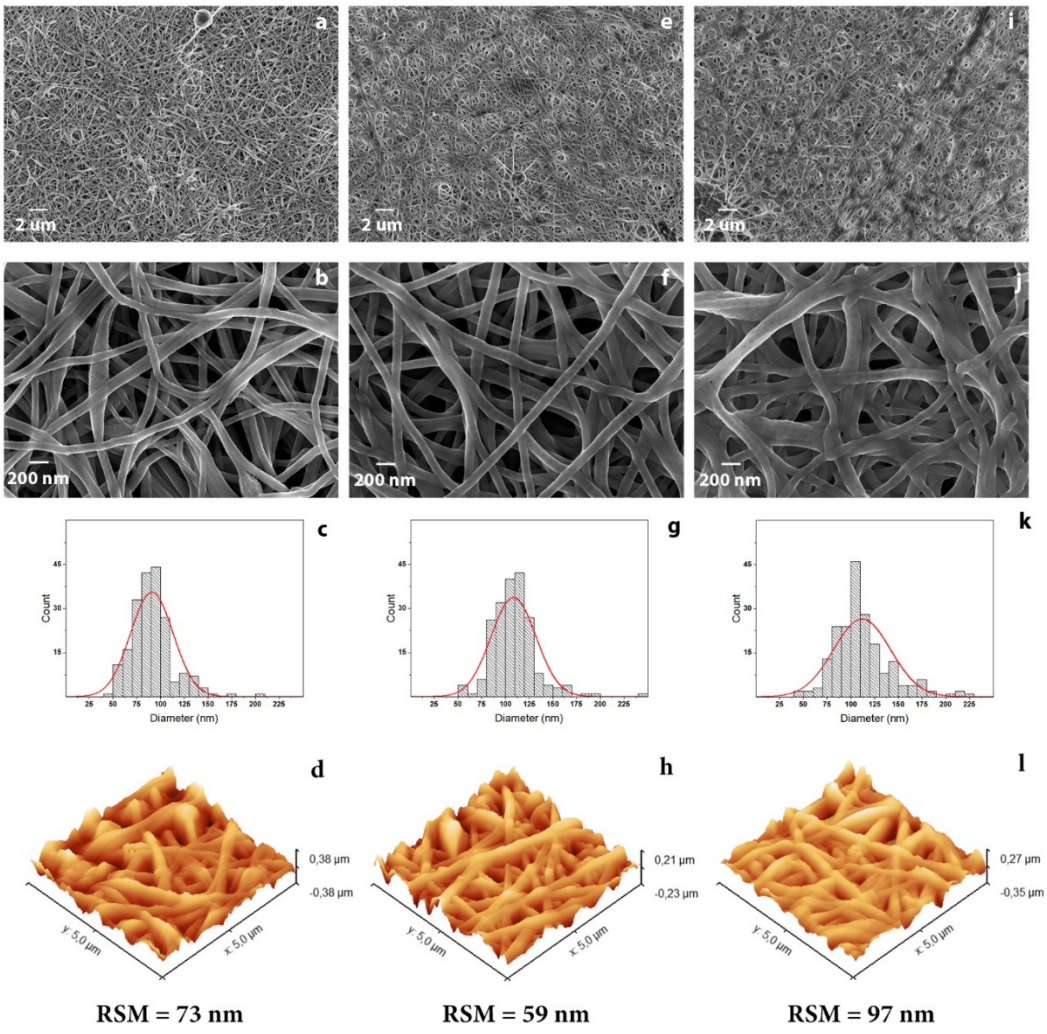

Figure 38. FESEM micrographs and related nanofiber dimension distribution for M.pyr (a, b, and c), L.hyp (e, f, and g), and A.nod (i, j, and k) electrospun samples. 3D representation of AFM micrographs for M.pyr (d), L.hyp (h), and A.nod (l).

All the three alginate – based solutions lead to homogeneous and defect – free nanofibers, with the applied washing – crosslinking protocol being once again proved able to crosslink alginate thereby endowing the nanofibers with water – resistance properties. In addition, as discussed above, such a treatment can completely remove PEO (i.e., co – spinning agent) from the

prepared mats, thus representing an easy and fast approach to obtain pure alginate nanofibers. Remarkably, only small morphological differences can be observed between the three prepared samples. Specifically, M.pyr mat presents slightly rough nanofibers with an average dimension of 90 nm creating an overall highly porous structure. Similarly, L.hyp sample is characterized by marginally bigger but smoother nanofibers with 110 nm average size able to maintain their individuality and generating a great number of interconnected pores. Finally, A.nod patch shows significantly rough nanofibers with an average dimension of 110 nm that partially tend to coalesce with each other reducing the structure porosity. Such results may be explained by considering the molecular weight and composition of the explored alginates. In detail, the predominance of G units in L.hyp sample allows indeed a fast and strong crosslinking of the polymer chains that leads to a striking well – defined morphology despite its low molecular weight. On the contrary, the predominance of mannuronic moieties in A.nod alginate, along with its short chains, reduces the effectiveness of the ionic crosslinking with Sr^{2+} ions, therefore promoting the swelling and the partial coalescence of the nanofibers with the consequent increase of the structural defects. On the contrary, despite the high M/G ratio, M.pyr alginate presents very long chains that somehow can help the crosslinking mechanism and allow to obtain almost defect – free and homogeneous nanofibers. This outcome may also be ascribed to the Sr^{2+} binding by long MG sequences that are present in M.pyr alginate at variance with the A.nod one.[324] Another interesting aspect of the nanofiber properties is their different dimension, which is likewise related to the concentration of the used polymer solution. Specifically, the higher polymer amount contained in L.hyp and A.nod – based solutions (i.e., 5 wt%), which is necessary to obtain a suitable viscosity value, promotes the formation of bigger nanofibers with respect to the less concentrated M.pyr – based mixture (i.e., 3.5 wt%). Further information on the mesh morphological properties was then obtained from AFM micrographs. In particular, the root mean squared roughness (RSM) was calculated to evaluate the mat surface properties, which cannot be evaluated via scanning electron microscopy but may be a critical factor in promoting cell adhesion and proliferation. Remarkably, in agreement with its smooth and defect – free nanofibers, L.hyp mat shows the smallest RSM values followed by M.pyr and A.nod samples. Consequently, it can be assumed that the rapid and efficient crosslinking ensured by a great number of G units in the alginate polymer backbone is able to reduce the surface roughness of alginate – based meshes. Conversely, the predominance of mannuronic moieties, along with low molecular weight, leads to rougher alginate – based electrospun nanofibrous yarns because of the less efficient crosslinking mechanism.

Aiming to deeply evaluate the ability of mammalian cells to interact with the three alginate – based mats, which are indeed different for the raw material molecular properties (i.e., molecular weight, composition, and charge density), four different cell lines were employed in cell adhesion experiments. Specifically, two skin cell lines, L929 fibroblasts and HaCaT keratinocytes, and two osteoblast cell lines, Mg – 63 and Saos – 2, were explored. Cells were allowed to adhere to the patches for 16h before performing an MTT assay to quantify the number of cells attached to the mats. The number of cells was calculated through the interpolation to a linear regression curve obtained for each cell line. Figure 39 reports the so achieved results.

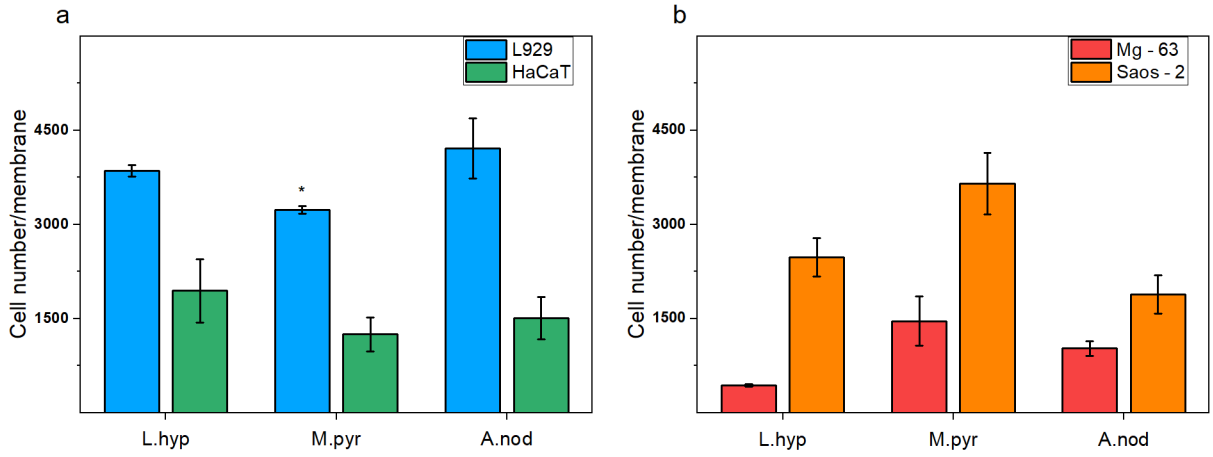

Figure 39. Cell adhesion evaluated by MTT test of attached cells after 16h incubation. (a) L929 murine fibroblasts (blue bars) and HaCaT human keratinocytes (green bars) on the three different alginate samples. Results are expressed as the number of adhered cells to each type of patch obtained by interpolation to a standard regression curve of cells seeded onto commercial cell culture 96-well plates. They are the mean ± S.D. of 3 experiments performed in triplicate. Asterisks indicate significance in Tukey test (* $p < 0.05$, M.pyr vs L.hyp and M.pyr vs A.nod). (b) Mg – 63 human osteoblasts (red bars) and Saos – 2 human osteoblasts (orange bars) on the three different alginate mats. Results are expressed as explained in (a). Asterisks indicate significance in Tukey test (* $p < 0.05$, M.pyr vs L.hyp and M.pyr vs A. Nod, in Saos – 2 bars; ** $p < 0.01$, M.pyr vs L.hyp and M.pyr vs A. Nod, in Mg – 63 bars).

Regarding the skin cell lines, whose results are displayed in Figure 39-a, no significant differences are depicted in their ability to adhere to the three different mats. In general, L929 fibroblasts (i.e., blue bars) show a higher percentage of attached cells to the three samples with respect to HaCaT keratinocytes (i.e., green bars). In particular, fibroblasts present a slightly higher preference for L.hyp and A.nod meshes compared to M.pyr sample. The percentage of attached cells with respect to the total number of seeded cells (i.e., 10000/well) is around 40% for the first two patches and 32% for the third one, respectively ($p < 0.05$). On the contrary, HaCaT keratinocytes display similar percentages of adhesion to the three meshes with a slight, but not significant, preference for L.hyp mat (i.e., 20% cell adhesion with respect to the initial

number of seeded cells) compared to M.pyr and A.nod samples (i.e., 12% and 15% cell adhesion, respectively). The reason keratinocytes show low adhesion abilities to the three alginate mats may be due to the fact that, at short adhesion time, these cells prefer mats and substrates of protein origin such as fibrin or collagen. Such molecules mimic more closely than alginate the basal membrane to which keratinocytes naturally adhere at the interface between epidermis and dermis.[325] These are fibrous proteins whose global charge at physiological pH tends to be slightly negative or neutral for fibrin and positive for collagen in consequence of their isoelectric points (i.e., 6.3 and 9, respectively).[326,327] Therefore, the fact that the three alginate mats have instead regions with dense negative charges may explain the low propensity of this type of cells to adhere to them since they seem to prefer neutral/positively charged surfaces. In the case of fibroblasts, their behaviour could be explained by the fact that in the dermis these cells are immersed in an extracellular matrix secreted by themselves, which is rich in highly negatively charged glycosaminoglycans and proteoglycans.[328] Hence, an environment of negatively charged sugar chains such as that of the three alginate meshes most likely mimics very well the natural milieu of fibroblasts and seem to facilitate their adhesion/proliferation, at least within the investigated time period. For what concerns the osteoblast cell lines (Figure 39-b), although Saos – 2 (i.e., orange bars) shows a significantly higher adhesion to all the patches with respect to Mg – 63 cells (i.e., red bars), the two cell lines display similar mat adhesion preferences. For instance, M.pyr is the mat showing the highest cell adhesion for both Saos – 2 and Mg – 63 cell lines (i.e., 36% and 15%, respectively, compared to the initial number of seeded cells), A.nod presents intermediate adhesion properties (i.e., 18% and 10%, respectively), meanwhile L.hyp is characterized by the lowest adhesion properties for Mg – 63 cells (i.e., only 5% adhesion to the sample) and intermediate adhesion properties for Saos – 2 cells (i.e., 25% adhesion to the sample). The difference in the percentage of cell adhesion in the two cell lines is always significant between M.pyr and A.nod ($p < 0.05$ for Saos – 2 and $p < 0.01$ for Mg – 63) and between M.pyr and L.hyp (again $p < 0.05$ for Saos – 2 and $p < 0.01$ for Mg – 63), but the differences between A.nod and L.hyp are not significant in both cell lines. In this case, both Saos – 2 and Mg – 63 cells present a clear preference for the M.pyr mat, which possesses the highest molecular weight and the greatest negative surface charge. Since osteoblasts are naturally immersed in a highly negatively charged ECM, constituted of 65 – 70% bone mineral hydroxyapatite,[329] it is quite predictable that the best performing mesh for the adhesion of these cells is comprised of the alginate sample displaying the highest negative charge (i.e., M.pyr).

Conclusions

The results discussed in this Section clarify the effect of alginate molecular weight and block composition on the cell adhesion properties of alginate – based electrospun patches. Indeed, despite crosslinked nanofibers with pretty much the same morphology can be easily obtained independently on the alginate molecular properties by properly modulating the solution viscosity, such factors are found to play a major role in conditioning alginate surface charge. Specifically, the majority of G moieties in the polymer backbone force the chains to assume a "zig – zag" structure where the exposure of the negatively charged carboxylate groups is somehow hindered. On the contrary, M – rich alginates present a predominantly "straight – line" chain structure, which in turn allows the complete exposition of the negative charges. As such, alginate samples with long and "straight – line" chains are macroscopically characterized by a higher surface charge with respect to short and "zig – zag" macromolecules, despite a lower charge density that can be most likely observed microscopically. Interestingly, for what concerns fibroblast and keratinocyte cells, the surface charge differences are found to play a minor role in conditioning their adhesion properties with similar results obtained for all the investigated mats, despite fibroblasts demonstrate a significantly higher affinity to alginate nanofibers with respect to keratinocytes at the investigated adhesion times. Conversely, osteoblast cells show a marked preference to adhere to highly negative charged substrates, most likely due to the greater resemblance with their natural environment where the presence of hydroxyapatite minerals induces the establishment of a strong negative charge. Although further studies will be required to fully understand alginate – cell interactions and their effective dependence, the achieved results undoubtedly indicate the importance of selecting the proper raw material to develop highly efficient wound healing patches depending on the wound site of interest.

4.1.4 Alginate – Poly(caprolactone) Multilayer Patches

This Section is substantially published at:

- *Dodero, A.; Alloisio, M.; Castellano, M.; Vicini, S. Multilayer Alginate-Polycaprolactone Electrospun Membranes as Skin Wound Patches with Drug Delivery Abilities. ACS Appl. Mater. Interfaces 2020, 12 (28), 31162–31171*

In the previous Sections, a simple, cheap, and scalable protocol was successfully developed to prepare electrospun alginate – based patches embedding ZnO nanoparticles with potential applications in the biomedical and pharmaceutical fields owing to their unique physical – chemical, antibacterial, and biological properties, as well as their capability to show a tuneable drug release behaviour. Despite such products have been shown extremely promising and versatile, their reduced mechanical stability and high hydrophilicity considerably limit the protective action displayed by the mats towards the external environment with respect to the wound site, hence preventing their efficient applications in large – scale wound treatments.
To overcome such limitations, a multilayer patch consisting of a protective electrospun layer of poly(caprolactone) (PCL) and in a bioactive electrospun layer of alginate – ZnO is here prepared and fully characterized in order explore its applicability as an advanced wound healing system. In this regard, PCL (Figure 40) was specifically selected as protective material owing to its biodegradability, solubility in non – toxic organic solvents, relative ease of processability via electrospinning technique, and marked hydrophobic properties.[330,331]

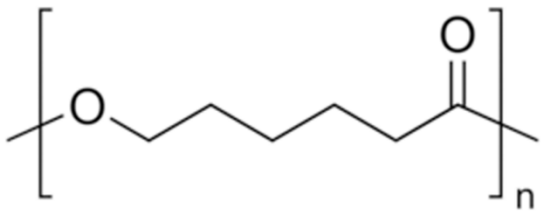

Figure 40. Chemical structure of PCL.

Firstly, the electrospinning of PCL ($\overline{M}_n$ = 80 kg/mol) was optimized by using either acetone (Ac), glacial acetic acid (GAA), or their mixtures as solvents. Indeed, despite the electrospinning of PCL is a well – established process, issues related to the polymer hydrolysis occurring in acid environments and the fast evaporation rate of the most common organic solvents are anything but unusual. As such, the choice of both solvent type and polymer concentration yet represents a critical factor to be considered. PCL solutions were prepared by

dissolving the polymer powder for 2h at T = 50 °C under magnetic stirring with a concentration ranging from 10 w/v% up to 30 w/v% in acetone, in glacial acetic acid, in glacial acetic acid – acetone 1 – 1 mixture, and in glacial acetic acid – acetone 3 – 1 mixture. Then, solutions were kept under stirring at room temperature for at least 1 day prior to the electrospinning process to ensure that an equilibrium state was reached.

Steady – state viscosity curves of the prepared PCL solutions are reported in Figure 41. To be noted that all measurements were carried out 24h after the solution preparation.

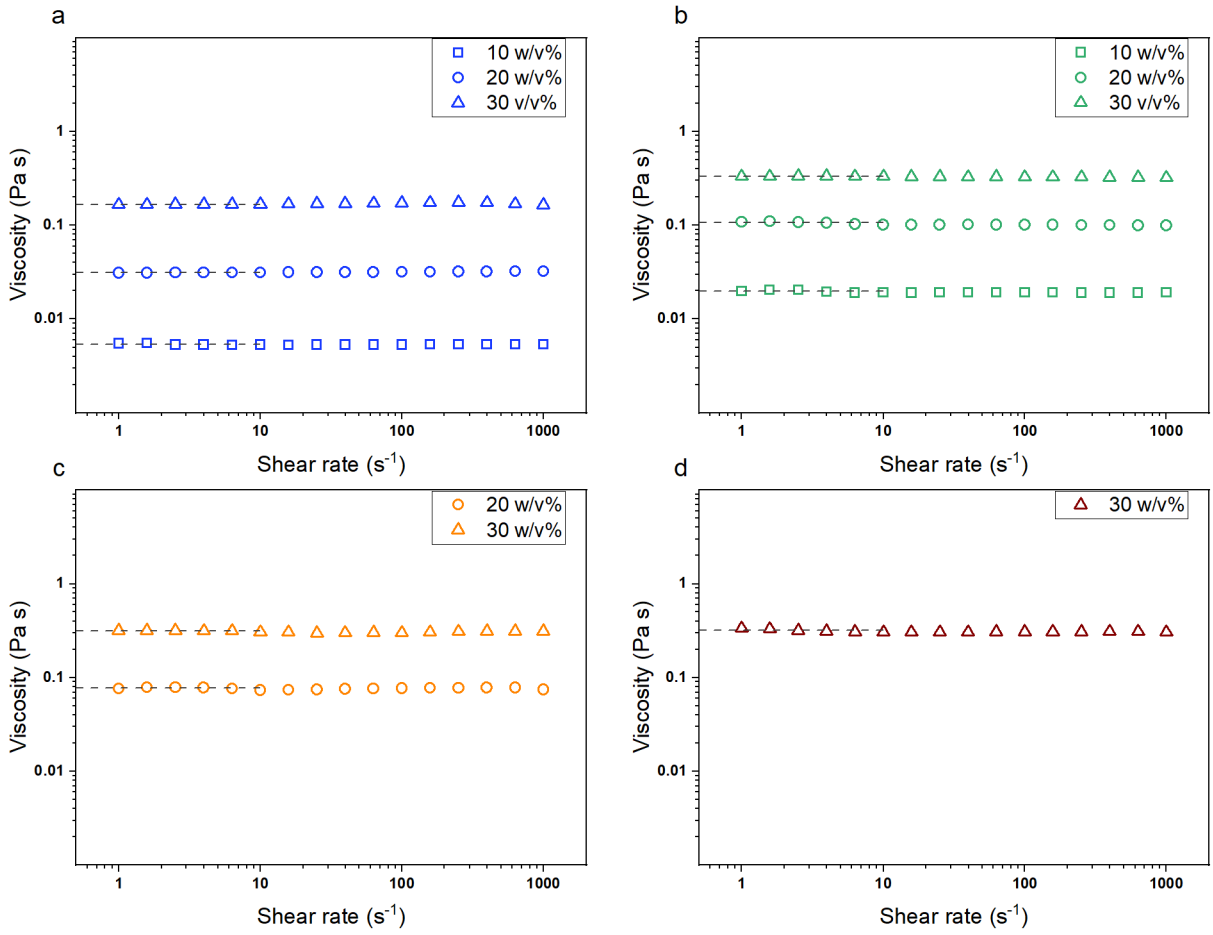

Figure 41. Steady – state viscosity curves at T = 20 °C of PCL solutions in (a) Ac, (b) in GAA, (c) in GAA – Ac 1 – 1 mixture, and (d) in GAA – Ac 3 – 1 mixture. Dashed lines represent the fitting of the experimental data with a straight line at low shear rate values.

In the investigated shear – rate range all the tested solutions are characterized by a nearly constant viscosity value showing with good approximation a Newtonian behaviour. This result is ascribable to the low molecular weight of the employed PCL, which precludes the formation of a dense polymer network due to the shortness of the chains hence reducing the viscoelastic response of the mixtures. To better compare the solution rheological properties, the zero – shear viscosity of each sample was determined by fitting the experimental data at low shear – rate

values with a straight line according to the Newtonian model.[332,333] Table 6 summarizes the calculated η_0 values.

Table 6. Zero – shear viscosity values of the tested PCL solutions 24h after their preparation.

Solvent	Polymer concentration (w/v%)	η_0 (mPa·s)
Acetone	10	5.4
	20	32
	30	169
Glacial acetic acid	10	19
	20	103
	30	329
GAA – Ac 1 – 1	20	76
	30	308
GAA – Ac 3 – 1	30	311

As expected, independently of the solvent type, a higher polymer concentration corresponds to a higher solution viscosity because of the greater number of polymer chains. However, significant rheological differences can be observed depending on the fact that PCL was solubilized in acetone, in acetic acid, or their mixtures. For instance, PCL solutions in GAA are characterized by a significantly higher viscosity than those in Ac, which is most likely due to a different affinity occurring between the polymer – solvent couples. As a matter of fact, PCL is reported to have a higher affinity for acetic acid with respect to Ac according to Hansen solubility parameters,[334] which in turn leads to a positive contribution to the chain hydrodynamic volume (i.e., polymer macromolecules assume a more expanded random – coil conformation), with a consequent increase of the solution viscosity.[335] Noticeably, PCL solutions in GAA – Ac mixtures present viscosity values very similar to those in pure GAA independently of the solvent ratio, hence suggesting that acetic acid has a predominant role with respect to acetone in influencing PCL chain conformations. In addition, as PCL is easily subjected to hydrolysis phenomena in acid conditions, the viscosity of the PCL 30 w/v% GAA – Ac 3 – 1 mixture was monitored over a time period of 48h after its preparation (i.e., t = 0h corresponds to when the solution was removed from the heater and allowed to cool down at room temperature). Besides a considerable decrement of the viscosity occurs at increasing time with respect to the initial system, which is related to a reduction of the polymer molecular weight, the process seems to stop after around 6h and significance differences cannot be detected after 24h or 48h. As such, it is rather safe to assume that in the investigated conditions,

PCL solutions reach an equilibrium state 6h after their preparation and can be stored or electrospun for a couple of days without the occurrence of viscosity – related effects.
On the basis of the calculated zero – shear viscosity values that were compared with the data reported in the literature,[336,337] only the solutions with the highest polymer concentration (i.e., 30 w/v%) were selected to be electrospun. In a typical procedure, 20 mL of PCL solution were electrospun on a rotating drum collector using a spinneret – collector distance of 20 cm, an infuse rate of 1 mL/h, a 22G flat – tip needle, an applied voltage of 15 kV, and a rotation speed of 100 rpm. PCL in pure Ac cannot be continuously electrospun because of the occurrence of an intense clogging phenomenon (i.e., the formation of a semi – solid deposit at the tip of the needle) affecting the process stability.[338,339] Conversely, PCL in pure GAA allows the ejection of a continuous polymer jet, which however leads to a highly sticky and not mechanically resistant mat with only small pieces that can be peeled off from the collector. This is most likely due to the high boiling point of the used solvent, which hinders its complete evaporation hence contributing to a not completely dried structure and a consequent poor mechanical consistency. Remarkably, the electrospinning of PCL in both the explored GAA – Ac mixtures is stable and allows to obtain consistent mats with good manageability, despite a slight clogging effect is observed for the GAA – Ac 1 – 1 system. As such, PCL 30 w/v% GAA – Ac 3 – 1 formulation is here selected as the most appropriate to prepare the external hydrophobic side of the investigated multilayer patch.
To this end, alginate – based mixture containing ZnO nanoparticles was prepared as described in Section 4.1.2 and 20 mL of the formulation were then directly electrospun on the PCL layer by using the working parameters previously optimized. Typically, 150 μm and 50 μm thicknesses were achieved for the PCL and SA layers, respectively. Once prepared, the multilayer mat was subjected to a washing – crosslinking treatment to remove the alginate co – spinning agent (i.e., PEO) simultaneously avoiding the alginate solubilization in aqueous media without modifying the sample nanofibrous structure by again exploiting its capability to crosslink when in contact in bivalent ions. Specifically, since PCL possesses a melting temperature around 60 °C, the washing – crosslinking protocol developed in Section 4.1.2 and consisting of the soaking of alginate – based meshes in hot ethanol could not be here applied. As such, the multilayer mat was simply immersed for 4h in a 3 w/v% $SrCl_2$ aqueous medium, rapidly washed in ethanol to reduce the fiber swelling, and finally dried under vacuum at T = 50 °C for 24h. The morphology of PCL and alginate nanofibrous layers, which was obtained via SEM after the applied washing – crosslinking treatment, is reported in Figure 42.

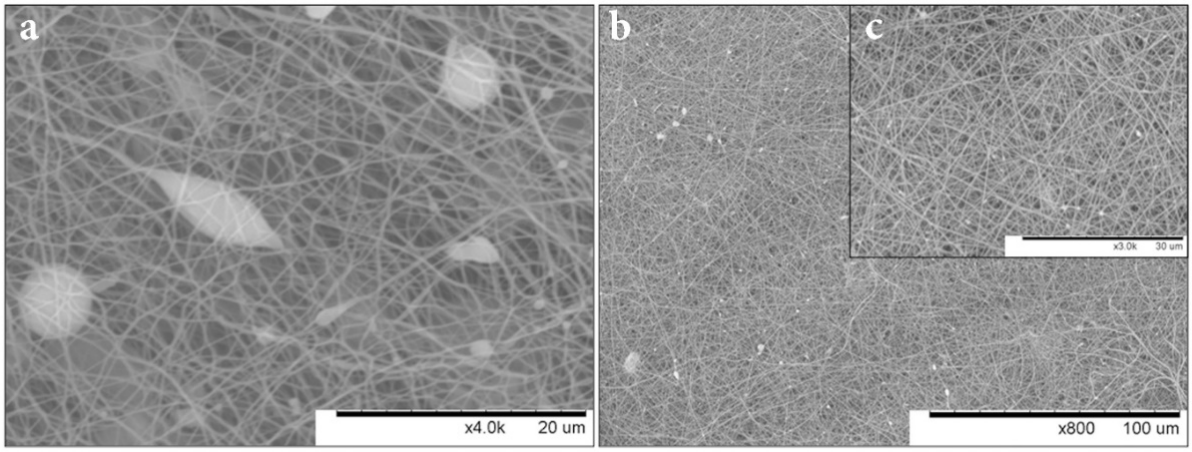

Figure 42. SEM micrographs of the crosslinked multilayer patch. PCL nanofibers are shown in (a), alginate – ZnO nanofibers in (b) at low magnification and in (c) the inset at high magnification.

PCL layer is characterized by homogeneous nanofibers with a mean diameter of 300 nm uniformly distributed in the sample structure with only a small number of detectable defects. In addition, the pores between the fibers appear to be highly regular with a dimension of a few micrometers, thus conferring to the sample a great porosity. Alginate – ZnO layer is instead comprised of much thinner nanofibers, whose diameter is around 100 nm, and a homogeneous porous structure similar to that of the natural extracellular matrix. As broadly described in Section 4.1.2, ZnO – NPs are proved to be well – dispersed within the electrospun alginate nanofibers and cannot be clearly detected by the morphological investigation, which further confirms the proficiency of electrospinning technique as an easy and cheap approach to prepare nanocomposite materials.

Aiming to evaluate the effective removal of the co – spinning agent from the multilayer mat, FTIR and TGA were employed to detect the typical spectroscopic and thermal signals of each polymer component. Figure 43 shows the FTIR spectra of alginate powder, PCL powder, and PEO powder, along with those of both sides of the washed – crosslinked mat. The main adsorption peaks of alginate (i.e., blue line), PCL (i.e., red line), and PEO (i.e., grey line) are assigned according to the literature.[340–342] For what concerns SA and PEO, a detailed description of the FTIR spectrum is reported in Section 4.1.2. Regarding PCL, $-CH_2$, C=O, and C-O stretching vibrations are observed at 2000 cm^{-1}, at 1722 cm^{-1}, and at 1172 cm^{-1}, respectively, whereas bending modes of $-CH_2$ groups are detected at 1472 cm^{-1}.

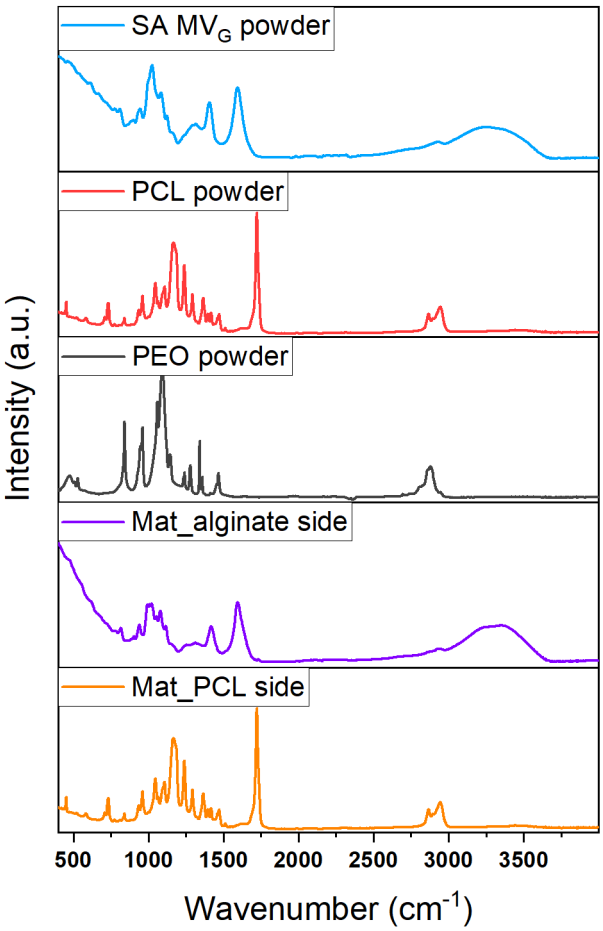

Figure 43. FTIR spectra collected in ATR mode of both sides of the washed – crosslinked multilayer mat along with those of the single polymer components.

By comparing the spectrum of alginate powder with that of alginate – based mat layer (i.e., violet line), nearly the same adsorption peaks can be observed with some slight shifts most likely related to the polymer crosslinking and to the presence of ZnO nanoparticles.[295] Additionally, the distinctive signals of PEO cannot be detected, hence suggesting the removal of the co – spinning agent owing to the long enough immersion in the aqueous crosslinking medium. Finally, PCL – based layer (i.e., orange line) is characterized by the same spectrum with respect to the polymer powder, indicating its ability to maintain the intrinsic chemical structure despite the several applied treatments.

To further evaluate the multilayer mat composition, as well as to obtain information concerning, thermal stability, TGA and DTG curves of the explored samples are reported in Figure 44.

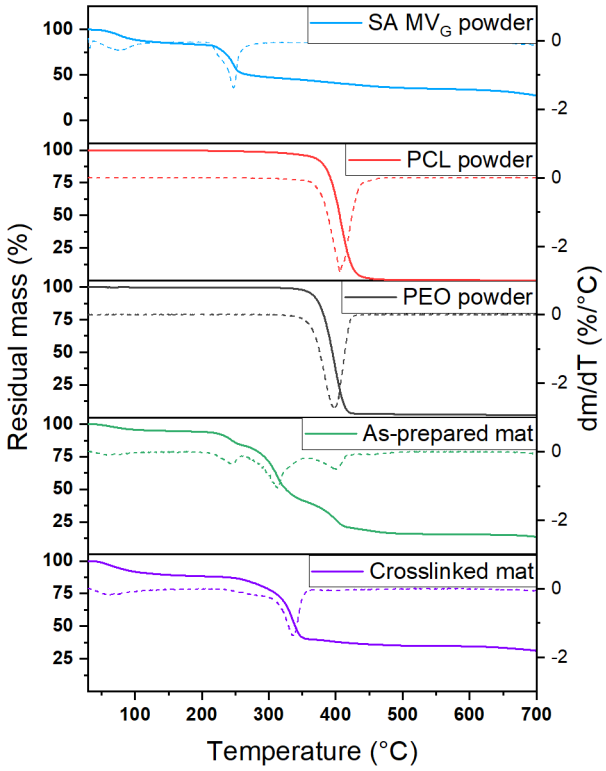

Figure 44. TGA and DTG profiles of alginate powder, PCL powder, PEO powder, as – prepared multilayer mat, and crosslinked multilayer mat.

As already described in the previous Section, alginate powder (i.e., blue line) presents three different degradation steps that can be ascribed to the vaporization of residual humidity and bounded water (i.e., T < 120 °C), to the breaking of polymer chains to form metal carbonates (i.e., T ~ 250 °C), and to the complete burning of the residual organic residues (i.e., T > 650 °C). On the contrary, both PCL (i.e., red line) and PEO (i.e., grey line) powders are characterized by a single sharp degradation phenomenon occurring at T ~ 400 °C. The as – prepared multilayer mat (i.e., green line) shows four distinct mass loss steps, which correspond to the residual humidity and bounded water vaporization at T < 120 °C and to alginate (i.e., T ~ 250 °C), PCL (i.e., T ~ 310 °C), and PEO (i.e., T ~ 400 °C) degradation, respectively. To this end, the lower temperature at which PCL thermal degradation is observed with respect to the polymer powder may be ascribable to the molecular mass reduction taking place during its solubilization in the glacial acetic acid – acetone mixture.[343] As a matter of fact, after the washing – crosslinking treatment the investigated multilayer mat is characterized by only three degradation steps (i.e., violet line). Specifically, the residual humidity and bounded water is remover at T < 120 °C, whereas alginate thermal degrades at T ~ 275 °C, which is slightly higher compared to the powder hence indicating the successful occurrence of the crosslinking reaction that is indeed able to stabilize the polymer. Similarly, PCL degradation phenomenon

seems to be retarded with respect to the as – prepared sample, which may indicate an increase of the polymer molecular weight and/or crystallization degree occurring during the mat drying step at T = 50 °C.[344] Remarkably, the thermal signal corresponding to the degradation of PEO is not detected in the crosslinked sample, hence suggesting its elimination and confirming the results obtained via FTIR.

The prepared crosslinked multilayer mat shows good thermal stability and proper resistance to the developed washing – crosslinking treatment. As such, its mechanical and water – related properties were fully investigated to evaluate its proficient applicability as a wound healing patch. Specifically, this kind of product should possess mechanical properties similar to those of human tissues, being at the same time able to remove exudates, provide sufficient gas exchange, and protect the wound from the external environment.[345,346] To this end, Table 7 summarizes the mechanical performances (i.e., Young modulus Y, tensile strength σ_b, and elongation at break ε_b) obtained via uniaxial tensile test at room temperature for the as – prepared and crosslinked multilayer mats as described in Section 3.5.

Table 7. Summary of the mechanical properties of the as – prepared and crosslinked multilayer mat.

Sample	Y (MPa)	σ_b (MPa)	ε_b (%)
As – prepared	69.6 ± 35.0	0.27 ± 0.10	3.3 ± 1.0
Crosslinked	144.3 ± 80.0	0.44 ± 0.21	3.2 ± 1.8

As clearly observed, the crosslinking process induces an increase of the sample mechanical stiffness with both the Young modulus and the tensile strength showing a doubled value with respect to the as – prepared sample, whereas no significant changes are detected for what concerns the elongation at break. Such result is mainly ascribed to the alginate crosslinking reaction, which is indeed able to form a stable polymer network that enriches the electrospun mat with enhanced mechanical response and stiffness, despite the removal of PEO may also contribute to the phenomenon. Nevertheless, even if the obtained values may be in the suitable range to promote cell adhesion and soft tissue regeneration,[347] the investigated multilayer scaffold shows considerably lower mechanical performances with respect to the single alginate layer reported in Section 4.1.2. Such finding is probably attributed to the layer of PCL electrospun nanofibers, which according to the literature are indeed reported to have a limited stiffness.[348,349] Apart from this, it can also be supposed that the completely different chemical

structure of alginate and PCL reduces the adhesion of the two electrospun layers, hence further lowering the mat mechanical response.

Despite such drawback, the water – related properties (i.e., water contact angle, moisture content, and water vapour permeability) of the crosslinked multilayer mat were explored as described in Section 3.8 with the results summarized in Table 8.

Table 8. Summary of the water – related properties of the crosslinked multilayer mat.

WCA – SA (°)	WCA – PCL (°)	MC (%)	WVP (g/m·Pa·s)
30.3 ± 7.7	161.5 ± 4.1	11.5 ± 2	$2.12 \cdot 10^{-12}$

For what concerns the water affinity, as expected, the alginate – based and PCL sides of the multilayer mat are characterized by significantly different properties. Specifically, the alginate layer is characterized by a strong hydrophilic behaviour in agreement with the polysaccharide capability to interact with water via hydrogen bonds and to adsorb great quantities of aqueous solvents. On the contrary, the PCL layer appears to be highly hydrophobic showing strong water – repellent properties. Additionally, the low MC value can undoubtedly help to preserve the sample properties over a long time period, meanwhile the high WVP should be able to provide a sufficient gas exchange with the external environment, hence promoting cell viability. Notwithstanding, with respect to the alginate – based electrospun monolayer mat investigated in Section 4.1.2, the multilayer electrospun mat here explored presents a lower WVP value due to both the marked hydrophobicity of the PCL layer and its greater overall thickness.

In general, the measured mechanical and water – related properties indicate the possibility to use the prepared multilayer mat as a wound healing patch able to provide a strong protection action towards the environment at the same time representing the ideal environment to promote cell viability. However, in addition to such features and as already discussed, wound healing patches should also possess particular and tuneable uptake – release capabilities to include within their structure and subsequently deliver drugs, vitamins, and/or growth factors. For instance, a slow controlled release may be helpful in the treatment of chronic wounds (e.g., diabetic ulcers), whereas a fast burst release is of particular importance in traumatic episodes (e.g., stab wounds). To this end, kinetic uptake, isotherm uptake, and kinetic release studies were performed as described in Section 3.7 by using methylene blue (Figure 33) and methyl

orange (MO) (Figure 45) as positively and negatively charges model molecules, respectively, in order test the capability of the multilayer mat to act as a drug delivery system.

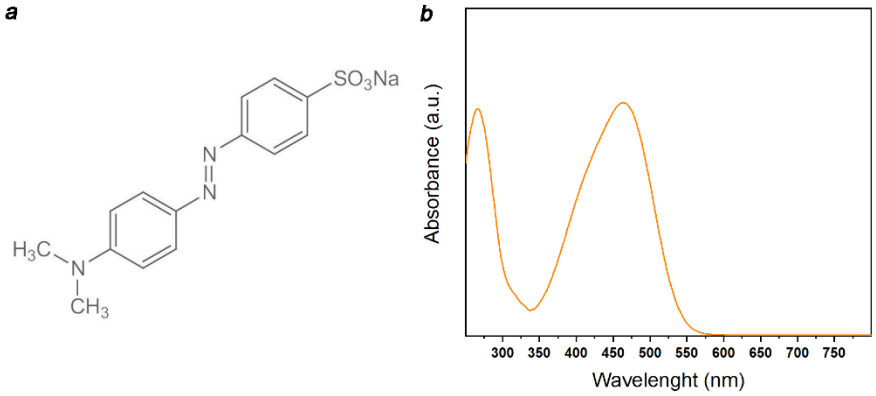

Figure 45. (a) Chemical structure and (b) solution UV – vis spectrum of methyl orange dye.

Specifically, kinetic uptake studies were first performed by soaking portions of the multilayer mat in dye solutions at different concentrations up to 6h, with the UV – vis spectrum of the resulting mixtures being periodically evaluated. The mat adsorption capacity for MB and MO as a function of the initial dye concentration and contact time is shown in Figure 46. As already observed in Section 4.1.2, marked differences can be depicted depending on the nature of the investigated dye. More in detail, in the case of MB, higher colorant amounts are adsorbed, and the process appears to continue even after 6h of immersion in the loading solutions, especially for the most concentrated one (i.e., 20 mg/L). Conversely, for MO in the same experimental conditions, q_t reaches slightly inferior values, and the adsorption phenomenon seems to stop after only 3h independently of the dye concentration. Once again, the higher affinity depicted for MB can be easily explained considering the negative charges present on alginate backbone that can attractively interact with the positively charged colorant molecules. However, as also MO is adsorbed within the multilayer mat despite it repulsively interacts with alginate chains, diffusive phenomena may as well play an important role in conditioning the process. As such, the experimental data were fitted according to a pseudo – first – order (Equation 5) and to a pseudo – second – order (Equation 6) kinetic model aiming to obtain additional insights about the adsorption phenomenon.[350] Interestingly, in both cases the pseudo – second – order model is found to better describe the adsorption phenomenon, hence suggesting the occurrence of both electrostatic and diffusive phenomena. Specifically, given the different results obtained for MB and MO in terms of adsorption capacity and rate, it can be supposed that in the case of the alginate – PCL multilayer mat, diffusive phenomena are preferred for negatively charged

molecules (i.e., MO), whereas electrostatic interactions somehow dominate when positively charged molecules (i.e., MB) are considered.[351,352]

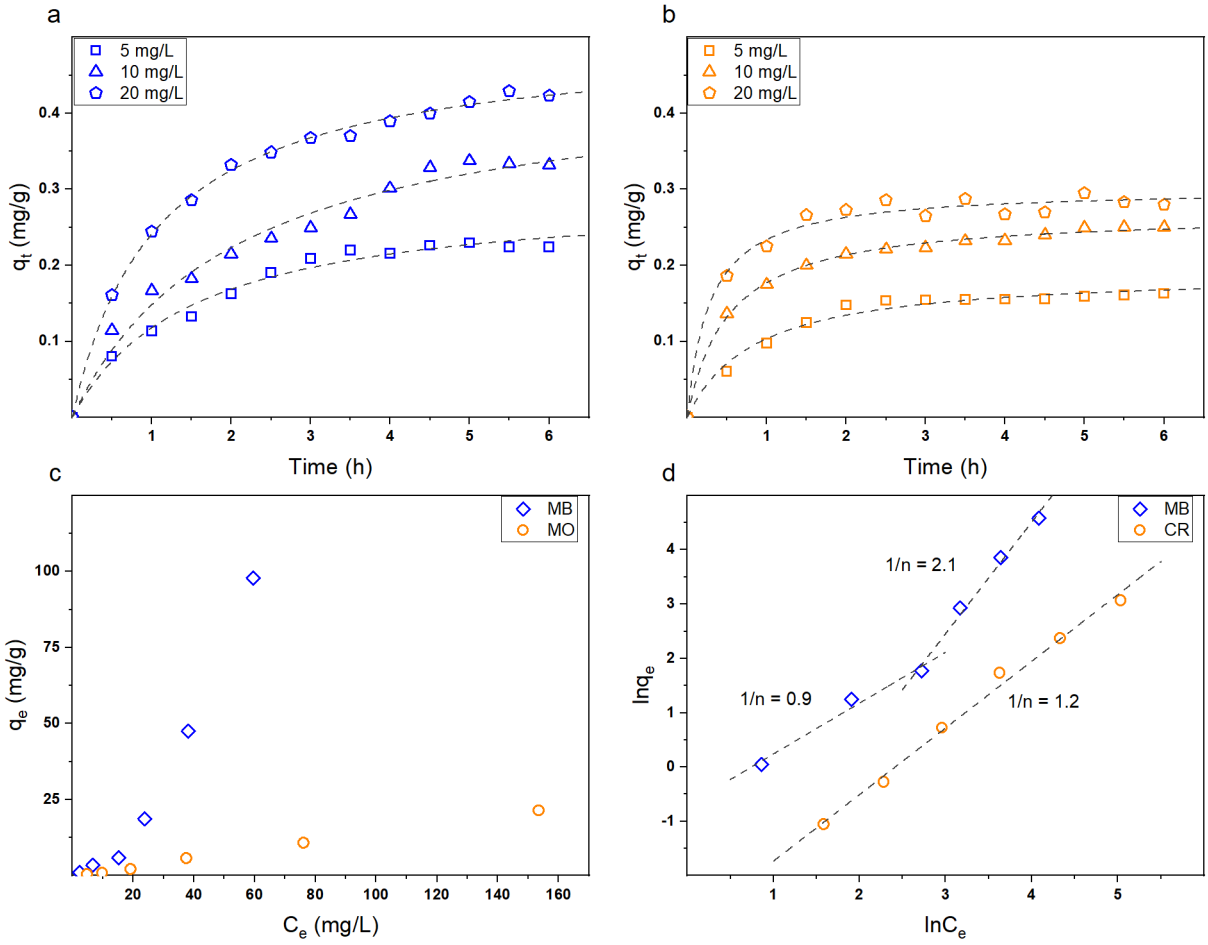

Figure 46. Adsorption kinetics of the investigated multilayer mat for (a) MB dye solutions and (b) MO dye solutions at increasing concentration. Dashed lines represent the fitting of the experimental data with a pseudo – second – order model. (c) Isotherms of adsorption of the investigated multilayer mesh. (d) Linearized Freundlich model.

In this regard, after the adsorption process of methylene blue, alginate – based and PCL layer display an intense blue and light blue colour, respectively, whereas no significant differences are detectable between the two layers for what concerns the adsorption on methyl orange.

To further investigate the capability of the multilayer mat to be uploaded with different drugs, equilibrium adsorption isotherms were investigated, with the results being analysed according to the Langmuir (Equation 8) and Freundlich (Equation 9) models. As clearly shown in Figure 46-c, the equilibrium adsorption capability q_e is found to increase with the equilibrium concentration C_e for both dyes, despite significantly higher values are obtained for MB likewise due to its greater affinity for alginate. More in detail, a strong increment of q_e can be observed for the positively charged dye when the loading concentration is raised above 20 mg/L. As

such, it can be assumed that MB uptake occurs at first mainly via electrostatic interactions but once all the available binding sites are occupied, for example if the loading concentration is high enough, the diffusive phenomenon assumes a critical role and a sharp increase of q_e is depicted. Conversely, a regular and almost linear behaviour can be observed for MO dye as the electrostatic interactions do not significantly contribute to the adsorption process. Interestingly, Langmuir model, which assumes that the equilibrium adsorption capacity is governed by the formation of a single adsorbate monolayer, completely fails to describe the experimental data for both dyes. Freundlich model, which instead considers that the adsorption process occurs on heterogeneous surfaces, provides a good fitting of the experimental data as evidenced in Figure 46-d. However, whereas MO data can be interpolated in the whole concentration range with a single straight line with a slope (i.e., 1/n) equal to 1.2, MB data are described by two distinct concentration regions (i.e., 0 – 20 and 20 – 160 mg/L) presenting a slope of 0.9 and 2.1, respectively. This parameter 1/n is directly correlated to the degree of curvature of the investigated isotherms, with values higher than 1 associated to S – type isotherms that are usually observed for compounds containing polar groups able to compete with water molecules for the adsorption sites.[353,354] In addition, n values are indicative of the intensity of the adsorption process, which becomes more favoured as n tends to a value close to zero. Being the adsorption of MB controlled by both electrostatic interactions and diffuse phenomena, it can be considered that above a certain dye concentration the two leading forces present a synergic effect able to considerably enhance the process, which indeed presents a n value equal to 0.5.

Noticeably, marked differences between the two investigated dyes were observed also in terms of delivery properties. Kinetic release studies were carried out in PBS at T = 37 °C for 6h as previously described (Section 3.8) with the results illustrated in Figure 47. Comparably to what was observed for the single alginate – ZnO electrospun layer investigated in Section 4.1.2, MB dye is immediately released independently on the loading concentration, whereas a slow and controlled release is observed for MO colorant. In addition, at the same experimental conditions, the released amount of MB is considerably greater with respect to MO, which indeed reflects the different phenomena governing the adsorption process.[355] In any case, the amount of released colorants seems to be proportional to the concentration of the loading media, which consequently assumes a critical role in the development of drug delivery systems with an appropriate release kinetic. The achieved results demonstrate the possibility to use the investigated multilayer electrospun patch to deliver different kinds of bioactive molecules with the possibility to easily modulate their release depending on the specific purpose.

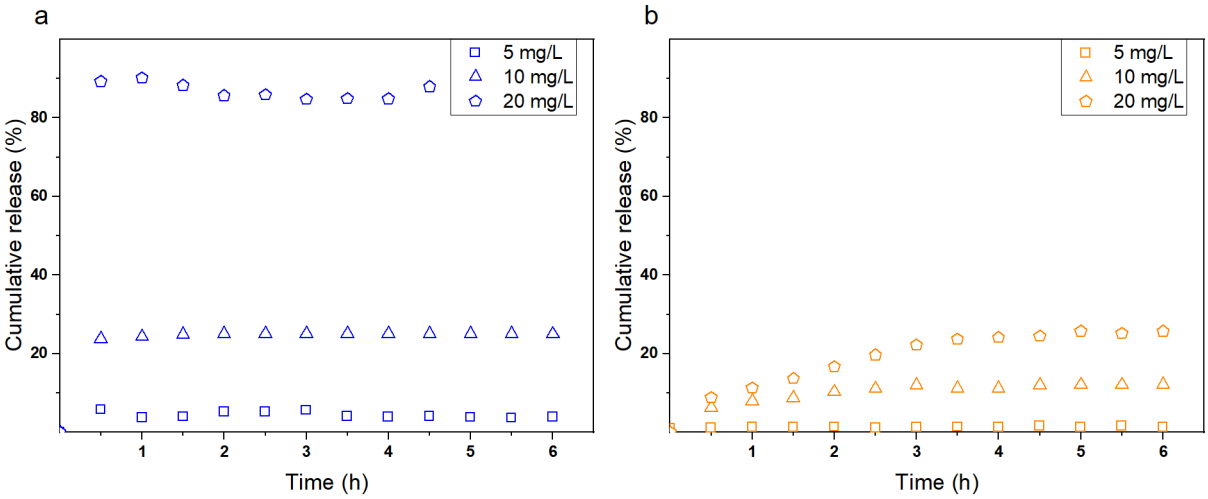

Figure 47. Release kinetics of the multilayer mat for (a) MB and (b) MO.

Conclusions

In this Section, a multilayer electrospun patch was explored as a potential wound healing patch with both the capability to promote cell adhesion and protect the site of interest from the external environment. In this regard, the external electrospun layer of the patch was prepared via the electrospinning of PCL, a biocompatible and biodegradable polymer widely employed in the biomedical and pharmaceutical industries, which was dissolved in acetic acid – acetone mixture. On the contrary, based on results discussed in the previous Sections, the internal electrospun layer of the patch was developed via the electrospinning of an alginate – based formulation enriched with ZnO nanoparticles. A specific washing – crosslinking protocol has then been optimized to ensure the elimination of alginate co – spinning agent (i.e., PEO) at the same time ensuring the stabilization of the polysaccharide nanofibers without interfering with the peculiar nanofibrous structure. As such, a multilayer mat able to combine the water – repellent properties of PCL, the capability to promote cell adhesion and tissue regeneration of alginate, and the antibacterial properties of ZnO nanoparticles, as well as capable to provide sufficient gas exchange and to deliver different bioactive molecules with the most appropriate release kinetic, is obtained. Nevertheless, despite all the aforementioned advantages indicate the prepared multilayer patch as a promising wound dressing product, its limited mechanical properties may represent a not negligible issue consequently limiting the applicability on large – scale wounds and the overall efficiency.

4.1.5 Alginate – Polyurethane Multilayer Mats

The work presented in this Section has been carried out in collaboration with the Institute of Chemistry and Processes for Energy, Environment and Health (ICPEES), which is a joint research unit with a partnership between the French National Research Council (CNRS) and the University of Strasbourg (UdS), under the supervision of Prof. Guy Schlatter and Prof. Anne Hébraud.

In the previous Sections, the preparation and the complete characterization of alginate – based electrospun meshes enriched with ZnO nanoparticles has been discussed. In particular, the development of a multilayer electrospun mat comprised of a protective external layer of PCL and a bioactive internal layer of alginate allowed to obtain a wound healing patch with promising biological, antibacterial, and water – related properties, as well as with the capability to act as advanced drug delivery systems. However, due to the poor mechanical performances obtained for the explored patch, the use of a different material for the preparation of the external protective layer was then evaluated within this Thesis project.

Specifically, polyurethanes (PUs) were selected for the purpose owing to their exceptional adhesive strength, mechanical response, and UV resistance.[356] PUs, which are segmented copolymers characterized by the presence of the urethane link exhibiting the alternation of hard and soft units,[357,358] show a marked elastomeric behaviour that can be tailored, together with their other physical – chemical properties, by selecting the appropriate monomers and controlling the synthesis conditions.[356,359] Owing to such versatility, PUs are widely used materials in adhesives,[360] binders,[361] filters,[362] protective textiles,[363] sensors,[364] and medical industries.[365] Noticeably, polyurethane – based electrospun meshes have been broadly produced and employed in the past decades for several applications.[366–368] Unfortunately, PUs require high amounts of volatile organic solvents (e.g., dimethylformamide, dimethyl sulfoxide, dimethyl acetamide, etc.) to be both synthesized and processed via electrospinning, therefore representing a considerable environmental burden as well as a not negligible cost.[369,370] To overcome such limitations, water – borne polyurethanes (WBPUs) have recently started to gain an increasing deal of interest from both the academic and industrial community due to the fact that water is the only solvent required in their manufacturing process. As such, WBPUs are much more environmentally friendly compared to traditional PUs as they are non – toxic, non – flammable, and do not generate polluted air or wastewater.[371,372] Despite such advantages that make them extremely promising for several industrial applications, water – borne polyurethanes are commonly prepared in the form of stable suspensions (i.e., solid phase

dispersed in water) that can be hardly electrospun due to the lack of strong cohesive forces between the polymer droplets.[373,374] Consequently, carrier polymers must be added to the WBPU formulations to achieve the proper viscoelastic properties to ensure the successful of the electrospinning procedure.[375] In the present Thesis work, a commercial WBPU batch formulation with a 59 w/v% polyurethane content, which was kindly provided by BASF, was employed as the starting mixture, whereas poly(ethylene oxide) ($\overline{M}_v$ = 900 kg/mol) was selected as carrier polymer owing to its great processability via electrospinning and ease of removal by simple post – processing treatments. In this regard, distinctive formulations were prepared by first solubilizing a proper amount of PEO powder in deionized water and then adding the WBPU batch system. PEO concentration was kept constant at 4 w/v% and WBPU – PEO weight ratio was varied from 0 up to 6.

Steady – state viscosity measurements were carried out on the prepared mixtures at T = 20 °C as described in Section 3.1 with the measured flow curves reported in Figure 48-a.

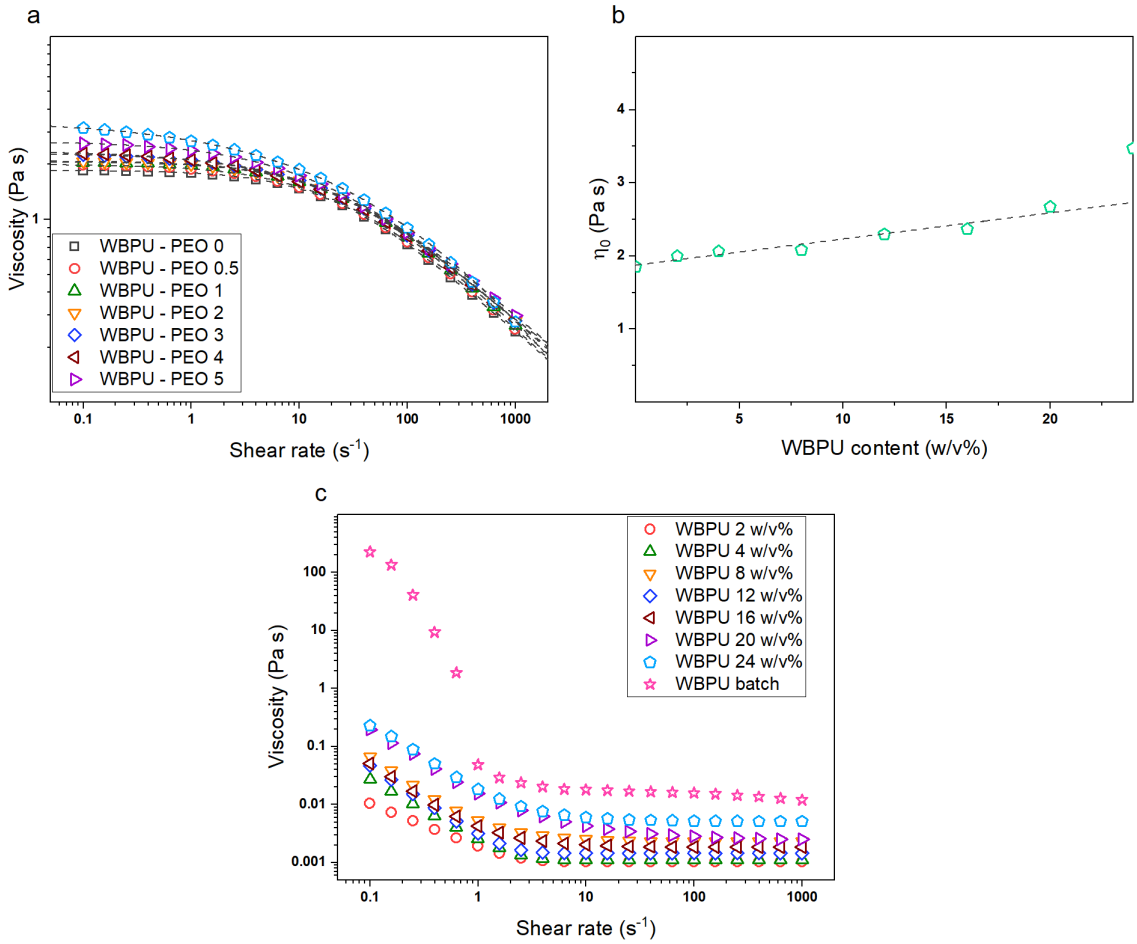

Figure 48. (a) Flow curves of WBPU – PEO formulations at different component ratio. Dashed lines represent the fitting of the experimental data with the Carreau – Yasuda model. (b) Zero – shear viscosity dependence upon the WBPU content for the tested WBPU – PEO formulations. (c) Flow curves of WBPU formulations at different concentrations.

All the tested formulations present the typical shear – thinning behaviour of polymer solutions characterized by an initial region in which the viscosity is nearly constant (i.e., Newtonian plateau) followed by a progressive viscosity decrease as the shear rate is raised due to the gradual chain orientation and entanglement disruption. Noticeably, as reported in Figure 48-b, the zero – shear viscosity of the investigated formulations, which was calculated with the Carreau – Yasuda model, linearly increases with the WBPU content up to a 20 w/v% value whereas a significant deviation from the linearity can be observed for the highest investigated concentration (i.e., 24 w/v%). As such, it can be supposed that within a certain concentration range, WBPU – PEO formulations follow an Einstein law due to the fact that the particles are independent and interact only with the carrier polymer or with water. However, as the concentration is raised above a certain limit, particle – particle interactions start to occur and deviations from this linear behaviour are observed.[376] To obtain further information on such phenomenon, steady – state viscosity measurements were carried out on pure WBPU aqueous formulations with a polyurethane amount ranging from 2 w/v% up to 59 w/v% (i.e., WBPU batch formulation) with the obtained flow curves represented in Figure 48-c. In any case, the typical performance of particle suspensions (i.e., Bingham fluids) can be depicted. Specifically, at rest, such systems present a high viscosity value due to the occurring inter – particle interactions that form a solid – like structure within the surrounding fluid. However, the application of a certain shear stress (i.e., yield stress) is able to destroy these cohesive forces hence promoting a rapid and strong viscosity decrement.[377] Clearly, increasing the polyurethane content corresponds to increasing both the required yield stress and resultant system viscosity. Remarkably, the fact that such a behaviour is not observed in WBPU – PEO formulations with an equal polyurethane content, which are indeed characterized by a well – defined Newtonian region, may indicate the capability of PEO chains to prevent the establishment of inter – particle interactions within a certain concentration range.

The rheological characterization demonstrates the possibility to use PEO – based solutions as promising carriers to electrospun WBPU suspensions owing to their homogeneity and ease of preparation. As such, the electrospinning of the prepared WBPU – PEO formulations was carried out by using a typical dry – collector electrospinning setup and the following working parameters: a spinneret – collector distance of 20 cm, a flow rate of 1 mL/h, a 20G flat – tip needle, and an applied voltage of 12.5 kV. The morphology of the as – prepared mats is reported in Figure 49.

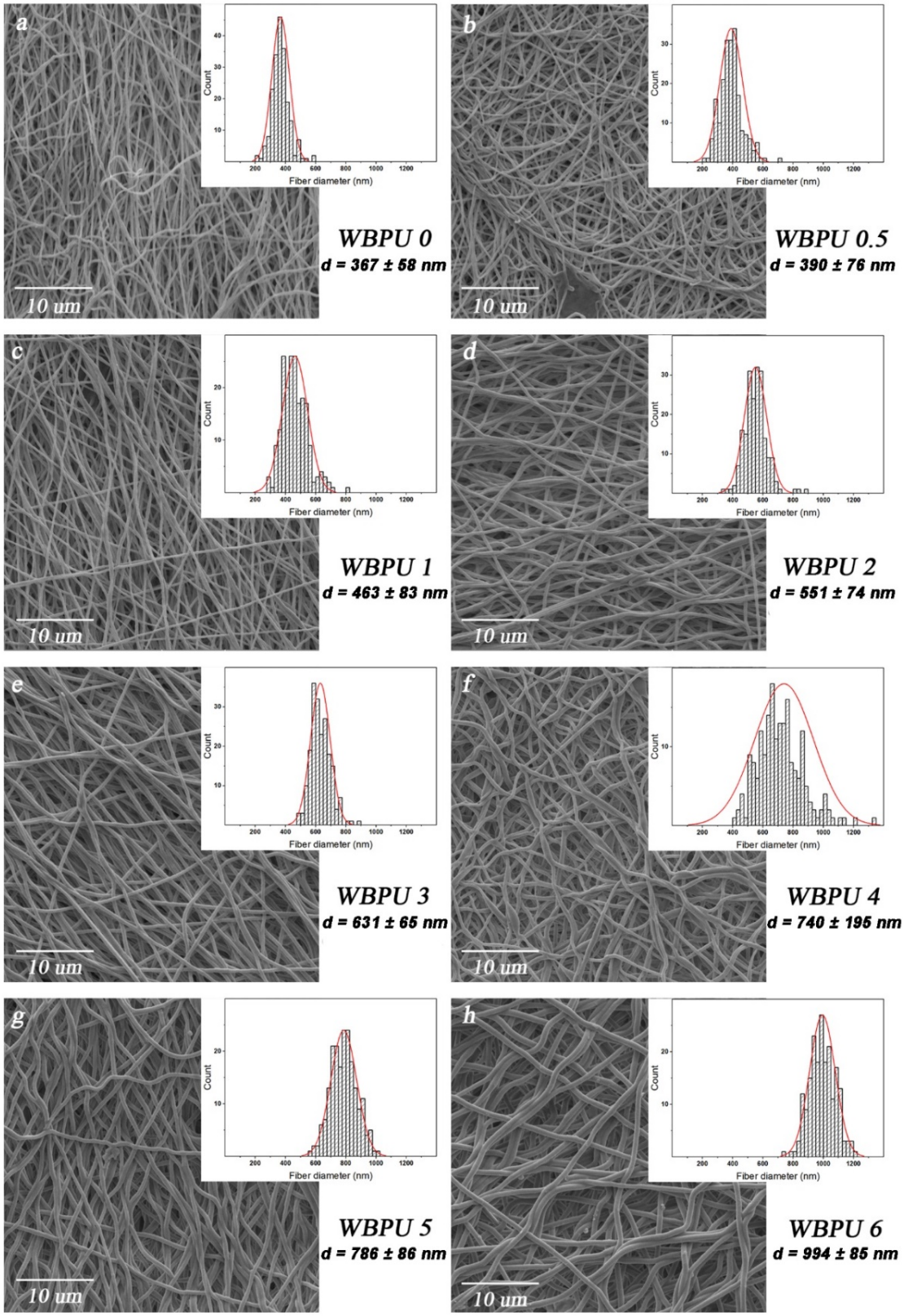

Figure 49. Morphology of the as – prepared mats together with the fiber diameter distribution. WBPU 0 is shown in (a), WBPU 0.5 in (b), WBPU 1 in (c), WBPU 2 in (d), WBPU 3 in (e), WBPU 4 in (f), WBPU 5 in (g), and WBPU 6 in (h).

Independently of the WBPU content, a well – defined, uniform, and highly porous structure is obtained for all the electrospun meshes. In particular, defect – free and randomly oriented nanofibers are clearly observable in the reported micrographs and they present a quite narrow dimension distribution. Nevertheless, marked differences can be depicted among the samples with a significant linear increment of the fiber diameter with the WBPU concentration as evidenced in Figure 50 (i.e., black squares). Such an outcome is most likely due to both the higher particle content in the starting suspensions and their greater viscosity. Indeed, on the one hand, systems with a higher viscosity produce bigger nanofibers, and on the other, the increment of the WBPU in the formulations forces the formation of greater fibers due to the greater polymer concentration.

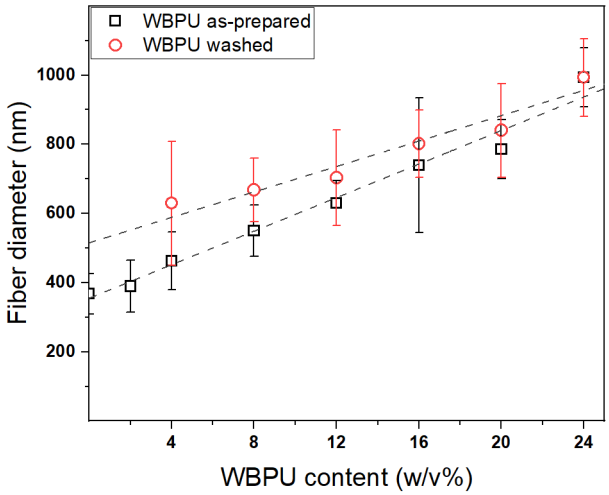

Figure 50. Dependence of the nanofiber diameter upon the WBPU content for the as – prepared (black squares) and washed (red circles) mats.

Even though polyurethane particles may be used to enhance the elastic properties of electrospun nanofibers by acting as reinforcement fillers, the aim of this Thesis work was to obtain a pure WBPU mat to be used in the preparation of a multilayer wound healing patch. As such, to remove the carrier polymer (i.e., PEO) from the as – prepared nanofibers, the samples were immersed in deionized water at room temperature overnight and subsequently dried under vacuum. Not surprisingly, due to the low polyurethane content and the high water solubility of poly(ethylene oxide), WBPU 0 and WBPU 0.5 samples are rapidly and completely dissolved once immersed in the washing medium. Conversely, the other samples retain their macroscopic structure despite WBPU 1 and WBPU 2 have the tendency to break into small pieces. SEM micrographs of the washed mats are shown in Figure 51 with the related diameter distribution.

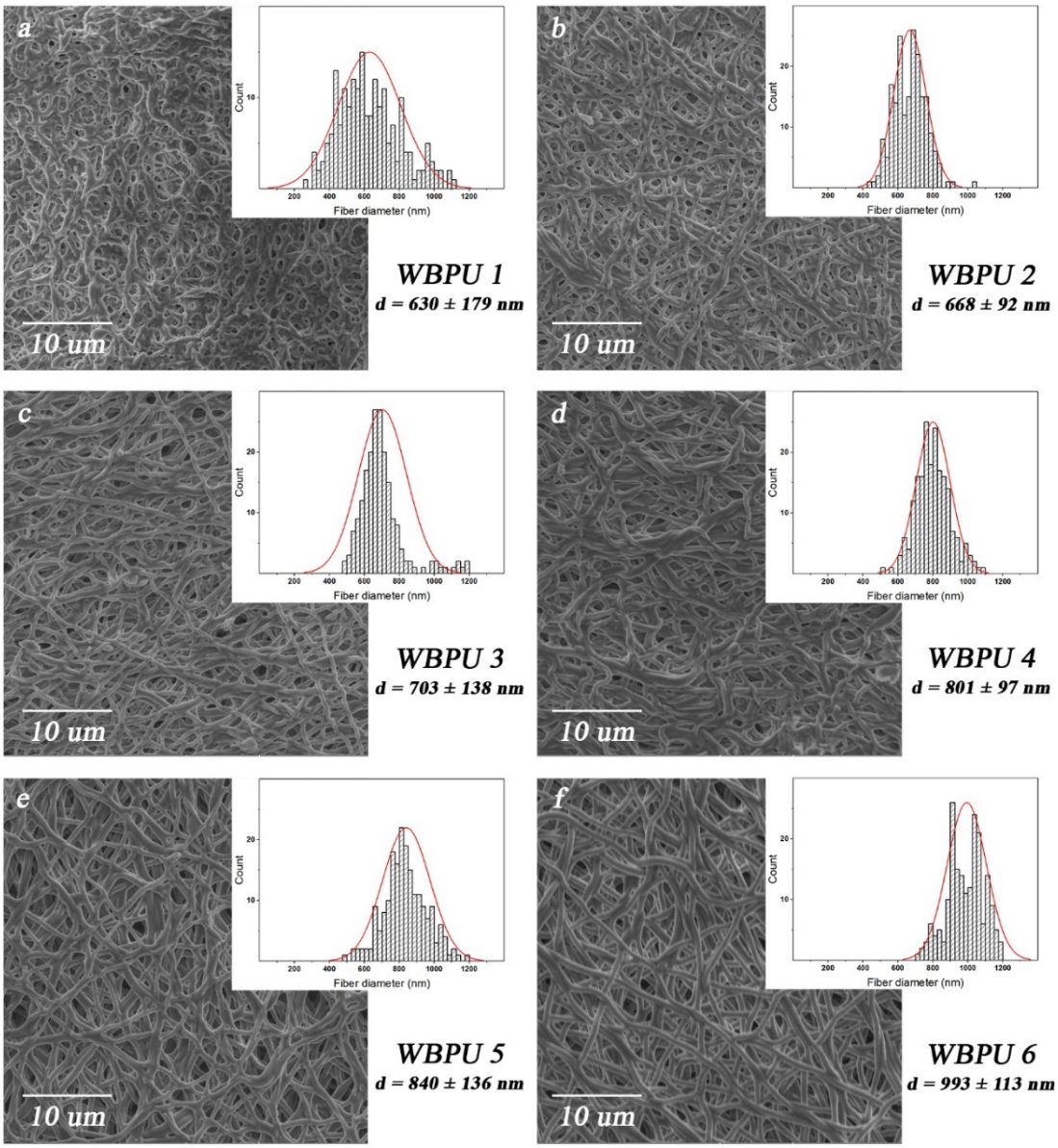

Figure 51. Morphology of the washed mats together with the fiber diameter distribution. WBPU 1 is shown in (a), WBPU 2 in (b), WBPU 3 in (c), WBPU 4 in (d), WBPU 5 in (e), and WBPU 6.

As clearly shown, samples obtained from the formulations with a high WBPU content can better maintain their microstructure with well – defined nanofibers and a high porosity with interconnected pores. On the contrary, WBPU 1 and partially also WBPU 2 are characterized by coalesced inhomogeneous nanofibers creating poorly porous structures presenting a high number of defects. As for the as – prepared meshes, a linear increment of the fiber diameter with the WBPU concentration is observed as reported in Figure 50 (i.e., red circles). However, contrary to what expected, an increase in the fiber diameter is observed after the washing step. Specifically, the lower the WBPU content, the greater is the diameter increment reflecting the nanofiber reduced stability. In this regard, WBPU 1 shows a diameter increase of 36%, whereas

WBPU 6 presents nearly the same fiber diameter before and after the washing procedure. Such an unexpected effect may be due to the swelling of PEO trapped inside the fiber. In addition, the concentration gradient of PEO between the core and the outside of the fiber leads to the diffusion of solubilized PEO towards the washing medium, hence generating an osmotic pressure that favours the increase of the fiber diameter. Indeed, as experimentally observed, this increase in the diameter is favoured at the lowest WBPU – PEO ratio, i.e., at the highest PEO content. However, when the WBPU – PEO ratio is high enough, the nanofibers do not show this behaviour indicating a much higher morphological stability.[378,379]

To check the nanofiber composition and the effective PEO removal, the thermal properties of the electrospun mats before and after the washing step were investigated via DSC from -80 °C up to 200 °C, as described in Section 3.3. The thermograms of the as – prepared samples are shown in Figure 52-a. For better comparison, the thermal behaviour of WBPU 0 mat (i.e., pure PEO nanofibers) and of a polyurethane film obtained by a solvent casting procedure at room temperature using the WBPU batch formulation is reported in Figure 52-b.

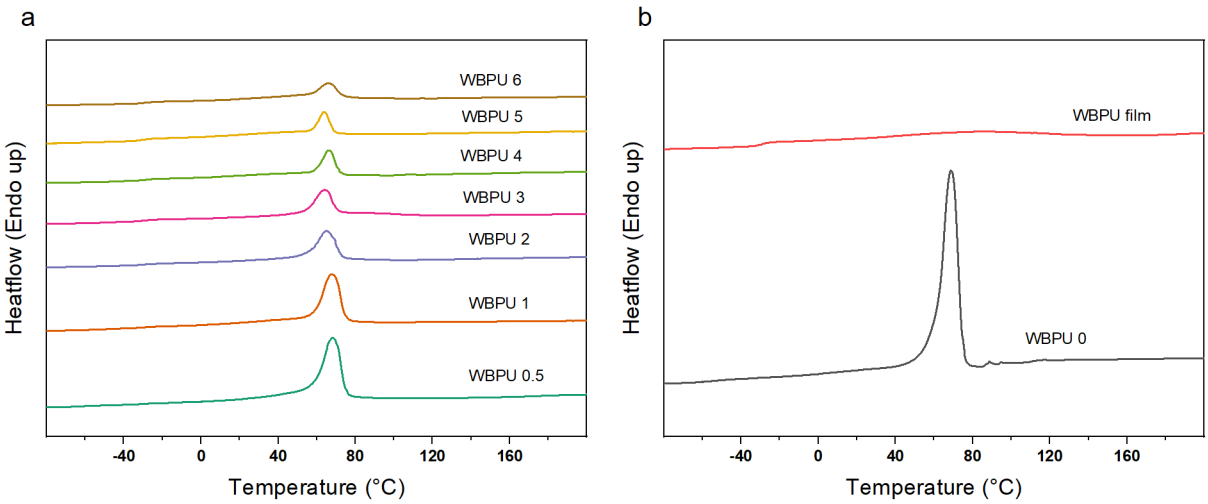

Figure 52. (a) Thermograms of the as – prepared WBPU – PEO mats and (b) thermograms of the as – prepared WBPU 0 mat and a WBPU film.

In detail, for the WBPU film (i.e., red line) a glass transition temperature (T_g) of around -30 °C is observed together with a broad endothermic signal in the temperature range 60 – 120 °C that can be ascribable to the vaporization of residual humidity.[380] Conversely, WBPU 0 presents a single sharp endothermic peak at T ~ 70 °C corresponding to the PEO melting temperature (i.e., grey line).[381] The as – prepared electrospun meshes are characterized by both the signals of WBPU and PEO with differences in the peak intensity depending on the ratio of the two components. Specifically, the higher is the polyurethane content, the greater is the T_g signal

and the lower is the carrier polymer melting peak. By a way of example, the thermograms of the WBPU 6 mat before (i.e., light brown line) and after (i.e., blue line) the washing cycle are reported in Figure 53 along with those of the WBPU 0 electrospun and WBPU film samples. Similar results were achieved for all the other prepared electrospun mats.

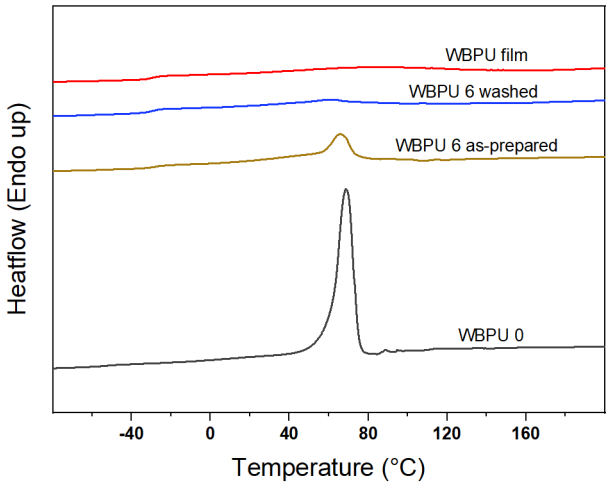

Figure 53. Thermograms of the as – prepared WBPU 0 sample, as – prepared WBPU 6 sample, washed WBPU 6 sample, and WBPU film sample.

As clearly evidenced, the melting signal of PEO is not detectable after the washing step in the water, therefore demonstrating its complete elimination from the electrospun nanofibers most likely due to its high solubility in aqueous media.

Consequently, it can be safely assumed that the developed procedure allows the easy fabrication of pure polyurethane electrospun mats by a straightforward, weakly environmentally impactful, and industrially scalable approach. To this end, since the mechanical response of a material is fundamental to obtain the appropriate performances with respect to the selected purpose, uniaxial tensile tests (Section 3.5) were carried out on both the as – prepared and washed WBPU – based meshes to evaluate the Young modulus, the tensile strength, and the elongation at break. To be noted that WBPU 1 and WBPU 2 were not tested because of their tendency to break into small pieces during the washing step owing to the low polyurethane amount. As a way of example, stress – deformation curves of WBPU 6 electrospun mat before and after the washing cycle are reported in Figure 54-a.

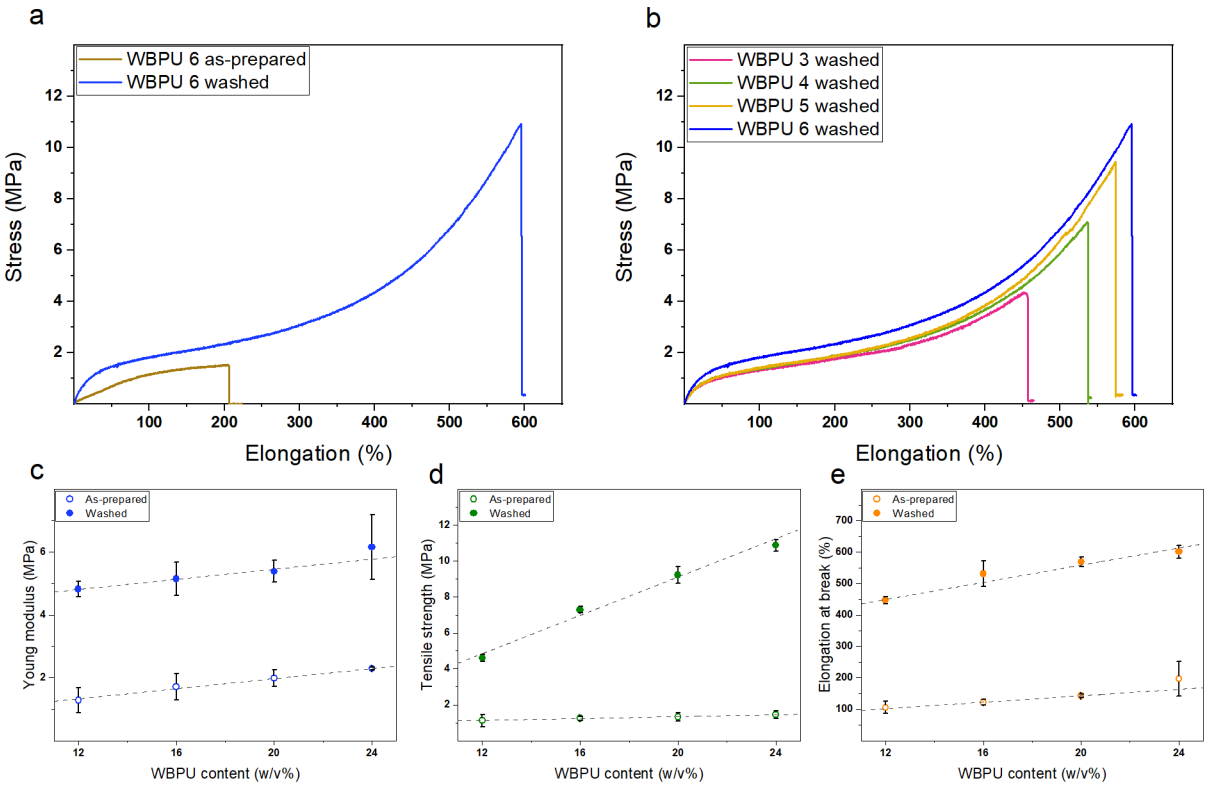

Figure 54. (a) Stress – deformation curves of the as – prepared and washed WBPU 6 electrospun mats. (b) Stress – deformation curved of the washed WBPU – based electrospun mats. (c) Dependence of the Young modulus, (d) dependence of the tensile strength, and (e) dependence of the elongation at break upon the WBPU content for as – prepared (i.e., empty symbols) and washed electrospun mats (i.e., full symbols).

Remarkably, it can be noticed that the removal of the carrier polymer considerably enhances the mat mechanical performance with a huge boost especially in the sample deformability, which is likewise due to the fact that PEO nanofibers are in general characterized by poor mechanical properties.[382,383] After the washing step, WBPU – based meshes show the typical behaviour of elastomeric material with the stress – deformation curves presenting three different regions: elastic deformation, plastic deformation, and a last region that may be ascribable to both the elastic spring back of polyurethane materials and the progressive fiber orientation.[384–386] Despite such a general finding is valid for all the tested mats, the WBPU content plays a strong role in conditioning the sample mechanical properties as shown in Figure 54-b. Specifically, the greater the WBPU content, the higher is the sample mechanical response. To better compare the investigated samples, the dependence of the Young modulus, of the tensile strength, and of the elongation at break upon the polyurethane concentration is reported in Figure 54-c, Figure 54-d, and Figure 54-e, respectively. Noticeably, the mat mechanical features linearly increase with the increasing the WBPU – PEO ratio for both the as – prepared and washed samples despite a much less marked rising is observed for Y with respect to σ_b and ε_b, which is consistent with the mat polyurethane nature. The observed results

can be most likely correlated to the different sample morphology, where bigger and more homogeneous nanofibers (i.e., WBPU 6) endow the electrospun yarns with the capability to sustain greater stresses and elongations before showing mechanical failure compared to thinner and defect – rich nanofibers (i.e., WBPU 3).[387]

Together with the mechanical behaviour, the capability of a material to interact with water is another important feature to be considered. As such, water – contact angle measurements were carried out on the washed WBPU – based electrospun meshes as described in Section 3.8. Table 9 summarizes the measured WCA values depending on the WBPU content. As well as what reported for the mechanical evaluation, WBPU 1 and WBPU 2 were not tested.

Table 9. Water contact angle values obtained for the washed WBPU – based nanofibers and WBPU film.

Sample	WCA (°)
WBPU 3	110 ± 3
WBPU 4	119 ± 3
WBPU 5	125 ± 4
WBPU 6	133 ± 3
WBPU film	93 ± 3

All electrospun samples appear to be highly hydrophobic with WCA values well above 90° and, remarkably, highly superior to that of the WBPU film used as control (i.e., 93°). Such an outcome is correlated to the typical microstructure of electrospun mats, in which the existence of the nanofibers is crucial to maintain the wetting behaviour in the Cassie – Baxter regime.[388] Usually, small nanofibers are expected to increase the mat hydrophobicity due to their higher surface area and reduced pore size. Nevertheless, rather than the fiber diameter, factors such as the surface roughness and fiber fraction have been shown to be the dominant ones in determining the wetting properties of electrospun mats.[389] To this end, taking into account the SEM micrographs shown in Figure 51, considerable differences can be supposed to exist between the prepared sample. Specifically, at the lowest explored WBPU content (i.e., WBPU 3) the nanofibers tend to some extent to coalesce hence forming dimensionally big defects, which in turn reduce the sample overall roughness and fiber fraction. Conversely, at the highest investigated WBPU content (i.e., WBPU 6) the nanofibers can maintain their individuality, thereby ensuring both great surface roughness and overall fiber fraction. In addition, it may also be considered that the potential existence of residual traces of PEO non – detectable by DSC measurements in the washed mats obtained from low WBPU – PEO ratio formulations

could accentuate such phenomenon owing to the high affinity between the carrier polymer and water. Consequently, in contrast to what is usually expected, increasing the WBPU content in the starting formulation allows achieving polyurethane – based electrospun meshes with strong liquid repellent properties.

Considering the results above – discussed, especially in terms of mechanical properties and surface wettability, WBPU 6 electrospun mat was then selected as the most promising one to be used for the preparation of the external protective stratum of the multilayer electrospun patch subject of this Thesis work. To this end, in a typical fabrication procedure, 5 mL of the WBPU 6 formulation were electrospun on a rotating drum collector using a spinneret – collector distance of 20 cm, an infuse rate of 1 mL/h, a 20G flat – tip needle, an applied voltage of 12.5 kV, and a rotation speed of 100 rpm. Subsequently, 15 mL of SA MV_G – based mixture containing ZnO nanoparticles (see Section 4.1.2 for the detailed preparation protocol) were directly electrospun on the polyurethane layer. Spinneret – collector distance of 15 cm, infuse rate of 0.75 mL/h, 22G flat – tip needle, applied voltage of 12.5 kV, and rotation speed of 100 rpm were employed as working parameters. Once prepared, the multilayer mat was soaked for 5 minutes in a 3 w/v% $SrCl_2$ aqueous solution to first crosslink the alginate nanofibers and subsequently immersed in deionized water overnight aiming to completely remove PEO from both the polyurethane layer, where it was used as carrier polymer, and the alginate layer, where it was used as co – spinning agent. Finally, the multilayer mat was dried under vacuum at room temperature and stored in desiccator. The morphology of the resultant nanofibers was analysed by means of scanning electron microscopy and atomic force spectroscopy, with the obtained micrographs reported in Figure 55. For what concerns the WBPU – based layer (Figure 55-a and Figure 55-b), as previously discussed in this Section, the high amount of polyurethanes allows to maintain the nanofiber morphology despite the long immersion in water, which is supposed to remove the carrier polymer. Regarding the alginate – based layer (Figure 55-c and Figure 55-d), as already deeply presented in the previous Sections, small and homogeneous nanofibers completely embedding ZnO nanoparticles are depicted leading to a highly porous structure that strongly resembles the human extracellular matrix.

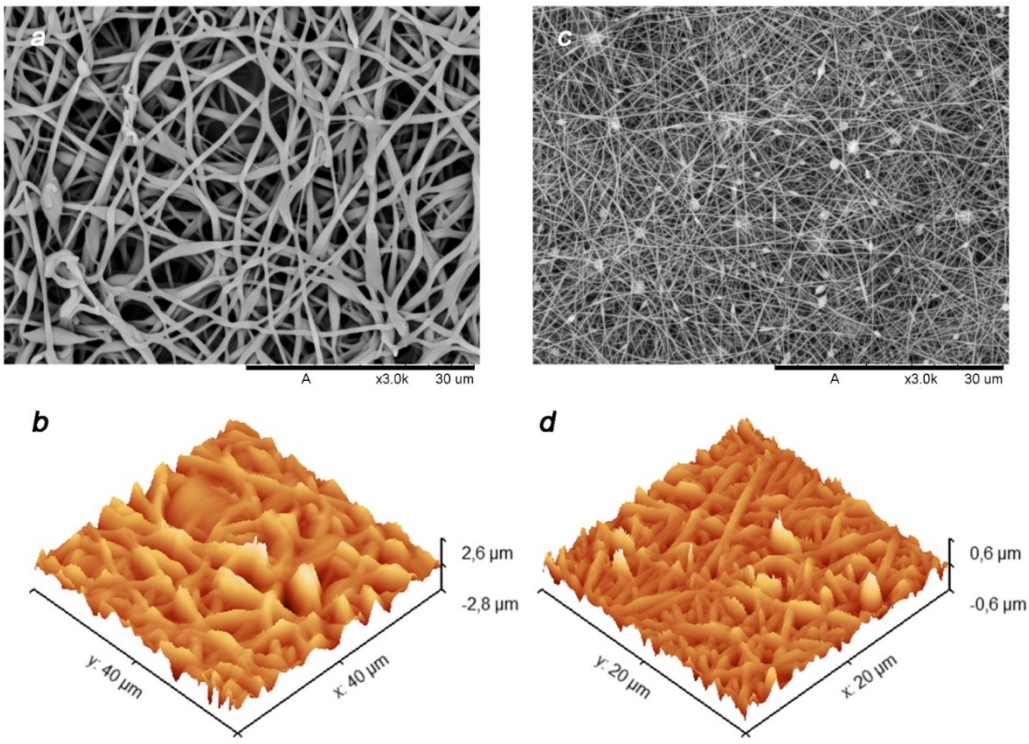

Figure 55. (a) and (c) SEM micrographs of WBPU – based and SA – based layers of the investigated multilayer electrospun mat, respectively. (b) and (d) AFM micrographs of WBPU – based and SA – based layers of the investigated multilayer electrospun mat, respectively.

To explore the composition of the multilayer mat after the washing – crosslinking treatment, hence confirming the PEO removal from both nanofibrous layers, DSC and TGA analysis were carried out as described in Section 3.3. Figure 56-a reports the thermograms of the multilayer patch before and after the above – mentioned treatment along with that of a PEO – based electrospun mat.

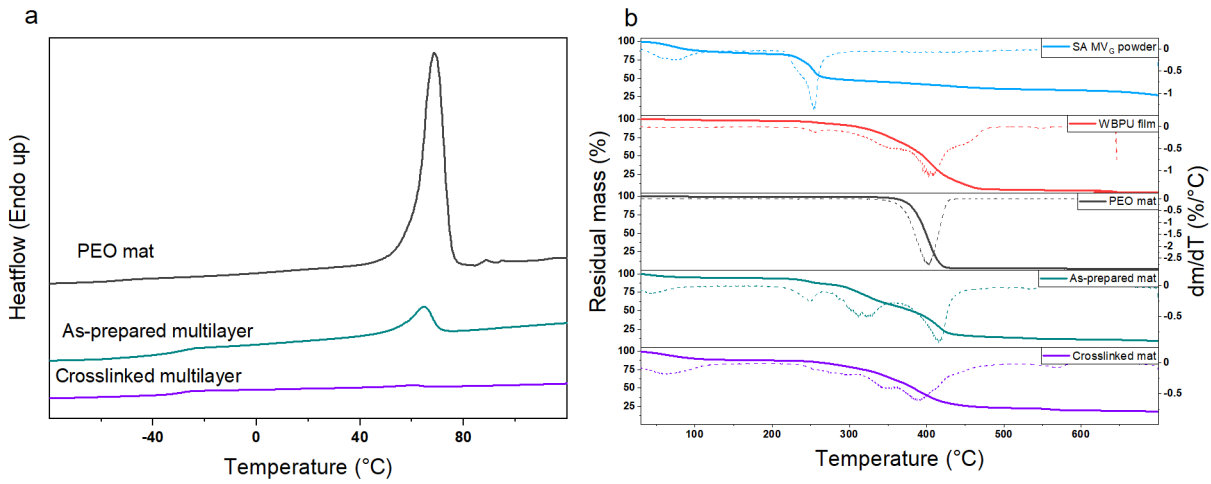

Figure 56. (a) DSC profiles of the as – prepared multilayer mat, crosslinked multilayer mat, and PEO mat. (b) TGA and DTG profiles of SA MV_G powder, WBPU film, PEO mat, as – prepared multilayer mat, and crosslinked multilayer mat.

As already observed in Figure 52-b (i.e., WBPU 0), PEO mat (i.e., grey line) is characterized by a sharp endothermic peak at T ~ 70 °C corresponding to the polymer melting. Such signal can be depicted also in the as – prepared multilayer mat (i.e., green line), which in addition presents an inflection point at T ~ -30° C in correspondence of polyurethane glass transition temperature. In this regard, the crosslinked multilayer mat (i.e., violet line) clearly displays the T_g signal but lacks the PEO one, hence indicating the removal of the carrier/co – spinning polymer during the washing treatment in deionized water.

Further information in this respect can be deduced from the TGA and DTG profiles reported in Figure 56-b. Due to the complex thermal degradation of polyurethanes (i.e., red line), which is partially overlapped to that of PEO (i.e., grey line) and seems to occur in at least three separate steps at T ~ 350 °C, T ~ 400 °C, and T ~ 450 °C, the obtained thermograms are of not easy interpretation. However, it can be observed that the washing – crosslinking protocol to which the multilayer mat has been subjected is able to increase alginate thermal stability but has no effect on the polyurethane nanofibers, at the same time being able to remove the carrier/co – spinning agent.

Aside from its composition, the capability of the prepared multilayer mat to effectively be used as a wound healing patch was explored investigating its mechanical and water – related properties. Figure 57 reports the mat dynamic – mechanical behaviour measured at T = 37 °C in extensional configuration.

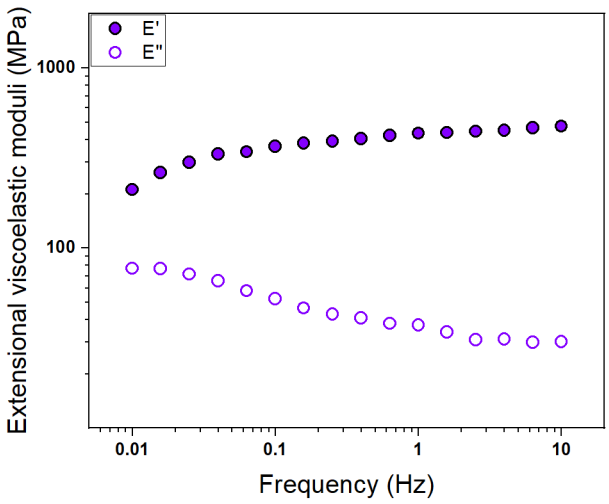

Figure 57. DMA spectrum at T = 37 °C obtained in extensional configuration with σ = 0.05 MPa.

A marked increase of the extensional storage modulus E' can be observed at low frequency values, corresponding to the terminal region of the viscoelastic spectrum, whereas a nearly constant trend is depicted at intermediate and high frequency values, corresponding to the

viscoelastic transition region. By comparing the achieved results with those obtained for a simple polyurethane electrospun layer and a simple alginate – based electrospun layer (Section 4.1.2), the latest seems to be the one predominantly affecting the mechanical behaviour of the multilayer mat. However, it can be supposed that the WBPU – based nanofibrous stratum may to some extent enhance the overall elasticity of the multilayer yarn, which should be consequently able to sustain considerable deformations without showing any mechanical failure. It is worth noting that the good adhesion between the two layers is most likely ensured by their nanofibrous structure with the small alginate – based nanofibers being able to fill the big pores formed by the WBPU nanofibers, thereby providing a sort of compatibilization effect. For what concerns the water – related properties (Section 3.8), the water contact angle of both sides, the moisture content, and the water vapour permeability of the explored multilayer mat are summarized in Table 10.

Table 10. Summary of the water – related properties measured for the crosslinked multilayer mat.

WCA WBPU (°)	WCA SA (°)	MC (%)	WVP (g/m·Pa·s)
133.0 ± 3.1	30.3 ± 7.7	6.6 ± 1.1	$2.8 \cdot 10^{-12}$

In the present Thesis project, the main aim beyond the preparation of a multilayer electrospun wound healing patch was to ensure, along with a proper structure to foster cell viability and promote tissue regeneration (i.e., artificial extracellular matrix), a marked protective capability towards the external environment. As such, the strong liquid repellent ability (i.e., WCA = 133°) of the WBPU – based layer together with its outstanding deformability are highly suitable to the purpose. In addition, the low moisture content, which is even lower with respect to that achieved for a single alginate – based nanofibrous layer (i.e., 6.6% vs 11%), can ensure the long storage of the patch without occurring in significant changes in its physical – chemical properties. Finally, the water vapour permeability displayed by the multilayer mat is well within the required range to provide a sufficient gas exchange to the wounds, hence further supporting cell viability.

Consequently, considering the presented results, it is not surprising that the proposed alginate – polyurethane multilayer electrospun mat clearly represents a novel and highly promising system for the development of various biomedical products. To this end, aiming to further prove the outstanding capability of such a patch, its use as a drug delivery system was evaluated following the procedures described in Section 3.7. Specifically, salicylic acid (SAc) (Figure

58), which is a key ingredient in many skincare products, was employed as a model drug molecule owing to its great water solubility.

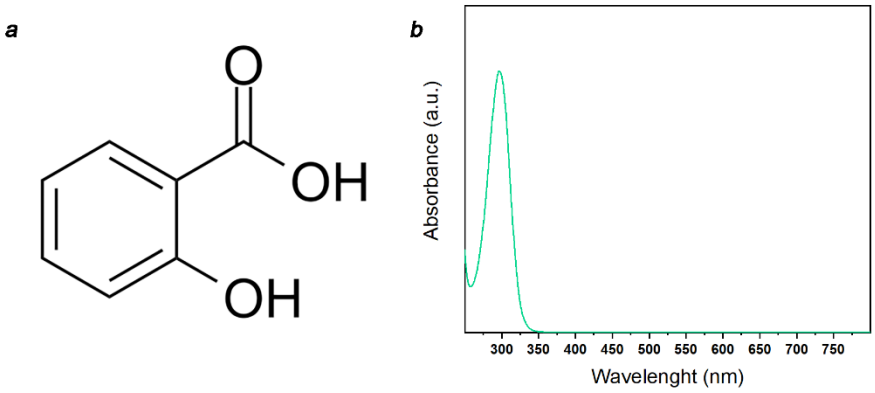

Figure 58. (a) Chemical structure and (b) solution UV – vis spectrum of salicylic acid drug.

Firstly, the possibility to upload the selected drug within the prepared multilayer mat via a simple impregnation method was evaluated via uptake kinetic studies. To this end, SAc batch solutions with a concentration of 250 mg/L and 500 mg/L were employed. Adsorption capacity dependence upon the impregnation time is reported in Figure 59-a.

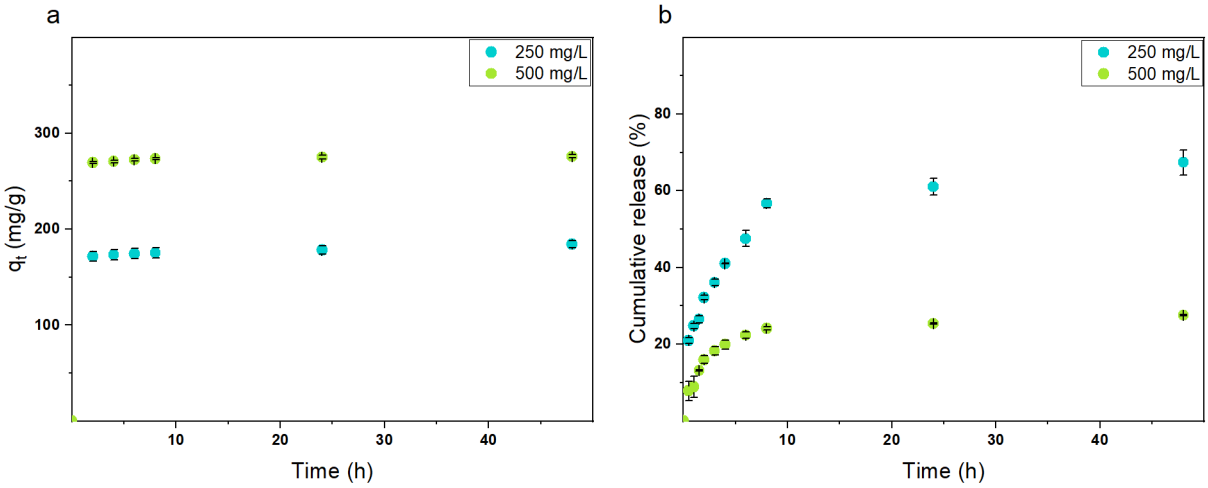

Figure 59. (a) Salicylic acid adsorption kinetics for the investigated multilayer patch. (b) Salicylic acid release kinetics for the investigated multilayer patch in PBS at T = 37 °C.

Remarkably, independently of the batch solution concentration, the drug uploading is found to occur extremely rapidly in the first 2h of the process with q_t subsequently showing a slow a moderate increment up to 48h. In addition, despite higher values are not surprisingly achieved for the 500 mg/L loading solution, the adsorption capacity reaches considerably high values in both cases. As such, most likely due to the great affinity between the prepared multilayer mat

and salicylic acid, this finding indicates the possibility to prepare drug delivery systems encapsulating a great amount of drug thereby being suitable in those applications where the administration of high dosages is required. It should be noted that both the pseudo – first – order (Equation 5) and pseudo – second – order (Equation 6) kinetic models completely failed to fit the experimental data, likewise due to the multicomponent nature of the investigated electrospun mat. Specifically, the extremely rapid initial uptake of the drug may be ascribed to the swelling of alginate nanofibers that are indeed able to entrap great quantities of water and various substances therein dissolved. Conversely, the slow and moderated drug uptake shown upon long impregnation times is most likely related to the occurrence of diffusive phenomena within the sample internal stratums.

More importantly, SAc release kinetics obtained in simulated physiological conditions (i.e., PBS at T = 37 °C) are reported in Figure 59-b. Despite some differences can be observed, a slow and controlled release of salicylic acid is achieved independently on the uploading concentration. In particular, the release appears to slow down after about 10h but continues even up to 48h of contact time. Additionally, the greater the amount of loaded drug, the lower is the cumulative release over time hence indicating its partial entrapment within the nanofibrous structure. As such, at longer times, which were not investigated in the present Thesis work, the progressive degradation of the alginate – based nanofibers may allow the release of an additional amount of the encapsulated drug to obtain long – term drug delivery systems. In general, the presented results demonstrate that the prepared alginate – polyurethane multilayer electrospun patch possesses marked drug delivery capability that can be achieved by simple impregnation procedures and easily tuned by selecting the proper working conditions.

Conclusions

In this Section, the possibility to prepare an advanced multilayer wound healing patch comprised of an external/superior electrospun stratum of polyurethane – based nanofibers and an internal/inferior electrospun stratum of alginate – based nanofibers embedding ZnO nanoparticles was explored. To this end, the electrospinning of polyurethanes starting from an aqueous suspension was first developed and optimized aiming to obtain a highly mechanically performing and protective nanofibrous layer with a simple, cost – effective, and green fabrication process. Specifically, WBPU – PEO formulations with a different component ratio were electrospun and the prepared mats were then subjected to a simple washing treatment in

water to remove the carrier polymer. Remarkably, beyond the nanofiber morphology, also the physical – chemical properties of the obtained mats were found to be strongly dependent on the component ratio in the starting formulations with increasing the polyurethane content corresponding to improve the yarn mechanical performances and hydrophobic capabilities. As such, once the best working conditions were identified, a polyurethane nanofibrous layer, which was supposed to act as a protective layer, was coupled with an alginate – ZnO layer, which was instead expected to act as a promoter of cell viability and tissue regeneration. Therefore, the obtained multilayer mat was subjected to a washing – crosslinking protocol able to remove the carrier/co – spinning agent from both layers at the same time ensuring proper stability to alginate – based nanofibers in physiological – like conditions. The resultant patch was proved to possess suitable mechanical features with good compatibility between the two distinct stratums, as well as a marked hydrophobicity for the WBPU – based layer and marked hydrophilicity for the alginate – based layer. Moreover, the multilayer mat showed promising drug delivery capabilities, which were above all demonstrated to be tuneable by simply modulating the drug uploading conditions. Generally speaking, by taking into account the results discussed in the previous Sections concerning the biocompatibility of alginate – based electrospun nanofibers, the explored multilayer alginate – polyurethane mat shows highly promising capabilities to be used as an advanced wound healing patch able to promote cell viability, to protect the site of interest from the external environment, and to avoid microbial contamination, as well as to deliver bioactive molecules with a tuneable kinetic.

4.2 Chitosan – Based Electrospun Mats

Among the great variety of naturally occurring polymers that can be electrospun, chitosan is currently assuming a major role in substituting the commonly employed synthetic polymers due to its unique properties. Chitosan is a cationic linear polysaccharide consisting in β-(1-4) linked D-glucose units and it is mainly derived from the partial deacetylation of chitin, the second most abundant polymer in nature after cellulose. As a matter of fact, the existence of amine groups on chitosan chains enables distinctive biological functions such as biocompatibility, biodegradability, bioactivity, antibacterial capabilities, non – toxicity, and good adsorption properties that make such polysaccharide extremely promising for biomedical and pharmaceutical purposes. To this end, it is not surprising that chitosan – based electrospun materials are gaining a great deal of interest to be used as wound healing patches owing to their unique structure able to promote cell adhesion and proliferation, at the same making them capable to rapidly adsorb wound exudates and to allow gas exchange. However, despite these advantages, the efficient electrospinning of chitosan, as well as of other naturally derived polymers, still represents a challenge and some experimental attentions (i.e., the addition of synthetic co – spinning agents and surfactants) are indeed required. Additionally, besides the low water solubility of the raw material, chitosan – based nanofibers need to be subjected to coagulation and/or crosslinking treatments to increase their stability and integrity in physiological – like conditions. Nevertheless, the commonly employed approaches rely on the use of hazardous solvents and/or chemicals that may lead to cytotoxicity issues and reduce the applicability of chitosan – containing biomedical products.

4.2.1 Optimization of Chitosan Electrospinning

This Section is substantially published at:

- *Dodero, A.; Brunengo, E.; Alloisio, M.; Sionkowska, A.; Vicini, S.; Castellano, M. Chitosan-Based Electrospun Membranes: Effects of Solution Viscosity, Coagulant and Crosslinker. Carbohydr. Polym. 2020, 235, 115976.*

Chitosan polysaccharide employed in this Thesis work was provided by Prof. Alina Sionkowska of the Department of Chemistry of Biomaterials and Cosmetics of Nicolaus Copernicus University in Toruń.

In this Section, chitosan – based electrospun mats were prepared by using a slightly acidic solvent aiming to develop highly biocompatible wound healing patches with a potentially scalable fabrication procedure. Specifically, chitosan (CS) with low molecular weight and a high degree of deacetylation DD = 78% was employed along with PEO ($\overline{M}_v$ = 900 kg/mol) as co – spinning synthetic polymer. At first, the effect of mixture viscosity on the electrospinning process and related nanofibers morphology was deeply investigated to define the best working conditions. Subsequently, different coagulation and crosslinking approaches, which were proved to be capable of increasing the mat stability in aqueous environments avoiding the loss of the nanofibrous structure at the same time removing the co – spinning agent, were explored. To this end, phosphate ions were especially employed as green and biocompatible chemicals able to induce the physical crosslinking of chitosan chains without occurring in both biocompatibility issues and significant environmental burden.

CS – PEO mixtures with a polymer concentration ranging from 5 wt% to 7 wt% were prepared by dissolving a proper amount of polymer powder in a 5 v/v% acetic acid aqueous solution keeping the component ratio 1 to 1. Triton^{TM} X-100 was always added at 1 wt% concentration to increase the formulation processability.

Steady – state viscosity measurements were carried out on the prepared mixtures as described in Section 3.1 with the related flow curves shown in Figure 60.

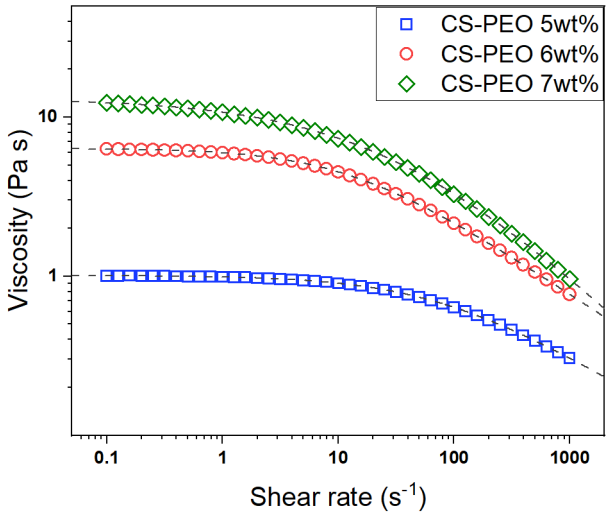

Figure 60. Flow curves of the investigated CS – PEO mixtures at different concentrations measured at T = 20 °C. Dashed lines represent the fitting of the experimental data with the Carreau – Yasuda model.

All the tested samples are characterized by the typical shear – thinning behaviour of polymer solutions consisting of the decrease of the viscosity as the shear rate increases due to the progressive orientation and disentangle of the chains. Remarkably, despite the Newtonian region is always observed, the critical shear rate at which the viscosity reduction starts to occur moves progressively at lower shear rate values as the polymer concentration is increased, in agreement with the formation of a thicker chain network. Additionally, a marked increment in the formulation zero – shear viscosity can be clearly depicted by comparing the three tested samples, as summarized in Table 11.

Table 11. Zero – shear viscosity values calculated for chitosan – based formulation at different polymer concentrations via the Carreau – Yasuda model.

Sample	η_0 (Pa·s)
CS – PEO 5 wt%	1.0
CS – PEO 6 wt%	6.4
CS – PEO 7 wt%	13.1

Here, the consistency of the experimental data with the applied theoretical model (i.e., Carreau – Yasuda) proves its applicability to the CS – based formulations and demonstrates their good homogeneity, which is above all a fundamental requirement for the electrospinning technique. It is particularly noteworthy that the amount of acetic acid used in the present Thesis work and required to obtain formulations with a good spinnability is considerably lower compared to most of the works reported in the literature (glacial acetic acid or concentration above 80% v/v),[390,391] thereby representing a great advantage reducing both environmental and

biocompatibility issues. As a matter of fact, to date, only a few studies have been carried out using low concentrated acid solutions to electrospun chitosan and they exclusively deal with the optimization of the electrospinning itself in terms of fiber morphology,[392] without taking into account any following treatment of the obtained materials.

Generally speaking, as already discussed in the previous Sections, solution viscosity is one of the main factors affecting electrospinning technique with too low viscous solutions usually leading to intermittent beads in the nanofiber structure, whereas a too high viscosity reduces the system processability.[393,394] For alginate – based mixtures, a zero – shear viscosity around 10 Pa·s was found to be the optimum to obtain mats characterized by a uniform nanofibrous structure with high porosity. Nevertheless, despite the chitosan – based formulation with the highest polymer concentration (i.e., 7% wt) seemed to be the most promising from a rheological point of view (i.e., η_0 value of 13.1 Pa·s), all the prepared solutions were electrospun to better evaluate the viscosity effect on the fiber morphology. To this purpose, a dry – collector electrospinning setup was employed by using a spinneret – collector distance of 20 cm, a flow rate of 0.15 mL/h, a 22G flat – tip needle, and an applied voltage of 17.5 kV as working parameters. The morphology of the so obtained chitosan – based mats is shown in Figure 61. In any case, consistent and manageable meshes are obtained but present a significantly different structure. In particular, the sample obtained by CS – PEO 5% wt formulation (i.e., Figure 61-a and Figure 61-b) shows a high number of inhomogeneous beads with a diameter ranging from 500 nm up to 2 μm and connecting the nanofibers, which are instead characterized by an average dimension of 150 ± 30 nm. Such a result confirms that low viscosity CS – based formulations cannot lead to acceptable electrospun mats. Conversely, the other two samples are both characterized by a similar structure with homogenous and smooth nanofibers with an average diameter of 300 ± 30 nm. However, the CS – based mat obtained by using the 6 wt% formulation (i.e., Figure 61-c and Figure 61-d) presents a high number of defects, such as beads, collapsed structures, low fiber density regions, whereas the one obtained by using the most concentrated formulation (i.e., Figure 61-e and Figure 61-f) undoubtedly shows the best structure in terms of fiber homogeneity. In addition, such a mat is characterized by high porosity, thus hypothetically providing the ideal environment to foster cell viability and is consequently selected to be further processed and characterized.

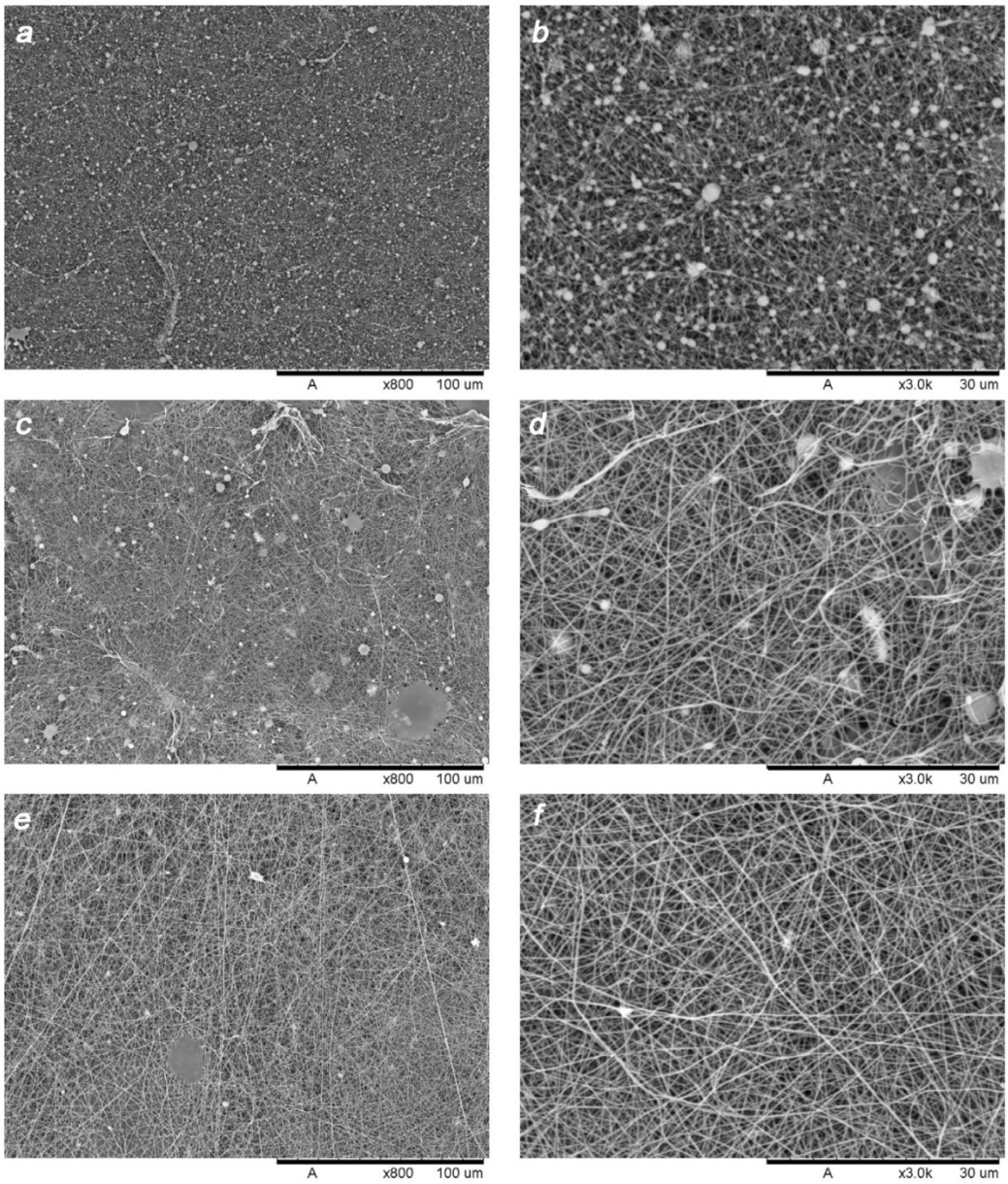

Figure 61. SEM micrographs of CS – based electrospun meshes obtained from (a – b) CS – PEO 5 wt% mixture, (c – d) CS – PEO 6 wt% mixture, and (e – f) CS – PEO 7 wt% mixture.

Despite chitosan raw materials are nearly insoluble in water, the presence of residual acetic acid in the nanofibers may significantly reduce their stability in aqueous environments. As such, a coagulation treatment consisting of a simple washing cycle with several basic media, which presented progressively higher pH values, was conducted on the explored mat to completely neutralize chitosan protonated amino groups and stabilize the polymer. To this end, the electrospun mat was soaked for 30 minutes in EtOH/NH_4OH/H_2O 7/2/1 (i.e., pH = 7.5), in NH_4OH (i.e., pH = 11.6), or in NaOH 0.5 mol/L (i.e., pH = 13.7), rapidly washed with deionized water and dried at T = 50 °C under vacuum. The effect of the coagulation media on

the mat morphology was then evaluated via SEM with the related micrographs reported in Figure 62.

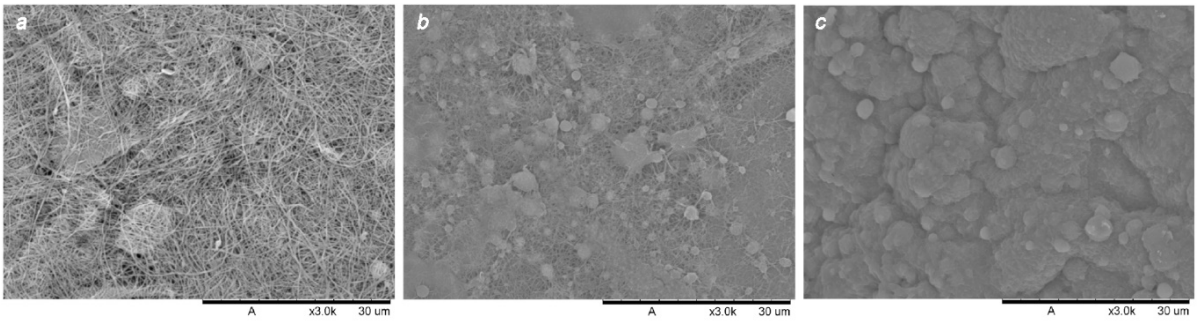

Figure 62. SEM micrographs of CS – based electrospun mesh subjected to coagulation in (a) EtOH/NH_4OH/H_2O 7/2/1, (b) NH_4OH, and (c) NaOH 0.5 mol/L.

Despite the investigated coagulation media are intensively reported in the literature to prepare stabilized CS – based products,[395–397] their effect on the nanofiber morphology appears to be strongly dissimilar likewise due to the different basic strength of the employed environments. EtOH/NH_4OH/H_2O mixture is indeed characterized by slight basicity with pH = 7.5, whereas NH_4OH and NaOH 0.5 mol/L solutions show considerably high pH values of 11.6 and 13.7, respectively. As evidenced in Figure 62-a, EtOH/NH_4OH/H_2O mixture seems to be able to neutralize the protonated amino groups of chitosan reducing its solubility and preserving at the same time the nanofiber arrangement. On the contrary, NH_4OH medium (Figure 62-b) induces the partial coalescence of the nanofibers leading to the establishment of an inhomogeneous beads – like structure with low porosity, whereas NaOH solution (Figure 62-c) appears to completely destroy the distinctive mat morphology with the consequent formation of a dense and compact structure characterized by the total absence of nanofibers. As such, it can be assumed that chitosan – based nanofibers are not able to withstand strongly basic environments and mixtures with a pH around 7.5/8 should be preferred in coagulation treatments.

Nevertheless, despite such a procedure considerably reduces the water solubility of chitosan – based materials, a crosslinking reaction is as well an important and critical requirement to obtain highly stable materials able to withstand contact with various liquids without losing their structure and properties in a short time period. In this sense, the most common approach is represented by the use of chemicals to induce the chitosan covalent crosslinking. However, the typically employed chemicals are highly toxic and may negatively influence the biological response of chitosan – based materials, thereby reducing their applicability in biomedical, pharmaceutical, food, and wastewater treatment applications. As a consequence, in this Thesis

work phosphate ions were chosen as alternative physical crosslinkers due to the absence of biocompatibility issues and to their ability to help bone regeneration.[398] The efficiency of such an approach was here compared to a more common covalent crosslinking method using ethylene glycol diglycidyl ether (EGDE) as the crosslinker. It should be noted that EGDE was specifically selected due to its lower cytotoxicity compared to other commonly employed chemicals such as glutaraldehyde and epichlorohydrin. Regarding the crosslinking procedure, the coagulated chitosan – based mat was immersed for 3h in a 10 w/v% sodium phosphate dibasic (Na_2HPO_4) aqueous solution at room temperature (i.e., physical crosslinking) or in a 2.5 v/v% EGDE aqueous solution at T = 60 °C (i.e., chemical crosslinking), washed several times with deionized water and dried at T = 50 °C under vacuum before being stored in desiccator. FESEM micrographs of the crosslinked chitosan – based meshes are reported in Figure 63 along with the related fiber diameter distributions.

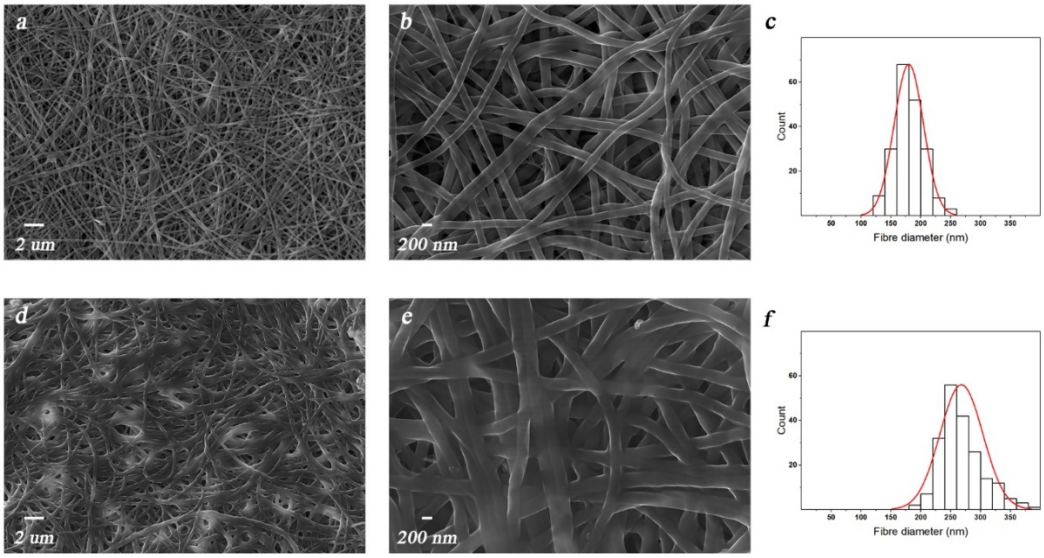

Figure 63. FESEM micrographs of chitosan – based mats after (a – b) the physical or (d – e) chemical crosslinking treatment. Fiber diameter distribution for (c) the physically crosslinked and (f) chemically crosslinked chitosan – based nanofibers.

For what concerns the physical crosslinking approach, sodium phosphate dibasic dissociates in water freeing HPO_4^{2-} anions, as well as Na^+ cations, which can bind the positive charges present on chitosan backbone creating physical bridges between the polymer chains via electrostatic interactions, thus stabilizing chitosan and improving its performances. Conversely, regarding the chemical crosslinking approach, the process likewise occurs via the reaction between chitosan amino groups and EGDE epoxy groups thus implying the formation of covalent bonds between the polymer chains, with the presence of residual crosslinker within the mat that may

negatively affect its biocompatibility. Schematics of the two crosslinking mechanisms are reported in Figure 64.

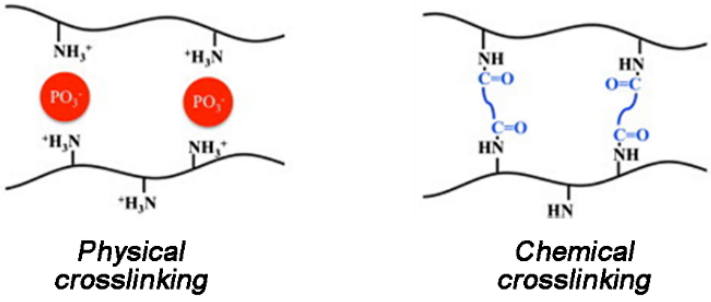

Figure 64. Schematics of chitosan physical and chemical crosslinking mechanism.

Despite a well – defined and homogenous nanostructure is obtained independently on the used crosslinking approach, significant morphological differences can be observed between the two prepared samples. As a matter of fact, physically crosslinked mat is characterized by thinner (i.e., an average diameter of 190 nm) and smoother nanofibers that completely maintain their individuality, therefore leading to the formation of a high number of interconnected pores. On the contrary, the chemical crosslinking treatment promotes the partial coalescence of the nanofibers, which in turn leads to the establishment of a much denser nanostructure presenting an average lower porosity. Such findings are to some extent unexpected but may be explained by considering the reticulation type mechanism and kinetic. Chemical crosslinking occurs via the formation of strong, stable, and not reversible covalent bonds between the polymer chains, whereas physical reticulation is based on the existence of weak and reversible links. However, such temporary crosslinking points require a much shorter time to be formed with respect to the covalent bonds, as they are immediately created when chitosan gets in contact with phosphate ions. Conversely, the chemical reaction occurring between chitosan amino groups and EGDE epoxy groups most likely necessitates a certain amount of time to happen, during which the nanofibers tend to swell thereby increasing their size (i.e., an average diameter of 270 nm) and partially collapsing and/or coalescing with each other. In this regard, it should be noted that both crosslinking approaches lead to smaller nanofibers with respect to the as – prepared electrospun mat (i.e., an average diameter of 300 nm). Such an outcome is indeed related to the elimination of the co – spinning agent (i.e., PEO) occurring during the crosslinking procedure owing to its great water solubility. In any case, both the prepared chitosan – based mats are characterized by a microstructure strongly similar to that of the

human extracellular matrix, hence being promising for the development of wound healing patches.

To verify the sample composition and PEO removal, FTIR and TGA measurements were carried out on the explored electrospun mats, as well as on the polymer powders, as described in Section 3.6 and Section 3.3, respectively. Figure 65 reports the measured FTIR spectra.

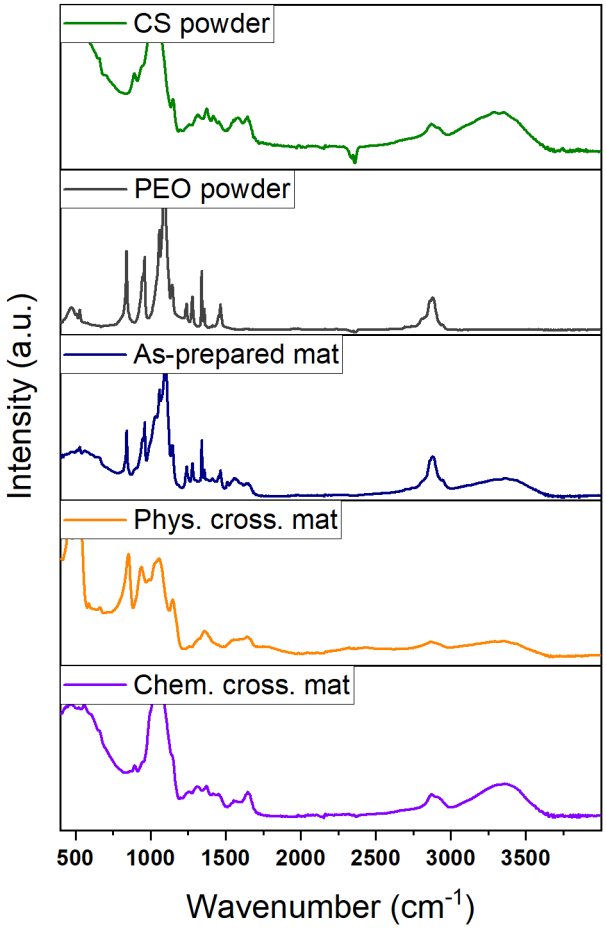

Figure 65. FTIR spectra of CS powder (i.e., green line), PEO powder (i.e., grey line), CS – based as – prepared mat (i.e., dark blue line), CS – based physically crosslinked mat (i.e., orange line), and CS – based chemically crosslinked mat (i.e., violet line).

The main adsorption bands in CS powder spectrum (i.e., green line) are assigned according to the literature.[399–401] The broad adsorption band around 3400 cm^{-1} can be ascribed to the presence of residual humidity, whereas the signals at 2920 cm^{-1} and 2875 cm^{-1} correspond to the asymmetric and symmetric stretching vibrations (ν_s) of the -CH groups, respectively. ν_a(C=O) of the amide (I) groups are located at 1645 cm^{-1}, whereas the correspondent symmetric stretching (ν_s) are individuated at 1575 cm^{-1}, as well as for the bending mode of $-NH_2$ groups. The band at 1375 cm^{-1} is due to the symmetric bending (δ_s) of $-CH_3$ groups and the one at 1313 cm^{-1} corresponds to the bending mode of -CH in the pyranose rings. Finally, ν_s(C-O-C) are

found at 1125 cm^{-1}. PEO powder spectrum (i.e., grey line) was characterized by the presence of four main adsorption bands as already described in Section 4.1.2. Briefly, the one at 2875 cm^{-1} is due to ν of the -CH groups, the one at 1095 cm^{-1} to the ν of C-O-C groups, the one at 960 cm^{-1} to ν of C-O groups, and the last at 840 cm^{-1} corresponds to the bending of C-O-C groups.[402,403] As expected, the as – prepared mat (i.e., dark blue line) presents the characteristic adsorption bands of both polymers with a slight shift of some of the signals due to the establishment of hydrogen interactions between the components. On the contrary, the crosslinked mats (i.e., orange and violet lines) do not show all the typical signals observed for PEO powder independently on the used crosslinking approach, hence suggesting its removal from the samples. More in detail, phosphate – crosslinked sample (i.e., orange line) presents an adsorption spectrum very similar to that of CS powder even if some shifts of the wavenumbers can be observed due to the established ionic interactions between chitosan and the phosphate ions. For what concerns the chemically crosslinked sample (i.e., violet line), it is characterized by the reduction or even the absence of the some of the bands assigned to the amine groups of chitosan, which indeed after the crosslinking step interact with the epoxy groups of EGDE.[404]

TGA and DTG curves of the explored samples are displayed in Figure 66. Chitosan powder (i.e., green line) is characterized by two well – defined degradation steps related to the vaporization of humidity (T < 120 °C) and the carbonization of the organic part (T ~ 300 °C), with the residual material slowly decomposing at a higher temperature. Conversely, PEO powder (i.e., grey line) shows a single and complete degradation step at T ~ 400 °C. The as – prepared mat (i.e., dark blue line) presents all three steps. However, chitosan seems to thermally decompose at a slightly lower temperature (T ~ 280 °C) with respect to the polymer in powder form most likely due to the partial degradation of chitosan caused by the used acid environment.[405,406] Interestingly, PEO degrades at a temperature slightly higher (T ~ 410 °C) than that of its powder, which may indicate the establishment of hydrogen interactions between the two polymers with a consequent increased thermal stability. The crosslinked samples (i.e., orange and violet lines) show similar behaviour between each other, but some differences can be detected. First of all, the degradation step of PEO cannot be clearly observed in either of them, further suggesting its elimination from the mats independently on the crosslinking approach, as already shown by FTIR results. Additionally, the thermal degradation of chitosan seems to occur at a different temperature depending on the used crosslinking approach. Specifically, the physically crosslinked mat (i.e., orange line) shows the degradation at T ~ 280

°C, whereas the chemically crosslinked sample (i.e., violet line) presents such phenomenon at a slightly higher temperature of around 300 °C. Such differences can be explained considering the nature of the two crosslinking approaches, with the chemical one able to create covalent bridges between the polymer chains thereby increasing the thermal stability of the polysaccharide.

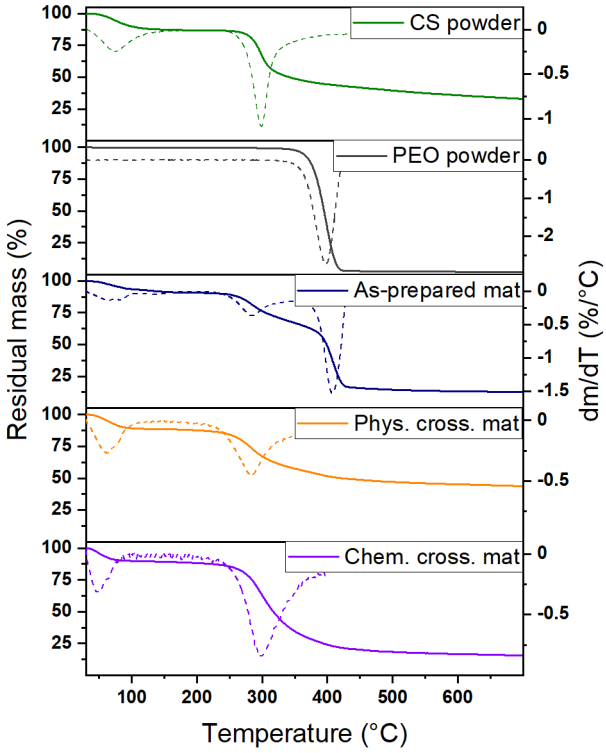

Figure 66. TGA and DTG profiles of CS powder (i.e., green line), PEO powder (i.e., grey line), CS – based as – prepared mat (i.e., dark blue line), CS – based physically crosslinked mat (i.e., orange line), and CS – based chemically crosslinked mat (i.e., violet line).

Combining the results obtained via FTIR and TGA investigation, it can be safely assumed that both the physical and the chemical crosslinking procedures are able to effectively reticulate chitosan allowing at the same time the complete elimination of poly(ethylene oxide) from the prepared mats. As a matter of fact, despite such a co – spinning agent is extremely helpful to increase chitosan – based solution spinnability mostly due to the ability to establish a great number of entanglements in solution, its poor biological response and high – water solubility are unwanted properties for biomedical purpose.

Conclusions

In this Section, chitosan – based patches were successfully prepared via electrospinning technique using an unusually low concentrated acetic acid solution (i.e., 5% v/v) as solvent and

poly(ethylene oxide) as co – spinning agent. Specifically, the homogeneity of the nanofibers and the global structure of the mats was found to improve as the polymer concentration (i.e., solution viscosity) increased, most likely due to the higher number of entanglements between the chains and their ability to help the solution spinnability. Remarkably, together with a coagulation procedure able to neutralize chitosan protonated amino groups able to rede the nanofiber tendency to dissolve in aqueous environments, the prepared mats were successfully treated by means of a physical or a chemical reticulation procedure. Despite both approaches were found able to induce chitosan crosslinking, the physical one, which consisted in the use of phosphate ions, led to electrospun mats able to completely maintain their peculiar morphology (i.e., thin, homogeneous nanofibers with a diameter of 190 nm and a high porosity) without the use of potentially toxic chemicals. Additionally, thermogravimetric analysis and Fourier – transform infrared spectroscopy proved the complete elimination of the co – spinning agent from the prepared mat, which represents an added benefit thinking about its use as biocompatible and bio responsive products. Consequently, the explored ionically crosslinked chitosan – based mat, owing to its structure and composition, represents a promising material to be used for the development of wound healing patches and drug delivery systems virtually without showing any cytotoxicity issue.

4.2.2 Biological, Physical – Chemical, and Uptake - Release Properties of Chitosan Mats

This Section is substantially published at:

- *Dodero, A.; Scarfì, S.; Mirata, S.; Sionkowska, A.; Vicini, S.; Alloisio, M.; Castellano, M. Effect of Crosslinking Type on the Physical-Chemical Properties and Biocompatibility of Chitosan-Based Electrospun Membranes. Polymers 2021, Vol. 13, Page 831, 13(5), 831.*

Chitosan polysaccharide employed in this Thesis work was provided by Prof. Alina Sionkowska of the Department of Chemistry of Biomaterials and Cosmetics of Nicolaus Copernicus University in Toruń.
The biological tests reported in this Section were carried out in collaboration with Prof. Sonia Scarfì of the Department of Earth, Environment and Life Sciences of the University of Genoa.

In the previous Section, the electrospinning process of chitosan – based formulations has been optimized with particular attention in the development of a simple, cheap, and non – toxic crosslinking approach aiming to obtain nanofibers with high stability in physiological – like conditions and marked biocompatibility. Since the so – obtained mats were supposed to be employed as wound healing patches, their complete physical – chemical and biological characterization is discussed in the following, along with their uptake – release features related to the possibility of preparing drug delivery systems. As a matter of fact, as already pointed out previously in this Thesis work, mechanical properties play a fundamental role in most biomedical devices where the presence of applied stresses and the existence of interfaces with native tissues are not negligible. Specifically, wound healing patches should display features similar to those of human tissues, at the same time providing integrity and stability to offer a sufficient protection action towards the external environment.[345,407,408] In this regard, electrospun nanofibers present a unique mechanical behaviour, which is related to their nanofibrous structure and can be easily modulated by changing the nanofiber size and spatial organization.[346,409]

Stress – deformation curves were obtained for both the physically and chemically crosslinked mats via uniaxial tensile test, as described in Section 3.5, and are reported in Figure 67-a. Mechanical properties values (i.e., Young modulus Y, elongation at break ε_b, and tensile strength σ_b) are summarized in Figure 67-b. Remarkably, the physically crosslinked electrospun mat presents superior mechanical performances with respect to the chemically crosslinked one. Specifically, the Young modulus and the tensile strength are almost twice

those of the EGDE – crosslinked mat, whereas a slighter difference is noticed for the elongation at break.

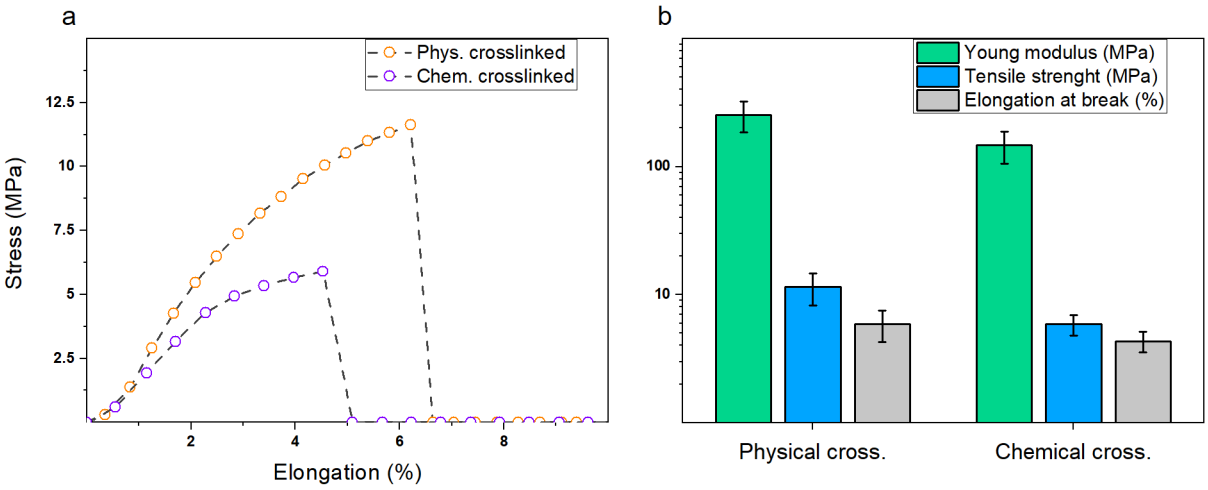

Figure 67. (a) Stress – deformation curves obtained from uniaxial tensile tests for physically (i.e., orange circles) and chemically crosslinked (i.e., violet circles) electrospun mats. (b) Summary of the calculated mechanical properties (i.e., Young modulus, elongation at break, and tensile strenght).

Rather than being directly related to the mechanism involved in chitosan reticulation, the observed dissimilarities are most likely ascribable to the mat morphologies. Indeed, the greater nanofiber homogeneity achieved via physical crosslinking leads to the development of a much more ordered three – dimensional macroscopic structure able to provide superior mechanical behaviour. Conversely, the coalescence of the nanofibers occurring during the chemical crosslinking induces the establishment of a defect – rich network being easily subjected to mechanical failure and characterized by an overall inferior response.[410,411]

Another key factor concerning wound healing patches is represented by their water – related behaviour.[412,413] Indeed, such systems must be able to adsorb a great quantity of exudate to keep the tissue dry (i.e., having high hydrophilicity) and allow a sufficient gas and vapour permeability (i.e., having a high porosity), at the same time being able to be stored over a long time period (i.e., having a low moisture content). With these premises, it is not surprising that electrospun meshes represent a promising material for the preparation of wound healing patches owing to their high surface area and porosity, which are able to meet the above – mentioned requirements. However, the type of polymer, the fiber spatial organization, as well as the post – production treatments (i.e., crosslinking, sterilization procedures, etc.) may influence the mat water – related behaviour and should be consequently considered. The water contact angle, the water vapour permeability, and the moisture content values of both

physically and chemically crosslinked chitosan – based mats were explored as described in Section 3.8 and are listed in Table 12.

Table 12. Summary of the water – related properties (i.e., water contact angle WCA, water vapour permeability WVP, and moisture content MC) evaluated for chitosan – based mats.

Crosslinking type	WCA (°)	WVP (g/m·Pa·s)	MC (%)
Physical	56 ± 5	$9.3 \cdot 10^{-12}$	11 ± 2
Chemical	71 ± 2	$2.1 \cdot 10^{-12}$	10 ± 1

Firstly, a marked discrepancy between the hydrophilicity of the samples can be observed, with the physically crosslinked mat showing a much lower WCA with respect to the chemically crosslinked one. Such a result is likewise related to both the crosslinking mechanism and nanofiber morphology. Chitosan, owing to the presence of residual acetyl groups, is characterized by poor water solubility that is even lowered after its crosslinking reaction. Therefore, the stronger the links between the macromolecular chains (i.e., chemical crosslinking), the smaller is the capability of chitosan to interact with water (i.e., lower hydrophilicity). Additionally, the thinner and defect – free nanofibers achieved via physical crosslinking present a higher surface area hence enriching the mat with a higher porosity, which in turn leads to capillarity effects that can promote the water – material compatibility.[389] Further evidence of such phenomena can be deduced from the water vapour permeability value, which is nearly an order of magnitude lower for the chemically crosslinked mat. As such, the presence of a great number of interconnected pores and the marked hydrophilicity of the mat obtained via physical crosslinking seem to provide a much higher WVP value. In any case, both samples present low moisture contents, thus being capable to be potentially stored over quite long time periods without occurring in degradation issues and/or physical – chemical modifications.

Based on the discussed results, physically crosslinked chitosan – based mat seems to be much more promising compared to the chemically crosslinked one for the development of performing wound healing patches to foster cell viability in different types of wounds (e.g., surgical, traumatic, chronic, etc.). Nevertheless, despite chitosan is a well – known biocompatible material,[414] different procedures performed in order to obtain 3D scaffolds may affect the propensity of cells to adhere or grow on top of them due to the chemical modifications of the original polysaccharide structure.[415,416] As such, in the present Thesis work, the two differently crosslinked chitosan mats were tested for their biocompatibility by both measuring cell adhesion and possible toxicity due to the release of chemicals that are entrapped within the

meshes and deriving from the reticulation procedures with potential negative effects on cell survival. Specifically, two skin cell lines, L929 fibroblasts and HaCaT keratinocytes, and an osteoblastic cell line, Saos – 2, were employed to assess the above – mentioned parameters. At first, cell adhesion was measured by MTT test after 16h of incubation onto the mats with the results reported in Figure 68.

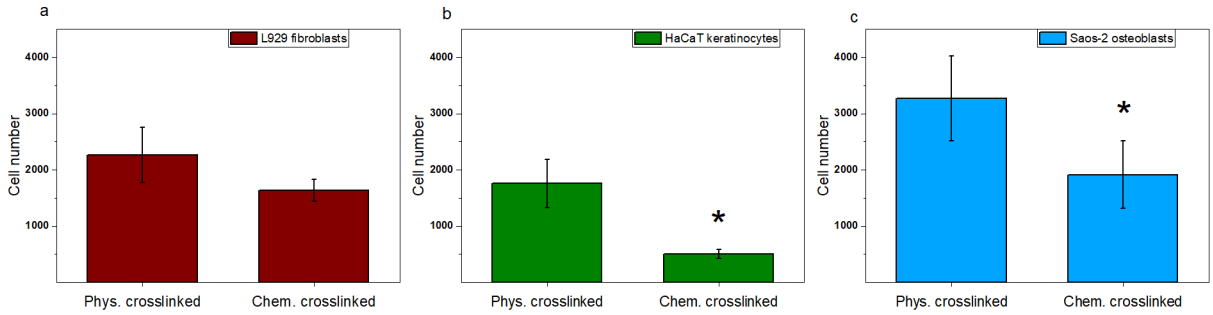

Figure 68. (a) L929 cell adhesion, (b) HaCaT cell adhesion, and (c) Saos – 2 cell adhesion to the physically and chemically crosslinked mats. Results are the mean ± S.D. of 3 experiments performed in triplicate. Asterisk indicates significance in the T – test ($p < 0.05$).

All cell types show a clear preference for the physically crosslinked sample with respect to the chemical one. More in detail, the osteoblast cell line, Saos – 2 (Figure 68-c), presents the highest number of attached cells to the physically crosslinked mat (i.e., 32% respect to the number of seeded cells 16h before) and this number is significantly higher than the 19% measured for the chemically crosslinked mat ($p < 0.05$). L929 fibroblasts (Figure 68-a) show 22% of adhesion to the physically crosslinked mesh and, although not significant, this percentage is higher than the 16% adhesion measured on the chemically crosslinked sample. Finally, HaCaT keratinocytes (Figure 68-b) are characterized the lowest values of cell adhesion on the chitosan meshes, with 18% of cell adhesion obtained on the physically crosslinked mat and a very poor 5% of adhesion to the chemically crosslinked one ($p < 0.05$). This latter result could be related to the fact that these cells preferentially adhere to fibrin or collagen substrates of protein origin. Such molecules, in fact, mimic more closely the basal membrane to which keratinocytes naturally adhere at the interface between epidermis and dermis,[325] thus it is expected a lower performance onto non – protein substrates such as chitosan and other polysaccharides. Overall, these data indicate that the bone cell line has a slightly superior preference than the skin cell lines for the chitosan patches, and that the physically crosslinked mat is always preferred by all cell types with respect to the chemical one.

The second important parameter evaluated was then the cytotoxicity of chemicals eventually leaked from the meshes in the cell culture media, which may affect both adhesion and

proliferation of cells on the patches. Therefore, the three cell lines were incubated for 24h in the presence or absence of the conditioned media obtained after a 24h soaking of the two different chitosan mats and cell viability was measured by MTT test. The obtained results are displayed in Figure 69.

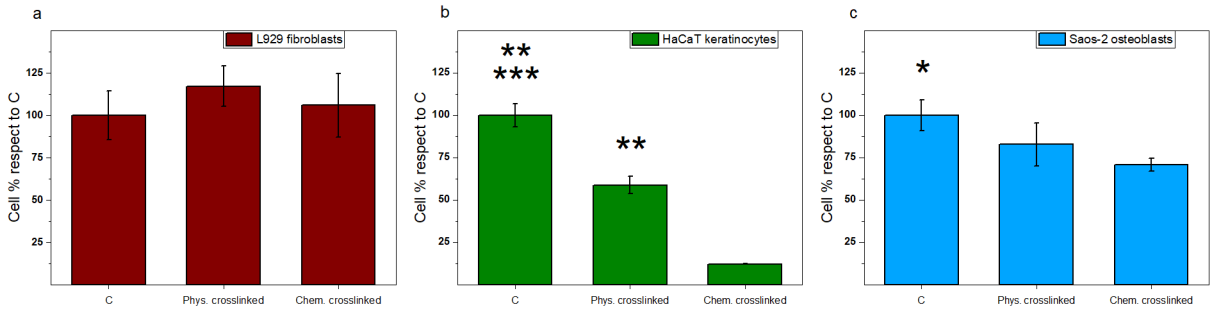

Figure 69. Cell toxicity, measured by MTT test, of conditioned culture media obtained by soaking the meshes for 24h in sterile conditions at 37°C and then adding the media diluted 1:1 to (a) L929 murine fibroblasts, (b) HaCaT human keratinocytes, or (c) Saos – 2 human osteoblasts (c) for further 24h. Results are expressed as percentages respect to control, untreated cells and are the mean ± S.D. of 3 experiments performed in quadruplicate. Asterisks indicate significance in T – test (panel b: ** $p < 0.0005$ C vs Phys – cross and Phys – cross vs Chem – cross, *** $p < 0.0001$ C vs Chem – cross, panel c: * $p < 0.005$ C vs Chem – cross).

In this test, a different degree of toxicity in the various cell lines is observed in the presence of the conditioned media from the physically and chemically crosslinked mats compared to control untreated cells. In particular, two cell lines out of three, namely HaCaT keratinocytes and Saos – 2 osteoblasts, are significantly affected by the conditioned media from the 24h soaking of the chemically crosslinked mesh, with a 88% and 30% cell mortality (Figure 69-b and Figure 69-c, respectively) compared to control cells ($p < 0.0001$ and $p < 0.005$, respectively). Conversely, only one cell line, namely the HaCaT keratinocytes, is significantly affected by the conditioned medium from the soaking of the physically crosslinked mat, with a cell mortality of 42% (Figure 69-b) compared to control cells ($p < 0.0005$). In contrast to this, no toxicity is observed in L929 fibroblasts (Figure 69-a) either in the presence of the conditioned media from the physically or the chemically crosslinked mesh, demonstrating to be the most resilient cell type. These data seem to indicate that the chemically crosslinked mat releases some chemicals in the culture media towards which cells show a different, and sometimes opposite, sensitivity, with fibroblasts growing completely unaffected, osteoblasts slightly affected, and keratinocytes that seem not able to survive in the presence of the released chemical (Figure 69-b). Since the chemically crosslinked patch uses EGDE to reticulate chitosan, residues of this toxic molecule may leak from the scaffolds causing cell death. This toxicity could also be one of the reasons why keratinocytes show the lowest adhesion capacity

with respect to the other cell types (Figure 68-b), other than being the chitosan mats a non – protein substrate. Conversely, the conditioned media from the physically crosslinked meshes shows only some toxicity on HaCaT keratinocytes (Figure 69-b), although anyway an 18% cell adhesion on these mats is measured (Figure 68-b), not far from the percentage measured for fibroblasts (i.e., 22% in Figure 68-a) which show no toxicity at all in the same conditions.

Overall, it can be safely concluded that the physically crosslinked mat is characterized by significantly better performances in terms of cell adhesion and low toxicity indicating this as the most suitable material to produce wound healing patches. In this sense, it should be noted that to date most of the commercially available wound healing patches have the unique role of promoting tissue regeneration by foster cell adhesion and proliferation.[345] As such, the development of wound dressing systems enriched with controlled drug delivery capabilities represents an interesting but to some extent poorly investigated research field.[345,417,418] Consequently, owing to its promising physical – chemical features and good biological response, the explored physically crosslinked chitosan – based mat as tested as DDS by its loading with methylene blue (Figure 33) and methyl orange (Figure 45) dyes, which were selected as positive and negative drug models, respectively. Firstly, the possibility to use a simple impregnation approach to upload the colorants within the mats was evaluated by using dye solutions at an increasing concentration as described in Section 3.7. Figure 70 reports the adsorption kinetics for MB and MO, respectively.

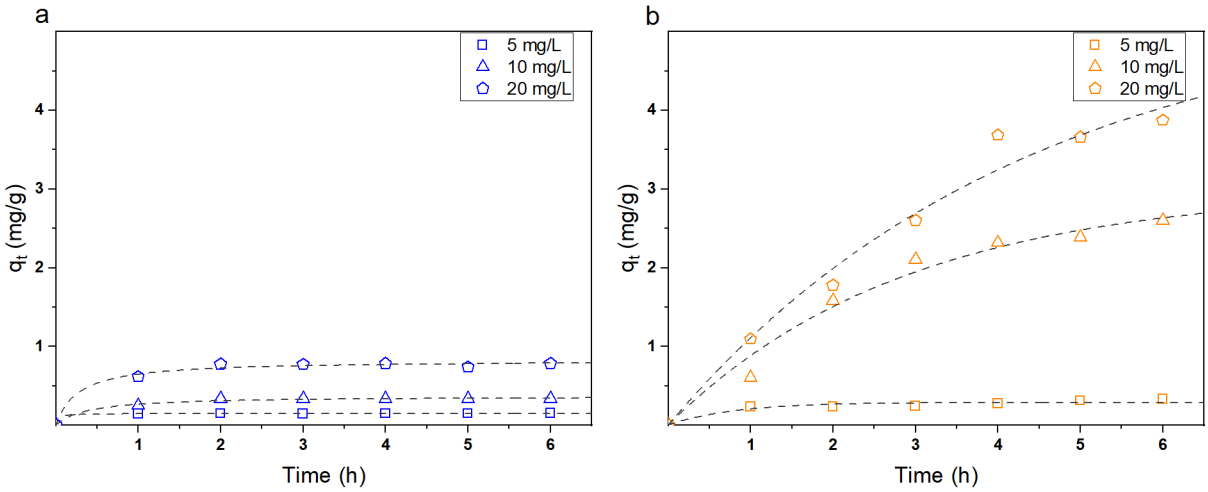

Figure 70. (a) and (b) Adsorption capacity of MB and MO on chitosan - based mats. Experimental data were fitted for MB and MO with a pseudo – second – order and with a pseudo – first – order kinetic model (dashed lines), respectively.

Independently on the colorant type, increasing both the solution concentration and contact time corresponds to increase the patch adsorption capacity. However, significant differences are

observed with respect to the investigated dye. MB is scarcely adsorbed by the mat with the process being almost arrested after only 2h for the explored concentration range. Conversely, MO is rapidly and much more efficiently entrapped by the electrospun mats with the phenomenon evolving even after 6h especially for the highest dye concentration. To better understand the kinetics of adsorption, pseudo – first – order (Equation 5) and pseudo – second – order (Equation 6) models were employed to fit the experimental data. Interestingly, it is possible to fit the adsorption phenomenon of MB only via the pseudo – second – order model, whereas the pseudo – first – order model better describes MO data. As previously observed for alginate – based electrospun meshes and deeply described in Section 4.1.2, these results suggest that a different adsorption mechanism occurs for MB and MO dyes, which is in agreement with their different charge. Specifically, being MB positively charged and considering the low q_t values, it can be supposed that strong repulsive interactions arise between chitosan chains and the colorant molecules. Therefore, the adsorption is most likely driven by diffusive phenomena but remains highly hindered due to the electrostatic repulsions. Conversely, owing to their opposite charge, chitosan and MO molecules can attractively interact thus enhancing the adsorption efficiency, as proved by the higher q_t values. Further confirmations of such phenomena were obtained by studying the isotherms of adsorption for both MB and MO dyes with the related results shown in Figure 71.

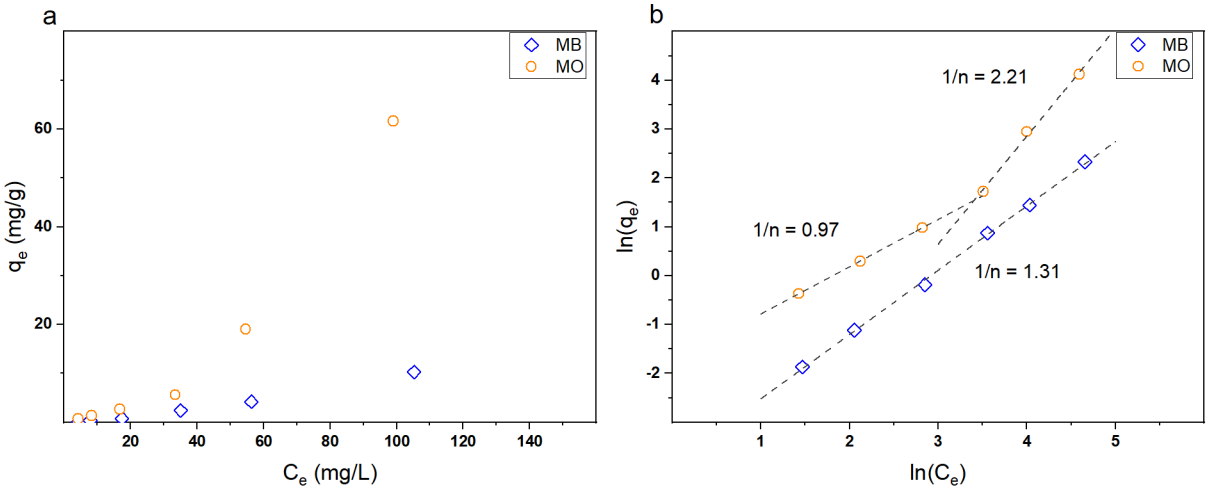

Figure 71. (a) Adsorption isotherm data of physically crosslinked chitosan mats and (b) their fitting with the linearized Freundlich model.

As clearly depicted, much higher adsorption efficiencies are obtained for MO, especially at high dye concentration, hence further confirming the greater affinity of the colorant with chitosan compared to MB. The experimental data were fitted with both Langmuir (Equation 8)

and Freundlich (Equation 9) models, with the first completely failing in describing the adsorption process whereas the data linear fitting according to Freundlich model is shown in Figure 71-b. Such a model relies on the assumption that the adsorption phenomenon occurs on a heterogeneous surface owing to the presence of numerous binding sites, which in turn leads to the formation of several adsorbate multilayers. Consequently, the greatest difference in the isotherm adsorption process is the presence of two distinct regions for MO dye, whereas one is observed for MB colorant. This finding is most likely ascribable to the involved adsorption mechanism. Specifically, MB dye is being entrapped within the mats only via a diffusion mechanism with the electrostatic repulsions reducing the process efficiency and a unique adsorption region is observed in the whole investigated concentration range. On the contrary, both attractive electrostatic interactions and diffuse phenomena are involved in the adsorption of MO with one being predominant over the other depending on the dye concentration. More information regarding the adsorption process can be derived from the slopes of Freundlich linear fitting corresponding to 1/n, which is a parameter indicative of the isotherm type and providing important insights on the intensity of the mechanism. 1/n values lower than 1 are commonly found in systems where the adsorption sites can be easily saturated (i.e., adsorption process is mainly driven by electrostatic interactions). Conversely, 1/n values higher than 1 are indicative of S – isotherm types and usually occur when polar molecules compete with water for the adsorption sites (i.e., the adsorption process is mainly driven by diffusive mechanisms). Therefore, the existence of these two distinct regions for MO is ascribable to the predominance of an electrostatic adsorption phenomenon at low dye concentration, whereas a diffusive adsorption process assumes a major role once the electrostatic binding sites are saturated (i.e., high dye concentration).

Beyond the possibility to load different drug molecules within the explored chitosan – based mat via a simple impregnation method was confirmed by the above – discussed results, much more interesting aspects arose by exploring the patch release capability (Section 3.7), which represents indeed a critical feature in the development of effective drug delivery systems. To this end, Figure 72 reports the dye cumulative release in simulated physiological conditions depending on the loading concentration. Noticeably, MB and MO dyes are characterized by different release kinetics comparably to what was previously observed in the present Thesis work for alginate – based nanofibers.

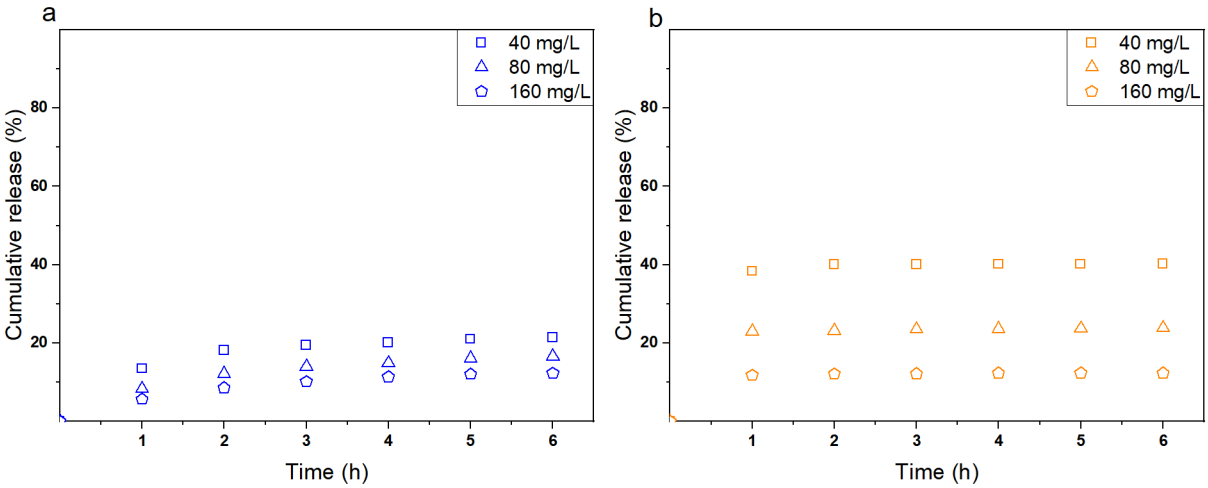

Figure 72. Cumulative release from chitosan mats in PBS at T = 37 °C after their loading in (a) MB or (b) MO batch solutions with different dye concentration (i.e., 40, 80, and 160 mg/L).

Specifically, MO is rapidly released from the loaded mat in the first hour, whereas MB presents a slow and much sustained release over a 6h time period. Such an outcome is likewise related to the different nature of the dyes and the related adsorption mechanism. Specifically, the negative ions in PBS may partially screen the positive charges of chitosan thereby promoting the almost immediate release of the electrostatically adsorbed dye, despite a significant amount of the diffusively adsorbed colorant is retained within the nanofibers. Conversely, since electrostatic attraction is not involved in the MB adsorption process, only a small fraction of the dye is released from the electrospun mat with the process occurring much slower with respect to MO. The achieved results represent a preliminary yet promising outcome in the development of simple, cheap, and efficient drug delivery systems comprised of chitosan – based nanofibers with modulable release kinetics. As a matter of fact, considering that negatively charged molecules are characterized by a higher affinity for the explored mat and positively charged ones show a better controlled release, depending on both the drug nature and loading concentration it could be indeed possible to obtain drug delivery systems able to provide a burst or a controlled release to satisfy the specific requirements.

Conclusions

In this Section, the effects of crosslinking type on the physical – chemical and biological properties of electrospun chitosan – based patches were assessed to evaluate their applicability as wound dressing products. Phosphate ions were specifically employed as physical crosslinkers to avoid toxicity issues, whereas ethylene glycol diglycidyl ether was selected as chemical crosslinkers and used as control. Beyond the fact that the physically crosslinked

chitosan – based mat presented a much more homogeneous and well – defined nanofibrous morphology, it also displayed superior mechanical properties with respect to the chemical crosslinked one, as well as more marked hydrophilicity and water vapour permeability. Above all, significant differences were depicted between the two investigated mats in terms of cell adhesion and cytotoxicity results. More in detail, the nanofibers treated with phosphate ions showed almost no toxicity towards the different tested cell lines along with the capability to strongly promote their adhesion and proliferation, especially for osteoblasts. On the contrary, the chemically crosslinked mat was proved to be to some extent toxic for keratinocyte and osteoblast cell lines, being able to marginally foster cell viability likewise due to the release of some residual chemicals. Additionally, the physically crosslinked mat was proved to possess promising tuneable drug delivery capabilities thereby being suitable for different routes of administration. In conclusion, besides further *in vitro* and *in vivo* experiments will be required, the proposed physically crosslinked chitosan – based mat represent a potential class of innovative, versatile, cheap, and highly efficient materials to be used as advanced wound healing patches with drug delivery properties.

4.3 Outcomes

In this Chapter the possibility to prepare polysaccharide – based electrospun meshes as potential wound healing patches with drug delivery capabilities was deeply explored. Nowadays, autologous, allogeneic, or xenogeneic grafting approaches are usually employed despite the existence of several drawbacks ranging from the low availability to the possibility of immunogenic reactions. As such, it is not surprising that the development of artificial systems able to induce tissue regeneration by promoting cell viability meanwhile providing protection towards the external environments represents an important research field. To this end, nanofibrous electrospun mats have been broadly demonstrated able to satisfy the above – mentioned requirements. Specifically, electrospun nanofibrous meshes constituted of polysaccharide materials represent a promising alternative to synthetic polymers owing to their superior biocompatibility, biodegradability, bioactive features, and non – toxicity, as well as low cost and limited environmental burden. As such, in the present Thesis work both alginate and chitosan – based electrospun mats were successfully developed by using a biocompatible co – spinning agent, which was however removed from the final products by a simple washing treatment in water. Additionally, the exploitation of a simple physical crosslinking approach, based on the capability of the used polysaccharides to electrostatically interact with different ions, allowed to effectively stabilize the nanofibers thereby improving their stability in physiological – like conditions. Remarkably, the obtained mats displayed morphological, mechanical, and water – related properties, and tuneable drug delivery features that make them extremely suitable for their use as wound healing patches. Above all, such systems were successfully proved able to promote the adhesion and the proliferation of different cell types, which may allow their employment for different wound sites such as skin, organs, and bones, without showing significant toxicity issues. In this sense, aiming to obtain even more performing and advanced products, the possibility to couple the polysaccharide – based electrospun layer with a protective stratum comprised of synthetic electrospun nanofibers was also explored. Such an approach led to multilayer nanofibrous patches capable of protecting the damaged tissue from the external environment owing to the external layer mechanical resistance and hydrophobicity, at the same time maintaining the capacity to promote the tissue reparation owing to the bioactive properties of the internal layer. The results presented and discussed in this Chapter undoubtfully prove the outstanding features of polysaccharide – based electrospun patches as biomedical and pharmaceutical products.

Chapter 5. Rheological Characterization of Sodium Alginate – Based Solutions

In the previous Chapter, alginate was proved to be an extremely promising material to be used for the preparation of wound healing patches with the capability to promote tissue regeneration. However, the great variability of the polysaccharide molecular structure represents an issue to its proficient use in a broad number of applications, especially where the system rheological properties play an instrumental role. In this sense, in the present Chapter, a deeply rheological characterization is carried out on various alginate samples in both salt – free and saline environments to correlate the molecular weight and composition of the polymer with its physical – chemical features.

5.1 Introduction

Sodium alginate is a naturally occurring polysaccharide composed of β-D-mannuronic acid (M units) and α-L- guluronic acid (G units) residues linked by a β-(1- 4) glycosidic bond as shown in Figure 12. SA is usually extracted from the cell walls of brown algae and it is nowadays widely employed in several fields, ranging from biomedical applications to the restoration of Cultural Heritage. One of the most interesting features of alginate is represented by the presence of negative charges along its backbone, which confer a polyelectrolyte nature to the polymer and strongly influence its solution rheological behaviour. Despite several rheological studies have been performed on alginate – based solutions over the past 50 years, its behaviour is not yet completely understood, which represents a not negligible limitation to the intensive use of such a promising material in many application fields (e.g., food and cosmetic products). This is mainly due to the fact that for polyelectrolytes, such as most of the polysaccharide materials, the classical approaches to polymer characterization (e.g., light scattering, viscosimetry, ultracentrifugation, etc.) can usually provide accurate information about solution properties, chain conformations, and thermodynamic interactions limitedly to very low concentrated systems where the macromolecules act as independent objects and a linear dependence of the solution viscosity with the concentration is observed.[419] In this regard, it is noteworthy to consider that polymer solutions present four different concentration regimes: (i) the dilute, the semi – dilute unentangled, the semi – dilute entangled, and the concentrated regime. At low concentration, corresponding to the dilute regime, single chains exist and do not interact with each other. When the polymer concentration is increased above the overlap concentration (i.e., c*) and the semi – dilute unentangled regime is reached, the chains start to overlap but entanglements do not occur yet. Further increasing the concentration above the entanglement concentration (i.e., c_e), the chains start to entangle with each other and are no longer isolated thereby creating a continuous polymer network, corresponding to the semi – dilute entangled regime, which eventually forms a highly dense structure once the concentrated regime is reached (i.e., c**). The main distinction between neutral polymers and polyelectrolytes in salt – free environments is represented by different scaling factors (i.e., α) characterizing the viscosity concentration dependence. Such an outcome is due to the fact that whereas neutral polymers show the typical random coil conformation, polyelectrolyte chains assume an extended rod – like conformation because of the electrostatic repulsions occurring between the backbone charges, which in turn considerably modify the solution properties. The greatest effect is a reduction of the scaling factors (i.e., the solution viscosity increases slower

with the polymer concentration) in both the semi – dilute regimes owing to the less important topological interactions between the polymer chains. Moreover, a much more extended semi – dilute unentangled regime is observed for polyelectrolytes compared to neutral polymers with the overlap concentration c* assuming extremely low values. In contrast, in the concentrated regime (i.e., c > c**) no significant differences are displayed for neutral polymers and polyelectrolytes since the high number of entanglements predominates upon the electrostatic repulsions. A schematic of polymer solution concentration regimes is reported in Figure 73.

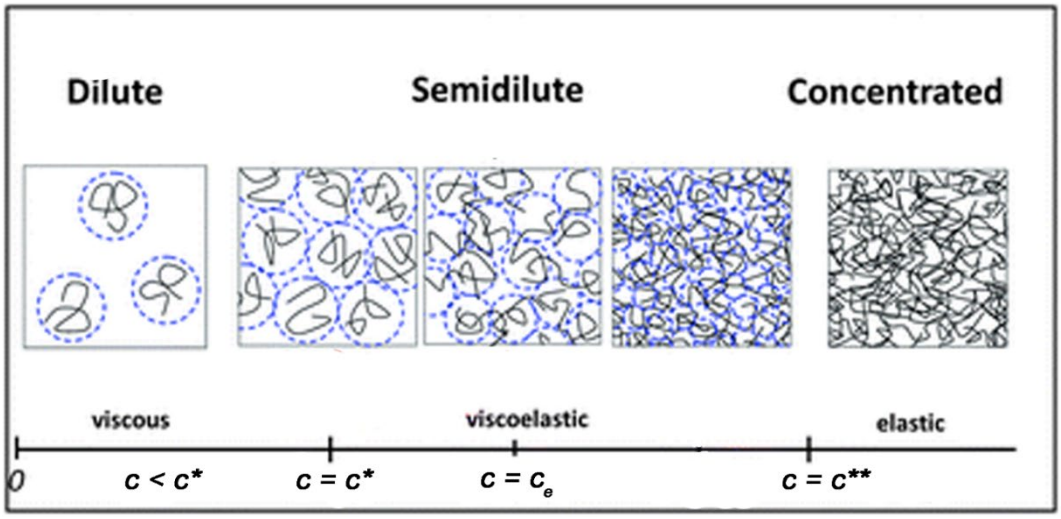

Figure 73. Schematic of polymer solution concentration regimes and chain behaviour.

5.2 Alginate Molecular Weight and Polyelectrolyte Effect Evaluation

This Section is substantially published at:

- *Dodero, A.; Vicini, S.; Alloisio, M.; Castellano, M. Sodium Alginate Solutions: Correlation between Rheological Properties and Spinnability. J. Mater. Sci. 2019, 54 (10), 8034–8046.*
- *Dodero, A.; Vicini, S.; Alloisio, M.; Castellano, M. Rheological Properties of Sodium Alginate Solutions in the Presence of Added Salt: An Application of Kulicke Equation. Rheol. Acta 2020, 59 (6).*
- *Dodero, A.; Donati, I.; Scarfì, S.; Mirata, S.; Alberti, S.; Lova, P.; Comoretto, D.; Alloisio, M.; Vicini, S.; Castellano, M. Effect of Sodium Alginate Molecular Structure on Electrospun Membrane Cell Adhesion. Mater. Sci. Eng. C 2021, 112067*

Some of the alginate samples employed in this Section were provided by Prof. Ivan Donati of the Department of Life Sciences of the University of Trieste.

In this Section, the molecular weight first and then the polyelectrolyte nature of various alginates samples were evaluated by means of rheological measurements. Specifically, alginates extracted from *Macrocystis pyrifera* with low viscosity (M.pyr LV, i.e., SA LV) and medium viscosity (M.pyr MV, i.e., SA MV_M), from *Laminaria hyperborea* (L.hyp), and from *Ascophyllum nodosum* (A.nod) were characterized. In this regard, one of the greatest issues regarding polyelectrolyte characterization is the accurate evaluation of the polymer average molecular weight $\overline{M}$, which is usually achieved via time and cost – consuming techniques such as size – exclusion chromatography (SEC) and matrix – assisted laser desorption/ionization (MALDI).[420] A faster and much easier alternative is instead represented by the Mark – Houwink equation, which correlating the viscosity average molecular mass $\overline{M}_v$ of the polymer with its intrinsic viscosity [η] by means of two parameters, k and *a*, as expressed in Equation 13:

Equation 13

$$[\eta] = k\overline{M}_v^a$$

It should be kept in mind that the proper evaluation of the polymer intrinsic viscosity represents a challenge for polyelectrolytes owing to the strongly repulsive electrostatic interactions that modify the hydrodynamic volumes assumed by chains. As a matter of fact, this issue can be to

some extent mitigated by adding an external salt to the polyelectrolyte – based solutions in a proper concentration. As the main consequence, the screening of the charges present on the polymer backbone allows the chains to take on the classic random coil conformation thereby to some extent reducing their behaviour to that of neutral polymers.

As such, steady – state viscosity measurements were carried out at T = 25 °C, as described in Section 3.1, on alginate solutions with a concentration ranging from 0.0005 g/mL up to 0.04 g/mL in 0.15 mol/L NaCl. Some of the obtained flow curves for each alginate sample are shown in Figure 74 as a way of example.

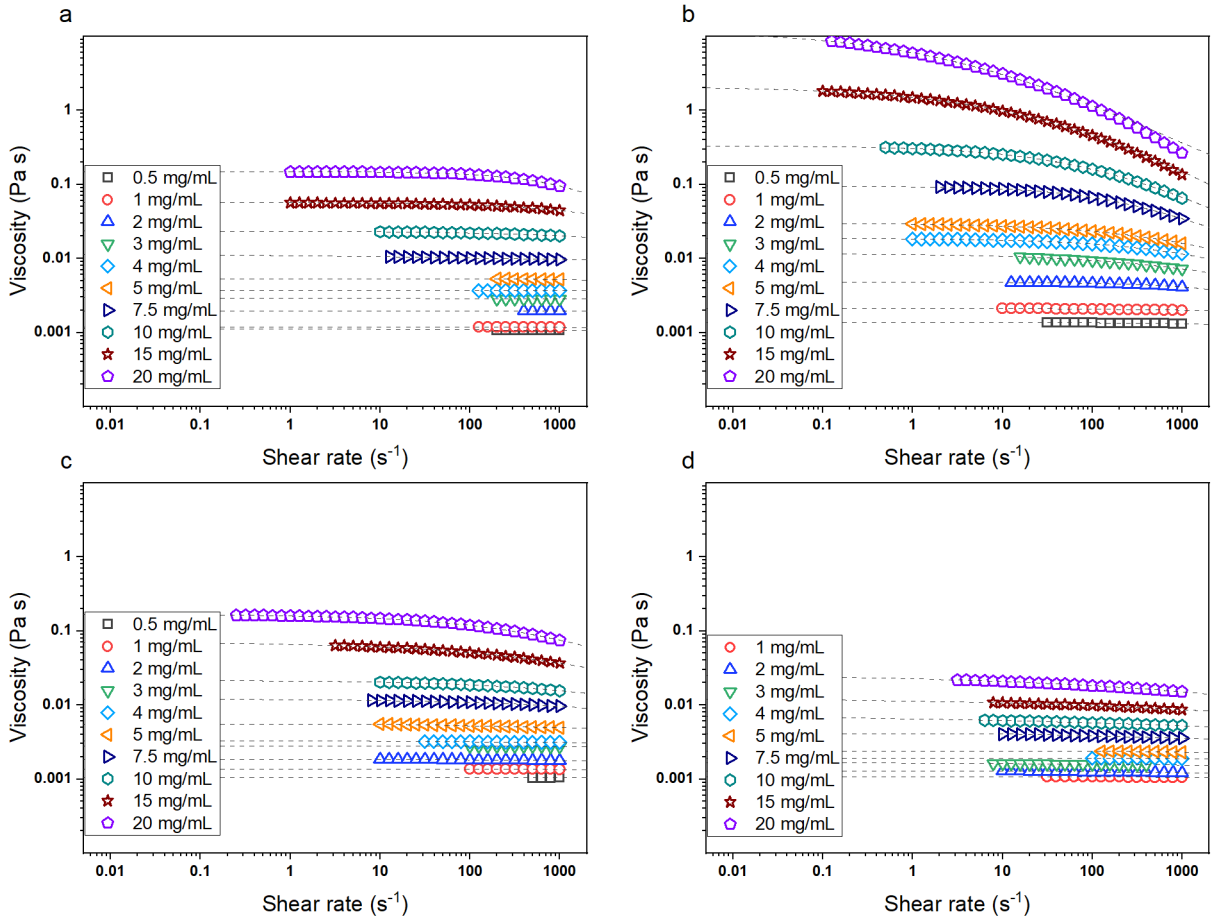

Figure 74. Flow behaviour at different polymer concentration for (a) M.pyr LV, (b) M.pyr MV, (c), L.hyp, and (d) A.nod alginate samples at T = 25 °C in o.15 mol/L NaCl. Dashed lines represent the fitting of the experimental data with Carreau – Yasuda model.

As clearly shown, in any case, a higher polymer concentration corresponds both to a higher solution viscosity and a more marked shear – thinning behaviour, i.e., a decrease of the viscosity as the shear rate increases. These results can be explained by the presence of entanglements, which increase with the polymer concentration and act as physical constraints hence significantly raising the solution viscosity.[421–423]

The much greater viscosity values observed for M.pyr MV seem to indicate this alginate as the one with the highest molecular weight, whereas no significant differences can be observed among the other three samples. To calculate $\bar{M}_v$ values, starting from the zero – shear viscosity values determined from the flow curves by means of the Carreau – Yasuda model, the intrinsic viscosity of each alginate sample was evaluated by three different approaches reported in the literature and deeply discussed in the following.

Huggins – Kraemer Method

Firstly, the reduced viscosity η_{red} and the inherent viscosity η_{inh} were calculated according to Equation 14 and Equation 15, respectively:

Equation 14

$$\eta_{red} = \frac{\eta_{sp}}{c}$$

Equation 15

$$\eta_{inh} = \frac{\ln\left(\frac{\eta_0}{\eta_s}\right)}{c}$$

where η_{sp} is the specific viscosity (i.e., $\eta_{sp} = \frac{\eta_0 - \eta_s}{\eta_s}$ with η_0 the zero – shear viscosity and η_s the solvent viscosity) and c is the polymer concentration. The calculated values were then plotted against c based on the models proposed by Huggins (Equation 16) and by Kraemer (Equation 17):

Equation 16

$$\eta_{red} = [\eta] + K_H[\eta]^2 c$$

Equation 17

$$\eta_{inh} = [\eta] - K_K[\eta]^2 c$$

where K_H and K_K are the dimensionless Huggins and Kraemer constants, respectively. Figure 75 reports the obtained results, with the polymer intrinsic viscosity that can be easily calculated

by the intercepts of the obtained straight lines. Despite this method is well – known and commonly employed to determine the intrinsic viscosity of polymers by means of viscosimetric analysis, its applicability is strongly limited to solutions with a concentration lower than the critical overlap concentration c* (i.e., within the dilute regime where the rheological response of solutions is due to the sum of the isolated chains and solvent contributions), thus reducing the accuracy of the obtained results due to the limited number of available experimental points especially in the case of high molecular weight polymers.

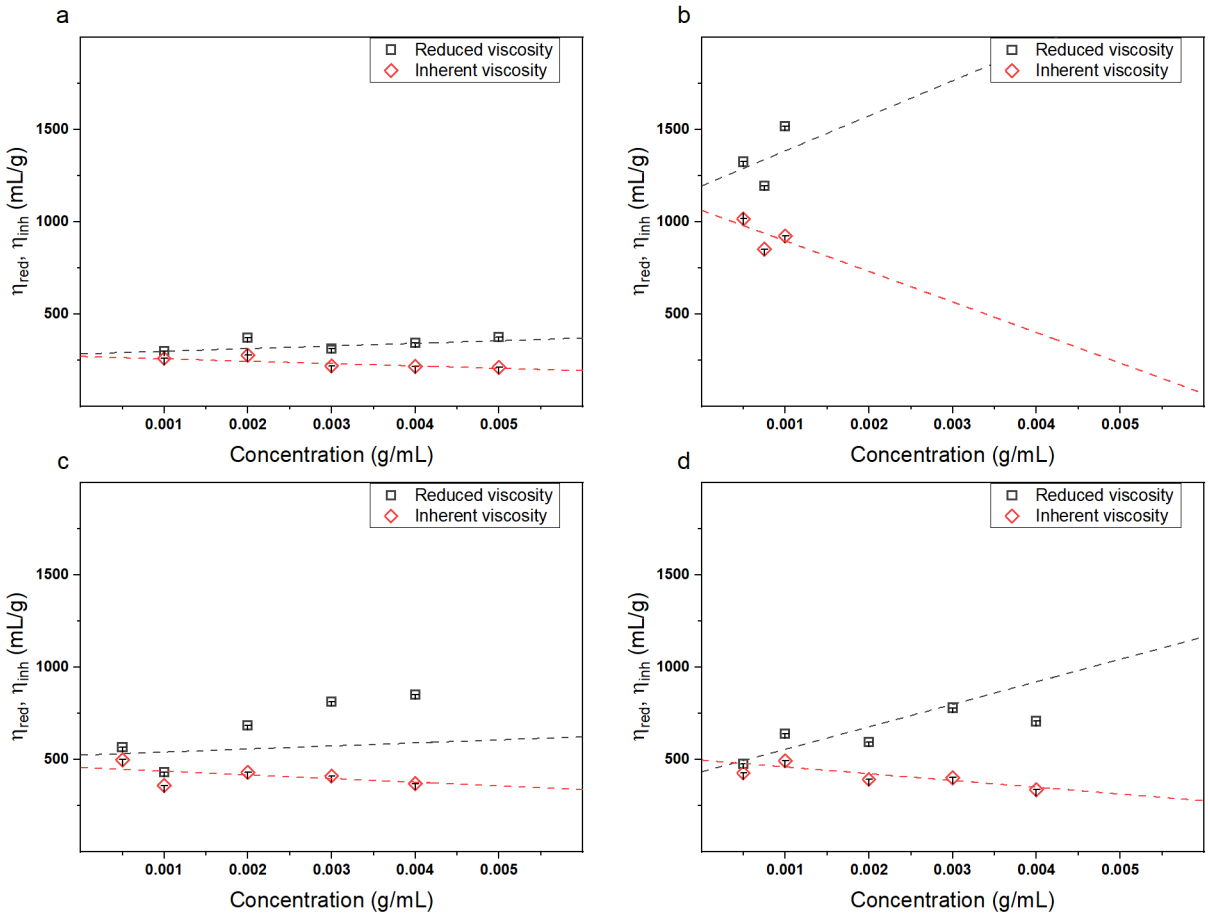

Figure 75. Evaluation of the intrinsic viscosity according to Huggins and Kraemer equations for (a) M.pyr LV, (b) M.pyr MV, (c) L.hyp, and (d) A.nod alginate samples.

Wolf Method

A more recent and sophisticated method was lately derived by Wolf on the basis of thermodynamic considerations.[424] Such an approach was especially developed to evaluate the intrinsic viscosity of polyelectrolytes in the absence of external salts, despite was then proved to be able to describe the viscosity behaviour upon the whole concentration range of both charged and uncharged polymers.[425] Generally speaking, the intrinsic viscosity can be easily

derived from the initial slope of the $\ln(\eta_r)$, with η_r being the relative viscosity (Equation 18), vs concentration plot according to Equation 19:

Equation 18

$$\eta_r = \frac{\eta_0}{\eta_r}$$

Equation 19

$$\ln\eta_r = A\left(1 - e^{-\frac{pc[\eta]}{A}}\right) + (1-p)c[\eta]$$

where p represents the relative difference between $[\eta]$ and $[\eta]^{\pm}$, which is a constant value assumed by the intrinsic viscosity as the ionic strength of the solvent is increased, and A defines the composition range within this modification takes place.[424] Fitting of the experimental data is shown Figure 76.

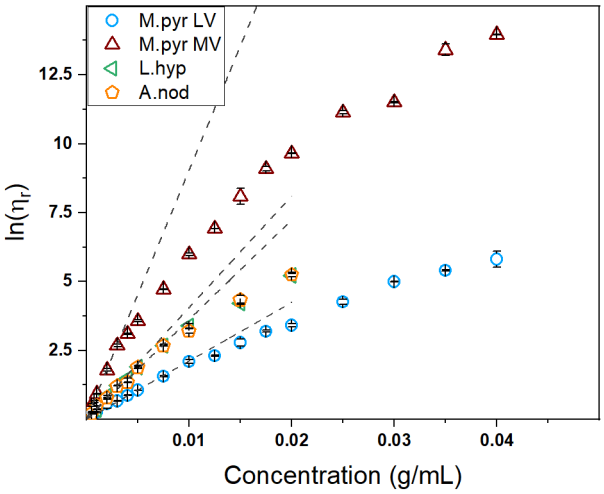

Figure 76. Evaluation of the intrinsic viscosity for different alginate samples according to Wolf method.

Fedors Method

An alternative, but less known, approach to calculate the polymer intrinsic viscosity is then based on Fedors equation:[426]

Equation 20

$$\frac{1}{2(\eta_r^{\frac{1}{2}}-1)} = \frac{1}{c[\eta]} - \frac{1}{c_{max}[\eta]}$$

where c_{max} represents the maximum concentration to which the macromolecules can be considered as packed rigid particles (i.e., the maximum concentration at which the equation can be successfully applied). Figure 77 reports the results obtained by applying Equation 20 to the experimental data.

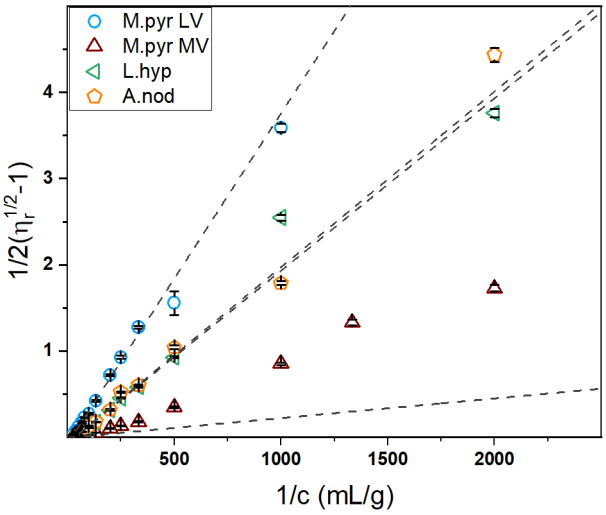

Figure 77. Evaluation of the intrinsic viscosity for different alginate samples according to Fedors method.

The intrinsic viscosity and c_{max} can be determined by the intercepts and the slopes of the obtained straight lines, respectively. It is noteworthy that to achieve results as accurate as possible, in the present Thesis work the best fitting was selected removing one by one the experimental data starting from the highest concentration until no significant differences were observed in the obtained parameters.

Table 13 summarizes the calculated [η] values for the explored alginate samples depending on the employed method.

Table 13. Summary of the alginate intrinsic viscosity values calculated according to Huggins – Kraemer, Wolf, and Fedors approaches. The average viscosity molecular weight and the Mark – Houwink parameters are reported along.

Sample	[η] Huggins – Kraemer (mL/g)	[η] Wolf (mL/g)	[η] Fedors (mL/g)	$\bar{M}_v$ (kg/mol)	k (mL/g)	*a*
M.pyr LV	299 ± 45	261 ± 9	278 ± 1	127	0.0072	0.92
M.pyr MV	1050 ± 52	987 ± 13	1001 ± 1	415	0.0072	0.92
L.hyp	490 ± 47	362 ± 24	490 ± 1	144	0.00485	0.97
A.nod	464 ± 44	405 ± 28	500 ± 1	148	0.00484	0.97

The three applied methods lead to similar and consistent results, which are also in agreement with those reported in literature,[427] besides some interesting differences can be observed. Specifically, taking into account Huggins – Kraemer (Equation 16 and Equation 17) and Fedors (Equation 20) approaches, it can be easily stated that the latter provides much more reliable results owing to the fact that it remains valid in a concentration range much wider than Huggins – Kraemer approach as it can be applied to the entire semi – dilute unentangled regime and partially to the semi – dilute entangled one. On the contrary, Wolf methodology (Equation 19), besides being able to describe the solution viscosity upon the whole concentration range, consists in the evaluation of the intrinsic viscosity as the initial slope of the relative viscosity natural logarithm dependence upon the polymer concentration and it is consequently limited to small concentration range, especially for solutions of polymers with a high molecular weight. In addition, despite this latest method is extremely useful for polyelectrolytes in salt – free solutions since it also considers the effect of the electrostatic repulsions, in solutions with a high enough salt concentration the difference in the [η] values become nearly negligible with respect to the other investigated methods. From the data reported in Table 13, it can be observed that no significant differences were obtained with respect to Fedors approach with only slightly lower values of the intrinsic viscosity. Because of the aforementioned reasons, [η] values determined via Fedors approach were selected as the most appropriate and are then used for the following evaluations described in the present Thesis work. Specifically, alginate average viscosity molecular weight values were calculated for each sample via Mark – Houwink equation (Equation 13) and are summarized in Table 13. To note that k and *a* parameters for the different alginates in the used solvent (i.e., 0.15 mol/L NaCl) were found in the literature.[427] Beyond being fundamental to evaluate $\bar{M}_v$ values, the polymer intrinsic viscosity can be employed to elaborate the viscosity experimental data to build a generalized master curve. Among the various theoretical models reported in the literature, the approach proposed by

Morris et al.[428] was used in this Thesis work to bring the data of the four studied alginates to collapse onto a single master curve. Briefly, the specific viscosity of polymer solutions with different $\bar{M}$ and concentration can be reported as a function of the dimensionless coil overlap parameter ($c[\eta]$), which represents a normalized concentration but cannot be used to identify the extent of coil overlap. Plotting the specific viscosity against such parameter, as shown in Figure 78, a striking generality of behaviour is obtained for the studied alginates within the investigated concentration range, with similar results previously observed for other polysaccharide – based solutions.[429]

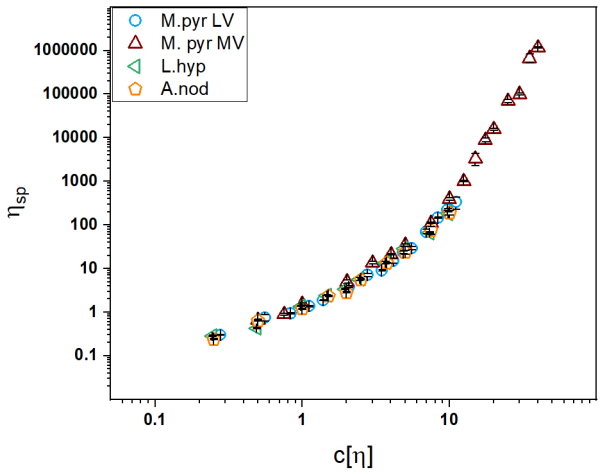

Figure 78. Master curve obtained from the experimental viscosity data using Morris approach.

Along with the molecular weight evaluation, the explored alginate samples were investigated in terms of polyelectrolyte effect by studying the concentration regimes (i.e., dependence of the solution specific viscosity upon the polymer concentration) in deionized water. In this regard, Figure 79 reports the behaviour of η_{sp} vs c. The experimental data were fitted according to a power law:

Equation 21

$$\eta_{sp} \propto c^{\alpha}$$

where α represent the scaling factors, which were calculated by the slopes of the obtained straight lines (double – logarithmic scale). Additionally, the intercepts between these lines were used to estimate the critical concentrations c* (i.e., overlap concentration, separating the dilute and the semi – dilute unentangled regimes), c_e (i.e., entanglement concentration, separating the semi – dilute unentangled and the semi – dilute entangled regimes), and c** (i.e., separating

the semi – dilute entangled and the concentrated regimes). To note that for M.pyr LV, M.pyr MV, and L.hyp samples the overlap concentration c* was evaluated by the empirical relation $\eta_{sp}(c^*) = 1$ being at too low values to be evaluated experimentally, whereas the concentrated regime (i.e., c**) was not reached for M.pyr and A.nod alginates. The obtained results are summarized in Table 14.

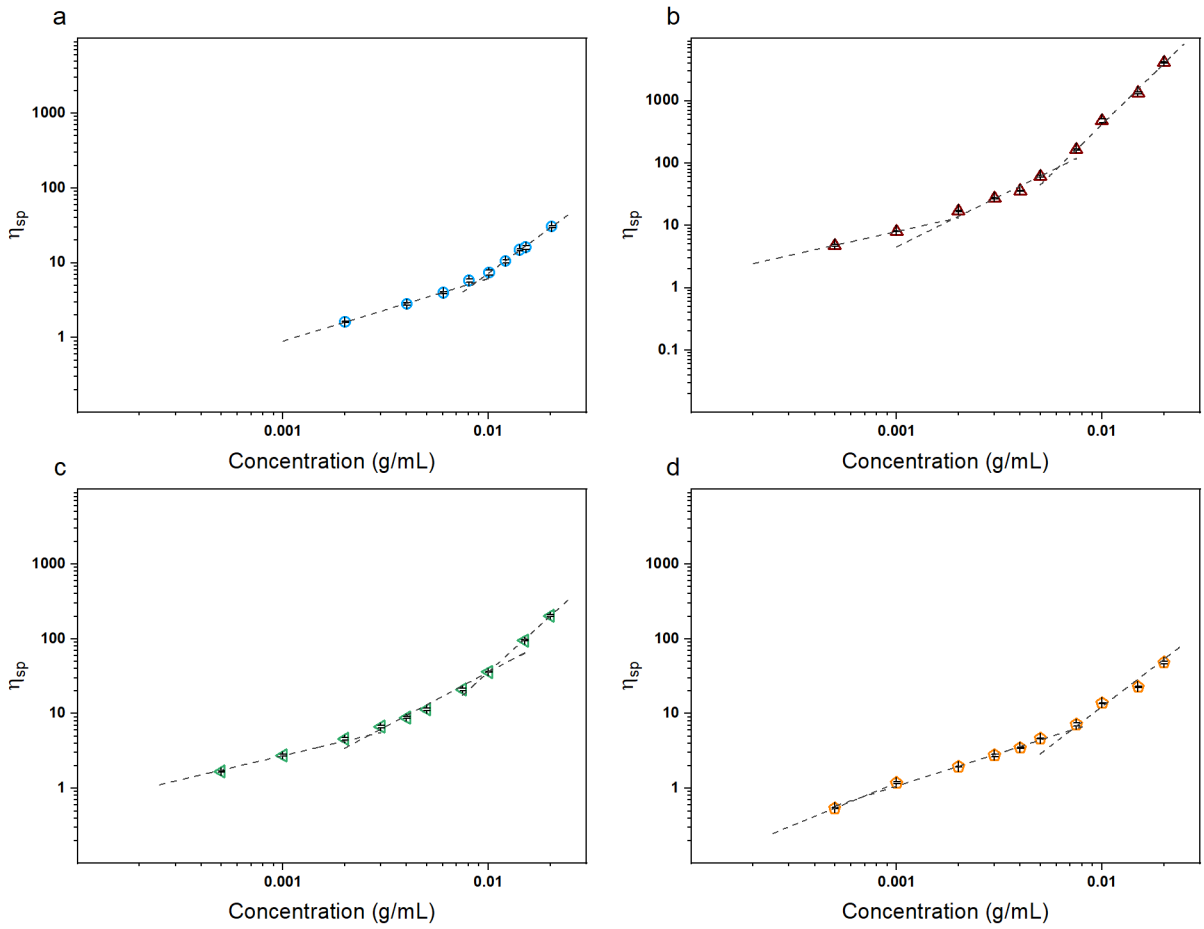

Figure 79. Scaling relation of the specific viscosity upon the polymer concentration for (a) M.pyr LV, (b) M.pyr MV, (c) L.hyp, and (d) A.nod alginate – based solutions. Dashed lines represent the fitting of the experimental data with a power law model.

Table 14. Summary of critical concentrations and scaling factors for alginate samples in deionized water. α_0 is related to the diluted regime, α_1 to the semi – dilute unentangled regime, α_2 to the semi – dilute entangled regime, and α^3 to the concentrated regime. For better comparison, the molecular weight and M/G ratio of the samples is reported along.

Sample	c* (g/mL)	c_e (g/mL)	c** (g/mL)	α_0	α_1	α_2	α_3	$\bar{M}_v$ (kg/mol)	M/G
M.pyr LV	0.0009	0.0081	--	--	0.89	2.01	--	127	1.56
M.pyr MV	0.0001	0.0014	0.0069	--	0.71	1.59	3.23	415	1.56
L.hyp	0.0002	0.0043	0.0138	--	0.80	1.74	2.91	144	0.53
A.nod	0.0008	0.0065	--	1.1	0.90	1.95	--	148	1.43

α_0 predicted value is 1 for both neutral polymers and polyelectrolytes.
α_1 predicted value is 1 for neutral polymers and 0.5 for polyelectrolytes.
α_2 predicted value is 2 – 2.5 for neutral polymers and 1.5 for polyelectrolytes.
α_3 predicted value is 3.5 – 4 for both neutral polymers and polyelectrolytes.

Remarkably, both the molecular weight and the M/G ratio influence the alginate – based solution behaviour in salt – free environments. For what concerns the critical concentrations, M.pyr MV shows the lowest values in agreement with its higher molecular weight. Specifically, long polymer chains can overlap and entangle at much smaller concentrations with respect to the short ones. Conversely, being characterized by the lowest molecular weight, M.pyr LV presents indeed the highest values of c* and c_e. Interestingly, despite the similar $\bar{M}_v$, L.hyp and A.nod samples are characterized by strongly dissimilar critical concentration values likewise due to their different composition and polyelectrolyte effect, as evidenced by the calculated scaling factors. Being L.hyp macromolecules composed of a great number of G units (i.e., M/G = 0.53), they present a more marked polyelectrolyte nature with respect to A.nod chains, which are instead comprised of a higher amount of mannuronic moieties (i.e., M/G = 1.43). Indeed, as depicted in Figure 12, a predominance of guluronic units leads to "zig – zag" chains characterized by the presence of cavities with a consequent increment of the chain charge density. Consequently, it can be supposed that stronger electrostatic repulsions occur thereby forcing the macromolecules to assume a rod – like conformation in agreement with the predicted behaviour for polyelectrolytes. However, even at high content of guluronic moieties, short alginate chains seem to not completely show the typical scaling factors of polyelectrolytes in absence of external salt (i.e., $\alpha_1 = 0.5$, $\alpha_2 = 1.5$, and $\alpha_3 = 3.5 – 4$), but present an intermediate behaviour. Consequently, it is not surprising that M.pyr MV sample (i.e., M/G = 1.56) has the lowest scaling factors in the whole investigated concentration range with respect to the other studied alginates in agreement with its higher molecular weight. The obtained results suggest that alginate polyelectrolyte nature in salt – free environments depend on both the chain length

and composition. Specifically, a predominance of G units in the polymer backbone enhances the charge density forcing the chains to assume a rod – like conformation and displaying a marked polyelectrolyte behaviour. However, decreasing the molecular weight seems to reduce such feature with the consequent establishment of an intermediate behaviour between that of polyelectrolytes and neutral polymers. In this sense, the predominance of M units allows the chains to take on to some extent a random coil conformation that reduces the polyelectrolyte effect in salt – free environments, with low molecular weight values further enhancing the phenomenon.

Conclusions

In this Section, alginate samples extracted from different natural sources were characterized in terms of molecular weight and polyelectrolyte behaviour via rheological measurements as a simple and effective alternative to time and cost – consuming sophisticated characterization techniques. Specifically, simple steady – state viscosity measurements carried out on alginate solutions at different concentration in the presence of added salt have been exploited to calculate the viscosity average molecular weight by using Mark – Houwink equation. To this end, the polymer intrinsic viscosity values were determined via various approaches, with Fedors equation selected as the most reliable one due to its applicability in a wide concentration range. As a matter of fact, the possibility to collapse the rheological data of the four explored alginates in a single master curve by using Morris model was proved as well. Additionally, steady – state viscosity measurements performed on alginate solutions at different concentration in a salt – free environment were utilized to investigate the dependence of the solution specific viscosity upon the polymer concentration, thereby obtaining important information about the sample polyelectrolyte nature. Noticeably, the results suggested that such a feature was influenced by both the alginate molecular weight and composition. In particular, increasing the chain length corresponded to accentuate the polyelectrolyte effect, which in turn led to a reduction of the viscosity scaling factors. Similarly, increasing the G unit moieties amount in the polymer backbone, due to the related increase of the chain charge density, corresponded to enhance the alginate polyelectrolyte behaviour. As such it can be safely stated that both molecular weight and composition of alginate samples must be considered when selecting the raw materials depending on the application of interest.

5.3 Alginate Depolymerization Via Ultrasonic Treatment

This Section is substantially published at:

- *Dodero, A.; Vicini, S.; Castellano, M. Depolymerization of Sodium Alginate in Saline Solutions via Ultrasonic Treatments: A Rheological Characterization. Food Hydrocoll. 2020, 109, 106128.*

In the previous Section, the wide variability of alginate molecular structure and its effect on the polymer physical – chemical were both discussed in terms of rheological properties. As a matter of fact, alginate molecular weight and M – G unit ratio and/or distribution are strongly dependent on the sources and methods of extraction, significantly affecting the reproducibility of alginate – based products and representing one of the greatest limitations regarding the industrial use of such polysaccharide. To this end, whereas alginate composition cannot be controlled without acting directly on the polymer natural source, obtaining chains with a specific length (i.e., average molecular weight) represents a much more realistic approach to achieve tailor – made materials. For example, Ramos et al.[430] investigated the effect of alginate chain length in the protection of probiotics, demonstrating that a low molecular weight led to much higher efficiency for this kind of application. Similarly, Jiao et al. [431] assessed the influence of the molecular weight in conditioning the alginate emulsifying properties. Therefore, it is not surprising that controlling alginate chain length represents a critical aspect in its proficient use potentially allowing to fabricate products with well – defined and reproducible physical – chemical, rheological, and mechanical properties depending on the selected purpose.[432] In this regard, in the last decades several degradation and/or depolymerization techniques have been applied to different polysaccharide – based systems in order to establish a simple and affordable route to obtain chains of controlled length. Ratnawati et al.[433] investigated the oxidative depolymerization of k – carrageenan by ozone treatment, Wang et al.[434] studied the stability of guar gum in acidic conditions, and Watthanaphanit et al.[435] evaluated the degradation of sodium alginate via a solution plasma process. A much simpler and cheaper depolymerization approach consists in the use of ultrasounds (i.e., acoustic frequency higher than 20 kHz) to treat polymer – based solutions. The cyclical pressure changes generated by the ultrasounds induce the formation of small vapour – filled bubbles/cavities, whose dimension increases with time, finally leading to their implosion. Such phenomenon, commonly called cavitation, is represented in Figure 80.

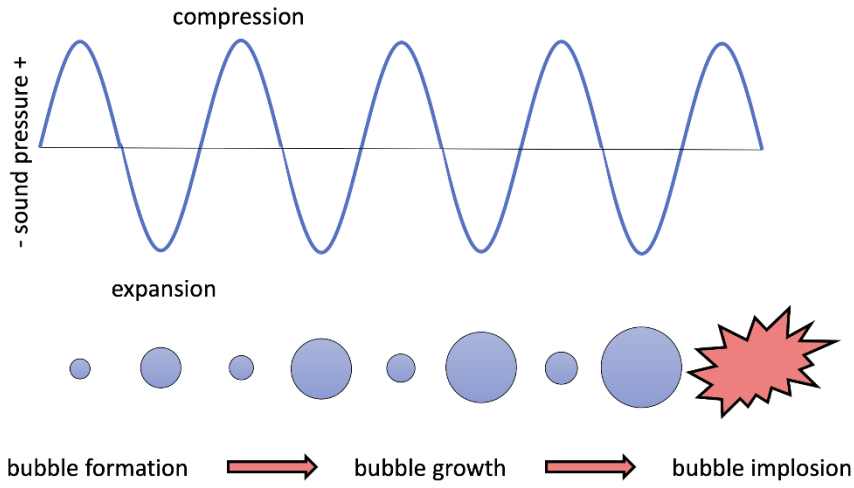

Figure 80. Schematic representation of the cavitation phenomenon induced by ultrasound treatments.

The shear forces raised by the bubble implosion are strong enough to break the covalent bonds between the monosaccharide units, thereby leading to a decrease of the polymer average molecular weight. Ultrasonic depolymerization offers a broad number of advantages compared to chemical, thermal, and enzymatic treatments. Specifically, it does not require any other substance, the polymer breakage tends to occur toward the middle of the chains without the formation of monomers, and side reactions do not usually take place. Consequently, molecules of nearly the same size are obtained via a fast and cheap method without the need for subsequent purification procedures.[436] Additionally, this treatment can be easily applied by means of ultrasonic baths or immersion probes, without the need for complex and expensive setups. Despite the above – mentioned advantages and the fact that several published works deal with the effect of ultrasonic treatments on the physical – chemical properties of several polysaccharides, their applicability to reduce the molecular weight of sodium alginate has not been yet completely understood.

In the present Thesis work, ultrasonic degradation was carried out on saline solutions of two sodium alginates with the same composition but different molecular mass, namely M.pyr LV (i.e., SA LV) and M.pyr MV (i.e., SA MV_M). To be noted that a saline environment was especially employed to screen the alginate negative charges thereby forcing the polymer chains to assume a random coil conformation, which represents a fundamental requirement for the here applied theoretical elaborations.[437] To this end, alginate powders were dissolved in 0.15 mol/L NaCl to prepare batch solutions with an initial polymer concentration of 0.015 g/mL, which were immersed in an ultrasonic bath operating at a frequency of 59 kHz and a temperature of 35 °C for 2 h or 4 h. The temperature of the ultrasonic bath was controlled by

using a cooling coil unit. Alginate depolymerization was monitored by measuring the viscosity average molecular weight of alginate samples at different treatment times. As such, after the treatment, alginate batch solutions were diluted with 0.15 mol/L NaCl to obtain solutions with a polymer concentration ranging from 0.0005 g/mL up to 0.015 g/mL. Untreated alginate batch solutions were diluted as well and used as control samples. Steady – state viscosity measurements were carried out on the prepared solutions as described in Section 3.1, with the experimental data then fitted with the Carreau – Yasuda model to calculate the zero – shear viscosity values.

Decreasing the polymer concentration leads to a decrement of the solution viscosity (data not shown) due to the lower number of polymer chains, which in turn induces a reduction of the topological (i.e., chain entanglements) and electrostatic (e.g., hydrogen bonds, etc.) interactions between each other. Additionally, except for the alginate solutions characterized by both a low concentration and a low molecular weight, the samples exhibit a shear – thinning behaviour consisting of the decrease of the viscosity as the shear rate increases owing to the progressive orientation of the polymer chains. As a way of example, the flow behaviour of alginate solutions with a concentration of 0.01 g/mL at different treatment times is depicted in Figure 81-a and Figure 81-b for M.pyr LV and M.pyr MV samples, respectively.

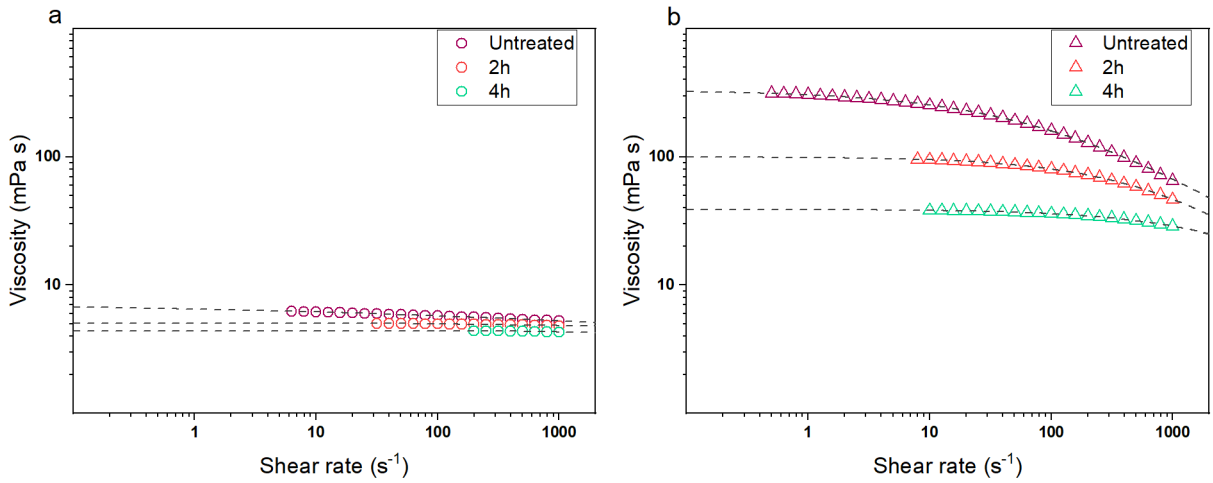

Figure 81. Flow behaviour of 0.01 g/mL alginate solutions for (a) M.pyr LV and (b) M.pyr MV samples. Dashed lines represent the fitting of the experimental data with the Carreau – Yasuda model.

As clearly visible, the ultrasonic treatment induces a decrease of the solution viscosity in both M.pyr LV and M.pyr MV alginates, thereby suggesting a reduction of the polymer molecular weight. However, important differences can be observed between the two samples. Specifically, η_0 is reduced from 329 mPa·s to 38 mPa·s (corresponding to a percentage decrease

of 88%) for the M.pyr MV – based solution after 4h of treatment, whereas values of 7 mPa·s and 4 mPa·s (corresponding to a percentage decrease of 43%) are obtained with the same treatment time for the M.pyr LV – based solution. Such result is likewise due to the fact that ultrasonic degradation is much more effective for high molecular weight polymers compared to short polymer chains. Nevertheless, aiming to better understand the degradation process, the viscosity average molecular weight of the explored polymers was calculated via Mark – Houwink equation using a k value of 0.0092 and *a* value of 0.92. As such, intrinsic viscosity values were first evaluated via Fedors approach as described in the previous Section with the obtained results depicted in Figure 82-a.

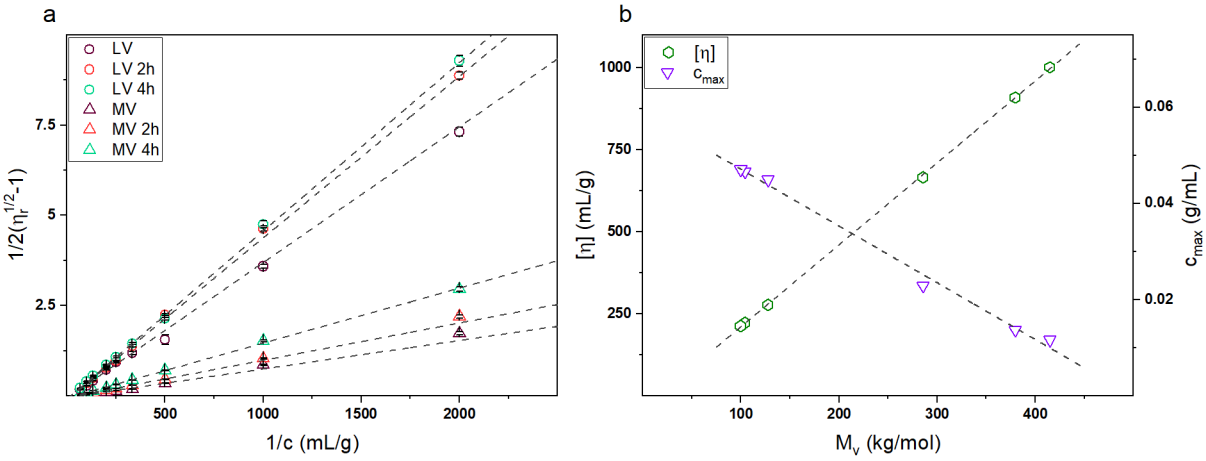

Figure 82. (a) Evaluation of the viscosity average molecular weight via Fedors approach and (b) its relationship with [η] and c_{max} values.

The intrinsic viscosity of the polymer can be easily estimated by the slope of the linear fitting, whereas c_{max} is obtained from its intercept by the extrapolation at $c \rightarrow 0$.[426] The dependence of both parameters upon the viscosity average molecular weight, which was calculated according to Equation 13, is depicted in Figure 82-b and summarized in Table 15.

Table 15. Summary of the calculated intrinsic viscosity, c_{max}, and viscosity average molecular weight values.

Sample	[η] (mL/g)	c_{max} (g/mL)	$\bar{M}_v$ (kg/mol)
LV	278	0.045	127
LV 2h	222	0.047	104
LV 4h	213	0.047	100
MV	1001	0.012	415
MV 2h	909	0.014	379
MV 4h	667	0.023	285

The calculated data clearly confirm the results obtained by the steady – state viscosity measurements. Specifically, it is evident that the ultrasonic treatment can strongly reduce the molecular weight of M.pyr MV but shows a much less marked effect on M.pyr LV, with M.pyr LV 2h and M.pyr LV 4h samples showing a very similar molecular weight despite the different treatment time. Additionally, it can be observed that c_{max} values considerably increase for M.pyr MV samples owing to the marked chain length reduction, but they assume a nearly constant value for M.pyr LV samples reflecting, in this case, the poor effect of the ultrasonic treatment. Such results indicate that the limiting molecular weight $\overline{M}_{lim}$ of alginate (i.e., lowest molecular weight of the polymer that can be reached by its depolymerization under well – defined operative conditions) is around 100 kg/mol in the explored experimental conditions. Aiming to better evaluate the depolymerization of SA, two different models were employed to fit the experimental data. A pseudo – first – order kinetic model was applied according to Equation 22:[433]

Equation 22

$$\frac{1}{\overline{M}_t} = \frac{1}{\overline{M}_0} + \frac{k_1}{m}t$$

where k_1 is the reaction rate constant, t is the treatment time, m is the average molecular weight of a disaccharide unit (i.e., 216.12 g/mol based on the assumption that all β-(1 → 4) glycosidic linkages show the same breakage susceptibility by ultrasounds), $\overline{M}_0$ and $\overline{M}_t$ are the initial average molecular weight and the average molecular weight of the polymer after a treatment time t. Such model considers the depolymerization as a non – specific random scission process leading to the formation of highly polydisperse chains and to a great number of monomers.[438] A mid – point – chain scission kinetic was then employed following a continuous distribution model, as suggested by Ratnawati et al.:[433]

Equation 23

$$\ln\left(\frac{1}{\overline{M}_{lim}} - \frac{1}{\overline{M}_t}\right) = -k_2\overline{M}_{lim}t + \ln\left(\frac{1}{\overline{M}_{lim}} - \frac{1}{\overline{M}_0}\right)$$

where k_2 is the reaction rate constant. According to this model, the depolymerization occurs via the breakage of the chains toward their middle points and thus leads to two molecules with

almost the same dimension, with the breaking process continuing until the limiting molecular mass of the polymer is reached. The fitting of the experimental data with the two described models is shown in Figure 83.

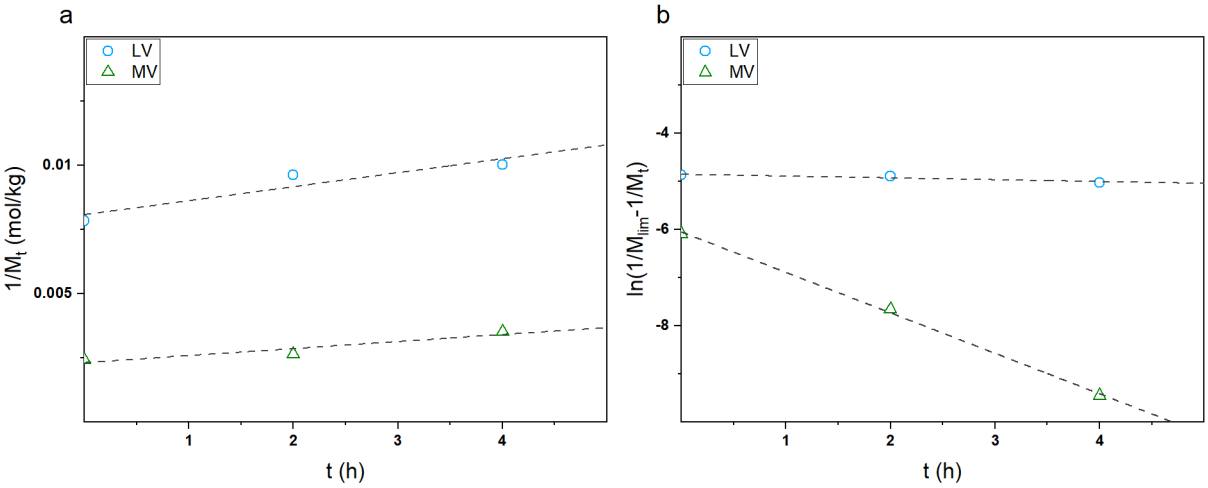

Figure 83. Fitting of the experimental data with a pseudo – first order (a) and a mid – point – chain (b) kinetic model.

Generally speaking, R^2 values indicate that the mid – point – chain scission model (Figure 83-a) is able to better describe the depolymerization of alginate compared to the pseudo – first – order kinetic one (Figure 83-b). However, it can be observed that this latter works to some extent in describing the chain length reduction of M.pyr MV samples. Such finding is probably related to the fact that long macromolecules can also limitedly undergo to a random scission process. Notwithstanding, the obtained results propose the ultrasonic treatment to be an extremely useful method to reduce alginate molecular weight in a well – controlled and defined way without some of the issues usually encountered with thermal and chemical methods (i.e., the existence of side reactions, the formation of a high number of monomers, the need of subsequent purifications, etc.).[438]

To deeply evaluate the weight reduction effect on alginate – based solution rheological behaviour, further information was deducted by investigating the concentration regimes as a function of the ultrasonic treatment time. The dependence of the solution specific viscosity upon the polymer concentration for the alginate samples is shown in Figure 84.

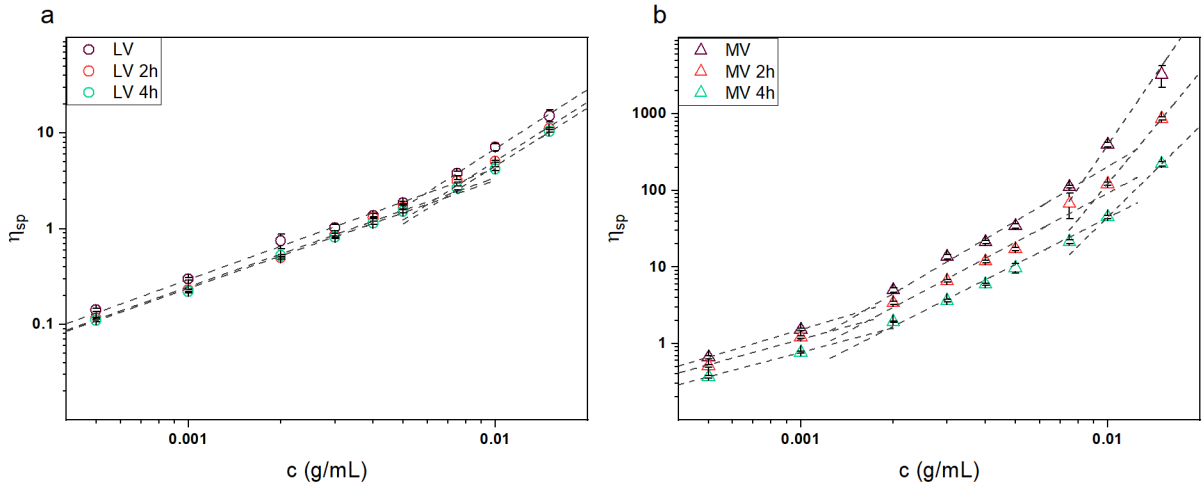

Figure 84. Concentration regimes for (a) M.pyr LV and (b) M.pyr – based solutions. Dashed lines represent the fitting of the experimental data with a power law model.

As described in the previous Section, the experimental data were fitted with a power law model (i.e., $\eta_{sp} \propto c^{\alpha}$) to evaluate the scaling factors and the critical concentrations of each of the investigated alginates. The calculated values are listed in Table 16.

Table 16. Critical concentrations and scaling factors of alginate-based solutions in 0.15 mol/L NaCl as a function of the polymer average molecular weight.

Sample	$\bar{M}_v$ (kg/mol)	c* (g/mL)	c_e (g/mL)	α_1	α_2	α_3
M.pyr LV	127	0.0058	---	1.1	2.0	---
M.pyr LV 2h	104	0.0070	---	1.1	2.0	---
M.pyr LV 4h	100	0.0071	---	1.1	2.0	---
M.pyr MV	415	0.0015	0.0084	1.2	2.4	5.9
M.pyr MV 2h	379	0.0017	0.0090	1.2	2.1	4.8
M.pyr MV 4h	285	0.0019	0.0098	1.1	2.0	3.9

As previously reported, decreasing the alginate average molecular weight leads to the shifting of the concentration regimes at higher concentrations. As a matter of fact, in order for overlapping and even creating entanglements, the presence of a considerably high number of short chains is required. Therefore, it is not surprising that M.pyr MV (i.e., highest average molecular weight) is characterized by a c* value nearly 5 times smaller with respect to M.pyr LV 4h (i.e., lowest average molecular weight). To note that it was not possible to determine the entanglement concentration c_e for M.pyr LV – based solutions in the investigated concentration range due to the extreme shortness of the polymer chains. Generally speaking, the scaling factors obtained for the investigated alginates are in agreement with those of neutral polymers in θ solvent,[439,440] which is not surprising owing to the saline environment used in

the present Thesis work (i.e., 0.15 mol/L NaCl). The high concentration of Na^+ ions contributes to the complete screening of alginate negative charges,[441] thereby granting the polymer chains with the capability to assume the classic random – coil conformation. Despite no significant differences can be observed in the dilute and semi – dilute regimes, a dependence of α_3 upon the average molecular weight can be clearly highlighted. In particular, the lower the chain length, the smaller is the viscosity concentration dependence. Such result can be explained by considering the behaviour of alginate in the used solvent (i.e., a neutral polymer in θ solvent). The screening of the negative charges allows the chains to strictly interact with each other by both entanglements and electrostatic interactions, whose intensity seems to be directly related to the average molecular weight of the polymer.[441,442] Consequently, in the semi – dilute entangled regime, long chains have a more marked contribution in increasing the solution viscosity compared to the short ones. Comparably to c_e, it was not possible to determine even α_3 for M.pyr LV – based systems in the investigated concentration range.

Since temperature is a key parameter in affecting the viscosity of polymer solutions due to the fact that chain behaviour is highly influenced by the system thermal energy, with a higher temperature corresponding to a more extended random coil conformation, steady – state viscosity measurements at various temperatures (i.e., 0 °C, 10 °C, 20 °C, 30 °C, 40 °C, 50 °C, and 60 °C) were carried out on M.pyr LV and M.pyr MV – based solutions with a concentration of 0.01 g/mL. The temperature dependence of the zero – shear viscosity of the tested solutions is shown in Figure 85.

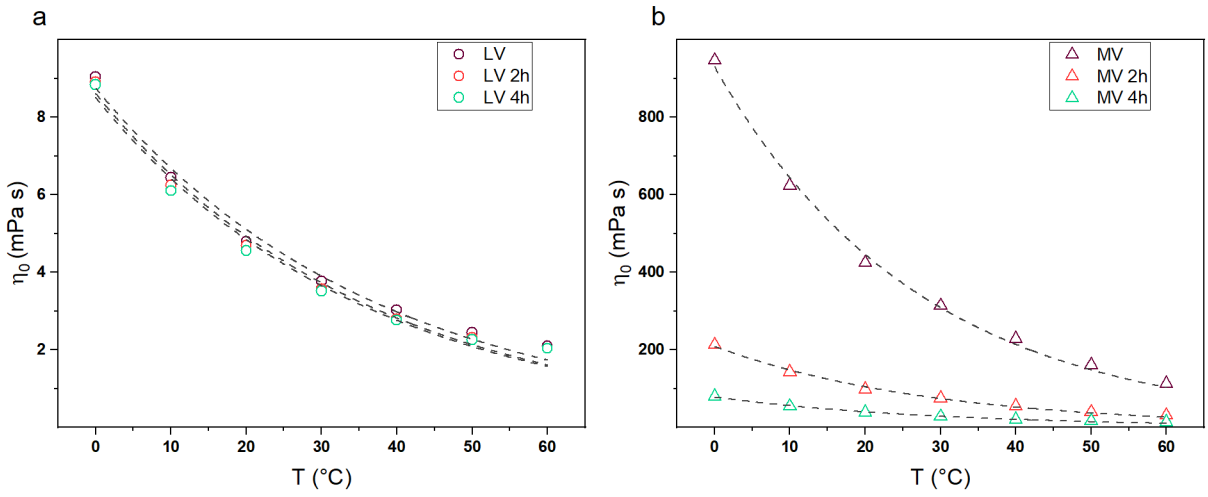

Figure 85. Temperature dependence of the zero – shear viscosity for (a) M.pyr LV and (b) M.pyr MV – based solutions with a concentration of 0.01 g/mL. Dashed lines represent the fitting of the experimental data with Arrhenius equation.

Independently of the tested alginate sample, increasing the temperature leads to a significant decrease of the solution viscosity. However, such reduction is much more marked for M.pyr MV samples and became progressively less evident with the reduction of the molecular weight of the alginate polymers. Such finding can be easily described considering the different chain lengths. Specifically, long chains (i.e., M.pyr MV) are indeed able to form a high number of entanglements leading to the establishment of a complex transient network with a definite mesh size (i.e., an average distance between two chains of the polymer network). As the temperature increases, the chains possess higher thermal energy and tend to assume an extended conformation, thus reducing the number of topological constraints. The main effect is the increase of the average system mesh size of the transient polymer network, which in turn leads to a decrease of the solution viscosity. However, short chains cannot properly form a dense network even at low temperatures and consequently, such phenomenon is slightly observed. Aiming to better evaluate the viscosity – temperature dependence of the investigated alginate – based solutions, the experimental data were fitted (Figure 85) with Arrhenius law as following:[443]

Equation 24

$$\eta_0 = Ae^{\frac{E_a}{RT}}$$

where A is a constant pre – exponential factor, R is the gas constant, and E_a is the flow activation energy. By linearizing Equation 24 and plotting $\ln(\eta_0)$ vs 1/T, as displayed in Figure 86, the pre – exponential factor and the activation energy can be derived from the intercept and the slope of the obtained straight lines, respectively. As clearly shown, a perfect agreement between the experimental data and Arrhenius law is obtained both in its exponential (Figure 85) and linear expression (Figure 86), thereby indicating the validity of such theoretical model to describe the viscosity temperature dependence of alginate – based solutions. It should be noted that Equation 24 applicability is actually limited to a defined temperature range, and deviations from the linear behaviour shown in Figure 86 should be expected at temperature values lower and higher with respect to those evaluated. However, considering that alginate is commonly used in water – based systems, the investigated temperature range provides reasonable and sufficient information for the typical applications. The calculated E_a values are listed in Table 17 together with the solution viscosity decrements.

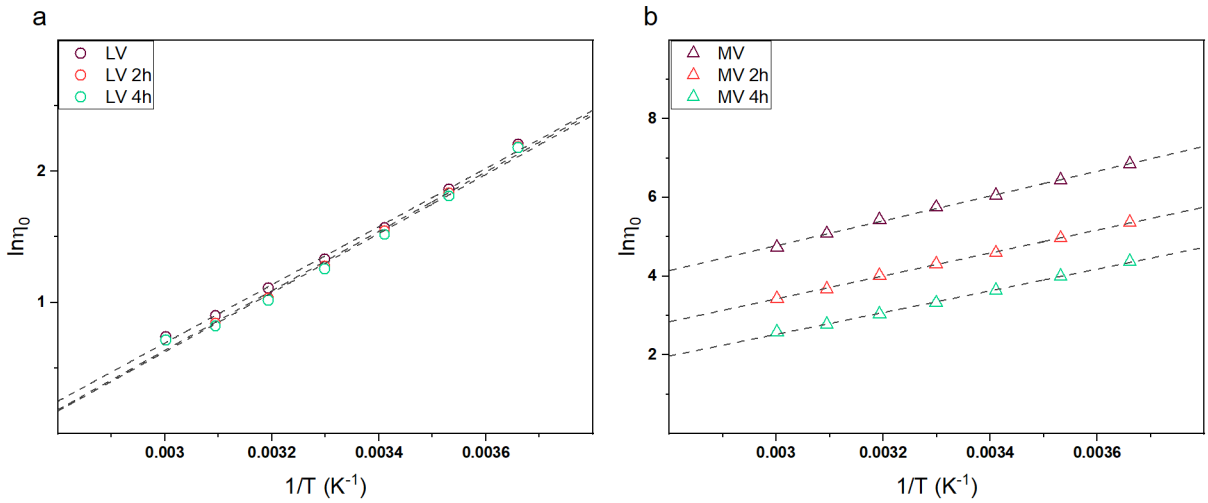

Figure 86. Linearized Arrhenius plot for (a) M.pyr LV and (b) M.pyr MV – based solutions with a concentration of 0.01 g/mL.

Table 17. Viscosity percentage decrements ($\Delta T_1 = 30$ and $\Delta T_1 = 60$) and flow activation energy as a function alginate average molecular mass.

Sample	$\bar{M}_v$ (kg/mol)	$\Delta\eta_0$ - ΔT_1 (%)	$\Delta\eta_0$ - ΔT_2 (%)	E_a (kJ/mol)
M.pyr LV	127	-59	-77	19.3
M.pyr LV 2h	104	-59	-77	18.8
M.pyr LV 4h	100	-59	-77	18.7
M.pyr MV	415	-67	-88	26.2
M.pyr MV 2h	379	-65	-85	24.2
M.pyr MV 4h	285	-64	-83	23.0

The flow activation energy E_a represents the energy needed by the polymer chains to be set in motion against the frictional forces of the system. In order to achieve such results, the total energy of the system should hence overcome the internal flow resistance, corresponding to the material – specific potential barrier.[444] Short chains are subjected to lower frictional forces due to the small number of entanglements and poor electrostatic interactions between each other, thus being characterized by lower activation energy. The dependence of the flow activation energy upon alginate average molecular weight is shown in Figure 87. In the investigated molecular weight range, a perfectly linear relationship is indeed achieved in agreement with the behaviour predicted for flexible polymer chains in the semi – dilute regime.

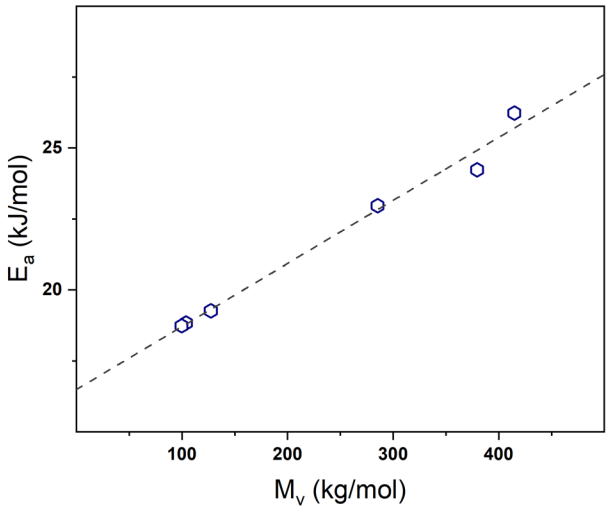

Figure 87. Dependence of the flow activation energy upon the polymer molecular weight.

Conclusions

In this Section, the possibility to exploit a simple, fast, cheap, and safe ultrasound treatment to reduce the molecular weight of alginate – based solutions in the presence of added salt was explored. Specifically, the depolymerization process was monitored by means of steady – state viscosity measurements, from which a decrease of the solution viscosity was observed as the treatment time increased. Remarkably, the depolymerization kinetic was demonstrated to follow a mid – point – chain model indicating the tendency of the macromolecules to break towards the middle of the chains. However, the process nearly stopped as a limiting value of $\bar{M}_v \sim 100$ kg/mol was reached, suggesting that more severe processing conditions should be used to obtain even shorter polymer chains. Interestingly, the study of the concentration regimes indicated that sodium alginate, independently of the molecular weight, behaves as a neutral polymer in θ solvent assuming a random coil conformation when solubilized in 0.15 mol/L NaCl. Additionally, alginate solution rheological response was found to be influenced by the temperature in a range from 0 up to 60 °C, perfectly obeying Arrhenius law and showing a linear relationship between the molecular weight and the flow activation energy E_a.

5.4 Outcomes

Sodium alginate represents nowadays one of the most promising polysaccharides to be used in various industrial applications owing to its unique features, such as biocompatibility, biodegradability, gelling abilities, and rheological properties. However, as a matter of fact, alginate physical – chemical characteristics are highly influenced by its molecular structure, which is in turn strongly dependent on the natural source and method of extraction. Therefore, developing a simple and fast approach able to correlate alginate molecular weight and block composition and/or distribution to its properties is of fundamental importance, especially considering the unusual polyelectrolyte behaviour showed by this polysaccharide. To this end, in the present Thesis work, rheology was successfully demonstrated to be an extremely powerful tool in providing useful information concerning alginate molecular properties. Specifically, simple steady – state viscosity measurements carried out on solutions prepared in a proper saline environment, which represents a key aspect to screen the electrostatic repulsion between the polymer chains, allowed to easily derive alginate intrinsic viscosity values and the related viscosity average molecular weight. More interestingly, the study of the solution concentration regimes (i.e., the dependence of the solution specific viscosity upon the polymer concentration along with the linked critical concentrations and scaling factors) in both salt – free and saline solutions provided important insights concerning the polysaccharide polyelectrolyte nature. Alginate was found to behave as a neutral polymer in θ solvents in the presence of added salt, whereas it displayed a certain degree of polyelectrolyte behaviour in salt – free environments. In this regard, both the alginate molecular weight and M/G ratio seemed to have an important role. Specifically, as a matter of fact, the polyelectrolyte degree of alginate was found to enhance with increasing the chain length and G-block moieties. Additionally, despite the block composition of alginate cannot be directly controlled, its molecular weight was found to be easily modulable via a simple, cost – effective, and safe ultrasonic treatment. In particular, the applied process allowed to reduce the alginate chain length in a well – controlled way with the consequent formation of a poorly polydisperse polymer. Despite the molecular weight reduction seemed to stop once a certain chain length was reached, the proposed approach possessed considerable advantages compared to other commonly employed depolymerization treatment. Remarkably, alginate – based solutions were demonstrated to follow a temperature dependence based on Arrhenius law, with the flow activation energy decreasing with the reduction of the average molecular weight of the polymer.

Chapter 6. Other Projects

This Chapter aims to provide a brief but comprehensive description of the various other projects that have been carried out in the past three years either on electrospun nanofibers or other product types.

6.1 Polysaccharide – Based Hydrogels

6.1.1 Alginate Hydrogels

6.1.1.1 Alginate – Based Hydrogels Prepared via an Ionic Gelation Methodology: An Experimental Design Study to Predict the Crosslinking Degree

This Section is substantially published at:

- *Dodero, A.; Pianella, L.; Vicini, S.; Alloisio, M.; Ottonelli, M.; Castellano, M. Alginate-Based Hydrogels Prepared via Ionic Gelation: An Experimental Design Approach to Predict the Crosslinking Degree. Eur. Polym. J. 2019, 118, 586–594.*

Alginate – based hydrogels can be obtained by the simple addition of bivalent ions to aqueous polysaccharide solutions without the use of toxic chemicals. Nevertheless, the hydrogels prepared by following such an approach often result inhomogeneous and scarcely reproducible due to the extremely fast crosslinking reaction. To overcome such limitations, in the present Thesis work a novel preparation approach is proposed and optimized. The method is based on the use of agar molds rich in bivalent ions as a diffusing system to modulate the release of Ca^{2+}, Sr^{2+}, and Ba^{2+} cations aiming to guarantee better control of the crosslinking process. Specifically, a full factorial experimental design is applied to assess the effects and the mutual interactions of three selected parameters (i.e., sodium alginate concentration, crosslinking agent concentration within the agar molds, and crosslinking time) on the gelation process. The swelling and mechanical properties of the prepared hydrogels are then investigated both in deionized water and in a saline environment able to simulate physiological conditions. Additionally, the hydrogels are characterized by means of thermogravimetric analysis and field – emission scanning electron microscopy. The results demonstrate that both the experimental variables and the environmental conditions have a significant influence on the structure and the performances of the resultant hydrogels. In particular, the use of either a high polymer concentration or crosslinking agent amount leads to strong hydrogels corresponding to a superior crosslinking degree. More in detail, Ba^{2+} ions show a great affinity for alginate leading to the hydrogels with the highest mechanical properties. Moreover, the ion – exchange occurring in the saline environment seems to strongly reduce the effective crosslinking degree of alginate hydrogels with a consequential loss of mechanical properties and stability. It is noteworthy that the collected data are finally elaborated through statistical analysis combined

with response surface methodology to develop theoretical models able to directly correlate the crosslinking degree to the experimental conditions, hence opening the way to the design and fabrication of alginate – based hydrogels with tailored morphology and mechanical properties.

6.1.1.2 Sodium Alginate Cross – Linkable Planar 1D Photonic Crystals as a Promising Tool for Pb^{2+} Detection in Water

This Section is substantially published at:

- *Dodero, A.; Lova, P.; Vicini, S.; Castellano, M.; Comoretto, D. Sodium Alginate Cross-Linkable Planar 1d Photonic Crystals as a Promising Tool for Pb2+ Detection in Water. Chemosensors 2020, 8 (2), 37.*

Due to its high toxicity, Pb^{2+} pollution is a serious threat to both human health and the environment. However, in situ real – time detection of Pb^{2+} pollution is difficult and laboratory instruments are usually required. As such, the possibility to monitor water quality via a simple and fast methodology could lead to the extensive assessment of polluted water sources, especially in rural environments and developing countries where large lead concentrations are often found in surface water. Consequently, simple colorimetric sensors are highly interesting in the field. In the present Thesis work disposable polymer planar 1D photonic crystals made of poly(N-vinylcarbazole), as high refractive index medium, and sodium alginate, as low refractive index and active medium, are for the first time reported for the detection of Pb^{2+} in water. Specifically, the detection relies on the ionic exchange occurring into the alginate matrix. This process effectively induces a physical crosslinking phenomenon, which inhibits water solubilization of the polymer. In turn, this affects the spectral response of the planar 1D photonic crystals modifying their colour.

6.1.2 Agar – Based Hydrogels

This Section is substantially published at:

- *Bertasa, M.; Dodero, A.; Alloisio, M.; Vicini, S.; Riedo, C.; Sansonetti, A.; Scalarone, D.; Castellano, M. Agar Gel Strength: A Correlation Study between Chemical Composition and Rheological Properties. Eur. Polym. J. 2020, 123, 109442.*

Agar – agar is a natural polymer commonly used in various fields of application ranging from cosmetics to the food industry. For over forty years agar gels have been used in the field of

conservation of Cultural Heritage where they are considered as one of the main well – performing tools in cleaning procedures. In the present Thesis work, the relation between the chemical composition and the mechanical strength of four different agar hydrogels is evaluated by comparing the results obtained via pyrolysis – gas chromatography/mass spectrometry and rheological characterization. Agar composition is studied by means of pyrolysis – gas chromatography/mass spectrometry approach to differentiate the anhydrous, galactose, and glucose units. Pristine agar gels, gels after double annealing, and gels with and without a chelating agent are then studied by means of amplitude, frequency and time sweep rheological tests to evaluate all the preparation approaches commonly used by conservators, also considering changes in the transparency via UV – vis spectroscopy. Specifically, a high percentage of anhydrous units in the polymer backbone is found to provide superior mechanical stiffness to the pristine hydrogels, even if it does not seem to affect their long – term stability. The annealing process significantly improves the rheological response of galactose – rich agar hydrogels likewise being able to promote the establishment of additional crosslinking points, whereas the additive presence shows to improve the hydrogel stiffness owing to a more structured polymer network. Moreover, the progressive reduction of the impurities and/or network defects within the hydrogels occurring due to the annealing process slightly increases the transparency of the hydrogels, which is an important aspect for applications in the conservation of Cultural Heritage.

6.2 Synthetic Polymer – based Electrospun Mats

6.2.1 Investigation of the Mechanical and Dynamic-Mechanical Properties of Electrospun Polyvinylpyrrolidone Mats: A Design of Experiment Approach

This Section is substantially published at:

- *Dodero, A.; Brunengo, E.; Castellano, M.; Vicini, S. Investigation of the Mechanical and Dynamic-Mechanical Properties of Electrospun Polyvinylpyrrolidone Membranes: A Design of Experiment Approach. Polymers (Basel). 2020, 12 (7), 1524.*

Polyvinylpyrrolidone electrospun mats characterized by randomly, partially, or almost completely oriented nanofibers are prepared using a drum collector in static (i.e., 0 rpm) or rotating (i.e., 250 rpm or 500 rpm) configuration. Besides a progressive alignment alongside the tangential speed direction, the nanofibers show a dimension increasing with the collector rotating speed in the range 410 – 570 nm. A novel design of experiment approach based on a face – centred central composite design is employed to describe mesh mechanical properties using the computation of mathematical models and their visualization via response surface methodology. The results demonstrate the anisotropic nature of the fiber – oriented mats with Young modulus values of 165 MPa and 71 MPa parallelly and perpendicularly to the alignment direction, respectively. Above all, the proposed approach is proved to be a promising tool from an industrial point of view to prepare electrospun meshes with a tailored mechanical response by simply controlling the collector speed.

6.2.2 Water – Borne Polyurethane Electrospun Mats Embedding TiO_2 Nanoparticles for Photocatalytic Applications

Owing to their unique features, water – borne polyurethanes represent a promising class of green materials to be used in various application fields, including wastewater dye removal. To this end, nanofibrous electrospun mats provide the ideal structure for the development of efficient filter materials able to adsorb great quantities of dyes. As such, in this Thesis work the possibility to embed titania nanoparticles with strong photocatalytic properties within water – borne polyurethane nanofibers is evaluated aiming to obtain long – lasting filter materials that can be regenerate with a simple UV – light treatment. Specifically, formulations containing

a proper quantity of polyurethanes and of ad – hoc synthesized titania nanoparticles, as well as an easily removable carrier polymer, are processed via a single – step electrospinning procedure. Beyond a well – defined nanofibrous morphology and proper dispersion of TiO_2 – NPs, the so obtained meshes are characterized by both marked mechanical and thermal stability hence being effectively suitable for their use as filter materials. Additionally, despite the photocatalytic results are still preliminary and further studies will be required to fully characterize the process, the prospect to completely degrade the adsorbed dyes without influencing the mat properties is to some extent demonstrate.

6.2.3 Composite Poly(vinyl alcohol) – Based Nanofibers Containing Gold Nanoparticles as SERS Amplifiers for Wastewater Monitoring

The development of novel nanomaterials with well – controlled morphologies and/or structures to achieve excellent activities/sensitivities in surface – enhanced Raman scattering (SERS) is crucial in advancing the high – performance SERS detections of chemical and biological species. In this Thesis work, poly(vinyl alcohol) nanofibrous mats embedding gold nanoparticles (Au – NPs) prepared via the technique of electrospinning followed by a simple thermal crosslinking treatment. In particular, nanoparticles with different shapes and dimensions (e.g., nanospheres, nanorods, nanowires, etc.) are employed aiming to evaluate the effect of their structure on SERS detection phenomenon. The achieved mats present a well – defined and homogenous morphology with an overall high porosity, as well as good mechanical performances, high thermal stability, and water resistance properties, therefore representing promising materials for the adsorption of various species from wastewater. Specifically, increasing the anisotropy of the employed nanoparticles should lead to a significant increase of the Raman signals, hence allowing to achieve a highly sensitive system via a simple and cost – effective preparation approach.

List of Figures and Tables

List of Figures

Figure 1. Summary of the development history of electrospinning. Reproduced with permission from Ref. [22].

Figure 2. (a) Basic setup for electrospinning. (b) Photographs showing the evolution of a pendant drop of poly(ethylene oxide) in water from a spherical to a conical shape, followed by the ejection of a jet. (c) Diagram showing the path of an electrospun jet. Reproduced with permission from Ref. [22].

Figure 3. (a) Examples of needle arrangement for multiple – needle electrospinning. Reproduced with permission from Ref. [51]. (b) Photograph of an electrospinning process that uses a jagged metallic plate as solid spinneret. Reproduced with permission from Ref. [48]. (c) Photograph of an electrospinning process that uses a stepped pyramid as solid spinneret. Reproduced with permission from Ref. [52]. (d) Schematic illustration of a coaxial electrospinning setup. Reproduced with permission from Ref. [50]. (e) Schematic illustration of an electrospinning setup using a spinneret comprised of three metallic needles inserted in an outer needle in the pattern of an equilateral triangle. Reproduced with permission from Ref. [53].

Figure 4. (a) Schematic illustration of a collector comprising two conductive substrates and (b) calculated electric field vectors. Reproduced with permission from Ref. [60]. (c) and (d) Schematic illustrations of patterned collectors consisting in gold electrodes deposited on an insulating substrate. Reproduced with permission from Ref. [59]. (e) Schematic illustration of rotatory solid collectors. Reproduced with permission from Ref. [64]. (f) Formation of a nanofibrous yarn using a rotatory metal funnel as collector. Reproduced with permission from Ref. [70]. (g) Schematic illustration of a liquid bath collector setup. Reproduced with permission from Ref. [67]. (h) Schematic illustration showing the use of a conductive liquid as collector and (i) SEM micrograph of a patterned mat. Reproduced with permission from Ref. [69].

Figure 5. (a) SEM micrograph of a typical example of electrospun nanofibers. (b) Schematic illustration of a setup for melt electrospinning onto a static collector. Reproduced with permission from Ref. [82]. (c) Temperature profiles showing the rapid cooling of electrospun nylon-6, poly(propylene), and poly(lactic acid) molten jets. Reproduced with permission from

Ref. [83]. (d) Electrospun structures obtained via melt electrospinning. Reproduced with permission from Ref. [84].

Figure 6. Summary of the most commonly electrospun natural derived polymers.

Figure 7. (a) SEM micrograph of composite poly(vinyl pyrrolidone) – TiO_2 electrospun nanofibers. Reproduced with permission from Ref. [104]. (b) and (c) TEM micrographics of nanofibers containing a different amount of Ag nanoparticles. Reproduced with permission from Ref. [108]. (d) SEM micrograph reporting the necklace – like structure of a composite poly(vinyl alcohol) – SiO_2 nanofiber. Reproduced with permission from Ref. [109]. (e) TEM micrograph of a composite poly(vinyl pyrrolidone) – based fibers containing aligned Ag nanowires. Reproduced with permission from Ref. [110].

Figure 8. (a) Schematic showing the localized treatment of skin tumour and wound healing with the use of a micropatterned nanofibrous scaffolds. (b) SEM micrograph showing the morphology of the micropatterned scaffold. (c) SEM micrograph showing the nanofiber morphology. Reprinted with permission from Ref. [115]. (d) Photograph and (e) SEM micrograph of a nanofiber yarn. (g) Schematic of the textile – weaving process. (f) Photograph and (h) SEM micrograph of a plain – weaving fabric made of PCL nanofiber yarns and multiple PLA filaments. Reproduced with permission from Ref. [116].

Figure 9. (a) Representative release curves, including (i) biphasic release, (ii) zero – order release, (iii) stimuli – triggered release, (iv) sequential release and (v) spatiotemporal release. Reprinted with permission from Ref. [145]. (b) Zero – order release from three – layered nanofibers fabricated using triaxial electrospinning. Reprinted with permission from Ref. [151]. (c) Stimuli – triggered release from nanofibers fabricated by coaxial electrospinning of stimuli-responsive polymers. Reprinted with permission from Ref. [150].

Figure 10. (a) Thermoresponsive properties of a three – layer mat for actuating. Reproduced with permission from Ref. [208]. (b) Series of photographs showing the shape – memory recovery process of composite electrospun nanofibers. Reproduced with permission from Ref. [209]. (c) Super hydrophilic and (d) super hydrophobic surfaces to form a film flow or a drop flow, respectively. Reproduced with permission from Ref. [22]. (e) Schematic of a self – healing composite containing nanofibers to be utilized as protective coating to avoid steel corrosion. Reproduced with permission from Ref. [210].

Figure 11. (a) Multiple – needle electrospinning developed by Inovenso Inc., which involves 110 needles and (b) a photograph of the industrial machine. Reproduced with permission from

Ref. [218]. (c) Needleless electrospinning with the Nanospider Production Line developed by Elmarco Inc., and (d) a photograph of the Nanospider NS 8S1600U industrial machine. Reproduced with permission from Ref. [219].

Figure 12. (a) Alginate chemical structure and chain structure depending on M/G ratio. (b) Schematic of alginate "egg - box" crosslinking model upon contact with bivalent ions.

Figure 13. Chitin and chitosan chemical structure.

Figure 14. Commonly observed fluid flow behaviours.

Figure 15. Typical frequency response of a viscoelastic liquid.

l structure of (a) PEO and (b) Triton X-100.

Figure 17. Flow curves of alginate – based formulations at T = 20 °C. Filled symbols represent pure component solutions, empty symbols represent blend solutions, and dashed lines represent the fitting of the experimental data with the Carreau – Yasuda model.

Figure 18. Viscoelastic spectrum of (a) SA LV, (b) SA MV_M, and (c) SA MV_G – based mixtures at T = 20 °C. Full and empty symbols represent the storage modulus G' and the loss modulus G", respectively.

Figure 19. Variation of the viscoelastic moduli for SA MV_G solution upon several thermal stress cycles.

Figure 20. FESEM micrographs of (a – b) SA MV_M and (c – d) SA MV_G – based nanofibrous mats obtained by means of dry – collector setup. FESEM micrographs of (e – f) SA MV_M and (g – h) SA MV_G – based mats obtained by means of a wet – collector setup.

Figure 21. TGA profiles of PEO powder, SA MV_M powder, as – prepared electrospun mat, and crosslinked electrospun mat

Figure 22. TGA profiles of PEO powder, SA MV_G powder, and crosslinked electrospun mat

Figure 23. (a) and (b) FESEM micrographs of the synthetized ZnO nanoparticles at low and high magnification. (c) TGA profile of the synthetized ZnO nanoparticles. (d) UV – vis spectrum of a 0.025 wt% aqueous suspension of the synthetized ZnO nanoparticles.

Figure 24. Flow curves of (a) SA LV, (b) SA MV_M, and (c) SA MV_G – based formulations containing ZnO - NPs. Dashed lines represent the fitting of the experimental data with the Carreau – Yasuda model. For comparison, flow curves of some alginate – based mixtures without nanoparticles are also reported with empty symbols.

Figure 25. FTIR spectra collected in ATR mode for PEO powder (grey line), SA MV_G powder (blue line), and washed – crosslinked SA MV_G – based mat (violet line).

Figure 26. (a) TGA and DTG profiles for PEO powder (grey line), SA LV powder (red line), and washed – crosslinked SA LV – based mat (violet line). (b) TGA and DTG profiles for PEO powder (grey line), SA MV_G powder (blue line), and washed – crosslinked SA MV_G – based mat (violet line).

Figure 27. FESEM micrographs and fiber diameter distribution for (a – c) SA LV and (d – f) SA MV_G – based crosslinked mats containing ZnO nanoparticles.

Figure 28. (a) EDX map of SA MV_G – based mat where strontium ions are represented in yellow and ZnO – NPs are represented in blue. (b) EDX mat of SA MV_G – based mat where ZnO – NPs distribution is indicated by red dots.

Figure 29. (a) DMA spectrum at T = 37 °C and (b) summary of the mechanical properties at room temperature of alginate – based mats with (violet) and without (green) nanoparticles. DMA analysis was carried out in torsional configuration with $\gamma = 0.002\%$.

Figure 30. Microscopic observation of HaCaT cell adhesion after 16h on (a) alginate nanofibers and (b) alginate – ZnO nanofibers. Microscopic observation of L929 cell adhesion after 16h on (c) alginate nanofibers and (d) alginate – ZnO nanofibers.

Figure 31. Cell cytotoxicity by the MTT test of mat extracts obtained by soaking them in complete medium for 6h and then adding to L929 fibroblasts (blue bars) or HaCaT keratinocytes (green bars) for (a) 24h and (b) 48h, respectively. Results are expressed as percentages with respect to control untreated cells (C). Cell adhesion and growth by the MTT test of (c) L929 fibroblasts and (d) HaCaT keratinocytes on the two different alginate patches and the collagen commercial scaffold after 16h (grey bars) and 72h (yellow bars) of incubation. Results are expressed as cell percentages with respect to the commercial collagen scaffold at the respective incubation time and are the mean ± S.D. of three experiments performed in quadruplicate. Asterisks indicate significance in Tukey's test ($p < 0.05$ vs the respective collagen).

Figure 32. (a) and (d) Serum protein adsorption on the different alginate meshes and commercial collagen incubated for the indicated times in the presence of FBS or HS, respectively. The asterisks and the hashtag indicate significance in Tukey's test (# $p < 0.05$, 0h vs the various incubation times; * $p < 0.05$, the mats at 48h vs the collagen at 48h). (b) and (e)

Cell adhesion (16h) by the MTT test of HaCaT keratinocytes on the different alginate patches and collagen commercial scaffold pre – incubated (green bars) or not (violet bars) for 48h in FBS or in HS, respectively. The asterisks and the hashtag indicate significance in Tukey's test (# $p < 0.05$, collagen without FBS vs collagen with FBS; * $p < 0.05$, compared to the respective collagen). (c) and (f) Ratio of the rate of cell adhesion between samples pre – incubated or not in FBS or HS, calculated using the data displayed in panels (b) and (e), respectively.

Figure 33. (a) Chemical structure and (b) normalized solution UV – vis spectra of methylene blue and congo red organic dyes.

Figure 34. (a) and (b) Adsorption capacity of MB and CR on alginate – ZnO mesh. Experimental data were fitted for MB and CR with a pseudo – first – order and with a pseudo – second – order kinetic model (dashed lines), respectively. (c) and (d) Intra – particle diffusion plots of MB and CR adsorbed by the composite electrospun mat. Dashed segments interpolating the experimental points represent the two kinetic regimes of the adsorption process.

Figure 35. Equilibrium adsorption isotherms of MB (blue points) and CR (red points). The experimental data were fitted with (a) Langmuir and (b) Freundlich models.

Figure 36. Cumulative release with time of MB and CR by dye – loaded patches at increasing dye concentration.

Figure 37. Flow curves of alginate – based solutions (SA – PEO weight ratio of 70 – 30) with a concentration of 3.5 wt% (M.pyr in green triangles) or 5.0 wt% (L.hyp in orange squares and A.nod in brown rhombus). Dashed lines represent the fitting of the experimental data with the Carreau – Yasuda model.

Figure 38. FESEM micrographs and related nanofiber dimension distribution for M.pyr (a, b, and c), L.hyp (e, f, and g), and A.nod (i, j, and k) electrospun samples. 3D representation of AFM micrographs for M.pyr (d), L.hyp (h), and A.nod (l).

Figure 39. Cell adhesion evaluated by MTT test of attached cells after 16h incubation. (a) L929 murine fibroblasts (blue bars) and HaCaT human keratinocytes (green bars) on the three different alginate samples. Results are expressed as the number of adhered cells to each type of patch obtained by interpolation to a standard regression curve of cells seeded onto commercial cell culture 96-well plates. They are the mean ± S.D. of 3 experiments performed in triplicate. Asterisks indicate significance in Tukey test (* $p < 0.05$, M.pyr vs L.hyp and M.pyr vs A.nod). (b) Mg – 63 human osteoblasts (red bars) and Saos – 2 human osteoblasts

(orange bars) on the three different alginate mats. Results are expressed as explained in (a). Asterisks indicate significance in Tukey test (* $p < 0.05$, M.pyr vs L.hyp and M.pyr vs A. Nod, in Saos – 2 bars; ** $p < 0.01$, M.pyr vs L.hyp and M.pyr vs A. Nod, in Mg – 63 bars).

Figure 40. Chemical structure of PCL.

Figure 41. Steady – state viscosity curves at T = 20 °C of PCL solutions in (a) Ac, (b) in GAA, (c) in GAA – Ac 1 – 1 mixture, and (d) in GAA – Ac 3 – 1 mixture. Dashed lines represent the fitting of the experimental data with a straight line at low shear rate values.

Figure 42. SEM micrographs of the crosslinked multilayer patch. PCL nanofibers are shown in (a), alginate – ZnO nanofibers in (b) at low magnification and in (c) the inset at high magnification.

Figure 43. FTIR spectra collected in ATR mode of both sides of the washed – crosslinked multilayer mat along with those of the single polymer components.

Figure 44. TGA and DTG profiles of alginate powder, PCL powder, PEO powder, as – prepared multilayer mat, and crosslinked multilayer mat.

Figure 45. (a) Chemical structure and (b) solution UV – vis spectrum of methyl orange dye.

Figure 46. Adsorption kinetics of the investigated multilayer mat for (a) MB dye solutions and (b) MO dye solutions at increasing concentration. Dashed lines represent the fitting of the experimental data with a pseudo – second – order model. (c) Isotherms of adsorption of the investigated multilayer mesh. (d) Linearized Freundlich model.

Figure 47. Release kinetics of the multilayer mat for (a) MB and (b) MO.

Figure 48. (a) Flow curves of WBPU – PEO formulations at different component ratio. Dashed lines represent the fitting of the experimental data with the Carreau – Yasuda model. (b) Zero – shear viscosity dependence upon the WBPU content for the tested WBPU – PEO formulations. (c) Flow curves of WBPU formulations at different concentrations.

Figure 49. Morphology of the as – prepared mats together with the fiber diameter distribution. WBPU 0 is shown in (a), WBPU 0.5 in (b), WBPU 1 in (c), WBPU 2 in (d), WBPU 3 in (e), WBPU 4 in (f), WBPU 5 in (g), and WBPU 6 in (h).

Figure 50. Dependence of the nanofiber diameter upon the WBPU content for the as – prepared (black squares) and washed (red circles) mats.

Figure 51. Morphology of the washed mats together with the fiber diameter distribution. WBPU 1 is shown in (a), WBPU 2 in (b), WBPU 3 in (c), WBPU 4 in (d), WBPU 5 in (e), and WBPU 6.

Figure 52. (a) Thermograms of the as – prepared WBPU – PEO mats and (b) thermograms of the as – prepared WBPU 0 mat and a WBPU film.

Figure 53. Thermograms of the as – prepared WBPU 0 sample, as – prepared WBPU 6 sample, washed WBPU 6 sample, and WBPU film sample.

Figure 54. (a) Stress – deformation curves of the as – prepared and washed WBPU 6 electrospun mats. (b) Stress – deformation curved of the washed WBPU – based electrospun mats. (c) Dependence of the Young modulus, (d) dependence of the tensile strength, and (e) dependence of the elongation at break upon the WBPU content for as – prepared (i.e., empty symbols) and washed electrospun mats (i.e., full symbols).

Figure 55. (a) and (c) SEM micrographs of WBPU – based and SA – based layers of the investigated multilayer electrospun mat, respectively. (b) and (d) AFM micrographs of WBPU – based and SA – based layers of the investigated multilayer electrospun mat, respectively.

Figure 56. (a) DSC profiles of the as – prepared multilayer mat, crosslinked multilayer mat, and PEO mat. (b) TGA and DTG profiles of SA MV_G powder, WBPU film, PEO mat, as – prepared multilayer mat, and crosslinked multilayer mat.

Figure 57. DMA spectrum at T = 37 °C obtained in extensional configuration

Figure 58. (a) Chemical structure and (b) solution UV – vis spectrum of salicylic acid drug.

Figure 59. (a) Salicylic acid adsorption kinetics for the investigated multilayer patch. (b) Salicylic acid release kinetics for the investigated multilayer patch in PBS at T = 37 °C.

Figure 60. Flow curves of the investigated CS – PEO mixtures at different concentrations measured at T = 20 °C. Dashed lines represent the fitting of the experimental data with the Carreau – Yasuda model.

Figure 61. SEM micrographs of CS – based electrospun meshes obtained from (a – b) CS – PEO 5 wt% mixture, (c – d) CS – PEO 6 wt% mixture, and (e – f) CS – PEO 7 wt% mixture.

Figure 62. SEM micrographs of CS – based electrospun mesh subjected to coagulation in (a) $EtOH/NH_4OH/H_2O$ 7/2/1, (b) NH_4OH, and (c) NaOH 0.5 mol/L.

Figure 63. FESEM micrographs of chitosan – based mats after (a – b) the physical or (d – e) chemical crosslinking treatment. Fiber diameter distribution for (c) the physically crosslinked and (f) chemically crosslinked chitosan – based nanofibers.

Figure 64. Schematics of chitosan physical and chemical crosslinking mechanism.

Figure 65. FTIR spectra of CS powder (i.e., green line), PEO powder (i.e., grey line), CS – based as – prepared mat (i.e., dark blue line), CS – based physically crosslinked mat (i.e., orange line), and CS – based chemically crosslinked mat (i.e., violet line).

Figure 66. TGA and DTG profiles of CS powder (i.e., green line), PEO powder (i.e., grey line), CS – based as – prepared mat (i.e., dark blue line), CS – based physically crosslinked mat (i.e., orange line), and CS – based chemically crosslinked mat (i.e., violet line).

Figure 67. (a) Stress – deformation curves obtained from uniaxial tensile tests for physically (i.e., orange circles) and chemically crosslinked (i.e., violet circles) electrospun mats. (b) Summary of the calculated mechanical properties (i.e., Young modulus, elongation at break, and tensile strenght).

Figure 68. (a) L929 cell adhesion, (b) HaCaT cell adhesion, and (c) Saos – 2 cell adhesion to the physically and chemically crosslinked mats. Results are the mean ± S.D. of 3 experiments performed in triplicate. Asterisk indicates significance in the T – test ($p < 0.05$).

Figure 69. Cell toxicity, measured by MTT test, of conditioned culture media obtained by soaking the meshes for 24h in sterile conditions at 37°C and then adding the media diluted 1:1 to (a) L929 murine fibroblasts, (b) HaCaT human keratinocytes, or (c) Saos – 2 human osteoblasts (c) for further 24h. Results are expressed as percentages respect to control, untreated cells and are the mean ± S.D. of 3 experiments performed in quadruplicate. Asterisks indicate significance in T – test (panel b: ** $p < 0.0005$ C vs Phys – cross and Phys – cross vs Chem – cross, *** $p < 0.0001$ C vs Chem – cross, panel c: * $p < 0.005$ C vs Chem – cross).

Figure 70. (a) and (b) Adsorption capacity of MB and MO on chitosan - based mats. Experimental data were fitted for MB and MO with a pseudo – second – order and with a pseudo – first – order kinetic model (dashed lines), respectively.

Figure 71. (a) Adsorption isotherm data of physically crosslinked chitosan mats and (b) their fitting with the linearized Freundlich model.

Figure 72. Cumulative release from chitosan mats in PBS at T = 37 °C after their loading in (a) MB or (b) MO batch solutions with different dye concentration (i.e., 40, 80, and 160 mg/L).

Figure 73. Schematic of polymer solution concentration regimes and chain behaviour.

Figure 74. Flow behaviour at different polymer concentration for (a) M.pyr LV, (b) M.pyr MV, (c), L.hyp, and (d) A.nod alginate samples at T = 25 °C in o.15 mol/L NaCl. Dashed lines represent the fitting of the experimental data with Carreau – Yasuda model.

Figure 75. Evaluation of the intrinsic viscosity according to Huggins and Kraemer equations for (a) M.pyr LV, (b) M.pyr MV, (c) L.hyp, and (d) A.nod alginate samples.

Figure 76. Evaluation of the intrinsic viscosity for different alginate samples according to Wolf method.

Figure 77. Evaluation of the intrinsic viscosity for different alginate samples according to Fedors method.

Figure 78. Master curve obtained from the experimental viscosity data using Morris approach.

Figure 79. Scaling relation of the specific viscosity upon the polymer concentration for (a) M.pyr LV, (b) M.pyr MV, (c) L.hyp, and (d) A.nod alginate – based solutions. Dashed lines represent the fitting of the experimental data with a power law model.

Figure 80. Schematic representation of the cavitation phenomenon induced by ultrasound treatments.

Figure 81. Flow behaviour of 0.01 g/mL alginate solutions for (a) M.pyr LV and (b) M.pyr MV samples. Dashed lines represent the fitting of the experimental data with the Carreau – Yasuda model.

Figure 82. (a) Evaluation of the viscosity average molecular weight via Fedors approach and (b) its relationship with [η] and c_{max} values.

Figure 83. Fitting of the experimental data with a pseudo – first order (a) and a mid – point – chain (b) kinetic model.

Figure 84. Concentration regimes for (a) M.pyr LV and (b) M.pyr – based solutions. Dashed lines represent the fitting of the experimental data with a power law model.

Figure 85. Temperature dependence of the zero – shear viscosity for (a) M.pyr LV and (b) M.pyr MV – based solutions with a concentration of 0.01 g/mL. Dashed lines represent the fitting of the experimental data with Arrhenius equation.

Figure 86. Linearized Arrhenius plot for (a) M.pyr LV and (b) M.pyr MV – based solutions with a concentration of 0.01 g/mL.

Figure 87. Dependence of the flow activation energy upon the polymer molecular weight.

List of Tables

Table 1. Calculated zero - shear viscosity values for alginate – based formulations.

Table 2. Summary of the zero – shear viscosity for the tested alginate – based formulations containing ZnO nanoparticles calculated with the Carreau – Yasuda model. *Data reported in brackets represent the values calculated for the correspondent formulations without nanoparticles.

Table 3. Summary of the water – related properties of alginate – based mats with and without ZnO nanoparticles.

Table 4. Evaluation of bacterial adhesion on different alginate electrospun mats and collagen scaffold.

Table 5. Summary of alginate sample molecular weight and composition. F_M, F_G, and M/G ratio represent the fraction of mannuronic moieties, the fraction of guluronic moieties, and the ratio between them, respectively.[322] Zeta potential of alginate aqueous solutions at a concentration of 0.001 g/mL is also reported.

Table 6. Zero – shear viscosity values of the tested PCL solutions 24h after their preparation.

Table 7. Summary of the mechanical properties of the as – prepared and crosslinked multilayer mat.

Table 8. Summary of the water – related properties of the crosslinked multilayer mat.

Table 9. Water contact angle values obtained for the washed WBPU – based nanofibers and WBPU film.

Table 10. Summary of the water – related properties measured for the crosslinked multilayer mat.

Table 11. Zero – shear viscosity values calculated for chitosan – based formulation at different polymer concentration

Table 12. Summary of the water – related properties (i.e., water contact angle WCA, water vapour permeability WVP, and moisture content MC) evaluated for chitosan – based mats.

Table 13. Summary of the alginate intrinsic viscosity values calculated according to Huggins – Kraemer, Wolf, and Fedors approaches. The average viscosity molecular weight and the Mark – Houwink parameters are reported along.

Table 14. Summary of critical concentrations and scaling factors for alginate samples in deionized water. α_0 is related to the diluted regime, α_1 to the semi – dilute unentangled regime, α_2 to the semi – dilute entangled regime, and α^3 to the concentrated regime. For better comparison, the molecular weight and M/G ratio of the samples is reported along.

Table 15. Summary of the calculated intrinsic viscosity, c_{max}, and viscosity average molecular weight values.

Table 16. Critical concentrations and scaling factors of alginate-based solutions in 0.15 mol/L NaCl as a function of the polymer average molecular weight.

Table 17. Viscosity percentage decrements ($\Delta T_1 = 30$ and $\Delta T_1 = 60$) and flow activation energy as a function alginate average molecular mass.

Appendix A: List of Publications

1) **Dodero, A.; Williams, R.; Gagliardi, S.; Vicini, S.; Alloisio, M.; Castellano, M.**
Characterization of Hyaluronic Acid by Dynamic Light Scattering and Rheological Techniques. In AIP Conference Proceedings; American Institute of Physics Inc., 2018; Vol. 1981, p 020184.

2) **Dodero, A.; Williams, R.; Gagliardi, S.; Vicini, S.; Alloisio, M.; Castellano, M.**
A Micro-Rheological and Rheological Study of Biopolymers Solutions: Hyaluronic Acid. Carbohydr. Polym. 2019, 203, 349–355.

3) **Dodero, A.; Vicini, S.; Alloisio, M.; Castellano, M.**
Sodium Alginate Solutions: Correlation between Rheological Properties and Spinnability. J. Mater. Sci. 2019, 54 (10), 8034–8046.

4) **Castellano, M.; Alloisio, M.; Darawish, R.; Dodero, A.; Vicini, S.**
Electrospun Composite Mats of Alginate with Embedded Silver Nanoparticles. J. Therm. Anal. Calorim. 2019, 137 (3), 767–778.

5) **Dodero, A.; Pianella, L.; Vicini, S.; Alloisio, M.; Ottonelli, M.; Castellano, M.**
Alginate-Based Hydrogels Prepared via Ionic Gelation: An Experimental Design Approach to Predict the Crosslinking Degree. Eur. Polym. J. 2019, 118, 586–594.

6) **Stocchino, A.; Nepita, I.; Repetto, R.; Dodero, A.; Castellano, M.; Ferrara, M.; Romano, M. R.**
Fluid Dynamic Assessment of Hypersonic and Guillotine Vitrectomy Probes in Viscoelastic Vitreous Substitutes. Transl. Vis. Sci. Technol. 2020, 9 (6).

7) **Dodero, A.; Alloisio, M.; Vicini, S.; Castellano, M.**
Preparation of Composite Alginate-Based Electrospun Membranes Loaded with ZnO Nanoparticles. Carbohydr. Polym. 2020, 227, 115371.

8) **Bertasa, M.; Dodero, A.; Alloisio, M.; Vicini, S.; Riedo, C.; Sansonetti, A.; Scalarone, D.; Castellano, M.**
Agar Gel Strength: A Correlation Study between Chemical Composition and Rheological Properties. Eur. Polym. J. 2020, 123, 109442.

9) **Dodero, A.; Scarfi, S.; Pozzolini, M.; Vicini, S.; Alloisio, M.; Castellano, M.**

Alginate-Based Electrospun Membranes Containing ZnO Nanoparticles as Potential Wound Healing Patches: Biological, Mechanical, and Physicochemical Characterization. ACS Appl. Mater. Interfaces 2020, 12 (3), 3371–3381.

10) **Dodero, A.; Brunengo, E.; Alloisio, M.; Sionkowska, A.; Vicini, S.; Castellano, M.**
Chitosan-Based Electrospun Membranes: Effects of Solution Viscosity, Coagulant and Crosslinker. Carbohydr. Polym. 2020, 235, 115976.

11) **Vita, S.; Ricotti, R.; Dodero, A.; Vicini, S.; Borchardt, P.; Pinori, E.; Castellano, M.**
Rheological, Mechanical and Morphological Characterization of Fillers in the Nautical Field: The Role of Dispersing Agents on Composite Materials. Polymers (Basel). 2020, 12 (6), 1339.

12) **Dodero, A.; Lova, P.; Vicini, S.; Castellano, M.; Comoretto, D.**
Sodium Alginate Cross-Linkable Planar 1d Photonic Crystals as a Promising Tool for Pb2+ Detection in Water. Chemosensors 2020, 8 (2), 37.

13) **Dodero, A.; Vicini, S.; Alloisio, M.; Castellano, M.**
Rheological Properties of Sodium Alginate Solutions in the Presence of Added Salt: An Application of Kulicke Equation. Rheol. Acta 2020, 59 (6).

14) **Dodero, A.; Brunengo, E.; Castellano, M.; Vicini, S.**
Investigation of the Mechanical and Dynamic-Mechanical Properties of Electrospun Polyvinylpyrrolidone Membranes: A Design of Experiment Approach. Polymers (Basel). 2020, 12 (7), 1524.

15) **Dodero, A.; Alloisio, M.; Castellano, M.; Vicini, S.**
Multilayer Alginate-Polycaprolactone Electrospun Membranes as Skin Wound Patches with Drug Delivery Abilities. ACS Appl. Mater. Interfaces 2020, 12 (28), 31162–31171.

16) **Dodero, A.; Vicini, S.; Castellano, M.**
Depolymerization of Sodium Alginate in Saline Solutions via Ultrasonic Treatments: A Rheological Characterization. Food Hydrocoll. 2020, 109, 106128.

17) **Dodero, A.; Vicini, S.; Lova, P.; Alloisio, M.; Castellano, M.**
Nanocomposite alginate-based electrospun membranes as novel adsorbent systems. Int. J. Biol. Macromol. 165 (2020) 1939–1948.

18) **Nepita, I.; Repetto, R.; Dodero, A.; Vicini, S.; Ferrara, M.; Romano, M.; Stocchino, A.**
Experimental assessment of the performance of vitreous cutters with fluids with different rheological properties. Graefe's Arch. Clin. Exp. Ophthalmol. 1–9 (2021).

19) **Dodero, A.; Scarfi, S.; Mirata, S.; Sionkowska, A.; Vicini, S.; Alloisio, M.; Castellano, M.**

Effect of Crosslinking Type on the Physical-Chemical Properties and Biocompatibility of Chitosan-Based Electrospun Membranes. Polymers (Basel). 2021, 13 (5), 831.

20) **Dodero, A.; Donati, I.; Scarfì, S.; Mirata, S.; Alberti, S.; Lova, P.; Comoretto, D.; Alloisio, M.; Vicini, S.; Castellano, M.**

Effect of Sodium Alginate Molecular Structure on Electrospun Membrane Cell Adhesion. Mater. Sci. Eng. C 2021, 112067

21) **Dodero, A.; Schlatter, G.; Hébraud, A.; Vicini, S.; Castellano, M.**

Polymer-free cyclodextrin and natural polymer-cyclodextrin electrospun nanofibers: A comprehensive review on current applications and future perspectives. Carbohydrate Polymers, 264, 118042.

22) **Dodero, A.; Escher, A.; Bertucci, S.; Castellano, M.; Lova, P.**

Intelligent Packaging for Real-Time Monitoring of Food-Quality: Current and Future Developments. Applied Sciences, 11(8), 3532.

Appendix B: Conference Contributions

Oral communications

1) Castellano, M.; Dodero, A.; Boccalero, G., Jean – Mistral, C., Boragno, C.

Silicone – based Elastomer Composites for Energy Harvesting and Actuation Applications

Elastomeri 4.0 – PLAST 2018, 30 May 2018, Milan (Italy)

2) Dodero, A.

Rheological Characterization of Sodium Alginate Solutions

Macrogiovani 2018, 14-15 June 2018, Salerno (Italy)

3) Dodero, A.; Vicini, S.; Alloisio, M.; Gaggero, G.; Castellano, M.

Alginate Solutions: Correlation Between Rheological Properties and Spinnability

XXIII Convegno Nazionale AIM, 9-12 September 2018, Catania (Italy)

4) Dodero, A.; Alloisio, M.; Pozzolini, M.; Scarfi, S.; Vicini, S.; Castellano, M.

Nanofibrous Electrospun Sodium Alginate Membranes Loaded with Zinc Oxide Nanoparticles

EUPOC 2019, 12-16 May 2019, Como (Italy)

5) Dodero, A.; Allosio, M.; Vicini, S.; Gagliardi, S.; Williams, R.; Castellano, M.

Viscosity Scaling Factors for Biopolymers in Aqueous Solutions

XVI Convegno Nazionale di Reologia, 18-21 June 2019, Roma (Italy)

6) Dodero, A.

Nanocomposite Alginate – ZnO Membranes Prepared via Electrospinning Technique

Macrogiovani 2019, 1-2 July 2019, Napoli (Italy)

7) Dodero, A.; Allosio, M.; Vicini, S.; Gagliardi, S.; Williams, R.; Castellano, M.

Viscosity Scaling Factors for Different Polysaccharides in Salt – Free Solutions

2nd Nordic-Italian Polymer Future, 2-3 September 2019, Copenaghen (Denmark)

8) Dodero, A.; Alloisio, M.; Scarfi, S.; Pozzolini, M.; Vicini, S.; Castellano, M.

Nanocomposite Alginate – Based Electrospun Membranes for Wound Healing Applications

PolyChar 27 – World Forum on Advanced Materials, 14-17 October 2019, Napoli (Italy)

9) Dodero, A.; Alloisio, M.; Vicini, S.; Castellano, M.

Polysaccharide – Based Electrospun Membranes for Wound Healing Applications

Macrogiovani – Digital Edition 2020, 26 June 2020 (Microsoft Teams)

10) Alberti, S.; Dodero, A.; Vicini, S.; Castellano, M.; Caratto, V.; Ferretti, M.

PDMS Polymeric Membrane Loaded with TiO_2 NPs with Antibacterial Properties

Macrogiovani – Digital Edition 2020, 26 June 2020 (Microsoft Teams)

11) Nepita, I.; Repetto, R.; Dodero, A.; Castellano, M.; Romano, M.; Ferrara, M.; Stocchino, A.

Fluid Dynamic Assessment of Hypersonic and Guillotine Vitrectomy Probes

Macrogiovani – Digital Edition 2020, 26 June 2020 (Microsoft Teams)

Poster Communications

1) Dodero, A.; Williams, R.; Gagliardi, S.; Vicini, S.; Alloisio, M.; Castellano, M.

Characterization of Hyaluronic Acid in Saline Environment by DLS Micro – Rheological and Conventional Rheological Measurements

AERC 2018, 17-20 April 2018, Sorrento (Italy)

2) Dodero, A.; Williams, R.; Gagliardi, S.; Vicini, S.; Alloisio, M.; Castellano, M.

Characterization of Hyaluronic Acid in Saline Environment by Dynamic Light Scattering and Rheological Techniques

9th Conference on Times of Polymers & Composite, 17-21 June 2018, Ischia (Italy)

3) Vicini, S.; Castellano, M.; Dodero, A.; Caratto, V.; Alloisio, M.

Alginate with Silver Nanoparticles Electrospun Membranes for Biomedical Applications

EUPOC 2019 – AIM, 12-16 May 2019, Como (Italy)

4) Dodero, A.; Alloisio, M.; Vicini, S.; Castellano, M.

Alginate Electrospun Composite Nanofibers Containing Zinc Oxide Nanoparticles for Biomedical Applications

EPF 2019, 9-14 June 2019, Heraklion Crete (Greece)

5) Dodero, A.; Pianella, L., Alloisio, M.; Vicini, S.; Castellano, M.

Development of a Model to Predict the Mechanical Properties and Effective Crosslinking Degree of Sodium Alginate – Based Hydrogels

EPF 2019, 9-14 June 2019, Heraklion Crete (Greece)

6) Alloisio, M.; Urso, D.; Dodero, A.; Castellano, M.; Vicini, S.; Becce, C.; Rolandi, R.

Chitosan – Based Systems as Drug Delivery Platforms for Periodontal Desease

EPF 2019, 9-14 June 2019, Heraklion Crete (Greece)

References

1. Shireesha, Y. & Nandipati, G. State of art review on natural fibers. *Mater. Today Proc.* **18**, 15–24 (2019).
2. Lefèvre, T. & Auger, M. Spider silk as a blueprint for greener materials: a review. *Int. Mater. Rev.* **61**, 127–153 (2016).
3. Woodings, C. Fibers, Regenerated Cellulose. in *Kirk-Othmer Encyclopedia of Chemical Technology* (John Wiley & Sons, Inc., 2003). doi:10.1002/0471238961.1805070523151504.a01.pub2.
4. US2012267A - Alkylene ester of polybasic acids - Google Patents. https://patents.google.com/patent/US2012267A/en.
5. US2071250A - Linear condensation polymers - Google Patents. https://patents.google.com/patent/US2071250A/en.
6. McIntyre, J. *Synthetic fibres : nylon, polyester, acrylic, polyolefin*. (CRC Press ;;Woodhead Pub., 2005).
7. *Manufactured Fibre Technology*. *Manufactured Fibre Technology* (Springer Netherlands, 1997). doi:10.1007/978-94-011-5854-1.
8. Ozipek, B. & Karakas, H. Wet spinning of synthetic polymer fibers. in *Advances in Filament Yarn Spinning of Textiles and Polymers* 174–186 (Elsevier Ltd., 2014). doi:10.1533/9780857099174.2.174.
9. Imura, Y., Hogan, R. M. C. & Jaffe, M. Dry spinning of synthetic polymer fibers. in *Advances in Filament Yarn Spinning of Textiles and Polymers* 187–202 (Elsevier Ltd., 2014). doi:10.1533/9780857099174.2.187.
10. Rawal, A. & Mukhopadhyay, S. Melt spinning of synthetic polymeric filaments. in *Advances in Filament Yarn Spinning of Textiles and Polymers* 75–99 (Elsevier Ltd., 2014). doi:10.1533/9780857099174.2.75.
11. Kuo, C. J. & Lan, W. L. Gel spinning of synthetic polymer fibres. in *Advances in Filament Yarn Spinning of Textiles and Polymers* 100–112 (Elsevier Ltd., 2014). doi:10.1533/9780857099174.2.100.
12. Bhat, G. & Kandagor, V. Synthetic polymer fibers and their processing requirements. in *Advances in Filament Yarn Spinning of Textiles and Polymers* 3–30 (Elsevier Ltd., 2014). doi:10.1533/9780857099174.1.3.

13. Luo, C. J., Stoyanov, S. D., Stride, E., Pelan, E. & Edirisinghe, M. Electrospinning versus fibre production methods: From specifics to technological convergence. *Chem. Soc. Rev.* **41**, 4708–4735 (2012).
14. Dzenis, Y. Spinning continuous fibers for nanotechnology. *Science (80-.).* **304**, 1917–1919 (2004).
15. Jian, S. *et al.* Nanofibers with diameter below one nanometer from electrospinning†. *RSC Adv.* **8**, 4794–4802 (2018).
16. Tucker, N., Stanger, J. J., Staiger, M. P., Razzaq, H. & Hofman, K. The history of the science and technology of electrospinning from 1600 to 1995. *J. Eng. Fiber. Fabr.* **7**, 63–73 (2012).
17. Larsen, G., Velarde-Ortiz, R., Minchow, K., Barrero, A. & Loscertales, I. G. A method for making inorganic and hybrid (organic/inorganic) fibers and vesicles with diameters in the submicrometer and micrometer range via sol-gel chemistry and electrically forced liquid jets. *J. Am. Chem. Soc.* **125**, 1154–1155 (2003).
18. Dai, H., Gong, J., Kim, H. & Lee, D. A novel method for preparing ultra-fine alumina-borate oxide fibres via an electrospinning technique. *Nanotechnology* **13**, 674–677 (2002).
19. Baji, A., Mai, Y. W., Wong, S. C., Abtahi, M. & Chen, P. Electrospinning of polymer nanofibers: Effects on oriented morphology, structures and tensile properties. *Compos. Sci. Technol.* **70**, 703–718 (2010).
20. Smit, E., Buttner, U. & Sanderson, R. D. Continuous yarns from electrospun fibers. *Polymer (Guildf).* **46**, 2419–2423 (2005).
21. Sun, Z., Zussman, E., Yarin, A. L., Wendorff, J. H. & Greiner, A. Compound Core-Shell Polymer Nanofibers by Co-Electrospinning. *Adv. Mater.* **15**, 1929–1932 (2003).
22. Xue, J., Wu, T., Dai, Y. & Xia, Y. Electrospinning and electrospun nanofibers: Methods, materials, and applications. *Chem. Rev.* **119**, 5298–5415 (2019).
23. Li, D. & Xia, Y. Electrospinning of nanofibers: Reinventing the wheel? *Adv. Mater.* **16**, 1151–1170 (2004).
24. Sun, B. *et al.* Advances in three-dimensional nanofibrous macrostructures via electrospinning. *Prog. Polym. Sci.* **39**, 862–890 (2014).
25. Reneker, D. H. & Fong, H. *Polymeric Nanofibers*. vol. 918 (American Chemical Society, 2006).
26. Taylor, G. R. Disintegration of water drops in an electric field. *Proc. R. Soc. London. Ser. A. Math. Phys. Sci.* **280**, 383–397 (1964).

27. Reneker, D. H. & Yarin, A. L. Electrospinning jets and polymer nanofibers. *Polymer (Guildf).* **49**, 2387–2425 (2008).
28. Collins, R. T., Jones, J. J., Harris, M. T. & Basaran, O. A. Electrohydrodynamic tip streaming and emission of charged drops from liquidcones. *Nat. Phys.* **4**, 149–154 (2008).
29. Reneker, D. H., Yarin, A. L., Fong, H. & Koombhongse, S. Bending instability of electrically charged liquid jets of polymer solutions in electrospinning. *J. Appl. Phys.* **87**, 4531–4547 (2000).
30. Hohman, M. M., Shin, M., Rutledge, G. & Brenner, M. P. Electrospinning and electrically forced jets. II. Applications. *Phys. Fluids* **13**, 2221–2236 (2001).
31. Fridrikh, S. V., Yu, J. H., Brenner, M. P. & Rutledge, G. C. Controlling the Fiber Diameter during Electrospinning. *Phys. Rev. Lett.* **90**, 4 (2003).
32. Duft, D., Achtzehn, T., Müller, R., Huber, B. A. & Leisner, T. Coulomb fission: Rayleigh jets from levitated microdroplets. *Nature* **421**, 128 (2003).
33. He, J. H., Wu, Y. & Zuo, W. W. Critical length of straight jet in electrospinning. *Polymer (Guildf).* **46**, 12637–12640 (2005).
34. Liu, F., Guo, R., Shen, M., Wang, S. & Shi, X. Effect of processing variables on the morphology of electrospun poly[(lactic acid)-co-(glycolic acid)] nanofibers. *Macromol. Mater. Eng.* **294**, 666–672 (2009).
35. Fong, H., Chun, I. & Reneker, D. H. Beaded nanofibers formed during electrospinning. *Polymer (Guildf).* **40**, 4585–4592 (1999).
36. Shin, Y. M., Hohman, M. M., Brenner, M. P. & Rutledge, G. C. Experimental characterization of electrospinning: The electrically forced jet and instabilities. *Polymer (Guildf).* **42**, 09955–09967 (2001).
37. Collins, G., Federici, J., Imura, Y. & Catalani, L. H. Charge generation, charge transport, and residual charge in the electrospinning of polymers: A review of issues and complications. *J. Appl. Phys.* **111**, 044701 (2012).
38. Han, T., Reneker, D. H. & Yarin, A. L. Pendulum-like motion of straight electrified jets. *Polymer (Guildf).* **49**, 2160–2169 (2008).
39. Hu, J. *et al.* One-step electro-spinning/netting technique for controllably preparing polyurethane nano-fiber/net. *Macromol. Rapid Commun.* **32**, 1729–1734 (2011).
40. Demir, M. M., Yilgor, I., Yilgor, E. & Erman, B. Electrospinning of polyurethane fibers. *Polymer (Guildf).* **43**, 3303–3309 (2002).
41. Huang, Y. *et al.* Electrohydrodynamic direct-writing. *Nanoscale* **5**, 12007–12017

(2013).

42. Lei, T. P., Lu, X. Z. & Yang, F. Fabrication of various micro/nano structures by modified near-field electrospinning. *AIP Adv.* **5**, 041301 (2015).
43. Parajuli, D., Koomsap, P., Parkhi, A. A. & Supaphol, P. Experimental investigation on process parameters of near-field deposition of electrospinning-based rapid prototyping. *Virtual Phys. Prototyp.* **11**, 193–207 (2016).
44. SalehHudin, H. S., Mohamad, E. N., Mahadi, W. N. L. & Muhammad Afifi, A. Multiple-jet electrospinning methods for nanofiber processing: A review. *Mater. Manuf. Process.* **33**, 479–498 (2018).
45. Varabhas, J. S., Chase, G. G. & Reneker, D. H. Electrospun nanofibers from a porous hollow tube. *Polymer (Guildf).* **49**, 4226–4229 (2008).
46. Sun, D., Chang, C., Li, S. & Lin, L. Near-field electrospinning. *Nano Lett.* **6**, 839–842 (2006).
47. Thoppey, N. M., Bochinski, J. R., Clarke, L. I. & Gorga, R. E. Unconfined fluid electrospun into high quality nanofibers from a plate edge. (2010) doi:10.1016/j.polymer.2010.07.046.
48. Lukas, D., Sarkar, A. & Pokorny, P. Self-organization of jets in electrospinning from free liquid surface: A generalized approach. *J. Appl. Phys.* **103**, 084309 (2008).
49. Jiang, G., Zhang, S. & Qin, X. High throughput of quality nanofibers via one stepped pyramid-shaped spinneret. *Mater. Lett.* **106**, 56–58 (2013).
50. Loscertales, I. G. *et al.* Micro/nano encapsulation via electrified coaxial liquid jets. *Science (80-.).* **295**, 1695–1698 (2002).
51. Akampumuza, O., Gao, H., Zhang, H., Wu, D. & Qin, X.-H. Raising Nanofiber Output: The Progress, Mechanisms, Challenges, and Reasons for the Pursuit. *Macromol. Mater. Eng.* **303**, 1700269 (2018).
52. Jiang, G., Zhang, S., Wang, Y. & Qin, X. An improved free surface electrospinning with micro-bubble solution system for massive production of nanofibers. *Mater. Lett.* **144**, 22–25 (2015).
53. Zhao, Y., Cao, X. & Jiang, L. Bio-mimic multichannel microtubes by a facile method. *J. Am. Chem. Soc.* **129**, 764–765 (2007).
54. Moghe, A. K. & Gupta, B. S. Co-axial electrospinning for nanofiber structures: Preparation and applications. *Polym. Rev.* **48**, 353–377 (2008).
55. Lee, G. H., Song, J. C. & Yoon, K. B. Controlled wall thickness and porosity of polymeric hollow nanofibers by coaxial electrospinning. *Macromol. Res.* **18**, 571–576

(2010).

56. Loscertales, I. G. *et al.* Electrically Forced Coaxial Nanojets for One-Step Hollow Nanofiber Design. *J. Am. Chem. Soc.* **126**, 5376–5377 (2004).
57. Ding, Z., Salim, A. & Ziaie, B. Selective nanofiber deposition through field-enhanced electrospinning. *Langmuir* **25**, 9648–9652 (2009).
58. Zhao, S., Zhou, Q., Long, Y. Z., Sun, G. H. & Zhang, Y. Nanofibrous patterns by direct electrospinning of nanofibers onto topographically structured non-conductive substrates. *Nanoscale* **5**, 4993–5000 (2013).
59. Li, D., Wang, Y. & Xia, Y. Electrospinning Nanofibers as Uniaxially Aligned Arrays and Layer-by-Layer Stacked Films. *Adv. Mater.* **16**, 361–366 (2004).
60. Li, D., Wang, Y. & Xia, Y. Electrospinning of polymeric and ceramic nanofibers as uniaxially aligned arrays. *Nano Lett.* **3**, 1167–1171 (2003).
61. Xie, J. *et al.* Radially aligned, electrospun nanofibers as dural substitutes for wound closure and tissue regeneration applications. *ACS Nano* **4**, 5027–5036 (2010).
62. Vaquette, C. & Cooper-White, J. J. Increasing electrospun scaffold pore size with tailored collectors for improved cell penetration. *Acta Biomater.* **7**, 2544–2557 (2011).
63. Xie, J. *et al.* Nanofiber membranes with controllable microwells and structural cues and their use in forming cell microarrays and neuronal networks. *Small* **7**, 293–297 (2011).
64. Persano, L., Camposeo, A., Tekmen, C. & Pisignano, D. Industrial upscaling of electrospinning and applications of polymer nanofibers: A review. *Macromol. Mater. Eng.* **298**, 504–520 (2013).
65. Matthews, J. A., Wnek, G. E., Simpson, D. G. & Bowlin, G. L. Electrospinning of collagen nanofibers. *Biomacromolecules* **3**, 232–238 (2002).
66. Kong, L. & Ziegler, G. R. Rheological aspects in fabricating pullulan fibers by electro-wet-spinning. *Food Hydrocoll.* **38**, 220–226 (2014).
67. Wu, J. & Hong, Y. Enhancing cell infiltration of electrospun fibrous scaffolds in tissue regeneration. *Bioact. Mater.* **1**, 56–64 (2016).
68. Park, S. M. & Kim, D. S. Electrolyte-assisted electrospinning for a self-assembled, free-standing nanofiber membrane on a curved surface. *Adv. Mater.* **27**, 1682–1687 (2015).
69. Park, S. M., Eom, S., Kim, W. & Kim, D. S. Role of Grounded Liquid Collectors in Precise Patterning of Electrospun Nanofiber Mats. *Langmuir* **34**, 284–290 (2018).
70. Ali, U., Zhou, Y., Wang, X. & Lin, T. Direct electrospinning of highly twisted, continuous nanofiber yarns. *J. Text. Inst.* **103**, 80–88 (2012).
71. Agarwal, S., Greiner, A. & Wendorff, J. H. Functional materials by electrospinning of

polymers. *Prog. Polym. Sci.* **38**, 963–991 (2013).

72. Liao, Y., Loh, C. H., Tian, M., Wang, R. & Fane, A. G. Progress in electrospun polymeric nanofibrous membranes for water treatment: Fabrication, modification and applications. *Prog. Polym. Sci.* **77**, 69–94 (2018).
73. Xue, J., Xie, J., Liu, W. & Xia, Y. Electrospun Nanofibers: New Concepts, Materials, and Applications. *Acc. Chem. Res.* **50**, 1976–1987 (2017).
74. Shenoy, S. L., Bates, W. D., Frisch, H. L. & Wnek, G. E. Role of chain entanglements on fiber formation during electrospinning of polymer solutions: Good solvent, non-specific polymer-polymer interaction limit. *Polymer (Guildf).* **46**, 3372–3384 (2005).
75. Luo, C. J., Stride, E. & Edirisinghe, M. Mapping the influence of solubility and dielectric constant on electrospinning polycaprolactone solutions. *Macromolecules* **45**, 4669–4680 (2012).
76. Husain, O., Lau, W., Edirisinghe, M. & Parhizkar, M. Investigating the particle to fibre transition threshold during electrohydrodynamic atomization of a polymer solution. *Mater. Sci. Eng. C* **65**, 240–250 (2016).
77. Talwar, S., Krishnan, A. S., Hinestroza, J. P., Pourdeyhimi, B. & Khan, S. A. Electrospun nanofibers with associative polymer-surfactant systems. *Macromolecules* **43**, 7650–7656 (2010).
78. Haider, A., Haider, S. & Kang, I. K. A comprehensive review summarizing the effect of electrospinning parameters and potential applications of nanofibers in biomedical and biotechnology. *Arab. J. Chem.* **11**, 1165–1188 (2018).
79. Angammana, C. J. & Jayaram, S. H. Analysis of the effects of solution conductivity on electrospinning process and fiber morphology. *IEEE Trans. Ind. Appl.* **47**, 1109–1117 (2011).
80. De Vrieze, S. *et al.* The effect of temperature and humidity on electrospinning. *J. Mater. Sci.* **44**, 1357–1362 (2009).
81. Yang, G. Z., Li, H. P., Yang, J. H., Wan, J. & Yu, D. G. Influence of Working Temperature on The Formation of Electrospun Polymer Nanofibers. *Nanoscale Res. Lett.* **12**, 55–55 (2017).
82. Brown, T. D., Dalton, P. D. & Hutmacher, D. W. Melt electrospinning today: An opportune time for an emerging polymer process. *Prog. Polym. Sci.* **56**, 116–166 (2016).
83. Zhmayev, E., Cho, D. & Lak Joo, Y. Electrohydrodynamic quenching in polymer melt electrospinning. *Phys. Fluids* **23**, 073102 (2011).
84. Robinson, T. M., Hutmacher, D. W. & Dalton, P. D. The Next Frontier in Melt

Electrospinning: Taming the Jet. *Adv. Funct. Mater.* **29**, 1904664 (2019).

85. Hutmacher, D. W. & Dalton, P. D. Melt electrospinning. *Chem. - An Asian J.* **6**, 44–56 (2011).
86. Molki, M. & Damronglerd, P. Electrohydrodynamic enhancement of heat transfer for developing air flow in square ducts. *Heat Transf. Eng.* **27**, 35–45 (2006).
87. Dalton, P. D., Grafahrend, D., Klinkhammer, K., Klee, D. & Möller, M. Electrospinning of polymer melts: Phenomenological observations. *Polymer (Guildf).* **48**, 6823–6833 (2007).
88. Liu, Y., Deng, R., Hao, M., Yan, H. & Yang, W. Orthogonal design study on factors effecting on fibers diameter of melt electrospinning. *Polym. Eng. Sci.* **50**, 2074–2078 (2010).
89. Mendes, A. C., Stephansen, K. & Chronakis, I. S. Electrospinning of food proteins and polysaccharides. *Food Hydrocoll.* **68**, 53–68 (2017).
90. Kakoria, A. & Sinha-Ray, S. A Review on Biopolymer-Based Fibers via Electrospinning and Solution Blowing and Their Applications. *Fibers* **6**, 45 (2018).
91. Noruzi, M. Electrospun nanofibres in agriculture and the food industry: a review. *J. Sci. Food Agric.* **96**, 4663–4678 (2016).
92. Ding, J. *et al.* Electrospun polymer biomaterials. *Prog. Polym. Sci.* **90**, 1–34 (2019).
93. Schiffman, J. D. & Schauer, C. L. A review: Electrospinning of biopolymer nanofibers and their applications. *Polym. Rev.* **48**, 317–352 (2008).
94. Bakshi, P. S., Selvakumar, D., Kadirvelu, K. & Kumar, N. S. Chitosan as an environment friendly biomaterial – a review on recent modifications and applications. *Int. J. Biol. Macromol.* **150**, 1072–1083 (2020).
95. de Farias, B. S., Sant'Anna Cadaval Junior, T. R. & de Almeida Pinto, L. A. Chitosan-functionalized nanofibers: A comprehensive review on challenges and prospects for food applications. *Int. J. Biol. Macromol.* **123**, 210–220 (2019).
96. Huang, T. *et al.* Fish gelatin modifications: A comprehensive review. *Trends Food Sci. Technol.* **86**, 260–269 (2019).
97. Galiano, F. *et al.* Advances in biopolymer-based membrane preparation and applications. *J. Memb. Sci.* **564**, 562–586 (2018).
98. Yi, Y., Xu, W., Wang, H. X., Huang, F. & Wang, L. M. Natural polysaccharides experience physiochemical and functional changes during preparation: A review. *Carbohydr. Polym.* **234**, 115896 (2020).
99. Valencia, G. A., Zare, E. N., Makvandi, P. & Gutiérrez, T. J. Self-Assembled

Carbohydrate Polymers for Food Applications: A Review. *Compr. Rev. Food Sci. Food Saf.* **18**, 2009–2024 (2019).

100. Soares, R. M. D., Siqueira, N. M., Prabhakaram, M. P. & Ramakrishna, S. Electrospinning and electrospray of bio-based and natural polymers for biomaterials development. *Mater. Sci. Eng. C* **92**, 969–982 (2018).
101. Allais, M. *et al.* Polymer-free electrospinning of tannic acid and cross-linking in water for hybrid supramolecular nanofibres. *Nanoscale* **10**, 9164–9173 (2018).
102. Topuz, F. & Uyar, T. Electrospinning of Cyclodextrin Nanofibers: The Effect of Process Parameters. *J. Nanomater.* **2020**, (2020).
103. Li, D., McCann, J. T., Xia, Y. & Marquez, M. Electrospinning: A simple and versatile technique for producing ceramic nanofibers and nanotubes. *J. Am. Ceram. Soc.* **89**, 1861–1869 (2006).
104. Li, D. & Xia, Y. Fabrication of titania nanofibers by electrospinning. *Nano Lett.* **3**, 555–560 (2003).
105. Dai, Y., Liu, W., Formo, E., Sun, Y. & Xia, Y. Ceramic nanofibers fabricated by electrospinning and their applications in catalysis, environmental science, and energy technology. *Polym. Adv. Technol.* **22**, 326–338 (2011).
106. Zhang, C. L. & Yu, S. H. Nanoparticles meet electrospinning: Recent advances and future prospects. *Chem. Soc. Rev.* **43**, 4423–4448 (2014).
107. Lu, X., Wang, C. & Wei, Y. One-dimensional composite nanomaterials: Synthesis by electrospinning and their applications. *Small* **5**, 2349–2370 (2009).
108. He, D., Hu, B., Yao, Q. F., Wang, K. & Yu, S. H. Large-scale synthesis of flexible free-standing SERS substrates with high sensitivity: Electrospun PVA nanofibers embedded with controlled alignment of silver nanoparticles. *ACS Nano* **3**, 3993–4002 (2009).
109. Jin, Y., Yang, D., Kang, D. & Xiang, X. Fabrication of necklace-like structures via electrospinning. *Langmuir* **26**, 1186–1190 (2010).
110. Zhang, C. L. *et al.* Macroscopic-scale alignment of ultralong Ag nanowires in polymer nanofiber mat and their hierarchical structures by magnetic-field-assisted electrospinning. *Small* **8**, 2936–2940 (2012).
111. Aamodt, J. M. & Grainger, D. W. Extracellular matrix-based biomaterial scaffolds and the host response. *Biomaterials* **86**, 68–82 (2016).
112. Hussey, G. S., Dziki, J. L. & Badylak, S. F. Extracellular matrix-based materials for regenerative medicine. *Nat. Rev. Mater.* **3**, 159–173 (2018).
113. Bancelin, S. *et al.* Determination of collagen fibril size via absolute measurements of

second-harmonic generation signals. *Nat. Commun.* **5**, 1–8 (2014).

114. Wang, X., Ding, B. & Li, B. Biomimetic electrospun nanofibrous structures for tissue engineering. *Mater. Today* **16**, 229–241 (2013).
115. Wang, X. *et al.* Electrospun Micropatterned Nanocomposites Incorporated with Cu2S Nanoflowers for Skin Tumor Therapy and Wound Healing. *ACS Nano* **11**, 11337–11349 (2017).
116. Wu, S., Wang, Y., Streubel, P. N. & Duan, B. Living nanofiber yarn-based woven biotextiles for tendon tissue engineering using cell tri-culture and mechanical stimulation. *Acta Biomater.* **62**, 102–115 (2017).
117. Cheng, J., Jun, Y., Qin, J. & Lee, S. H. Electrospinning versus microfluidic spinning of functional fibers for biomedical applications. *Biomaterials* **114**, 121–143 (2017).
118. Xu, C., Huang, Y., Wu, J., Tang, L. & Hong, Y. Triggerable degradation of polyurethanes for tissue engineering applications. *ACS Appl. Mater. Interfaces* **7**, 20377–20388 (2015).
119. Wise, S. G. *et al.* A multilayered synthetic human elastin/polycaprolactone hybrid vascular graft with tailored mechanical properties. *Acta Biomater.* **7**, 295–303 (2011).
120. Braghirolli, D. I., Steffens, D. & Pranke, P. Electrospinning for regenerative medicine: A review of the main topics. *Drug Discov. Today* **19**, 743–753 (2014).
121. Wang, J. & Windbergs, M. Functional electrospun fibers for the treatment of human skin wounds. *Eur. J. Pharm. Biopharm.* **119**, 283–299 (2017).
122. Dias, J. R., Granja, P. L. & Bártolo, P. J. Advances in electrospun skin substitutes. *Prog. Mater. Sci.* **84**, 314–334 (2016).
123. Sundaramurthi, D., Krishnan, U. M. & Sethuraman, S. Electrospun nanofibers as scaffolds for skin tissue engineering. *Polym. Rev.* **54**, 348–376 (2014).
124. Sun, L. *et al.* Enhanced wound healing in diabetic rats by nanofibrous scaffolds mimicking the basketweave pattern of collagen fibrils in native skin. *Biomater. Sci.* **6**, 340–349 (2018).
125. Ma, B., Xie, J., Jiang, J. & Wu, J. Sandwich-type fiber scaffolds with square arrayed microwells and nanostructured cues as microskin grafts for skin regeneration. *Biomaterials* **35**, 630–641 (2014).
126. Norouzi, M., Boroujeni, S. M., Omidvarkordshouli, N. & Soleimani, M. Advances in Skin Regeneration: Application of Electrospun Scaffolds. *Adv. Healthc. Mater.* **4**, 1114–1133 (2015).
127. Sousa, M. P. *et al.* Bioinspired multilayer membranes as potential adhesive patches for

skin wound healing. *Biomater. Sci.* **6**, 1962–1975 (2018).

128. Cheng, L. *et al.* Surface biofunctional drug-loaded electrospun fibrous scaffolds for comprehensive repairing hypertrophic scars. *Biomaterials* **83**, 169–181 (2016).
129. Lv, F. *et al.* A conducive bioceramic/polymer composite biomaterial for diabetic wound healing. *Acta Biomater.* **60**, 128–143 (2017).
130. Li, J. *et al.* A patterned nanocomposite membrane for high-efficiency healing of diabetic wound. *J. Mater. Chem. B* **5**, 1926–1934 (2017).
131. Sankar, S., Sharma, C. S., Rath, S. N. & Ramakrishna, S. Electrospun nanofibres to mimic natural hierarchical structure of tissues: application in musculoskeletal regeneration. *J. Tissue Eng. Regen. Med.* **12**, e604–e619 (2018).
132. Ju, Y. M., Atala, A., Yoo, J. J. & Lee, S. J. In situ regeneration of skeletal muscle tissue through host cell recruitment. *Acta Biomater.* **10**, 4332–4339 (2014).
133. Hajiali, F., Tajbakhsh, S. & Shojaei, A. Fabrication and Properties of Polycaprolactone Composites Containing Calcium Phosphate-Based Ceramics and Bioactive Glasses in Bone Tissue Engineering: A Review. *Polym. Rev.* **58**, 164–207 (2018).
134. Ko, E. *et al.* Electrospun Silk Fibroin Nanofibrous Scaffolds with Two-Stage Hydroxyapatite Functionalization for Enhancing the Osteogenic Differentiation of Human Adipose-Derived Mesenchymal Stem Cells. *ACS Appl. Mater. Interfaces* **10**, 7614–7625 (2018).
135. Singh, B. N. & Pramanik, K. Development of novel silk fibroin/polyvinyl alcohol/sol-gel bioactive glass composite matrix by modified layer by layer electrospinning method for bone tissue construct generation. *Biofabrication* **9**, (2017).
136. Nasajpour, A. *et al.* A Multifunctional Polymeric Periodontal Membrane with Osteogenic and Antibacterial Characteristics. *Adv. Funct. Mater.* **28**, 1703437 (2018).
137. Zhou, P. *et al.* Organic/inorganic composite membranes based on poly(l-lactic-co-glycolic acid) and mesoporous silica for effective bone tissue engineering. *ACS Appl. Mater. Interfaces* **6**, 20895–20903 (2014).
138. Sophia Fox, A. J., Bedi, A. & Rodeo, S. A. The basic science of articular cartilage: Structure, composition, and function. *Sports Health* **1**, 461–468 (2009).
139. Garrigues, N. W., Little, D., Sanchez-Adams, J., Ruch, D. S. & Guilak, F. Electrospun cartilage-derived matrix scaffolds for cartilage tissue engineering. *J. Biomed. Mater. Res. - Part A* **102**, 3998–4008 (2014).
140. Xu, T., Miszuk, J. M., Zhao, Y., Sun, H. & Fong, H. Electrospun Polycaprolactone 3D Nanofibrous Scaffold with Interconnected and Hierarchically Structured Pores for Bone

Tissue Engineering. *Adv. Healthc. Mater.* **4**, 2238–2246 (2015).

141. Weinreb, J. H. *et al.* Tendon structure, disease, and imaging. *Muscles. Ligaments Tendons J.* **4**, 66–73 (2014).
142. Yang, G., Lin, H., Rothrauff, B. B., Yu, S. & Tuan, R. S. Multilayered polycaprolactone/gelatin fiber-hydrogel composite for tendon tissue engineering. *Acta Biomater.* **35**, 68–76 (2016).
143. Jiang, T., Carbone, E. J., Lo, K. W. H. & Laurencin, C. T. Electrospinning of polymer nanofibers for tissue regeneration. *Prog. Polym. Sci.* **46**, 1–24 (2015).
144. Jana, S., Levengood, S. K. L. & Zhang, M. Anisotropic Materials for Skeletal-Muscle-Tissue Engineering. *Adv. Mater.* **28**, 10588–10612 (2016).
145. Chen, S., Li, R., Li, X. & Xie, J. Electrospinning: An enabling nanotechnology platform for drug delivery and regenerative medicine. *Adv. Drug Deliv. Rev.* **132**, 188–213 (2018).
146. Thakkar, S. & Misra, M. Electrospun polymeric nanofibers: New horizons in drug delivery. *Eur. J. Pharm. Sci.* **107**, 148–167 (2017).
147. Mendes, A. C., Gorzelanny, C., Halter, N., Schneider, S. W. & Chronakis, I. S. Hybrid electrospun chitosan-phospholipids nanofibers for transdermal drug delivery. *Int. J. Pharm.* **510**, 48–56 (2016).
148. Goyal, R., Macri, L. K., Kaplan, H. M. & Kohn, J. Nanoparticles and nanofibers for topical drug delivery. *J. Control. Release* **240**, 77–92 (2016).
149. Li, H. *et al.* Therapeutic angiogenesis in ischemic muscles after local injection of fragmented fibers with loaded traditional Chinese medicine. *Nanoscale* **7**, 13075–13087 (2015).
150. Han, D., Yu, X., Chai, Q., Ayres, N. & Steckl, A. J. Stimuli-Responsive Self-Immolative Polymer Nanofiber Membranes Formed by Coaxial Electrospinning. *ACS Appl. Mater. Interfaces* **9**, 11858–11865 (2017).
151. Yu, D. G. *et al.* Nanofibers Fabricated Using Triaxial Electrospinning as Zero Order Drug Delivery Systems. *ACS Appl. Mater. Interfaces* **7**, 18891–18897 (2015).
152. Han, F. *et al.* Performance of a multilayered small-diameter vascular scaffold dual-loaded with VEGF and PDGF. *Biomaterials* **34**, 7302–7313 (2013).
153. Chen, M., Li, Y.-F. & Besenbacher, F. Electrospun Nanofibers-Mediated On-Demand Drug Release. *Adv. Healthc. Mater.* **3**, 1721–1732 (2014).
154. Li, Y., Xiao, K., Zhu, W., Deng, W. & Lam, K. S. Stimuli-responsive cross-linked micelles for on-demand drug delivery against cancers. *Adv. Drug Deliv. Rev.* **66**, 58–73

(2014).

155. Jhaveri, A., Deshpande, P. & Torchilin, V. Stimuli-sensitive nanopreparations for combination cancer therapy. *J. Control. Release* **190**, 352–370 (2014).
156. Yang, G. *et al.* From nano to micro to macro: Electrospun hierarchically structured polymeric fibers for biomedical applications. *Prog. Polym. Sci.* **81**, 80–113 (2018).
157. PK Papyrus Covered Coronary Stent System - H170004 | FDA. https://www.fda.gov/medical-devices/recently-approved-devices/pk-papyrus-covered-coronary-stent-system-h170004.
158. Jeong, S. *et al.* High Efficiency, Transparent, Reusable, and Active PM2.5 Filters by Hierarchical Ag Nanowire Percolation Network. *Nano Lett.* **17**, 4339–4346 (2017).
159. Koo, W. T. *et al.* Hierarchical Metal-Organic Framework-Assembled Membrane Filter for Efficient Removal of Particulate Matter. *ACS Appl. Mater. Interfaces* **10**, 19957–19963 (2018).
160. Liu, K. *et al.* Core-Shell Nanofibrous Materials with High Particulate Matter Removal Efficiencies and Thermally Triggered Flame Retardant Properties. *ACS Cent. Sci.* **4**, 894–898 (2018).
161. Wang, Y., Li, W., Xia, Y., Jiao, X. & Chen, D. Electrospun flexible self-standing γ-alumina fibrous membranes and their potential as high-efficiency fine particulate filtration media. *J. Mater. Chem. A* **2**, 15124–15131 (2014).
162. Wang, C. *et al.* Silk nanofibers as high efficient and lightweight air filter. *Nano Res.* **9**, 2590–2597 (2016).
163. Liu, B., Zhang, S., Wang, X., Yu, J. & Ding, B. Efficient and reusable polyamide-56 nanofiber/nets membrane with bimodal structures for air filtration. *J. Colloid Interface Sci.* **457**, 203–211 (2015).
164. Liu, C. *et al.* Transparent air filter for high-efficiency PM 2.5 capture. *Nat. Commun.* **6**, 1–9 (2015).
165. Cho, B. M., Nam, Y. S., Cheon, J. Y. & Park, W. H. Residual charge and filtration efficiency of polycarbonate fibrous membranes prepared by electrospinning. *J. Appl. Polym. Sci.* **132**, (2015).
166. Zhu, M. *et al.* Electrospun Nanofibers Membranes for Effective Air Filtration. *Macromol. Mater. Eng.* **302**, (2017).
167. Li, X. *et al.* Electreted polyetherimide-silica fibrous membranes for enhanced filtration of fine particles. *J. Colloid Interface Sci.* **439**, 12–20 (2015).
168. Zhang, R. *et al.* Nanofiber air filters with high-temperature stability for efficient PM2.5

removal from the pollution sources. *Nano Lett.* **16**, 3642–3649 (2016).

169. Ramakrishna, S. *et al.* Electrospun nanofibers: Solving global issues. *Mater. Today* **9**, 40–50 (2006).
170. Wen, Q. *et al.* Flexible inorganic nanofibrous membranes with hierarchical porosity for efficient water purification. *Chem. Sci.* **4**, 4378–4382 (2013).
171. Dai, Y. *et al.* Hierarchical nanostructures of K-birnessite nanoplates on anatase nanofibers and their application for decoloration of dye solution. *J. Mater. Chem.* **20**, 3157–3162 (2010).
172. Ge, J. *et al.* Advanced Sorbents for Oil-Spill Cleanup: Recent Advances and Future Perspectives. *Adv. Mater.* **28**, 10459–10490 (2016).
173. Wang, Y. *et al.* TiO2-SiO2 composite fibers with tunable interconnected porous hierarchy fabricated by single-spinneret electrospinning toward enhanced photocatalytic activity. *J. Mater. Chem. A* **2**, 12442–12448 (2014).
174. Zhan, S., Chen, D., Jiao, X. & Song, Y. Mesoporous TiO2/SiO2 composite nanofibers with selective photocatalytic properties. *Chem. Commun.* 2043–2045 (2007) doi:10.1039/b618905a.
175. Wang, N., Zhang, X., Wang, Y., Yu, W. & Chan, H. L. W. Microfluidic reactors for photocatalytic water purification. *Lab Chip* **14**, 1074–1082 (2014).
176. Meng, Z., Zhang, X. & Qin, J. A high efficiency microfluidic-based photocatalytic microreactor using electrospun nanofibrous TiO2 as a photocatalyst. *Nanoscale* **5**, 4687–4690 (2013).
177. Ahmed, F. E., Lalia, B. S. & Hashaikeh, R. A review on electrospinning for membrane fabrication: Challenges and applications. *Desalination* **356**, 15–30 (2015).
178. Wang, C. *et al.* In Situ Growth of ZIF-8 on PAN Fibrous Filters for Highly Efficient U(VI) Removal. *ACS Appl. Mater. Interfaces* **10**, 24164–24171 (2018).
179. Dai, Y., Formo, E., Li, H., Xue, J. & Xia, Y. Surface-Functionalized Electrospun Titania Nanofibers for the Scavenging and Recycling of Precious Metal Ions. *ChemSusChem* **9**, 2912–2916 (2016).
180. Ye, R., Hurlburt, T. J., Sabyrov, K., Alayoglu, S. & Somorjai, G. A. Molecular catalysis science: Perspective on unifying the fields of catalysis. *Proc. Natl. Acad. Sci. U. S. A.* **113**, 5159–5166 (2016).
181. Ji, X., Wang, P., Su, Z., Ma, G. & Zhang, S. Enabling multi-enzyme biocatalysis using coaxial-electrospun hollow nanofibers: Redesign of artificial cells. *J. Mater. Chem. B* **2**, 181–190 (2014).

182. Li, X. & Zhi, L. Graphene hybridization for energy storage applications. *Chem. Soc. Rev.* **47**, 3189–3216 (2018).
183. Sun, G., Sun, L., Xie, H. & Liu, J. Electrospinning of nanofibers for energy applications. *Nanomaterials* **6**, (2016).
184. Avouris, P. & Chen, J. Nanotube electronics and optoelectronics. *Mater. Today* **9**, 46–54 (2006).
185. Persano, L., Camposeo, A. & Pisignano, D. Active polymer nanofibers for photonics, electronics, energy generation and micromechanics. *Prog. Polym. Sci.* **43**, 48–95 (2015).
186. Lin, C. C. *et al.* Water-Resistant Efficient Stretchable Perovskite-Embedded Fiber Membranes for Light-Emitting Diodes. *ACS Appl. Mater. Interfaces* **10**, 2210–2215 (2018).
187. Cui, Y., Zhong, Z., Wang, D., Wang, W. U. & Lieber, C. M. High Performance Silicon Nanowire Field Effect Transistors. *NANO Lett.* **3**, 149–152 (2003).
188. Ye, D. *et al.* Large-Scale Direct-Writing of Aligned Nanofibers for Flexible Electronics. *Small* **14**, 1703521 (2018).
189. Chen, J. Y., Kuo, C. C., Lai, C. S., Chen, W. C. & Chen, H. L. Manipulation on the morphology and electrical properties of aligned electrospun nanofibers of poly(3-hexylthiophene) for field-effect transistor applications. *Macromolecules* **44**, 2883–2892 (2011).
190. Wang, C. *et al.* High-performance field-effect transistors based on gadolinium doped indium oxide nanofibers and their application in logic gate. *Appl. Phys. Lett.* **112**, 213501 (2018).
191. Huang, C. *et al.* Stimuli-responsive electrospun fibers and their applications. *Chem. Soc. Rev.* **40**, 2417–2434 (2011).
192. Cao, S., Hu, B. & Liu, H. Synthesis of pH-responsive crosslinked poly[styrene-co-(maleic sodium anhydride)] and cellulose composite hydrogel nanofibers by electrospinning. *Polym. Int.* **58**, 545–551 (2009).
193. Stuart, M. A. C. *et al.* Emerging applications of stimuli-responsive polymer materials. *Nat. Mater.* **9**, 101–113 (2010).
194. Yao, Y., Xu, Y., Wang, B., Yin, W. & Lu, H. Recent development in electrospun polymer fiber and their composites with shape memory property: A review. *Pigment Resin Technol.* **47**, 47–54 (2018).
195. Lei, M., Chen, Z., Lu, H. & Yu, K. Recent progress in shape memory polymer composites: Methods, properties, applications and prospects. *Nanotechnol. Rev.* **8**, 327–

351 (2019).

196. Chen, H. *et al.* Electrospun shape memory film with reversible fibrous structure. *J. Mater. Chem.* **22**, 22387–22391 (2012).
197. Lendlein, A. & Kelch, S. Shape-memory polymers. *Angew. Chemie - Int. Ed.* **41**, 2034–2057 (2002).
198. Yao, Y. *et al.* Fabrication of hybrid membrane of electrospun polycaprolactone and polyethylene oxide with shape memory property. *Compos. Part B Eng.* **83**, 264–269 (2015).
199. Zhuo, H., Hu, J., Chen, S. & Yeung, L. Preparation of polyurethane nanofibers by electrospinning. *J. Appl. Polym. Sci.* **109**, 406–411 (2008).
200. Wang, S., Liu, K., Yao, X. & Jiang, L. Bioinspired surfaces with superwettability: New insight on theory, design, and applications. *Chem. Rev.* **115**, 8230–8293 (2015).
201. Sas, I., Gorga, R. E., Joines, J. A. & Thoney, K. A. Literature review on superhydrophobic self-cleaning surfaces produced by electrospinning. *J. Polym. Sci. Part B Polym. Phys.* **50**, 824–845 (2012).
202. Sheng, J., Zhang, M., Xu, Y., Yu, J. & Ding, B. Tailoring Water-Resistant and Breathable Performance of Polyacrylonitrile Nanofibrous Membranes Modified by Polydimethylsiloxane. *ACS Appl. Mater. Interfaces* **8**, 27218–27226 (2016).
203. Bedford, N. M. & Steckl, A. J. Photocatalytic self cleaning textile fibers by coaxial electrospinning. *ACS Appl. Mater. Interfaces* **2**, 2448–2455 (2010).
204. Blossey, R. Self-cleaning surfaces - Virtual realities. *Nat. Mater.* **2**, 301–306 (2003).
205. Toohey, K. S., Sottos, N. R., Lewis, J. A., Moore, J. S. & White, S. R. Self-healing materials with microvascular networks. *Nat. Mater.* **6**, 581–585 (2007).
206. Wu, X.-F. & Yarin, A. L. Recent progress in interfacial toughening and damage self-healing of polymer composites based on electrospun and solution-blown nanofibers: An overview. *J. Appl. Polym. Sci.* **130**, 2225–2237 (2013).
207. Lee, M. W., An, S., Yoon, S. S. & Yarin, A. L. Advances in self-healing materials based on vascular networks with mechanical self-repair characteristics. *Adv. Colloid Interface Sci.* **252**, 21–37 (2018).
208. Apsite, I. *et al.* Porous Stimuli-Responsive Self-Folding Electrospun Mats for 4D Biofabrication. *Biomacromolecules* **18**, 3178–3184 (2017).
209. Gong, T. *et al.* Remotely actuated shape memory effect of electrospun composite nanofibers. *Acta Biomater.* **8**, 1248–1259 (2012).
210. Doan, T. Q. *et al.* Characterization of core-shell microstructure and self-healing

performance of electrospun fiber coatings. *Polymer (Guildf).* **107**, 263–272 (2016).

211. Zussman, E. Encapsulation of cells within electrospun fibers. *Polym. Adv. Technol.* **22**, 366–371 (2011).
212. Murínová, S. & Dercová, K. Response mechanisms of bacterial degraders to environmental contaminants on the level of cell walls and cytoplasmic membrane. *Int. J. Microbiol.* **2014**, (2014).
213. Li, Z. *et al.* Highly sensitive and stable humidity nanosensors based on LiCl doped TiO2 electrospun nanofibers. *J. Am. Chem. Soc.* **130**, 5036–5037 (2008).
214. Senthamizhan, A., Balusamy, B. & Uyar, T. Glucose sensors based on electrospun nanofibers: A review Fiber-based Platforms for Bioanalytics. *Anal. Bioanal. Chem.* **408**, 1285–1306 (2016).
215. Yang, D. *et al.* Electrospinning of poly(dimethylsiloxane)/poly(methyl methacrylate) nanofibrous membrane: Fabrication and application in protein microarrays. *Biomacromolecules* **10**, 3335–3340 (2009).
216. Li, M. *et al.* Electrospinning: A facile method to disperse fluorescent quantum dots in nanofibers without förster resonance energy transfer. *Adv. Funct. Mater.* **17**, 3650–3656 (2007).
217. Nanofibers Market: Global Industry Analysis, Trends, Market Size, and Forecasts up to 2025. https://www.researchandmarkets.com/reports/4840868/nanofibers-market-global-industry-analysis#rela0-3941976.
218. Industrial Electrospinning/Spraying nanofiber machine | Inovenso, innovative engineering solutions. https://www.inovenso.com/portfolio-view/nanospinner416/.
219. Nanospider^{TM} electrospinning equipment | Elmarco. https://www.elmarco.com/.
220. Cooke, C. L., Hyun, J. A., Kim, J., Solnick, J. V. & Lebrilla, C. B. Method for profiling mucin oligosaccharides from gastric biopsies of rhesus monkeys with and without Helicobacter pylori infection. *Anal. Chem.* **79**, 8090–8097 (2007).
221. Dube, D. H. & Bertozzi, C. R. Glycans in cancer and inflammation - Potential for therapeutics and diagnostics. *Nat. Rev. Drug Discov.* **4**, 477–488 (2005).
222. Varki, A. Biological roles of oligosaccharides: all of the theories are correct. *Glycobiology* **3**, 97–130 (1993).
223. Varki, A., Cummings, R., Esko, J., Stanley, P. & Hart, G. *Essentials of Glycobiology*. (2015).
224. Zhang, H. Bioactive Natural Products: Detection, Isolation, and Structural Determination. *Phytomedicine Int. J. Phyther. & Phytopharm.* **18**, 902–903 (2011).

225. Mäki-Arvela, P., Salmi, T., Holmbom, B., Willför, S. & Murzin, D. Y. Synthesis of sugars by hydrolysis of hemicelluloses- A review. *Chem. Rev.* **111**, 5638–5666 (2011).
226. An, H. J. & Lebrilla, C. B. Structure elucidation of native N- and O-linked glycans by tandem mass spectrometry (tutorial). *Mass Spectrom. Rev.* **30**, 560–578 (2011).
227. Yang, L. & Zhang, L. M. Chemical structural and chain conformational characterization of some bioactive polysaccharides isolated from natural sources. *Carbohydr. Polym.* **76**, 349–361 (2009).
228. Gatti, G., Casu, B., Hamer, G. K. & Perlin, A. S. Studies on the Conformation of Heparin by 1H and 13C NMR Spectroscopy. *Macromolecules* **12**, 1001–1007 (1979).
229. Colegate, S. M., Molyneux, R. J. & Molyneux, R. J. *Bioactive Natural Products*. *Bioactive Natural Products* (CRC Press, 2007). doi:10.1201/9781420006889.
230. Cheng, H. *et al.* Structural characterization and antioxidant activities of polysaccharides extracted from Epimedium acuminatum. *Carbohydr. Polym.* **92**, 63–68 (2013).
231. Le Normand, M. *et al.* Hot-water extracts from the inner bark of Norway spruce with immunomodulating activities. *Carbohydr. Polym.* **101**, 699–704 (2014).
232. Song, T., Pranovich, A. & Holmbom, B. Separation of polymeric galactoglucomannans from hot-water extract of spruce wood. *Bioresour. Technol.* **130**, 198–203 (2013).
233. Jin, M., Huang, Q., Zhao, K. & Shang, P. Biological activities and potential health benefit effects of polysaccharides isolated from Lycium barbarum L. *Int. J. Biol. Macromol.* **54**, 16–23 (2013).
234. Rinaudo, M. Main properties and current applications of some polysaccharides as biomaterials. *Polym. Int.* **57**, 397–430 (2008).
235. Lee, K. Y. & Mooney, D. J. Alginate: Properties and biomedical applications. *Prog. Polym. Sci.* **37**, 106–126 (2012).
236. Smidsrød, O. & Skjåk-Bræk, G. Alginate as immobilization matrix for cells. *Trends Biotechnol.* **8**, 71–78 (1990).
237. George, M. & Abraham, T. E. Polyionic hydrocolloids for the intestinal delivery of protein drugs: Alginate and chitosan - a review. *J. Control. Release* **114**, 1–14 (2006).
238. LeRoux, M. A., Guilak, F. & Setton, L. A. Compressive and shear properties of alginate gel: Effects of sodium ions and alginate concentration. *J. Biomed. Mater. Res.* **47**, 46–53 (1999).
239. Lee, J. & Lee, K. Y. Local and sustained vascular endothelial growth factor delivery for angiogenesis using an injectable system. *Pharm. Res.* **26**, 1739–1744 (2009).
240. Orive, G. *et al.* Biocompatibility of microcapsules for cell immobilization elaborated

with different type of alginates. *Biomaterials* **23**, 3825–3831 (2002).

241. Sakiyama-Elbert, S. & Hubbell, J. Functional Biomaterials: Design of Novel Biomaterials. *Annu. Rev. Mater. Res.* **31**, 183–201 (2001).
242. Lee, K. Y. & Yuk, S. H. Polymeric protein delivery systems. *Prog. Polym. Sci.* **32**, 669–697 (2007).
243. Varghese, S. & Elisseeff, J. H. Hydrogels for musculoskeletal tissue engineering. *Adv. Polym. Sci.* **203**, 95–144 (2006).
244. Grant, G. T., Morris, E. R., Rees, D. A., Smith, P. J. C. & Thom, D. Biological interactions between polysaccharides and divalent cations: The egg-box model. *FEBS Lett.* **32**, 195–198 (1973).
245. Kuo, C. K. & Ma, P. X. Ionically crosslinked alginate hydrogels as scaffolds for tissue engineering: Part 1. Structure, gelation rate and mechanical properties. *Biomaterials* **22**, 511–521 (2001).
246. Augst, A. D., Kong, H. J. & Mooney, D. J. Alginate hydrogels as biomaterials. *Macromol. Biosci.* **6**, 623–633 (2006).
247. Drury, J. L., Dennis, R. G. & Mooney, D. J. The tensile properties of alginate hydrogels. *Biomaterials* **25**, 3187–3199 (2004).
248. Szekalska, M. *et al.* Alginate: Current Use and Future Perspectives in Pharmaceutical and Biomedical Applications. *Int. J. Polym. Sci.* **2016**, (2016).
249. Rehm, B. H. A. & Moradali, M. F. *Alginates and Their Biomedical Applications*. vol. 11 (Springer Singapore, 2018).
250. Kothale, D. *et al.* Alginate as Promising Natural Polymer for Pharmaceutical, Food, and Biomedical Applications. *Curr. Drug Deliv.* **17**, 755–775 (2020).
251. Aranaz, I. *et al.* Functional Characterization of Chitin and Chitosan. *Curr. Chem. Biol.* **3**, 203–230 (2009).
252. Yeul, V. S. & Rayalu, S. S. Unprecedented Chitin and Chitosan: A Chemical Overview. *J. Polym. Environ.* **21**, 606–614 (2013).
253. Rahman Bhuiyan, M. A., Hossain, M. A., Zakaria, M., Islam, M. N. & Zulhash Uddin, M. Chitosan Coated Cotton Fiber: Physical and Antimicrobial Properties for Apparel Use. *J. Polym. Environ.* **25**, 334–342 (2017).
254. Ravi Kumar, M. N. V. A review of chitin and chitosan applications. *React. Funct. Polym.* **46**, 1–27 (2000).
255. Croisier, F. & Jérôme, C. Chitosan-based biomaterials for tissue engineering. *Eur. Polym. J.* **49**, 780–792 (2013).

256. Tan, H., Chu, C. R., Payne, K. A. & Marra, K. G. Injectable in situ forming biodegradable chitosan-hyaluronic acid based hydrogels for cartilage tissue engineering. *Biomaterials* **30**, 2499–2506 (2009).

257. Kim, S. K. & Rajapakse, N. Enzymatic production and biological activities of chitosan oligosaccharides (COS): A review. *Carbohydr. Polym.* **62**, 357–368 (2005).

258. Roberts, G. A. F. *Chitin Chemistry*. *Chitin Chemistry* (Macmillan Education UK, 1992). doi:10.1007/978-1-349-11545-7.

259. Kasaai, M. R. Various methods for determination of the degree of N-acetylation of chitin and chitosan: A review. *J. Agric. Food Chem.* **57**, 1667–1676 (2009).

260. No, H. K. & Meyers, S. P. Preparation and characterization of chitin and chitosan- a review. *J. Aquat. Food Prod. Technol.* **4**, 27–52 (1995).

261. Klaykruayat, B., Siralertmukul, K. & Srikulkit, K. Chemical modification of chitosan with cationic hyperbranched dendritic polyamidoamine and its antimicrobial activity on cotton fabric. *Carbohydr. Polym.* **80**, 197–207 (2010).

262. Tomihata, K. & Ikada, Y. In vitro and in vivo degradation of films of chitin and its deacetylated derivatives. *Biomaterials* **18**, 567–575 (1997).

263. Zhang, H. & Neau, S. H. In vitro degradation of chitosan by a commercial enzyme preparation: Effect of molecular weight and degree of deacetylation. *Biomaterials* **22**, 1653–1658 (2001).

264. Lim, S. H. & Hudson, S. M. Synthesis and antimicrobial activity of a water-soluble chitosan derivative with a fiber-reactive group. *Carbohydr. Res.* **339**, 313–319 (2004).

265. Khan, F. & Ahmad, S. R. Polysaccharides and Their Derivatives for Versatile Tissue Engineering Application. *Macromol. Biosci.* **13**, 395–421 (2013).

266. De Andrade, J. R., Oliveira, M. F., Da Silva, M. G. C. & Vieira, M. G. A. Adsorption of Pharmaceuticals from Water and Wastewater Using Nonconventional Low-Cost Materials: A Review. *Ind. Eng. Chem. Res.* **57**, 3103–3127 (2018).

267. Yasuda, K., Armstrong, R. C. & Cohen, R. E. Shear flow properties of concentrated solutions of linear and star branched polystyrenes. *Rheol. Acta* **20**, 163–178 (1981).

268. Largitte, L. & Pasquier, R. A review of the kinetics adsorption models and their application to the adsorption of lead by an activated carbon. *Chem. Eng. Res. Des.* **109**, 495–504 (2016).

269. Langmuir, I. The adsorption of gases on plane surfaces of glass, mica and platinum. *J. Am. Chem. Soc.* **40**, 1361–1403 (1918).

270. Ayawei, N., Ebelegi, A. N. & Wankasi, D. Modelling and Interpretation of Adsorption

Isotherms. *J. Chem.* **2017**, (2017).

271. ASTM E96 / E96M - 16 Standard Test Methods for Water Vapor Transmission of Materials. https://www.astm.org/Standards/E96.htm.
272. Chhabra, R. P. Non-Newtonian fluids: An introduction. in *Rheology of Complex Fluids* 3–34 (Springer New York, 2010). doi:10.1007/978-1-4419-6494-6_1.
273. Colby, R. H. Structure and linear viscoelasticity of flexible polymer solutions: comparison of polyelectrolyte and neutral polymer solutions. *Rheol. Acta* **49**, 425–442 (2010).
274. Mewis, J. & Wagner, N. J. Thixotropy. *Adv. Colloid Interface Sci.* **147**–**148**, 214–227 (2009).
275. Oseli, A., Aulova, A., Gergesova, M. & Emri, I. Time-Temperature Superposition in Linear and Non-linear Domain. *Mater. Today Proc.* **3**, 1118–1123 (2016).
276. Ma, J., Lin, Y., Chen, X., Zhao, B. & Zhang, J. Flow behavior, thixotropy and dynamical viscoelasticity of sodium alginate aqueous solutions. *Food Hydrocoll.* **38**, 119–128 (2014).
277. Rheology for Stability: Rapid screening methods to support ageing studies. https://www.rheologylab.com/articles/pharma/rapid-stability-testing/.
278. Stijnman, A. C., Bodnar, I. & Hans Tromp, R. Electrospinning of food-grade polysaccharides. *Food Hydrocoll.* **25**, 1393–1398 (2011).
279. He, H., Kara, Y. & Molnár, K. In Situ Viscosity-Controlled Electrospinning with a Low Threshold Voltage. *Macromol. Mater. Eng.* **304**, 1900349 (2019).
280. Shi, C. *et al.* Structure, rheology and electrospinning of zein and poly(ethylene oxide) in aqueous ethanol solutions. *Chinese Chem. Lett.* **30**, 305–310 (2019).
281. Rasmussen, J. W., Martinez, E., Louka, P. & Wingett, D. G. Zinc oxide nanoparticles for selective destruction of tumor cells and potential for drug delivery applications. *Expert Opin. Drug Deliv.* **7**, 1063–1077 (2010).
282. Jones, N., Ray, B., Ranjit, K. T. & Manna, A. C. Antibacterial activity of ZnO nanoparticle suspensions on a broad spectrum of microorganisms. *FEMS Microbiol. Lett.* **279**, 71–76 (2008).
283. Webster, T. J. & Seil, I. Antimicrobial applications of nanotechnology: methods and literature. *Int. J. Nanomedicine* **7**, 2767 (2012).
284. Sirelkhatim, A. *et al.* Review on zinc oxide nanoparticles: Antibacterial activity and toxicity mechanism. *Nano-Micro Lett.* **7**, 219–242 (2015).
285. Colon, G., Ward, B. C. & Webster, T. J. Increased osteoblast and decreased

Staphylococcus epidermidis functions on nanophase ZnO and TiO2. *J. Biomed. Mater. Res. - Part A* **78**, 595–604 (2006).

286. Padmavathy, N. & Vijayaraghavan, R. Enhanced bioactivity of ZnO nanoparticles—an antimicrobial study. *Sci. Technol. Adv. Mater.* **9**, 035004 (2008).
287. Trandafilović, L. V., Božanić, D. K., Dimitrijević-Branković, S., Luyt, A. S. & Djoković, V. Fabrication and antibacterial properties of ZnO-alginate nanocomposites. *Carbohydr. Polym.* **88**, 263–269 (2012).
288. Matinise, N., Fuku, X. G., Kaviyarasu, K., Mayedwa, N. & Maaza, M. ZnO nanoparticles via Moringa oleifera green synthesis: Physical properties & mechanism of formation. *Appl. Surf. Sci.* **406**, 339–347 (2017).
289. Abou Oualid, H., Amadine, O., Essamlali, Y., Dânoun, K. & Zahouily, M. Supercritical CO2 drying of alginate/zinc hydrogels: A green and facile route to prepare ZnO foam structures and ZnO nanoparticles. *RSC Adv.* **8**, 20737–20747 (2018).
290. Pal, A., Esumi, K. & Pal, T. Preparation of nanosized gold particles in a biopolymer using UV photoactivation. *J. Colloid Interface Sci.* **288**, 396–401 (2005).
291. Klingshirn, C. F., Meyer, B. K., Waag, A., Hoffmann, A. & Geurts, J. *Zinc Oxide*. vol. 120 (Springer Berlin Heidelberg, 2010).
292. Sharma, S., Sanpui, P., Chattopadhyay, A. & Ghosh, S. S. Fabrication of antibacterial silver nanoparticle - Sodium alginate-chitosan composite films. *RSC Adv.* **2**, 5837–5843 (2012).
293. Boyer, F., Guazzelli, É. & Pouliquen, O. Unifying suspension and granular rheology. *Phys. Rev. Lett.* **107**, 188301 (2011).
294. van der Vaart, K. *et al.* Rheology of concentrated soft and hard-sphere suspensions. *J. Rheol. (N. Y. N. Y).* **57**, 1195–1209 (2013).
295. Kanmani, P. & Rhim, J. W. Properties and characterization of bionanocomposite films prepared with various biopolymers and ZnO nanoparticles. *Carbohydr. Polym.* **106**, 190–199 (2014).
296. Salarbashi, D. *et al.* Development of new active packaging film made from a soluble soybean polysaccharide incorporating ZnO nanoparticles. *Carbohydr. Polym.* **140**, 220–227 (2016).
297. Zheng, Y., Monty, J. & Linhardt, R. J. Polysaccharide-based nanocomposites and their applications. *Carbohydr. Res.* **405**, 23–32 (2015).
298. Carp, O. *et al.* Biopolymer starch mediated synthetic route of multi-spheres and donut ZnO structures. *Carbohydr. Polym.* **115**, 285–293 (2015).

299. Gómez-Ordóñez, E. & Rupérez, P. FTIR-ATR spectroscopy as a tool for polysaccharide identification in edible brown and red seaweeds. *Food Hydrocoll.* **25**, 1514–1520 (2011).
300. Leal, D., Matsuhiro, B., Rossi, M. & Caruso, F. FT-IR spectra of alginic acid block fractions in three species of brown seaweeds. *Carbohydr. Res.* **343**, 308–316 (2008).
301. Li, D., Chen, L., Yi, X., Zhang, X. & Ye, N. Pyrolytic characteristics and kinetics of two brown algae and sodium alginate. *Bioresour. Technol.* **101**, 7131–7136 (2010).
302. Ho, D. L., Hammouda, B., Kline, S. R. & Chen, W.-R. Unusual phase behavior in mixtures of poly(ethylene oxide) and ethyl alcohol. *J. Polym. Sci. Part B Polym. Phys.* **44**, 557–564 (2006).
303. Vadukumpully, S., Paul, J., Mahanta, N. & Valiyaveettil, S. Flexible conductive graphene/poly(vinyl chloride) composite thin films with high mechanical strength and thermal stability. *Carbon N. Y.* **49**, 198–205 (2011).
304. Ghasemlou, M., Khodaiyan, F. & Oromiehie, A. Physical, mechanical, barrier, and thermal properties of polyol-plasticized biodegradable edible film made from kefiran. *Carbohydr. Polym.* **84**, 477–483 (2011).
305. Al-Turaif, H. A. Effect of nano TiO2 particle size on mechanical properties of cured epoxy resin. *Prog. Org. Coatings* **69**, 241–246 (2010).
306. Islam, M. N., Rahman, M. R., Haque, M. M. & Huque, M. M. Physico-mechanical properties of chemically treated coir reinforced polypropylene composites. *Compos. Part A Appl. Sci. Manuf.* **41**, 192–198 (2010).
307. Agache, P. G., Monneur, C., Leveque, J. L. & De Rigal, J. Mechanical properties and Young's modulus of human skin in vivo. *Arch. Dermatol. Res.* **269**, 221–232 (1980).
308. Pailler-Mattei, C., Bec, S. & Zahouani, H. In vivo measurements of the elastic mechanical properties of human skin by indentation tests. **30**, 599–606 (2008).
309. Guo, S., Zhu, X. & Loh, X. J. Controlling cell adhesion using layer-by-layer approaches for biomedical applications. *Mater. Sci. Eng. C* **70**, 1163–1175 (2017).
310. Roy, N., Saha, N., Humpolicek, P. & Saha, P. Permeability and biocompatibility of novel medicated hydrogel wound dressings. *Soft Mater.* **8**, 338–357 (2010).
311. Patil, B. S., Mastiholimath, V. S. & Kulkarni, A. R. Development and evaluation of psyllium seed husk polysaccharide based wound dressing films. *Orient. Pharm. Exp. Med.* **11**, 123–129 (2011).
312. Kusum Devi, V., Saisivam, S., Maria, G. R. & Deepti, P. U. Design and evaluation of matrix diffusion controlled transdermal patches of verapamil hydrochloride. *Drug Dev.*

Ind. Pharm. **29**, 495–503 (2003).

313. Willershausen, I. *et al.* Non-cross-linked collagen type I/III materials enhance cell proliferation: In vitro and in vivo evidence. *J. Appl. Oral Sci.* **22**, 29–37 (2014).
314. Vandebriel, R. J. & De Jong, W. H. A review of mammalian toxicity of ZnO nanoparticles. *Nanotechnol. Sci. Appl.* **5**, 61–71 (2012).
315. Collier, T. O., Jenney, C. R., DeFife, K. M. & Anderson, J. M. Protein adsorption on chemically modified surfaces. *Biomed. Sci. Instrum.* **33**, 178–183 (1997).
316. Deepthi, S., Nivedhitha Sundaram, M., Deepti Kadavan, J. & Jayakumar, R. Layered chitosan-collagen hydrogel/aligned PLLA nanofiber construct for flexor tendon regeneration. *Carbohydr. Polym.* **153**, 492–500 (2016).
317. Diamond, M. P. Clinical implications of postsurgical adhesions. *Hum. Reprod. Update* **7**, 567–576 (2001).
318. Yao, C., Li, X., Neoh, K. G., Shi, Z. & Kang, E. T. Surface modification and antibacterial activity of electrospun polyurethane fibrous membranes with quaternary ammonium moieties. *J. Memb. Sci.* **320**, 259–267 (2008).
319. Li, Z. *et al.* Adsorption of congo red and methylene blue dyes on an ashitaba waste and a walnut shell-based activated carbon from aqueous solutions: Experiments, characterization and physical interpretations. *Chem. Eng. J.* **388**, 124263 (2020).
320. Rożek, P., Król, M. & Mozgawa, W. Lightweight geopolymer-expanded glass composites for removal of methylene blue from aqueous solutions. *Ceram. Int.* **46**, 19785–19791 (2020).
321. Alver, E., Metin, A. Ü. & Brouers, F. Methylene blue adsorption on magnetic alginate/rice husk bio-composite. *Int. J. Biol. Macromol.* **154**, 104–113 (2020).
322. Donati, I. *et al.* New hypothesis on the role of alternating sequences in calcium-alginate gels. *Biomacromolecules* **6**, 1031–1040 (2005).
323. Amran Tengku Mohd, T. *et al.* Measurement of Streaming Potential in Downhole Application: An Insight for Enhanced Oil Recovery Monitoring. in *MATEC Web of Conferences* vol. 87 (EDP Sciences, 2016).
324. Li, L., Fang, Y., Vreeker, R., Appelqvist, I. & Mendes, E. Reexamining the egg-box model in calcium - Alginate gels with X-ray diffraction. *Biomacromolecules* **8**, 464–468 (2007).
325. ter Horst, B., Chouhan, G., Moiemen, N. S. & Grover, L. M. Advances in keratinocyte delivery in burn wound care. *Adv. Drug Deliv. Rev.* **123**, 18–32 (2018).
326. Ho, H. O., Hsiao, C. C., Sokoloski, T. D., Chen, C. Y. & Sheu, M. T. Fibrin-based drug

delivery systems III: The evaluation of the release of macromolecules from microbeads. *J. Control. Release* **34**, 65–70 (1995).

327. Mesquida, P. *et al.* Evaluation of surface charge shift of collagen fibrils exposed to glutaraldehyde. *Sci. Rep.* **8**, 1–7 (2018).
328. Sarker, B. *et al.* Evaluation of fibroblasts adhesion and proliferation on alginate-gelatin crosslinked hydrogel. *PLoS One* **9**, (2014).
329. Habibah, T. U. & Salisbury, H. G. *Dental Materials, Hydroxyapatite*. *StatPearls* (StatPearls Publishing, 2018).
330. Sensini, A. *et al.* Morphologically bioinspired hierarchical nylon 6,6 electrospun assembly recreating the structure and performance of tendons and ligaments. *Med. Eng. Phys.* **71**, 79–90 (2019).
331. Suwantong, O. Biomedical applications of electrospun polycaprolactone fiber mats. *Polym. Adv. Technol.* **27**, 1264–1273 (2016).
332. Nouri, J. M., Umur, H. & Whitelaw, J. H. Flow of Newtonian and Non-Newtonian Fluids in Concentric and Eccentric Annuli. *J. Fluid Mech.* **253**, 617–641 (1993).
333. Ballal, B. Y. & Rivlin, R. S. Flow of a Newtonian fluid between eccentric rotating cylinders: Inertial effects. *Arch. Ration. Mech. Anal.* **62**, 237–294 (1976).
334. Bordes, C. *et al.* Determination of poly(ε-caprolactone) solubility parameters: Application to solvent substitution in a microencapsulation process. *Int. J. Pharm.* **383**, 236–243 (2010).
335. Pingping, Z., Haiyang, Y. & Shiqiang, W. Viscosity behavior of poly-€-caprolactone (PCL)/poly(vinyl chloride) (PVC) blends in various solvents. *Eur. Polym. J.* **34**, 91–94 (1998).
336. Ho, M. H. *et al.* Effects of an Acetic Acid and Acetone Mixture on the Characteristics and Scaffold–Cell Interaction of Electrospun Polycaprolactone Membranes. *Appl. Sci.* **9**, 4350 (2019).
337. Van Der Schueren, L., De Schoenmaker, B., Kalaoglu, Ö. I. & De Clerck, K. An alternative solvent system for the steady state electrospinning of polycaprolactone. *Eur. Polym. J.* **47**, 1256–1263 (2011).
338. Augustine, R., Kalarikkal, N. & Thomas, S. Clogging-Free Electrospinning of Polycaprolactone Using Acetic Acid/Acetone Mixture. *Polym. - Plast. Technol. Eng.* **55**, 518–529 (2016).
339. Potrč, T. *et al.* Electrospun polycaprolactone nanofibers as a potential oromucosal delivery system for poorly water-soluble drugs. *Eur. J. Pharm. Sci.* **75**, 101–113 (2015).

340. Hou, L. & Wu, P. Exploring the hydrogen-bond structures in sodium alginate through two-dimensional correlation infrared spectroscopy. *Carbohydr. Polym.* **205**, 420–426 (2019).
341. Pucić, I. & Jurkin, T. FTIR assessment of poly(ethylene oxide) irradiated in solid state, melt and aqeuous solution. *Radiat. Phys. Chem.* **81**, 1426–1429 (2012).
342. Unger, M., Vogel, C. & Siesler, H. W. Molecular weight dependence of the thermal degradation of poly(ε-caprolactone): A thermogravimetric differential thermal fourier transform infrared spectroscopy study. *Appl. Spectrosc.* **64**, 805–809 (2010).
343. Ponjavic, M. *et al.* Degradation behaviour of PCL/PEO/PCL and PCL/PEO block copolymers under controlled hydrolytic, enzymatic and composting conditions. *Polym. Test.* **57**, 67–77 (2017).
344. Labet, M. & Thielemans, W. Synthesis of polycaprolactone: A review. *Chem. Soc. Rev.* **38**, 3484–3504 (2009).
345. Saghazadeh, S. *et al.* Drug delivery systems and materials for wound healing applications. *Adv. Drug Deliv. Rev.* **127**, 138–166 (2018).
346. Liu, M., Duan, X. P., Li, Y. M., Yang, D. P. & Long, Y. Z. Electrospun nanofibers for wound healing. *Mater. Sci. Eng. C* **76**, 1413–1423 (2017).
347. Gomes, S. R. *et al.* In vitro and in vivo evaluation of electrospun nanofibers of PCL, chitosan and gelatin: A comparative study. *Mater. Sci. Eng. C* **46**, 348–358 (2015).
348. Baker, S. R., Banerjee, S., Bonin, K. & Guthold, M. Determining the mechanical properties of electrospun poly-ε-caprolactone (PCL) nanofibers using AFM and a novel fiber anchoring technique. *Mater. Sci. Eng. C* **59**, 203–212 (2016).
349. Croisier, F. *et al.* Mechanical testing of electrospun PCL fibers. *Acta Biomater.* **8**, 218–224 (2012).
350. Simonin, J. P. On the comparison of pseudo-first order and pseudo-second order rate laws in the modeling of adsorption kinetics. *Chem. Eng. J.* **300**, 254–263 (2016).
351. Belhouchat, N., Zaghouane-Boudiaf, H. & Viseras, C. Removal of anionic and cationic dyes from aqueous solution with activated organo-bentonite/sodium alginate encapsulated beads. *Appl. Clay Sci.* **135**, 9–15 (2017).
352. Jeon, Y. S., Lei, J. & Kim, J. H. Dye adsorption characteristics of alginate/polyaspartate hydrogels. *J. Ind. Eng. Chem.* **14**, 726–731 (2008).
353. Mustapha, S. *et al.* Adsorption isotherm, kinetic and thermodynamic studies for the removal of Pb(II), Cd(II), Zn(II) and Cu(II) ions from aqueous solutions using Albizia lebbeck pods. *Appl. Water Sci.* **9**, 3 (2019).

354. Mushtaq, M., Bhatti, H. N., Iqbal, M. & Noreen, S. Eriobotrya japonica seed biocomposite efficiency for copper adsorption: Isotherms, kinetics, thermodynamic and desorption studies. *J. Environ. Manage.* **176**, 21–33 (2016).

355. Jain, D. & Bar-Shalom, D. Alginate drug delivery systems: Application in context of pharmaceutical and biomedical research. *Drug Dev. Ind. Pharm.* **40**, 1576–1584 (2014).

356. Akindoyo, J. O. *et al.* Polyurethane types, synthesis and applications-a review. *RSC Adv.* **6**, 114453–114482 (2016).

357. Saunders, K. J. Polyurethanes. in *Organic Polymer Chemistry* 358–387 (Springer Netherlands, 1988). doi:10.1007/978-94-009-1195-6_16.

358. Petrović, Z. S. & Ferguson, J. Polyurethane elastomers. *Progress in Polymer Science* vol. 16 695–836 (1991).

359. Engels, H. W. *et al.* Polyurethanes: Versatile materials and sustainable problem solvers for today's challenges. *Angew. Chemie - Int. Ed.* **52**, 9422–9441 (2013).

360. Banea, M. D., da Silva, L. F. M. & Campilho, R. D. S. G. The Effect of Adhesive Thickness on the Mechanical Behavior of a Structural Polyurethane Adhesive. *J. Adhes.* **91**, 331–346 (2015).

361. Garcia Gonzalez, M. N., Levi, M. & Turri, S. Development of polyester binders for the production of sustainable polyurethane coatings: Technological characterization and life cycle assessment. *J. Clean. Prod.* **164**, 171–178 (2017).

362. Chen, R. *et al.* Transparent thermoplastic polyurethane air filters for efficient electrostatic capture of particulate matter pollutants. *Nanotechnology* **30**, 015703 (2019).

363. Rahman Bhuiyan, M. A., Wang, L., Shaid, A., Shanks, R. A. & Ding, J. Polyurethane-aerogel incorporated coating on cotton fabric for chemical protection. *Prog. Org. Coatings* **131**, 100–110 (2019).

364. Zhang, S. *et al.* Ultrasensitive and Highly Compressible Piezoresistive Sensor Based on Polyurethane Sponge Coated with a Cracked Cellulose Nanofibril/Silver Nanowire Layer. *ACS Appl. Mater. Interfaces* **11**, 10922–10932 (2019).

365. Joseph, J., Patel, R. M., Wenham, A. & Smith, J. R. Biomedical applications of polyurethane materials and coatings. *Trans. IMF* **96**, 121–129 (2018).

366. Kucinska-Lipka, J., Gubanska, I., Janik, H. & Sienkiewicz, M. Fabrication of polyurethane and polyurethane based composite fibres by the electrospinning technique for soft tissue engineering of cardiovascular system. *Mater. Sci. Eng. C* **46**, 166–176 (2015).

367. Xu, Y., Sheng, J., Yin, X., Yu, J. & Ding, B. Functional modification of breathable polyacrylonitrile/polyurethane/TiO2 nanofibrous membranes with robust ultraviolet resistant and waterproof performance. *J. Colloid Interface Sci.* **508**, 508–516 (2017).
368. AMINI, G., SAMIEE, S., GHAREHAGHAJI, A. A. & HAJIANI, F. Fabrication of Polyurethane and Nylon 66 Hybrid Electrospun Nanofiber Layer for Waterproof Clothing Applications. *Adv. Polym. Technol.* **35**, 419–427 (2016).
369. Byrne, F. P. *et al.* Tools and techniques for solvent selection: green solvent selection guides. *Sustain. Chem. Process.* **4**, 1–24 (2016).
370. Kairytė, A. *et al.* Cleaner production of polyurethane foam: Replacement of conventional raw materials, assessment of fire resistance and environmental impact. *J. Clean. Prod.* **183**, 760–771 (2018).
371. Honarkar, H. Waterborne polyurethanes: A review. *J. Dispers. Sci. Technol.* **39**, 507–516 (2018).
372. Yu, F., Xu, X., Lin, N. & Liu, X. Y. Structural engineering of waterborne polyurethane for high performance waterproof coatings. *RSC Adv.* **5**, 72544–72552 (2015).
373. Madbouly, S. A., Xia, Y. & Kessler, M. R. Rheological behavior of environmentally friendly castor oil-based waterborne polyurethane dispersions. *Macromolecules* **46**, 4606–4616 (2013).
374. Bhavsar, R. A. & Nehete, K. M. Rheological approach to select most suitable associative thickener for water-based polymer dispersions and paints. *J. Coatings Technol. Res.* **16**, 1089–1098 (2019).
375. Zhang, C., Feng, F. & Zhang, H. Emulsion electrospinning: Fundamentals, food applications and prospects. *Trends Food Sci. Technol.* **80**, 175–186 (2018).
376. Einarsson, J., Yang, M. & Shaqfeh, E. S. G. Einstein viscosity with fluid elasticity. *Phys. Rev. Fluids* **3**, 013301 (2018).
377. Kim, H. S. & Mason, T. G. Advances and challenges in the rheology of concentrated emulsions and nanoemulsions. *Adv. Colloid Interface Sci.* **247**, 397–412 (2017).
378. Gu, X. & Mather, P. T. Entanglement-based shape memory polyurethanes: Synthesis and characterization. *Polymer (Guildf).* **53**, 5924–5934 (2012).
379. Chagnon, L., Arnold, G., Giljean, S. & Brogly, M. Elastic recovery and creep properties of waterborne two-component polyurethanes investigated by micro-indentation. *Prog. Org. Coatings* **76**, 1337–1345 (2013).
380. Jeong, J. H., Han, Y. C., Yang, J. H., Kwak, D. S. & Jeong, H. M. Waterborne polyurethane modified with poly(ethylene glycol) macromer for waterproof breathable

coating. *Prog. Org. Coatings* **103**, 69–75 (2017).

381. Jayaramudu, T. *et al.* Adhesion properties of poly(ethylene oxide)-lignin blend for nanocellulose composites. *Compos. Part B Eng.* **156**, 43–50 (2019).
382. Chen, S.-H., Chou, P.-Y., Chen, Z.-Y. & Lin, F.-H. Electrospun Water-Borne Polyurethane Nanofibrous Membrane as a Barrier for Preventing Postoperative Peritendinous Adhesion. *Int. J. Mol. Sci.* **20**, 1625 (2019).
383. Banitaba, S. N., Semnani, D., Heydari-Soureshjani, E., Rezaei, B. & Ensafi, A. A. Effect of titanium dioxide and zinc oxide fillers on morphology, electrochemical and mechanical properties of the PEO-based nanofibers, applicable as an electrolyte for lithium-ion batteries. *Mater. Res. Express* **6**, 0850d6 (2019).
384. Xu, J. *et al.* Extremely Stretchable, Self-Healable Elastomers with Tunable Mechanical Properties: Synthesis and Applications. *Chem. Mater.* **30**, 6026–6039 (2018).
385. Wang, S. X. *et al.* Inherently flame-retardant rigid polyurethane foams with excellent thermal insulation and mechanical properties. *Polymer (Guildf).* **153**, 616–625 (2018).
386. Nguyen Dang, L. *et al.* Synthesis and characterization of castor oil-segmented thermoplastic polyurethane with controlled mechanical properties. *Eur. Polym. J.* **81**, 129–137 (2016).
387. Kim, H. H., Kim, M. J., Ryu, S. J., Ki, C. S. & Park, Y. H. Effect of fiber diameter on surface morphology, mechanical property, and cell behavior of electrospun poly(ε-caprolactone) mat. *Fibers Polym.* **17**, 1033–1042 (2016).
388. Kurusu, R. S. & Demarquette, N. R. Surface modification to control the water wettability of electrospun mats. *Int. Mater. Rev.* **64**, 249–287 (2019).
389. Szewczyk, P. *et al.* Roughness and Fiber Fraction Dominated Wetting of Electrospun Fiber-Based Porous Meshes. *Polymers (Basel).* **11**, 34 (2018).
390. Kalantari, K., Afifi, A. M., Jahangirian, H. & Webster, T. J. Biomedical applications of chitosan electrospun nanofibers as a green polymer – Review. *Carbohydr. Polym.* **207**, 588–600 (2019).
391. Balagangadharan, K., Dhivya, S. & Selvamurugan, N. Chitosan based nanofibers in bone tissue engineering. *Int. J. Biol. Macromol.* **104**, 1372–1382 (2017).
392. Duan, B., Dong, C. & Yuan, X. Electrospinning of chitosan solutions in acetic acid with poly (ethylene oxide). *J. Biomater. Sci. , Polym. Ed.* **15**, 797–811 (2004).
393. Nezarati, R. M., Eifert, M. B. & Cosgriff-Hernandez, E. Effects of Humidity and Solution Viscosity on Electrospun Fiber Morphology. *Tissue Eng. Part C Methods* **19**, 810–819 (2013).

394. Levitt, A. S., Vallett, R., Dion, G. & Schauer, C. L. Effect of electrospinning processing variables on polyacrylonitrile nanoyarns. *J. Appl. Polym. Sci.* **135**, 46404 (2018).

395. Nie, J., Wang, Z. & Hu, Q. Difference between Chitosan Hydrogels via Alkaline and Acidic Solvent Systems. *Sci. Rep.* **6**, 36053 (2016).

396. Vega-Cázarez, C. A. *et al.* Preparation and Properties of Chitosan–PVA Fibers Produced by Wet Spinning. *J. Polym. Environ.* **26**, 946–958 (2018).

397. Mirabedini, A., Foroughi, J., Thompson, B. & Wallace, G. G. Fabrication of Coaxial Wet-Spun Graphene-Chitosan Biofibers. *Adv. Eng. Mater.* **18**, 284–293 (2016).

398. Ratnayake, J. T. B., Mucalo, M. & Dias, G. J. Substituted hydroxyapatites for bone regeneration: A review of current trends. *J. Biomed. Mater. Res. Part B Appl. Biomater.* **105**, 1285–1299 (2017).

399. Paulino, A. T., Simionato, J. I., Garcia, J. C. & Nozaki, J. Characterization of chitosan and chitin produced from silkworm crysalides. *Carbohydr. Polym.* **64**, 98–103 (2006).

400. Sini, T. K., Santhosh, S. & Mathew, P. T. Study on the production of chitin and chitosan from shrimp shell by using Bacillus subtilis fermentation. *Carbohydr. Res.* **342**, 2423–2429 (2007).

401. Ibrahim, M., Osman, O. & Mahmoud, A. A. Spectroscopic Analyses of Cellulose and Chitosan: FTIR and Modeling Approach. *J. Comput. Theor. Nanosci.* **8**, 117–123 (2011).

402. Cheng, F., Gao, J., Wang, L. & Hu, X. Composite chitosan/poly(ethylene oxide) electrospun nanofibrous mats as novel wound dressing matrixes for the controlled release of drugs. *J. Appl. Polym. Sci.* **132**, n/a-n/a (2015).

403. Wu, J., Lin, H. & Meredith, J. C. Poly(ethylene oxide) bionanocomposites reinforced with chitin nanofiber networks. *Polymer (Guildf).* **84**, 267–274 (2016).

404. Aqil, A. *et al.* Preparation and characterizations of EGDE crosslinked chitosan electrospun membranes. *Clin. Hemorheol. Microcirc.* **60**, 39–50 (2015).

405. Varum, K. M., Ottoy, M. H. & Smidsrod, O. Acid hydrolysis of chitosans. *Carbohydr. Polym.* **46**, 89–98 (2001).

406. Il'ina, A. V. & Varlamov, V. P. Hydrolysis of chitosan in lactic acid. *Appl. Biochem. Microbiol.* **40**, 300–303 (2004).

407. Dorsett-Martin, W. A. Rat models of skin wound healing: A review. *Wound Repair Regen.* **12**, 591–599 (2004).

408. Janis, J. E. & Harrison, B. Wound Healing. *Plast. Reconstr. Surg.* **133**, 199e-207e (2014).

409. Azimi, B. *et al.* Bio-based electrospun fibers for wound healing. *J. Funct. Biomater.* **11**, 67 (2020).
410. Hivechi, A., Hajir Bahrami, S. & Siegel, R. A. Investigation of morphological, mechanical and biological properties of cellulose nanocrystal reinforced electrospun gelatin nanofibers. *Int. J. Biol. Macromol.* **124**, 411–417 (2019).
411. Baniasadi, M. *et al.* Correlation of annealing temperature, morphology, and electro-mechanical properties of electrospun piezoelectric nanofibers. *Polymer (Guildf).* **127**, 192–202 (2017).
412. Li, Y. *et al.* Surface Wettability Switched Cell Adhesion and Detachment on Conducting Polymer Nanoarray. *Adv. Mater. Interfaces* **3**, 1600598 (2016).
413. Cacicedo, M. L. *et al.* Chitosan-bacterial cellulose patch of ciprofloxacin for wound dressing: Preparation and characterization studies. *Int. J. Biol. Macromol.* **147**, 1136–1145 (2020).
414. Mohebbi, S. *et al.* Chitosan in Biomedical Engineering: A Critical Review. *Curr. Stem Cell Res. Ther.* **14**, 93–116 (2018).
415. Pellá, M. C. G. *et al.* Chitosan-based hydrogels: From preparation to biomedical applications. *Carbohydr. Polym.* **196**, 233–245 (2018).
416. Wegrzynowska-Drzymalska, K. *et al.* Crosslinking of Chitosan with Dialdehyde Chitosan as a New Approach for Biomedical Applications. *Materials (Basel).* **13**, 3413 (2020).
417. Derakhshandeh, H., Kashaf, S. S., Aghabaglou, F., Ghanavati, I. O. & Tamayol, A. Smart Bandages: The Future of Wound Care. *Trends Biotechnol.* **36**, 1259–1274 (2018).
418. Bagherifard, S. *et al.* Dermal Patch with Integrated Flexible Heater for on Demand Drug Delivery. *Adv. Healthc. Mater.* **5**, 175–184 (2016).
419. Hara, M. & Nakajima, A. Anomalies in Light Scattering from Polyelectrolyte in Semi-Dilute Solution Region. *Polym. J.* **12**, 711–718 (1980).
420. Jeon, B. J. & Muthukumar, M. Determination of molecular weights in polyelectrolyte mixtures using polymer translocation through a protein nanopore. *ACS Macro Lett.* **3**, 911–915 (2014).
421. Costanzo, S. *et al.* Shear and Extensional Rheology of Polystyrene Melts and Solutions with the Same Number of Entanglements. *Macromolecules* **49**, 3925–3935 (2016).
422. Xu, X., Chen, J. & An, L. Shear thinning behavior of linear polymer melts under shear flow via nonequilibrium molecular dynamics. *J. Chem. Phys.* **140**, 174902 (2014).
423. Torres, M. D., Hallmark, B. & Wilson, D. I. Effect of concentration on shear and

extensional rheology of guar gum solutions. *Food Hydrocoll.* **40**, 85–95 (2014).

424. Wolf, B. A. Polyelectrolytes revisited: Reliable determination of intrinsic viscosities. *Macromol. Rapid Commun.* **28**, 164–170 (2007).
425. Wolf, B. A. Coil overlap in moderately concentrated polyelectrolyte solutions: Effects of self-shielding as compared with salt-shielding as a function of chain length. *RSC Adv.* **6**, 38004–38011 (2016).
426. Fedors, R. F. An equation suitable for describing the viscosity of dilute to moderately concentrated polymer solutions. *Polymer (Guildf).* **20**, 225–228 (1979).
427. Masuelli, M. A. & Illanes, C. O. Review of the characterization of sodium alginate by intrinsic viscosity measurements . Comparative analysis between conventional and single point methods. *Int. J. Biomater. Sci. Eng.* **1**, 1–11 (2014).
428. Morris, E. R., Cutler, A. N., Ross-Murphy, S. B., Rees, D. A. & Price, J. Concentration and shear rate dependence of viscosity in random coil polysaccharide solutions. *Carbohydr. Polym.* **1**, 5–21 (1981).
429. Clasen, C. & Kulicke, W.-M. Determination of viscoelastic and rheo-optical material functions of water-soluble cellulose derivatives. *Prog. Polym. Sci.* **26**, 1839–1919 (2001).
430. Ramos, P. E. *et al.* Effect of alginate molecular weight and M/G ratio in beads properties foreseeing the protection of probiotics. *Food Hydrocoll.* **77**, 8–16 (2018).
431. Jiao, W. *et al.* Effects of Molecular Weight and Guluronic Acid/Mannuronic Acid Ratio on the Rheological Behavior and Stabilizing Property of Sodium Alginate. *Molecules* **24**, 4374 (2019).
432. Pathak, V. M. & Navneet. Review on the current status of polymer degradation: a microbial approach. *Bioresour. Bioprocess.* **4**, 1–31 (2017).
433. Ratnawati, R., Prasetyaningrum, A. & Wardhani, D. H. Kinetics and thermodynamics of ultrasound-assisted depolymerization of K-carrageenan. *Bull. Chem. React. Eng. Catal.* **11**, 48–58 (2016).
434. Wang, Q., Ellis, P. R. & Ross-Murphy, S. B. The stability of guar gum in an aqueous system under acidic conditions. *Food Hydrocoll.* **14**, 129–134 (2000).
435. Watthanaphanit, A. & Saito, N. Effect of polymer concentration on the depolymerization of sodium alginate by the solution plasma process. *Polym. Degrad. Stab.* **98**, 1072–1080 (2013).
436. Schittenhelm, N. & Kulicke, W.-M. Producing homologous series of molar masses for establishing structure-property relationships with the aid of ultrasonic degradation.

Macromol. Chem. Phys. **201**, 1976–1984 (2000).

437. Kulicke, W.-M., Kniewske, R. & Klein, J. Preparation, characterization, solution properties and rheological behaviour of polyacrylamide. *Prog. Polym. Sci.* **8**, 373–468 (1982).
438. Goodwin, D. J. *et al.* Ultrasonic degradation for molecular weight reduction of pharmaceutical cellulose ethers. *Carbohydr. Polym.* **83**, 843–851 (2011).
439. Dobrynin, A. V., Colby, R. H. & Rubinstein, M. Scaling Theory of Polyelectrolyte Solutions. *Macromolecules* **28**, 1859–1871 (1995).
440. Carrillo, J.-M. Y. & Dobrynin, A. V. Polyelectrolytes in Salt Solutions: Molecular Dynamics Simulations. *Macromolecules* **44**, 5798–5816 (2011).
441. Rinaudo, M. & Graebling, D. On the viscosity of sodium alginates in the presence of external salt. *Polym. Bull.* **15**, 253–256 (1986).
442. Liu, S., Ghosh, K. & Muthukumar, M. Polyelectrolyte solutions with added salt: A simulation study. *J. Chem. Phys.* **119**, 1813–1823 (2003).
443. Durand, A. Aqueous solutions of amphiphilic polysaccharides: Concentration and temperature effect on viscosity. *Eur. Polym. J.* **43**, 1744–1753 (2007).
444. Toth, G., Nagy, D., Bata, A. & Belina, K. Determination of polymer melts flow-activation energy a function of wide range shear rate. **1045**, 12040 (2018).